2001

Giant Herbig-Haro flows: identification and consequences

Stacy Lyall Mader
University of Wollongong

Giant Herbig–Haro Flows: Identification And Consequences

A thesis submitted in fulfilment of the
requirements for the award of the degree

DOCTOR OF PHILOSOPHY

from

UNIVERSITY OF WOLLONGONG

by

STACY LYALL MADER
M.Sc. (Hons), University of Wollongong, 1995
B.Sc. (Hons), University of Western Australia, 1993

Department of Engineering Physics
December, 2001

Contents

List of Figures

List of Tables

Abstract

Herbig-Haro (HH) objects are the optical components of outflows associated with young stellar objects. Characteristic spectra of HH objects include strong Hα and [SII] emission (6717/6737Å) which arises as the stellar wind from a source impacts with the surrounding interstellar medium. With the discovery that HH flows can attain sizes of a parsec or more, a natural course of action is to determine their distribution in star forming regions and what effect they have on the surrounding interstellar medium. As most known giant HH flows extend up to several degrees on the sky, only the largest CCD imaging cameras can provide the necessary field of view to identify new candidates. Enter the AAO/UKST Hα survey of the Southern Galactic Plane. With its large field of view ($4^\circ \times 4^\circ$) and superb imaging resolution (provided by the Hα filter and TechPan emulsion combination), the survey is particularly suited to identifying new HH objects and giant flows in southern star formation regions.

The first part of this thesis aims to determine the effectiveness of wide-field material from the ESO/SERC Southern Sky Atlases in characterising HH flows. Comparison of IIIaJ, IIIaF and IVN films shows they are extremely useful in characterising HH flows by distinguishing between reflection and emission nebulosity, tracing excitation conditions along a flows length and identifying their energy sources which can range from optically-visible T Tauri stars to deeply embedded Class 0 protostars. We present an ESO/SERC, CCD imaging and IRAS HIRES survey of a number of poorly–studied HH objects which have yet to have their energy source identified. For the majority of surveyed objects, we argue most are part of giant HH flows.

The second part of this thesis utilises AAO/UKST Hα wide-field material to search for giant HH flows in Orion L1630/L1641 and Canis Major OB1/R1. For the Orion region, we find a large number of giant HH flows associated with the L1641-N infrared cluster and one in the Ori I–2 cometary globule. Giant HH flows were also associated with V380 Ori and a Class 0 protostar near NGC 2023. For the Canis Major region, the HH flow from Z CMa was found to be much larger than previously thought. By combining AAO/UKST Hα and ^{13}CO data, we show that for the majority of giant flows in L1630 and L1641, there is at least one large-scale cavity projected against the terminal bow shock of the HH flow. By comparing the location of dense CS cores with respect to these cavities, we suggest that giant HH flows can account for the current and future modes of star formation within L1641.

Certification

I, Stacy L. Mader, declare that this thesis, submitted in full fulfilment of the requirements for the award of Doctor of Philosophy, in the Department of Engineering Physics, University of Wollongong, is wholly my own work unless otherwise referenced or acknowledged. The document has not been submitted for qualifications at any other academic institution.

Stacy Mader
17 December 2001

Acknowledgements

First, I would like to extend my gratitude to my thesis supervisor, Bill Zealey. In 1993 I arrived in his office for the first time and was asked what kind of project I was interested in. From a list of possibilities, I remember saying something along the lines of "those jet-things from young stars seem interesting!" Bill has always had an answer to a question, or a suggestion for a course of action. Over the years, this has prompted me to often go down avenues of research I wouldn't have thought of myself and I don't hesitate to say that if I didn't go down those little avenues, much of that presented in this document would not be here. Finally, I thank Bill for his insightful and clear perspective on my work, no matter how often I strayed from the starry path.

I would also like to thank the original Shenton House staff at the University of Western Australia - Jill Millroy, Amanda Bell, Sue Spiers and Gabrielle Garratt. These people gave me a chance to show I could achieve what I really wanted to do in life, despite an education system which told me I couldn't (or shouldn't). I am thankful for people like these looking out for people like me. I would also like to note that this research would not have been possible were it not for a scholarship provided to me by the Department of Employment, Education and Training. I wish to thank all those people in that department with whom I have talked to over the years. I also would like to thank the University of Wollongong for providing me with HECS assistance.

I would also like to thank Quentin Parker and Malcolm Hartley for allowing me near photographic survey material at the UK Schmidt Telescope. Thanks also go to Bill, Quentin and Mike Masheder for their efforts in getting me involved with the AAO/UKST Hα Survey and for their help on the work done in the Orion region. As much of the work presented here has stemmed from that wonderful survey, I look forward to my continued involvement with the survey and people involved.

Going back through old emails, I have found that over the years I have hounded many researchers about getting preprints, data or asking what they meant by something in published works. Although acknowledgements can be found throughout the text, I would like to add Bo Reipurth, Patrick Hartigan, Robina Optrupcek, Lawrence Chernin, Guillem Anglada, Leo Blitz and Maria Hunt. Within the Department of Engineering Physics at Wollongong University, I found an extremely helpful bunch of guys (Michael Lerch, Philip Randall and Andrew Warner) who got me into using LaTeX and always helped out when I needed it. Paul Nulsen often helped me on some aspect of our Unix workstations. I also appreciate help supplied from fellow "astro" students Vincent McIntyre, Mirjam Jonkman, Andrew Walker and

the rookie, Erik Muller. Whether it be installing a program, helping out on an observing run or just having a yarn, I thank them for their efforts.

Some of my closest and oldest friends deserve a mention as they were usually the ones who suffered the ups and downs I experienced over the years. They are: Maurice "Carlton Supporter" Agale, Lara "Men Tell Stupid Jokes" Brncic, Grant "Where's My Dockers Cap?" Dodd, Brian "Poor Form" Edmonds, Kane "Kactus" Hardingham, Brenda "Tell Me" Leung, Dick "Malonies Rules" Herman, Michelle "Missy" May, Gayle "Send A Joke" Smythe, Matthew "We Love It Up Here" Timbrell, Andrew "Chasey Rules" Weeks and last but not least, Trevor "Dettol Man" Wilson. Whether it be receiving a funny email, or having a beer or three in various places across Australia, these people most likely helped me keep my sanity. Thank you.

This thesis is dedicated to the following:

My family and friends
For putting up with me through it all

The staff at Shenton House
For giving me the chance

...and Aunty Angie
Who always made me laugh

Publications

Mader, S.L., Zealey, W.J., Parker, Q.A. & Masheder, M.R.W., 1999, **New Herbig–Haro Objects and Giant Flows in Orion**, MNRAS, 310, 331

Zealey, W.J. & Mader, S.L., 1998, **Image Digitisation of outflows and the AAO/UKST Hα survey**, PASA, 15, 165.

Zealey, W.J. & Mader, S.L., 1997, **Image Digitising and Analysis of Outflows from Young Stars**, PASA, 14, 200.

Chapter 1

Protostars and Outflows

1.1 An Introduction to Protostar Evolution

Out of the 100 billion or so stars in the Milky Way Galaxy, our nearest star, the Sun is considered to be a middle of the road main-sequence object with a surface temperature $\sim$ 6000 K and spectral type of G2. Despite this, the Sun shares a common origin with all stars: they were all born in molecular clouds. Representing the denser parts of the interstellar medium, molecular clouds come in all shapes and sizes. From the massive giant molecular clouds ($\sim 10^{4-6}\ M_{\odot}$) to relatively small Bok globules ($< 10^{3}\ M_{\odot}$), these regions posses sufficient density (10^{2-3} cm^{-3}) for stars to form. However, these regions are supported against gravitational collapse by the presence of magnetic fields[1]. For a neutral molecular cloud under magnetic support, the neutrals within only "feel" the field through the interaction of ionized particles, which are tied to the field. For sufficiently dense cores, cosmic rays alone dominate the ionization (McKee 1989) and so the weak ion-neutral coupling induces a systematic drift (or ambipolar diffusion) of neutrals with respect to the ions which separates the magnetic field from the neutral gas and allows the cloud to collapse via self-gravitation.

As the core contracts, the released gravitational energy is converted into thermal energy which allows the collapsing core to remain isothermal. As the core continues to contract, the interior temperature of the protostar becomes high enough for thermonuclear reactions to begin. With the conversion of hydrogen into helium, the resulting heat ($\sim 10^{6}$ K) and internal pressure

[1]Thermal and turbulent pressures are present as well, but magnetic fields play a far more important role in preventing core collapse.

are enough to halt contraction and achieve hydrostatic equilibrium. The hydrostatic core builds up its central mass via the accretion of material from the in-falling surrounding envelope. Before the onset of accretion, the mass of the surrounding envelope far exceeds that of the hydrostatic core. In the model of Shu, Adams & Lizano (1987), the rate of infall is constant ($\sim 1 \times 10^{-5}\ M_{\odot}\ \mathrm{yr}^{-1}$) in time. The T Tauri phase will continue for another $\sim 10^6$ years in which the star will continue to accrete mass from the remnant circumstellar disk.

Due to the extremely dense material surrounding newly-formed protostars, early researchers found it difficult to characterise the star formation process and constrain theory. However, the dusty circumstellar material surrounding the protostellar core becomes heated and re-radiates its thermal energy at infrared wavelengths. Therefore, it should not come as a surprise to learn that it is the amount of circumstellar dust surrounding a protostellar core which has been the key element in providing an evolutionary sequence. The currently favoured picture has been based on developments in wide field near-infrared detectors and sub-millimetre bolometers. For example, Class 0 sources (André, Ward–Thompson & Barsony 1993) are detectable for wavelengths $> 10\mu$m, usually in sub-millimetre continuum maps, while Classes I, II and III are classified on the slope $\alpha_{IR} = \mathrm{dlog}(\lambda F_{\lambda})/\mathrm{dlog}(\lambda)$ of their Spectral Energy Distributions (SEDs) for wavelengths long-ward of 2μm (Lada 1987; Wilking, Lada & Young 1989). Class I corresponds to sources with $\alpha_{IR} > 0$, Class II with $-2 < \alpha_{IR} < 0$, and Class III with $\alpha_{IR} < -2$.

Class 0 objects ($t \leq 10^4$ yr) show compact centimeter radio continuum and/or sub-millimetre emission. They display a high ratio of sub-millimetre to bolometric luminosity which suggests the envelope mass exceeds that of the central stellar mass. Their SEDs resemble a single temperature blackbody with $T \sim$ 15-30 K. Class I objects ($t \sim 1\text{-}2 \times 10^5$ yr) are detectable for $\lambda > 2\mu$m and represent evolved protostars. Their SEDs have been successfully modelled in terms of a protostellar object surrounded by both a disk and diffuse circumstellar envelope[2]. The stellar core mass exceeds that of the surrounding circumstellar envelope and the majority of their luminosity stems from accretion. Class II objects ($t \sim 10^6$ yr) correspond to the classical T Tauri stars which are surrounded by an optically thick circumstellar disk for $\lambda \leq 10\mu$m. Their SEDs can be characterised by broadened blackbodies with circumstellar disks smaller than those of the Class I objects. Finally, Class III objects ($t \sim 10^7$ yr) represent the weak-lined, or naked T Tauri objects (Walter 1987) which lack the emission phenomena (Hα emission and metallic line emission) but are strong X-ray emitters. Their SEDs are comparable

[2]Class 0 protostars display spherical circumstellar dust envelopes only (and no disk emission).

to a normal blackbody function with weak infrared excess, suggesting small amounts of circumstellar dust.

1.2 Outflows from Young Stellar Objects

From the theory of isolated star formation (Shu et al. 1987), a protostellar object forms via the accretion of mass from a large circumstellar envelope. It was of some surprise when observations showed young protostellar objects and T Tauri stars were loosing mass by ejecting gas along two narrow, oppositely directed jets. At first it was unknown how outflow fitted in with infall, but once it was realised that rotation of the parental cloud core causes material to spiral inward to add to the mass of the growing protostar, the core gains angular momentum from which a central protostar and flattened circumstellar disk are formed. Outflows provide a mechanism by which accreting protostars loose excess angular momentum. For the rest of this section, a brief introduction to the different components of outflows from protostars is presented. More detailed discussions can be found in Bachiller (1996), Cabrit, Raga & Gueth (1997), Reipurth & Raga (1999) and references therein.

1.2.1 Herbig-Haro Objects

During objective-prism and photographic surveys near the NGC 1999 region in Orion, Herbig (1950, 1951) and Haro (1952, 1953) noted the presence semi-stellar knots which emitted, among others, Balmer Hα, strong forbidden emission at [OI] (6363Å), [OII] (3726/3729Å), [SII] (6717/6731Å), faint emission at [FeII] (4244/4245Å), [OIII] (4959/5006Å) and permitted emission at CaII (4571Å). Herbig (1951) suggested these "blobs" were evidence of (1) faint blue, high-temperature stars or (2) an interaction of a late-type dwarf star with the surrounding nebular material. As these Herbig-Haro (HH) objects were located in the vicinity of dark clouds and the newly-discovered T Tauri stars (Joy 1942), they were thought to be related to the star formation process. From the detailed spectrophotometric analysis of HH objects, Böhm (1956), Osterbrock (1958) and Haro & Minkowski (1960) found that the forbidden-line emission takes place in regions where the average electron temperature and the mean electron density are $T_e \sim 10^4$ K and $n_e \sim 10^4$ cm^{-3} respectively.

In order to isolate excitation mechanism(s) in HH objects, Strom, Grasdalen & Strom (1974) suggested HH objects were reflection nebulae illuminated by very young variable emission-line stars. Although this hypothesis was disputed by Schmidt & Miller (1979), Strom et al. (1974) found their selection of HH objects display radial velocities as high as $\sim$ 150 km s^{-1}. Using proper motion data of HH 28/29 in the L1551 dark cloud, Cudworth & Herbig (1979) found that both objects have tangential velocities $\sim$ 145 km s^{-1}. They suggested if the proper motion vectors of these objects were extended backwards, the projected lines pass very close to the position of L1551 IRS5, which is a deeply embedded protostar identified by Strom, Strom & Vrba (1976) and a possible point of origin for HH 28/29. In a series of papers on the proper motions of HH objects, Herbig & Jones (1981; 1983) and Jones & Herbig (1974; 1982), showed that HH objects displayed motions away from embedded sources. For the HH 1/2 system, they found the velocity vectors pointing away from the now accepted driving source HH 1/2 VLA1 (Pravdo et al. 1985; Rodríguez et al. 1990)[3]. By the early to mid 1980's, it was generally accepted that HH objects were evidence of wind ejection taking place in the vicinity of young stellar objects.

A major step in characterising HH objects was provided by Schwartz (1978). By comparing the observed emission-line spectrum of HH 1 and the N49 supernova in the Large Magellanic Cloud, he proposed the emission could be produced by a supersonic wind ejected from a nearby young stellar object interacting with small ambient cloudlets. As the wind interacts with these cloudlets, a bow shock (facing the source) forms and the resulting radiating gas from this bow shock cools and emits the observable lines seen in HH objects. Since the shocked-cloudlet model of Schwartz, HH objects have been modelled as plane-parallel shocks (Dopita 1978; Raymond 1979; Hartigan, Morse & Raymond 1995) and bow shocks (Hartmann & Raymond 1984; Raga & Böhm 1987; Cantó & Raga 1998). The currently favoured model sees HH objects as "working surfaces", where the jet-like flow interacts directly with the surrounding environment (Raga 1988; Blondin, Königl & Fryxell 1989; Raga & Cabrit 1993; Raga et al. 1993). Within the working surface, there are two shocks in operation: a bow shock which accelerates and excites ambient material and the Mach disk (jet shock) which decelerates jet material impinging on the ambient medium. High pressure gas exists between these two shocks and becomes ejected sideways and forms an envelope around the HH jet. As this envelope has a radius much larger than the radius of the jet beam, it presents a larger area to the surrounding ambient material which is entrained and seen as the CO outflow (see Raga & Cabrit 1993 and Raga et al. 1993 for more details).

[3]In fact, the source is part of a binary system with the other component (HH 1/2 VLA2) driving HH 144, which is almost perpendicular to the HH 1/2 outflow (see Reipurth et al. 1993; et al. 2000.)

From the early photographic plates (Herbig 1974) and CCD imaging (Mundt & Fried 1983), it was apparent that HH objects display morphologies ranging from clumpy knots to highly-collimated jet-like structures emanating from T Tauri stars or low-luminosity embedded sources. Some of the most highly-collimated jets are found in HH 47 (Dopita, Evans & Schwartz 1982; see chapter 2, Figure 2.4), HH 34 (Reipurth et al. 1986; see chapter 2, Figure 2.2) and HH 111 (Reipurth, Raga & Heathcote 1992).

1.2.2 Near-Infrared H_2 (2.12μm) Outflows

Although HH objects and jets represent the optical component of outflows, there must also be unseen shocks occurring when outflows from extremely young protostars (such as Class 0 objects) interact with their parental molecular cloud. As the bulk of all molecular clouds are composed of molecular hydrogen (H_2), do we see evidence of shock-excited emission? The first such evidence of shock-excited H_2 emission in a protostellar outflow was identified by Beckwith et al. (1978), who identified H_2 (2.12μm), $\nu = 1 \rightarrow 0$ S(1) emission associated with the HH nebulosity surrounding T Tau. Later, Elias (1980) detected H_2 emission associated with six HH objects and from line intensities, suggested that the H_2 emission arises from moderate-density ($n \sim 10^4$ cm^{-3}), shock-heated gas moving with velocities $\sim$ 15 km s^{-1}. With the detection of H_2 in HH objects, it was unknown how both the optical and near-infrared emission could be associated with the same shocked region. As the optical spectra of HH objects usually require velocities $>>$ 40 km s^{-1}, it was expected that such velocities would dissociate any H_2. For a number of HH flows, Zealey et al. (1986), Zinnecker et al. (1989) and Stapelfeldt et al. (1991) showed that the H_2-emitting regions are usually located at (1) the wings of bow shocks which form at the working surfaces of the protostellar jet or (2) boundary layers where external molecular gas is entrained along the jet and/or at the outflow/cavity wall boundary[4].

H_2 (2.12μm) emission arises in low-velocity ($\sim$ 40-50 km s^{-1}) post-shock regions which are located in dense media ($n \leq 10^6$ cm^{-3}) with temperatures $\sim 10^3$ K. However, the exciting mechanism of H_2 in protostellar outflows is unknown, with continuous (C-type) and jump (J-type) shocks being used to describe line intensities (Smith 1993; 1994). For C-type shocks, a magnetised medium of low ionization is required to display a continuous change in shock properties within the shock structure. J-type shocks require high velocities which result in a jump in various parameters such as density, temperature and pressure. For this to occur, the medium must be of higher ionization

[4]See Figure 2.5 (chapter 2) which shows this in the HH 46/47 outflow.

and have a lower magnetic field strength than that seen in C-type shocks. In a number of HH flows, the H_2 emission has been modelled as either C-type (Ceph E; Eislöffel et al. 1996), J-type (HH 91; Gredel 1994), or both (HH 1; Noriega-Crespo & Garnavich 1994). For HH 7, it has been shown that the H_2 emission can be modelled in terms of C-type bow shocks and fluorescence (Fernandes & Brand 1995).

Recently, a number of protostellar outflows have been identified purely by their H_2 (2.12μm) emission. For example, the Class 0 protostar IC 348 IR (McCaughrean, Rayner & Zinnecker 1994) drives a highly-collimated jet seen only in the infrared with faint outer bow-shocks seen on deep CCD images. The absence of optical HH lines such as Hα and [SII] can be explained if the outflow has not yet broken out of its parental molecular cloud. Similar to IC 348 IR is IRAS 00342+6347/HH 288 (McCaughrean 1997), which is associated with very faint HH emission at the most distant bow shocks. This suggests the flow is just beginning to break out of its parental molecular cloud.

1.2.3 Molecular CO outflows

With the introduction of millimetre-wave receivers in the 70's, an important discovery was made when high-velocity carbon monoxide (CO) gas was discovered towards the Kleinmann-Low Infrared Nebula in Orion (Zuckerman et al. 1976; Kwan & Scoville 1976). When Snell, Loren & Plambeck (1980) mapped the L1551 region in Taurus, they found a double-lobed CO structure extending in opposite directions from the deeply embedded protostar, L1551 IRS5. This was the first detection of a molecular, bipolar outflow. They interpreted the CO lobes as dense shells of material swept up from a stellar wind originating from L1551 IRS5. Also located in the L1551 cloud are the objects HH 28/29 and HH 102[5] (Herbig 1974; Strom et al. 1974). Snell et al. (1980) found that all of these objects lie within the southwest (blue-shifted) CO lobe and suggested both HH objects and CO outflow may have a common origin[6].

To begin with, bipolar CO outflows were modelled in terms of molecular shells driven by wide-angled winds (Snell et al. 1980) or steady-state filled

[5]This is actually a large amorphous reflection nebula illuminated by L1551 IRS5.

[6]Recent work by Devine, Reipurth & Bally (1999) suggests HH 28/29 are driven by L1551 NE which may also energize the southern part of the blue-shifted lobe of the L1551 outflow. Also, L1551 IRS5 is a binary which drives two distinct jets aimed towards HH 102 on the northern rim of the outflow cavity. Therefore, the blue-shifted lobe of the L1551 outflow is probably powered by several sources.

flows with internal stratification (Levreault 1988a,b; Cabrit & Bertout 1990). As more young stellar objects were found associated with HH objects, jets and bipolar CO flows (e.g Bally & Lada 1983; Edwards & Snell 1983; 1984), the idea of "jet-driven" CO outflows became increasingly attractive. Masson & Chernin (1993) showed how optically-visible HH jets were able to drive CO outflows with bow shocks sweeping up ambient material and accelerating forward. The CO outflow is identified with this swept-up material. Although their model produces outflow cavities that are narrower than observed, they suggest a wandering jet can carve out a broad cavity. Raga & Cabrit (1993) proposed another model of CO outflows driven by highly-collimated jets. In their model, a bow shock compresses and sweeps up ambient material, which later re-expands into the cavity left behind and forms a turbulent wake identified as the CO outflow. As these bow shocks propagate further from the source, the decrease in cloud density causes them to expand and create widened cavities.

From $\sim$ 200 known molecular CO outflows (i.e. Bally & Lada 1983; Fukui 1989; Wu, Huang & He 1996), their morphologies tend to display either poorly-collimated systems like L1551 IRS5 (Snell et al. 1980) and L43-RNO 91 (Bence et al. 1998; see Figure 1.1c), or highly-collimated jet systems seen in L1448 (Bachiller et al. 1990), IRAS 03282+3035 (Bachiller, Martin-Pintada & Planesas 1991) and HH 211 (Gueth & Guilloteau 1999; see Figure 1.1a). For the latter group, the higher degree of collimation is also seen in CO and/or SiO emission which is of extremely high-velocity ($\sim$ 100 km s^{-1}) and rather than being continuous, displays well-defined peaks (bullets) along the axis of the flow.

1.2.4 Radio Jets

The energy sources of outflows are usually detectable at centimetre wavelengths. In many instances, the emission is weak ($\sim$ mJy levels), compact and elongated. From computations of the spectral index[7], the emission from Class 0, Class I and Class II protostars is thermal free-free ($\alpha >$ -0.1) with a small contribution from heated dust which dominates at millimetre and infrared wavelengths. Negative spectral indices are characteristic of non-thermal sources seen in more evolved objects, such as radio-emitting, weak-lined T Tauri stars (Class III objects). For cases where the emission is elongated, the major axis of the elongation corresponds with the axis seen in larger scale H_2, HH and/or CO outflows. These thermal jets appear within 10 AU of the exciting star (Anglada et al. 1998) and provide evidence of high

[7]The spectral index, α, is defined as $S_\nu \propto \nu^\alpha$.

collimation even closer to the star than what is seen at optical and infrared wavelengths. In some cases, individual condensations within this distance of the driving source have been shown to move with velocities 600-1400 km s^{-1} (Martí, Rodríguez & Reipurth 1993; 1998). Thermal radio jets can be one-sided (VLA1623; Bontemps & André 1997), bipolar (HH 80/81; Martí et al. 1993; 1998) and even quadrupolar, in which case the system presumably contains two young stars (L723; Anglada, Rodríguez & Torrelles 1996, HH 111; Reipurth et al. 1999).

1.2.5 Source and Outflow Evolution

For Class 0 objects, the majority of known sources display highly collimated molecular H_2/CO outflows which suggests infall and outflow are occurring at the same time. An example of this class is HH 211-mm (McCaughrean et al. 1994; see Figure 1.1a). In Class I objects, outflow begins to dominate over infall and the outflow is usually detectable at optical (HH objects), near-infrared (shocks) and millimetre (bipolar CO lobes) wavelengths. An example of this class includes RNO 43-mm (Bence, Richer & Padman 1996, Eisöffel & Mundt 1997; see Figure 1.1b). By the time a source is in the Class II stage, outflow is nearing completion (i.e., L43-RNO 91 (Schild, Weir & Mathieu 1989, Bence et al. 1998; see Figure 1.1c) and at the Class III stage, outflow activity has stopped completely. An example of this class is the X-ray source HBC 647/ROX 47A (André & Montmerle 1994).

The most striking differences between outflows from Class 0-II sources can be seen if one look at the jets, collimation and presence/absence of shock-excited emission. For example, HH 211 displays a highly collimated jet, a wandering jet may be present in RNO 43 while L43-RNO 91 does not show any evidence of a jet. The collimation (i.e., length to width ratio) decreases from 10 in HH 211, 8 in RNO 43, and $\sim$ 2 in L43-RNO 91. There is also a progressive decline in base cavity opening angles, with $\theta_c \sim 30°$ in HH 211 and $\theta_c > 90°$ in L43-RNO 91. As to the presence/absence of shock-excited emission, HH 211 displays only shock-excited H_2 emission, RNO 43 contains co-existent HH/H_2 emission along the entire flow, while L43-RNO 91 shows no evidence of HH emission but faint and extended H_2 emission has been identified near the outflow source (Kumar, Anandarao & Davis 1999). The presence of strong H_2 emission in HH 211 and lack of strong HH and/or H_2 emission in the L43-RNO 43 outflow supports the idea that outflow strength declines with increasing source age (i.e., Bontemps et al. 1996; Saraceno et al. 1996).

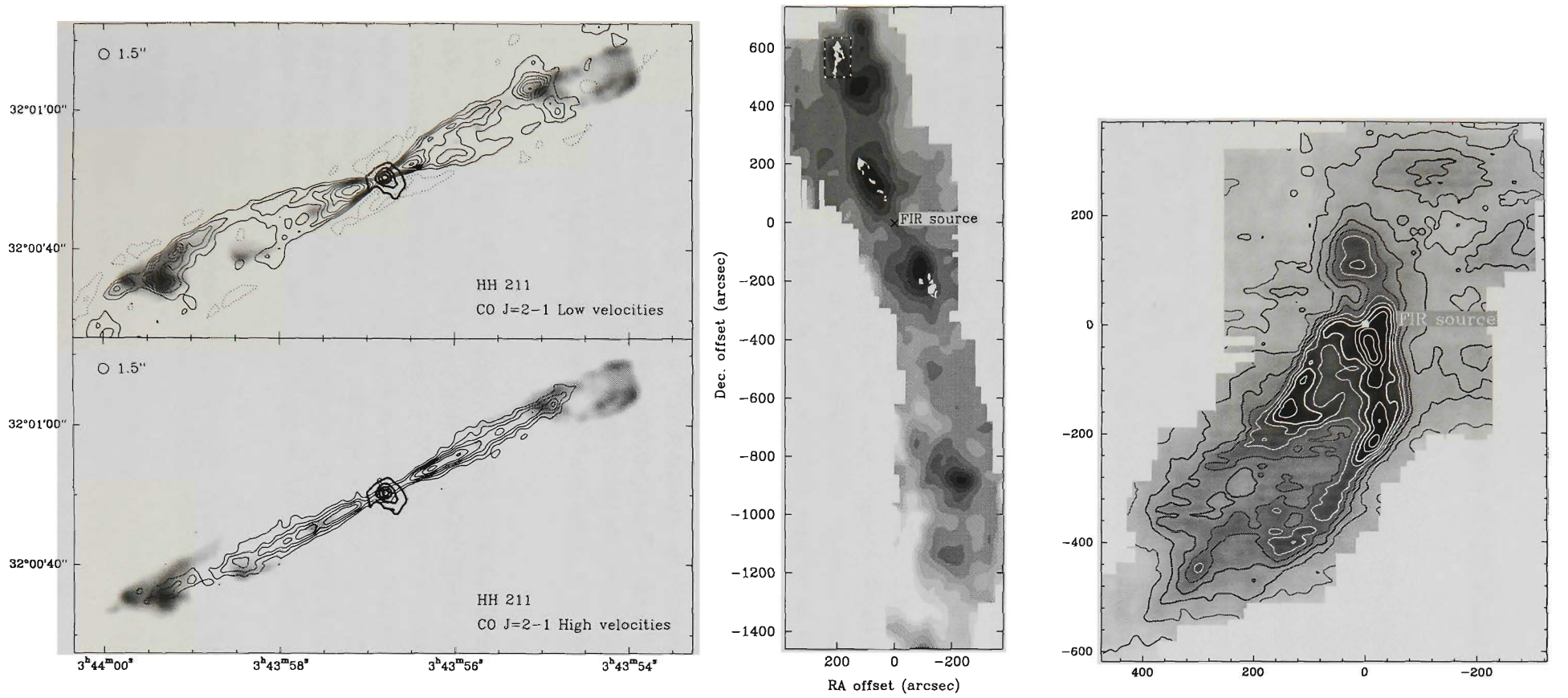

Figure 1.1: Examples of Class 0, I and II protostellar objects. **left:** Class 0: HH 211. The top panel shows low-velocity CO emission outlining the cavity, whereas the lower panel shows high-velocity CO emission traces a highly collimated jet. The grey-scale emission is from shock-excited H_2 emission (from Gueth & Guilloteau 1999). **middle:** Class I: RNO 43. Position of HH objects (white markers) overlaid on the ^{12}CO emission. Both the optical and CO emission display a "wandering" (from Bence et al. 1996). **right:** Class II: L43-RNO 91. ^{12}CO emission outlines a wide limb-brightened cavity. No HH, but faint H_2 emission is seen in this flow (from Bence et al. 1998).

1.3 Giant Herbig-Haro Outflows

Prior to 1994, it was generally believed that the extent of HH outflows was $\sim$ 0.3 pc for regions such as Orion ($D \sim 470$ pc). It is interesting that the inferred sizes of these outflows was typically the same as the field-of-view of most optical CCD detectors of the time. Although larger (> 1 pc) flows such as R Mon/HH 39 (Herbig 1968), RNO 43 (Ray 1987), Z CMa/HH 160[8] (Poetzel, Mundt & Ray 1989) and HH 80/81 (Martí et al. 1993) were known, their lengths were generally attributed to the higher luminosity of the driving source ($\sim 10^{3-4}\ L_{\odot}$). Bally & Devine (1994) were the first to question the true length of outflows from low-luminosity sources by suggesting that the well-known HH 34 outflow in the L1641 (Orion A) molecular cloud was not $\sim$ 0.3 pc in length, but in fact $\sim$ 3 pc!

To the north of the driving source (HH 34IRS), there is a string of HH objects[9] for which many optical, near-infrared and far-infrared surveys have failed to detect plausible energy sources. Likewise, another chain of known HH objects[10] are found to the south of HH 34IRS. Like the northern group, no energy source had been found for these objects. Existing velocity information on HH 33/40 to the north of HH 34IRS suggests these objects have radial motions $V_{lsr} \sim$ 70-130 km s^{-1}, which is similar in magnitude but opposite in direction to the velocities seen in the blue-shifted HH 34 jet and HH 34S. With this information, they suggested that the northern string of objects lie in the red-shifted lobe, while those to the south of HH 34IRS lie in the blue-shifted lobe. Finally, from a ^{13}CO integrated intensity map of the region, they found large-scale cavities symmetrically placed about $8'$ to the north and south of HH 34IRS. Each cavity coincides with the northern (HH 33/40) and southern (HH 86-88) terminal bow shocks of the suggested giant HH flow.

Using deep red Schmidt plates, Ogura (1995) proposed that the known HH 1/2 (Orion A; L1641) and HH 124 (NGC 2264) outflows were in fact associated with flows of lengths 5.9 pc and 5.4 pc respectively. Another hint that low-mass sources drive parsec-scale flows was shown when Bence et al. (1996) identified a 5 pc CO outflow associated with the Class 0/I source RNO 43-mm[11]. With the confirmation that HH 34 is indeed part of a 3 pc flow (Devine et al. 1997), Eislöffel & Mundt (1997) and Reipurth, Bally &

[8]See chapter 5.

[9]With decreasing distance from HH 34IRS: HH 33, HH 40, HH 85, HH 126 and HH 34N.

[10]With increasing distance from HH 34IRS: HH 34 jet, HH 34S, HH 34X, HH 173 and HH 86-88.

[11]RNO 43-mm also drives a 3.4 pc HH flow consisting of HH 179 and HH 243-245. See Eislöffel & Mundt (1997) and Reipurth et al. (1997).

Devine (1997; hereafter RBD97) each conducted a CCD imaging survey of known HH flows to determine if they extended over parsec-scale distances. RBD97 identified HH 111/113/311 as the largest at a staggering projected length of 7.7 pc! All of the above surveys found that the true extent of HH flows may have been underestimated by factors as high as ten. Since 1997, increases in the field of view afforded by CCD detectors (> 20-30′) have led to the discovery of roughly 2-3 dozen giant HH flows associated with low-mass young stellar objects.

1.3.1 Implications of Giant Herbig-Haro Flows

Eislöffel & Mundt (1997) and RBD97 discuss the implications of giant outflows from low-mass stars, but the most important was the realisation that HH flows were now able to drive molecular CO outflows associated with the same source. Prior to the discovery of giant HH flows, mass-loss estimates from optical HH jets showed typical values between 10^{-6}-10^{-8} $M_{\odot}$ yr^{-1} (Mundt, Brugel & Bürke 1987). These figures were up to 10-100 times lower than typical mass-loss rates estimated from CO observations. From a historical perspective, the discrepancy is probably related to the intrinsic difficulty in measuring the neutral component of HH jets (see Bacciotti & Eislöffel 1999 and references therein). For a jet of radius 1″ with $n_e = 100$ cm^{-3} and velocity = 300 km s^{-1}, $\dot{M} \geq 2 \times 10^{-7}/x_e$ $M_{\odot}$ yr^{-1} where x_e is the ionization fraction. In a spectroscopic survey of HH jets, Bacciotti & Eislöffel (1999) presented a model-independent method for determining x_e. In most cases, they found $x_e \leq 0.1$, which implies $\dot{M} \geq 2 \times 10^{-6}$ $M_{\odot}$ yr^{-1}. The resulting decrease in x_e implies higher mass-loss rates comparable to the associated CO outflows.

As mentioned in Eislöffel & Mundt (1997) and RBD97, the increased length of HH flows beyond 1 pc yields dynamical ages $\tau_{dyn} \sim 10^4$ d_{pc}/ν where d_{pc} is the projected distance in pc and ν represents the highest observed velocity in terms of 100 km s^{-1}. For giant HH flows, τ_{dyn} is up to 10 times larger than previously found[12] and once this is factored in, the total momentum of HH jets (0.5-10 $M_{\odot}$ km s^{-1}) is comparable with the total momentum in a number of CO outflows (1-20 $M_{\odot}$ km s^{-1}; Cabrit & Bertout 1992).

With increased projected lengths and accurate measurements of the optical flow mass, it appears that HH jets are indeed capable of driving molecular CO outflows.

[12]See Mundt et al. (1987).

1.4 Aims of this Thesis

As the number of known giant HH flows increases, a natural question to ask is what percentage of known and newly detected HH flows extend out to parsec-scale lengths? With well over 450 known HH objects (Reipurth 1999), it is quite plausible that some are in fact associated with known HH flows as nearly 50% of objects have yet to be associated with an energy source. With the identification of large-scale CO cavities at the terminal working surfaces, the HH 34 outflow may have dire consequences for the future evolution of the L1641 molecular cloud. What are the consequences of these cavities in terms of the molecular cloud being able to continue forming stars?

This thesis attempts to answer the above questions by conducting a wide-field survey of star forming regions to (a) identify new giant HH flows and (b) characterise their effect on their parental molecular clouds.

The format of this thesis is as follows: As giant HH flows tend to extend up to several degrees on the sky, chapter 2 presents ESO/SERC Southern Sky Atlas material of known HH flows to determine if wide-field ($6° \times 6°$) Schmidt plates are capable of characterising outflows in general and identifying giant HH flows. Chapter 3 presents a multi-wavelength (ESO/SERC, CCD narrow and broad-band optical imaging, IRAS) study of known HH objects which have yet to have an energy source positively identified and determine if they are part of giant HH flows. Chapter 4 presents results of a search for giant HH flows using wide field-of-view ($4° \times 4°$) material from the new Anglo-Australian (AAO) and United Kingdom Schmidt Telescope (UKST) Hα survey of the Southern Galactic Plane. This chapter combines the methods and techniques developed in the previous two chapters to identify giant HH flows and characterise their effect on the L1630 and L1641 giant molecular clouds in Orion. Initial results of an AAO/UKST Hα survey for giant HH flows in the Canis Major region are presented in chapter 5. Finally, chapter 6 concludes with a summary of the major findings of this thesis.

Chapter 2

The ESO/SERC Sky Atlas & Herbig-Haro Flows

2.1 Introduction

It is well known now that outflow activity usually accompanies the evolution of a young star even at the earliest stages (i.e. Lada 1985). Bipolar molecular outflows are common in the deeply embedded protostellar stage. In fact, these outflows often are the first observable signs of star formation. A number of jets, visible in the near infrared at 2.12μm (1-0 S(1) line of molecular hydrogen), have been found to have their source still heavily embedded (i.e. Zinnecker, McCaughrean & Rayner 1997). Many young stars, i.e. T Tauri stars, are associated with optically visible Herbig-Haro (HH) jets. The origin of the outflows as well as the acceleration- and collimation- mechanisms are still very unclear, but inner accretion disks at a few to a few tens of AU seem to play a crucial role (Königl 1995). Thus it is of great importance to identify the outflow sources, to learn as much as possible about their nature, and to relate their properties to the properties of their outflows. The difficulty in identifying outflow sources is shown by Reipurth (1999), who lists well over 450 known HH objects, but as yet only $\sim$ 50% have known energy sources. With the identification that HH flows can extend up to a degree on the sky (Eislöffel & Mundt 1997; Reipurth, Bally & Devine 1997; hereafter RBD97), we have initiated a program to determine how effective wide-field ESO/SERC material is in identifying energy sources and large-scale flows.

The availability of the ESO/SERC Sky Survey has made scanning of the southern skies for planetary nebulae, supernova remnants and dark nebulae such as HH objects possible. Several catalogues of sources found on these

plates have been published, sometimes accompanied by photographs of the more important objects. Although the matching deep IIIaJ and IIIaF plates of the Southern Sky have been searched for HH objects, little systematic use has been made of combining the IIIaJ, IIIaF and IVN to identify the driving sources of these flows. With the advent of low cost PCs, frame grabbers and video cameras, it has become possible to digitise and enhance areas of interest on these survey plates. Applying digital techniques to the images from the IIIaJ, IIIaF and IVN surveys allows the separation of line and continuum sources in the galactic plane (i.e. Zealey & Mader 1997; 1998). Objects lying close to bright reflection nebula are often swamped by reflected light on IIIaJ and IIIaF plates, but digital imagery allows sophisticated enhancement techniques to be applied to areas of interest. Use of photographic and more recently digital unsharp masking techniques allows the detection of new emission sources (i.e. Malin, Ogura & Walsh 1987).

Currently, the Anglo-Australian Observatory (AAO) in conjunction with the United Kingdom Schmidt Telescope (UKST) are undertaking a Hα emission-line survey of the Southern Galactic Plane, Magellanic Clouds and selected areas. This survey provides deep, high resolution images allowing the detection of new filamentary sources such as HH objects. As we will see in chapter 4, the combination of existing ESO/SERC and new AAO/UKST Hα material provides us with the opportunity to better study the morphology and environment of new and existing HH complexes. The wide field-of-view ($\sim 5°$) provided by such material allows us to obtain an unbiased sample of young stellar objects in various evolutionary stages. In this chapter we present images of known HH complexes digitised from ESO/SERC Southern Sky Survey plates. In some instances, comparative AAO/UKST Hα material will also be presented. Section 2.2 outlines the properties of the ESO/SERC material, while section 2.3 outlines how the film material is put into digital form. Section 2.4 shows several examples of how the ESO/SERC material can be used to study HH outflows. A summary is presented in section 2.5.

2.2 Properties of ESO/SERC Material

Figure 2.1 and Table 2.1 shows spectral responses and properties of the IIIaJ/GG395 (hereafter IIIaJ), IIIaF/RG630 (hereafter IIIaF) and IVN/RG715 (hereafter IVN) emulsion/filter combinations. For comparison, the spectral responses of various narrow-band filters such as [OIII] (5007Å), Hα (6590Å) and [SII] (6737Å) are also shown. The location of the narrow-band [OIII] and Hα/[SII] filter transmission peaks lie close to the peak of the transmission curves for the IIIaJ and IIIaF respectively.

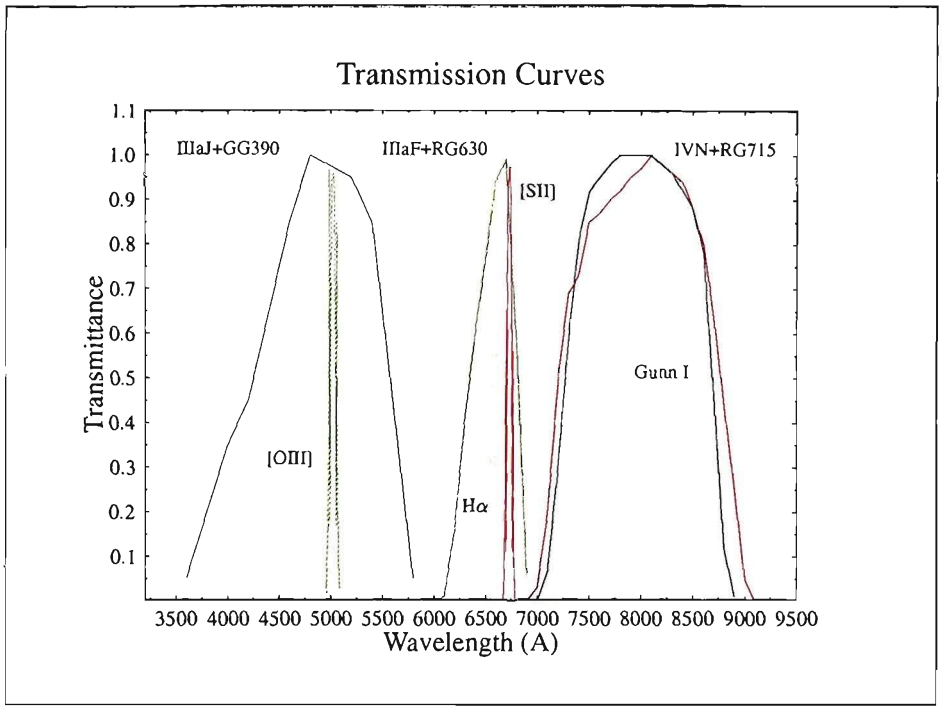

Figure 2.1: Transmission curves of various filter/emulsion combinations. In addition to the ESO/SERC curves, several narrow-band ([OIII], Hα, [SII]) filters are also shown (ESO/SERC curves from UKST handbook (1983); other curves from http://www.aao.gov.au/local/www/cgt/ccdimguide/filters/).

Table 2.1: Properties of ESO/SERC IIIaJ, IIIaF and IVN Schmidt Plates.

Emulsion/Filter	IIIaJ/GG395	IIIaF/RG630	IVN/RG715
Range (Å)	3950-5400	6300-6900	6950-9000
Peak (Å)	4500	6700	8000
Characteristic HH Line(s)	[OII] (3727Å) [OIII] (5007Å)	Hα (5690Å) [SII] (6737Å)	continuum
Limiting Magnitude	$B_J = 22.5$	$R = 22.0$	$I = 19.5$
Extinction† (A_λ/A_V)	1.000	0.748	0.482

†Assuming the interstellar extinction law of Reike & Lebofsky (1985) and IIIaJ/GG395 $\equiv$ CCD B; IIIaF/RG630 $\equiv$ CCD R and IVN/RG715 $\equiv$ CCD I.

Therefore, these emission lines, which feature prominently in HH objects, are strongly represented and will enable one to trace shocked emission within an outflow complex. Although the bandpass of the IVN does contain lines seen in some HH objects (Böhm & Solf 1990 see section 2.4.2), these are not as common or bright as Hα, [SII], [OII] and [OIII]. The IVN images are therefore essentially dominated by continuum emission. Therefore, emission-line sources are bright in the IIIaJ and on IIIaF plates but not in IVN plates. Continuum sources suffering from high extinction are strong in the IVN plates but often are not detected in IIIaF and/or IIIaJ plates.

An additional advantage of using an optical three colour survey lies in the fact that extinction (column density) decreases with increasing wavelength - this is the interstellar extinction law (i.e., Rieke & Lebofsky 1985). Table 2.1 displays values for A_λ/A_V for the IIIaJ, IIIaF and IVN material assuming that each is approximated by CCD B ($\equiv$ IIIaJ[13]), R ($\equiv$ IIIaF) and I ($\equiv$ IVN) band systems respectively. The extinction in the IVN decreases by a factor of 2 for a source in the IIIaJ that has an extinction of $A_V \sim 1$ mag. By blinking corresponding IIIaJ, IIIaF and IVN images, we can peer deeper into cloud cores to search for outflows sources not visible in the IIIaJ and IIIaF. Therefore, if a source displays no change in brightness in all three images, it is considered a foreground/background object. If a source shows an increase in brightness with increasing wavelength and lies within the optical boundary of the cloud, it is considered an embedded object, but one has to be careful as the source may be an unrelated reddened background object.

2.3 A Video Digitising System

In order to transfer images from Schmidt plates to digital form, a low cost PC/AT video digitising system was developed at the Department of Engineering Physics of the University of Wollongong using commercially available hardware and software. The image digitising facility provides for the real time, 8-bit (256 grey scale), video digitising and analysis of photographic plate material (Zealey et al. 1994). The image digitiser system uses a PC/AT based video frame grabber. The digitising board used is a PCVisionPlus, later upgraded to a MATROX. Computer controlled Look Up Tables allow the stored 768×576 pixel image to be displayed in pseudo colour on a dedicated RGB image monitor. The video digitiser accepts video input from a Phillips CCD video camera mounted on a Polaroid Laboratory Camera.

[13]Although colour terms are needed to match one to the other (i.e., Bessell 1979), the values in Table 2.1 are sufficient for this discussion.

Lens combinations allow for both wide-field (300mm square; 6mm pixels) and microscopic (5mm square; 10 μm pixels) imaging. Plate illumination is provided either by a Chromega colour enlarger head for regions up to 5cm square or a light box for larger areas. Although flatbed scanners can provide higher resolution images, the adjustable camera head allows one to zoom in and out of regions with more ease. In addition, flatbed scanners do not deliver the same dynamic range as a CCD chip which is important when dealing with faint nebulosity in regions masked by strong reflection emission and faint sources lying close to the magnitude limits listed in Table 2.1. Various software packages such as Jandell's JAVA and Adobe Photoshop allow for real time enhancement and measurement of the digitised images. Operations such as spatial filtering, contrast enhancement, thresholding, simple back-grounding and source counting as well as photometric analysis can be performed. Images can be stored as 8 bit Tagged Image File Format (TIFF) and then transfered to the Flexible Image Transport System (FITS) which are readable by a wide range of image processing software. In the next section, examples of the ESO/SERC digital material are shown to highlight their usefulness in the study of HH complexes.

2.4 Examples of the Digital Images

2.4.1 HH 34

The L1641 molecular cloud in Orion (D = 470 pc; Reipurth 1999) contains the archetypal outflow HH 34 which is one of the most studied outflows at visible, infrared and millimetre wavelengths (see Reipurth 1999 for references to the literature). Inspection of the digitised IIIaJ, IIIaF and Hα[14] images in Figure 2.2 show similar features to those visible in the deep [SII] image of Mundt (1988). The Hα image shows the opposing bow shaped emission nebulosities HH 34N and HH 34S where HH 34S is the brighter of the two and represents the part of the flow which is moving away from the molecular cloud. HH 34N is fainter because the flow is moving into the molecular cloud. The IVN image identifies the continuum reflection nebula Re 24 (Reipurth 1985) and many of the strong infrared sources including HH 34IRS, IRS5 (which illuminates Re 24; Scarrot 1988) and Re 22 (Reipurth 1985). By comparing the IIIaF, Hα and IVN images we can identify the energy source of the HH flow since the highly collimated jet can be traced back to the reddened Class I source HH 34IRS.

[14]Image taken from the AAO/UKST Hα plate of the Orion region. See chapter 4 for details.

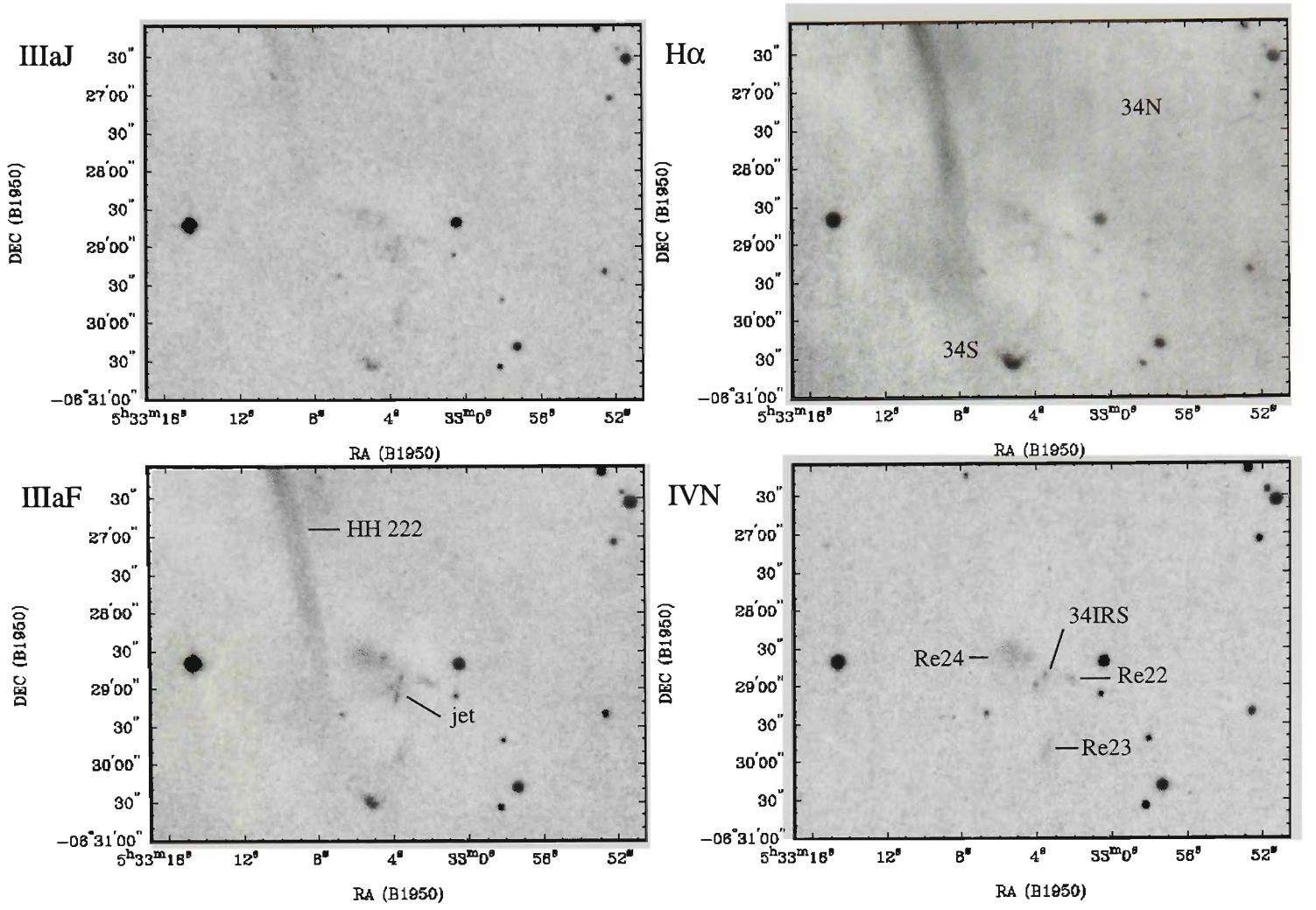

Figure 2.2: IIIaJ, Hα, IIIaF and IVN images of the HH 34 system. The location of the energy source (labelled 34IRS) is clearly seen in the IVN band. The large tongue-like object to the north-east is HH 222. Other objects in the field are discussed in the text.

It is interesting to note that the jet intensity in the Hα frame is weaker compared to the IIIaF. As the latter includes both the Hα and [SII] lines, it appears the jet is a low excitation object with a [SII]/Hα ratio > 1. The working surface HH 34S displays increasing brightness in the IIIaJ, IIIaF and Hα images. As there is no emission associated with HH 34S in the IVN, the IIIaJ emission may represent oxygen [OII] (3727Å) and/or [OIII] (5007Å). Finally, the northern working surface HH 34N displays its brightest emission in Hα with relatively weak emission in the IIIaF. This suggest HH 34N is a high excitation object and is moving into the molecular cloud with velocities > 100 km s^{-1}. All the above inferences have been confirmed by the optical spectroscopy of Morse et al. (1993).

The reflection nebulosity, Re 23 (Reipurth 1985), was originally thought to represent the brightest part of the western wall of a cavity containing the HH 34 jet. Re 23 shows a different morphology in the IIIaJ, IIIaF and Hα images and has been associated with a linear H_2 emission structure which has been identified as a separate unrelated flow (Zealey et al. 1993; Stanke, McCaughrean & Zinnecker 1998). No counterparts to an arc of infrared emission north of HH 34IRS (Zealey et al. 1993) are seen in the optical.

Bally & Devine (1994) suggested HH 34 is part of a much larger flow which includes previously known objects HH 126, HH 85 and HH 33/40 to the north and HH 173, HH 86-88 to the south (see Figure 2.3). Subsequent spectroscopic observations by Devine et al. (1997) showed all HH objects south of HH 34IRS are blue-shifted with proper motions to the south, while all HH objects to the north are red-shifted with proper motions to the north. Their results established HH 34 as a 3 pc flow. In conjunction with RNO 43 (Ray 1987), the results for HH 34 showed that large-scale outflows from low-mass, young stellar objects are common.

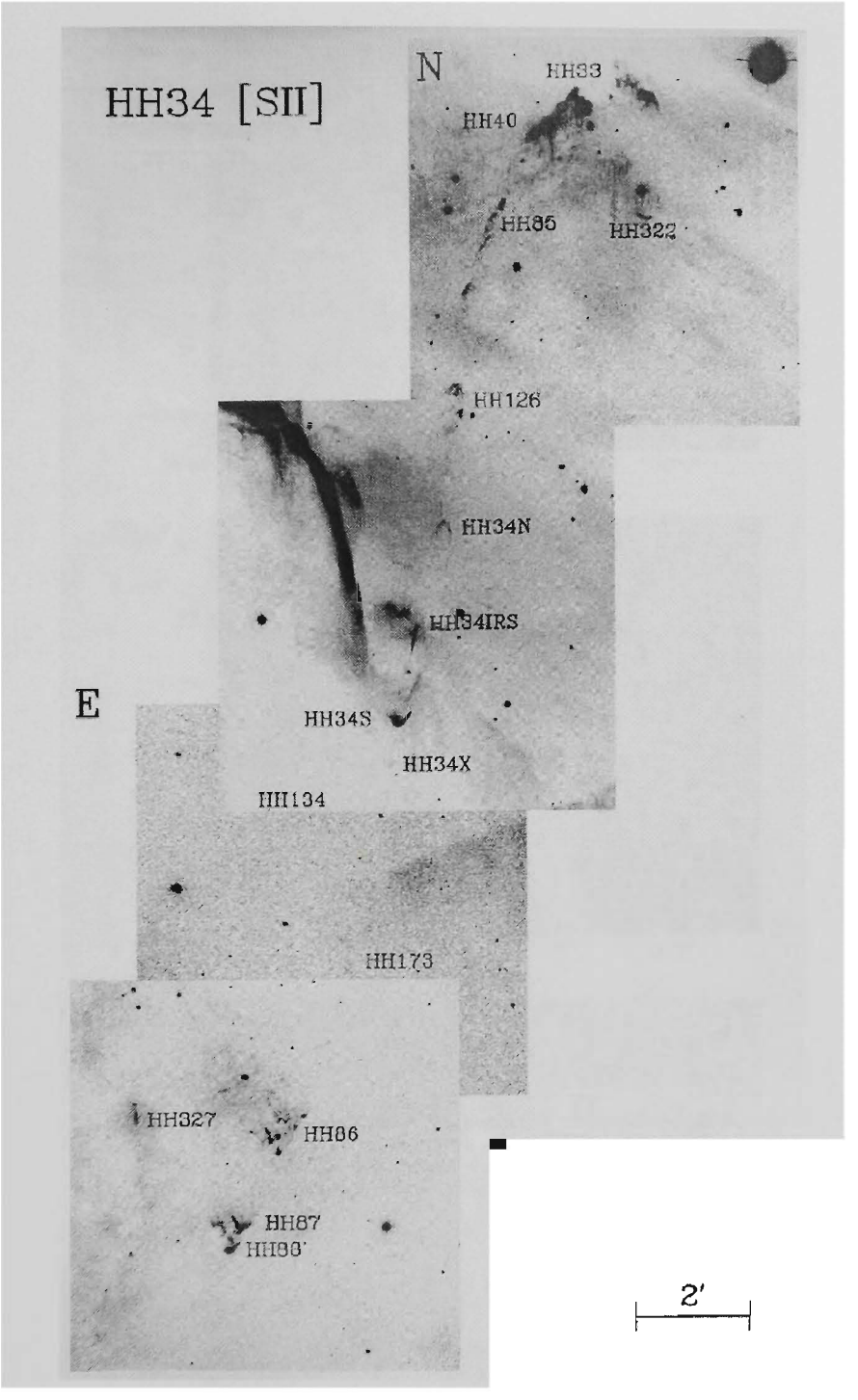

Figure 2.3: [SII] image of the HH 34 parsec-scale flow. Previously, the northern (HH 126, HH 85, HH 33/40) and southern (HH 173, HH 86-88) objects were thought to belong to separate outflows, but have now been associated with HH 34IRS. Image from Eislöffel & Mundt (1997).

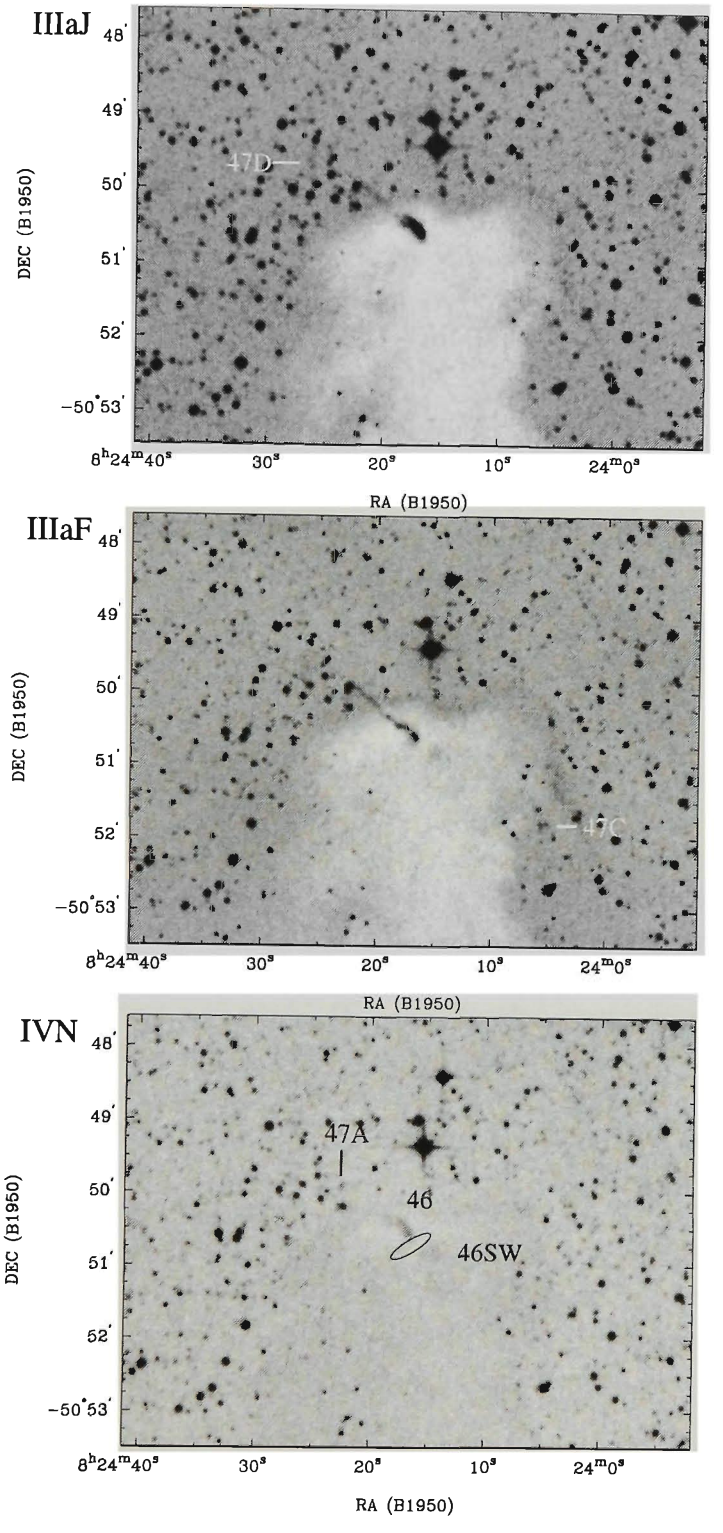

Figure 2.4: ESO/SERC images of the HH 46/47 system. The IRAS positional error ellipse of HH 46/47 IRS and various knots of the HH flow are indicated.

2.4.2 HH 46/47

HH 46/47 is also a well studied flow at visible, infrared and millimetre wavelengths (see Stanke, McCaughrean & Zinnecker 1999 for a review). Many of the optical features discovered using CCD techniques are clearly visible on the ESO/SERC survey films, without enhancement. The ESO/SERC images of HH 46/47 in Figure 2.4 show the faint emission features associated with the blue-shifted, bow shaped nebulosity HH 47D and red-shifted bow shock working surface HH 47C as observed in the CCD [SII] images of Eislöffel and Mundt (1994). The fact that HH 47D is seen in the IIIaJ image suggests it contains higher excitation lines. In their [OII] (3727Å) image of HH 47D, Hartigan, Raymond & Meaburn (1990) found the wings of the bow shock extend all the way back to the reflection nebulosity HH 46. As the [OII] (3727Å) line lies towards the blue-ward edge of IIIaJ the spectral curve, the observed emission most probably represents a contribution from the [OII] (3727Å) and [OIII] (5007Å) lines, which have been detected by Dopita, Evans & Schwartz (1982).

The strong reflection nebulosity surrounding the Class I embedded T Tauri source IRAS 08242-5050 (hereafter HH 46/47 IRS) dominates the IIIaJ image. Blinking the IIIaJ, IIIaF and IVN images fails to detect a reddened source within the IRAS uncertainty ellipse (see Figure 2.4) which neatly bisects the reflection nebulosities HH 46 and HH 46SW. However, the infrared image in Figure 2.5 (Zealey et al. 1993) also fails to show a central point source at the position of HH 46/47 IRS due to the presence of a dense obscuring disk surrounding the source. With the exception of HH 47C (which has just appeared from the far side of the globule) and the reflection nebulosity HH 46SW, none of the IVN, IIIaF or IIIaJ images show emission from the red-shifted flow which is clearly seen in the 2.12μm image. This again indicates the high obscuration in this direction due to the dark cloud in which HH 46/47 IRS is embedded. We note also that the IIIaJ, IIIaF and 2.12μm H_2 images show brightening towards the northern edge of the dark cloud. This may be reflected radiation from galactic plane sources or a photo-dissociation region at the cloud edge.

It is interesting that the IVN image shows emission at the location of HH 47A. Although red continuum is frequently seen in HH objects located close to their exciting star, given the distance of HH 47A from HH 46/47 IRS ($\sim$ 1.'4 or 0.17 pc for D = 450 pc) and the fact that one does not seen IVN emission associated with the cavity walls delineated by the H_2 emission, the clumped emission at the position of HH 47A is not reflection but emission arising from lower excitation lines. In a spectroscopic (3700Å-10830Å) study of HH 1, Solf, Böhm & Raga (1988; see their Table 1) identified medium to

strong emission[15] from lines such as [FeII] (7155.1Å), [CaII] (7323.9Å), [FeII] (8617.0Å) and [SII] lines at 10284.3Å and 10317.7Å. These are all bright in low-excitation HH objects like HH 47A, HH 7 and HH 43 (i.e., Böhm, Mannery & Brugel 1980; Böhm & Solf 1990). Because the reddening is lower, the IVN lines are enhanced over what they would be with no dust along the line of sight.

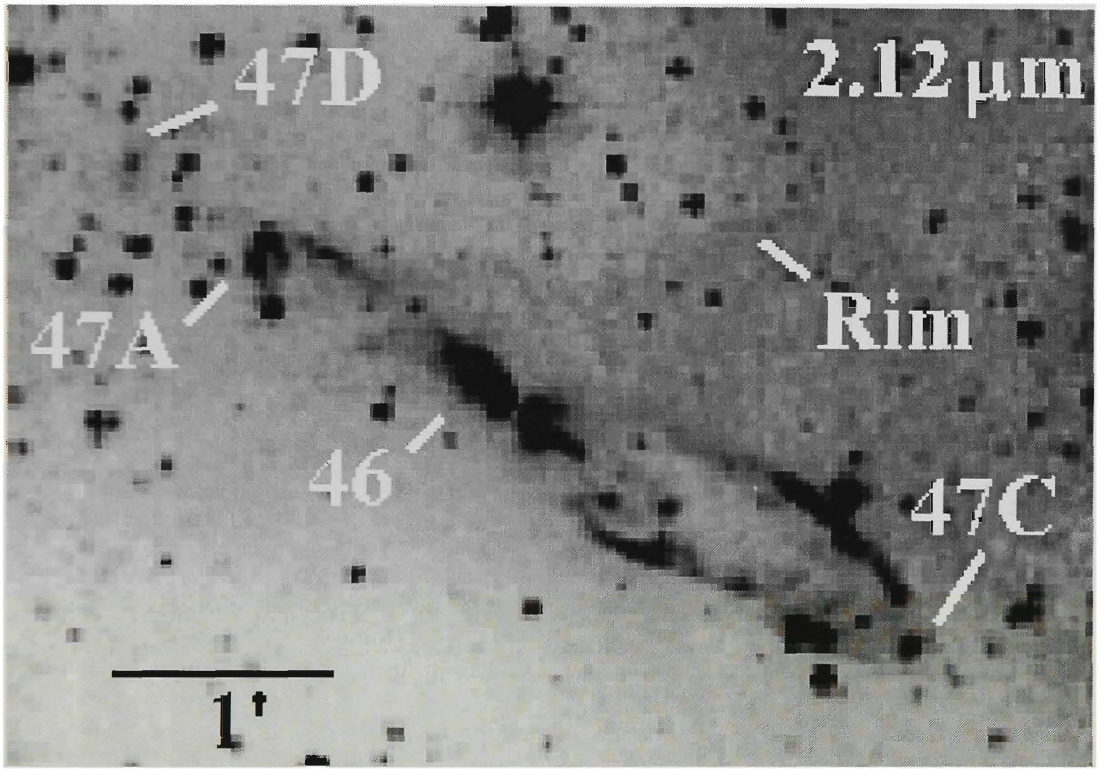

Figure 2.5: H_2 image of the HH 46/47 system from Zealey et al. (1993). The blue-shifted working surface, HH 47D displays bright emission while the red-shifted lobe occupying the lower right of the image can be traced back to HH 46/47 IRS, at field centre.

Recently, Stanke et al. (1999) discovered large HH-type structures $\sim 10'$ (1.3 pc for $D = 450$ pc) to the north-east (HH 47NE) and south-west (HH 47SE) of the driving source (see Figure 2.6). They argue that for a projected length of 2.6 pc across the sky, the outflow is another example of a giant HH outflow from a low mass star.

[15]These lines have $I_{line}/I_{H\beta} > 20$; where I_{line} is the intensity relative to $I_\beta = 100$.

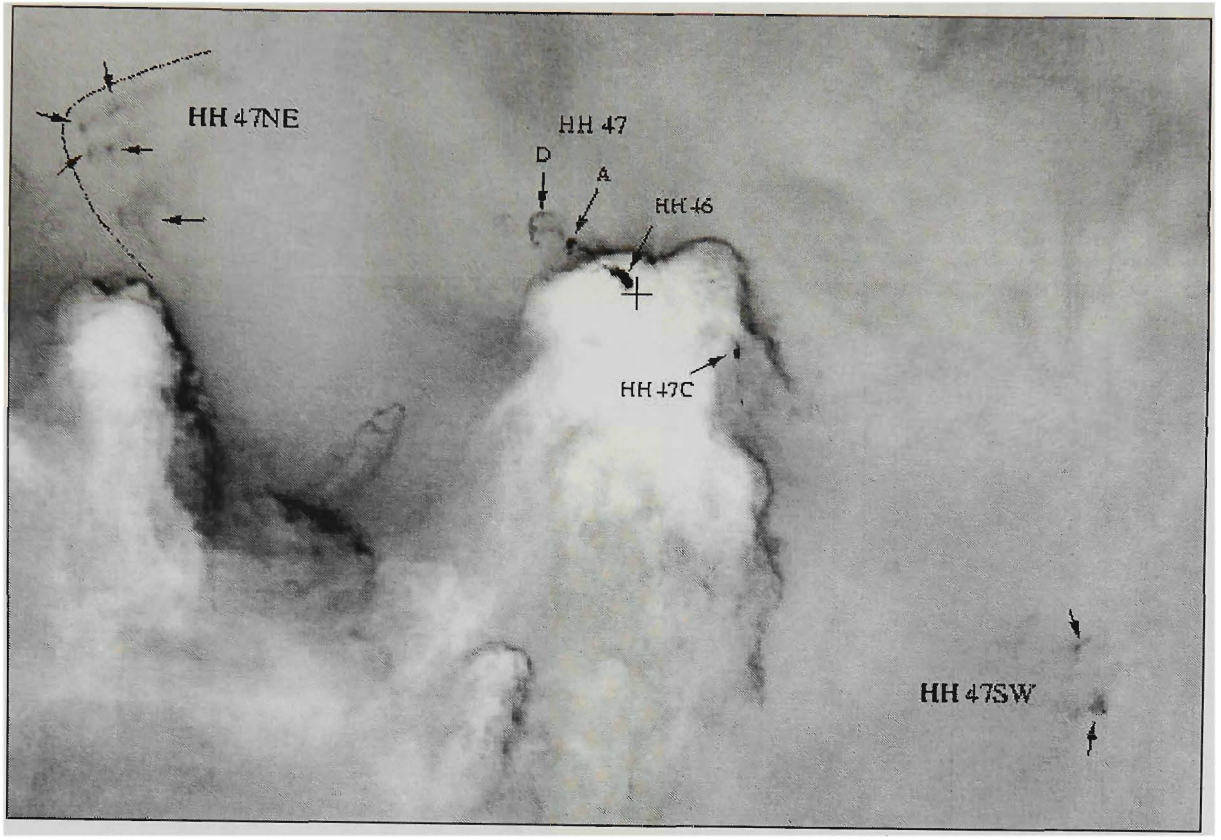

Figure 2.6: Continuum subtracted Hα image of the HH 46/47 parsec-scale outflow. The inner flow (see Figures 2.4 and 2.5) and the driving source, HH 46IRS (marked by the cross) are marked. HH 47NE forms a large bow shock, while the morphology of HH 47SW is not well defined. The image size is $21' \times 14'$. Image from Stanke et al. (1999).

2.4.3 HH 49/50

Figure 2.7 shows IIIaJ, IIIaF and IVN images of the region near the reflection nebula Ced 110 and objects HH 49/50. First discovered by Schwartz (1977) these objects are located in a high extinction region of the Chameleon I cloud at a distance of 140 pc. Cohen & Schwartz (1987) suggested IRAS 11054-7706C as a candidate energy source for HH 49/50. Prusti et al. (1991) showed this source is a blend of two Class I sources (IRS4 and IRS6), but suggests IRS4 as the driving source for HH 49/50 as it lies along the axis defined by the HH flow. A molecular outflow with axis parallel to HH 49/50 was identified by Mattila, Liljeström & Toriseva (1988) and Prusti et al. (1991), of which both propose IRS4 as the driving source of the CO and HH outflow. The radial velocity data for HH 49 and HH 50 (Schwartz & Dopita 1980) suggests red-shifted velocities of 25 and 30 km s^{-1} respectively, which agrees with their location in the red-shifted lobe of the molecular CO outflow.

Recently, Reipurth, Nyman & Chini (1996) obtained 1300μm observations of the region and found a source (their Cha-MMS1) 76″ to the south-east of IRS4 and propose this as the energy source for HH 49/50 as it lies closer to the midpoint of the CO outflow lobes. The low luminosity ($\sim 1\ L_{\odot}$) and temperature ($T_{bol} = 95$ K; Chen et al. 1997) places the source in the Class I range.

The nebulosity associated with Ced 110 is clearly seen in the IIIaJ, IIIaF and IVN images. The spectroscopy of Schwartz & Dopita (1980) identified extremely strong [OII] (3727Å) and [OIII] (5007Å) emission associated with HH 49/50. As both are seen in the IIIaJ image, this would confirm the IIIaJ is detecting the oxygen lines. The absence of HH 49/50 from the IVN image confirms they are emission-line objects and the emission in the IIIaJ is not reflection.

As IRS4 and Cha-MMS1 are highly obscured, we do not see any reddened sources at their locations in the IVN image. However, all images show a reflection nebulosity located slightly north-east of IRS4 which could be associated with the embedded source and not Ced 110. The distance between Cha-MMS1 and the southern most tip of HH 49 is $\sim$ 10′.25, or 0.42 pc at a distance of 140 pc.

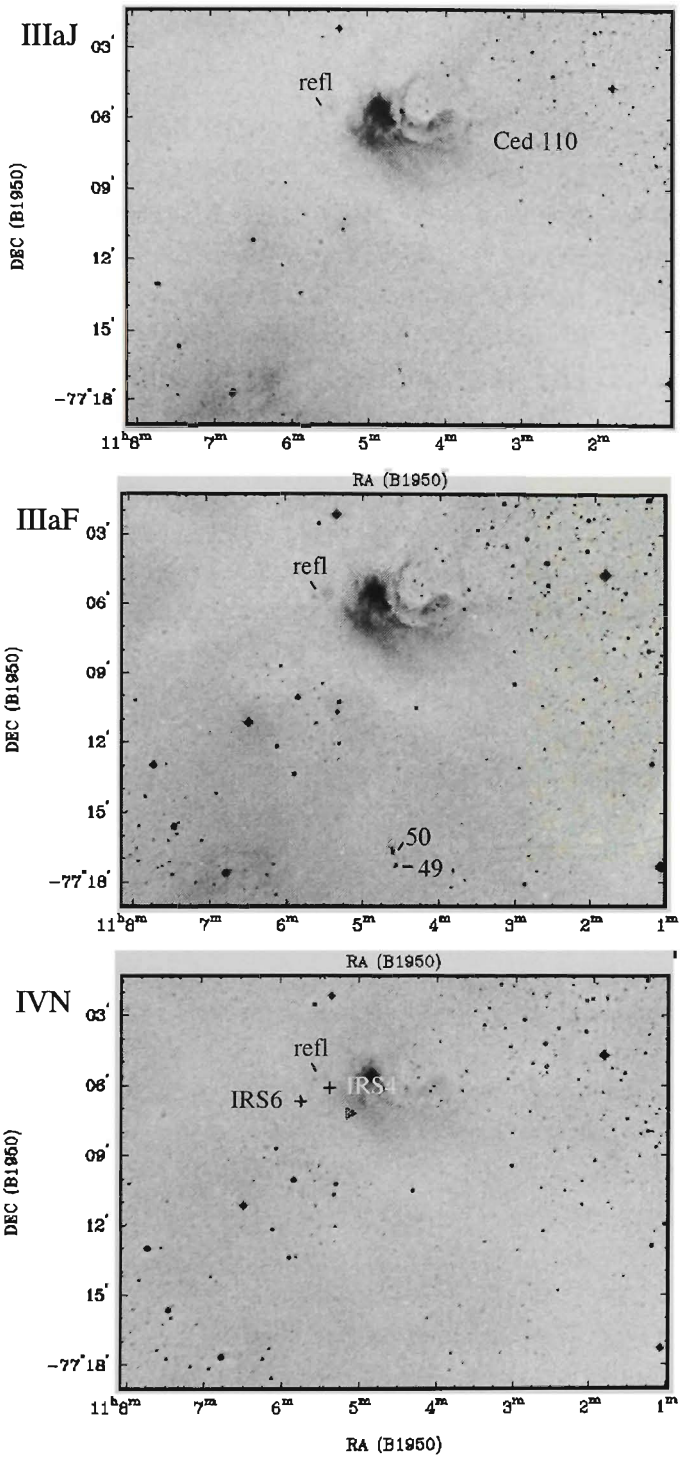

Figure 2.7: ESO/SERC images of Ced 110 and HH 49/50. The crosses in the IVN show positions of the Class I objects IRS4 and IRS6. A faint reflection nebulosity (marked as refl) may be scattered light from IRS4. The diamond marks the location of the 1300μm source Cha-MMS1. See text for discussion.

2.4.4 IRAS 05329-0505

Located between M42 and M43, RBD97 suggested the bipolar nebulosity associated with IRAS 05329-0505 (= MMS7; Chini et al. 1997) may be the driving source for a group of objects HH 41/42 and HH 128/129 (Schwartz 1977; Ogura & Walsh 1991) which are $\sim 11'$ to the east of MMS7. To the west, RBD97 identified a jet (HH 294) emanating from MMS7 and a cluster of objects, HH 295 A-I which lie on the axis defined by the jet and mirrors the position of HH 41/42 and HH 128/129 with respect to MMS7. For a total length of $\sim 23\ '$, the projected flow length is 3.16 pc for $D = 470$ pc. With a number of protostars and outflows in the region (i.e., Chini et al. 1997; Yu, Bally & Devine 1997; see Figure 2.9), RBD97 point out that some of these cannot be excluded as energy sources for HH 41/42, HH 128/129 and HH 295. For example, the 1300μm source MMS9 (Chini et al. 1997; Figure 2.9) also powers a bipolar CO outflow with an east-west orientation which intersects with HH 41 and HH 128.

RBD97 mention in passing that the background structure of nebulosity in the vicinity of HH 41/42 and HH 128/129 and HH 295 displays large-scale ordered motions along an east-west axis. Figure 2.8 shows the IIIaF and a Hα[16] image of the region. What is immediately obvious is that HH 41, 42, 128 and 129 lie approximately between two large streamers where extend along an east-west axis. Similarly, HH 295 lies within two more filaments though not as extended. Although faint in the IIIaF, these features are present and in combination with the Hα image, the streamers imply one or more outflows have extended far beyond the position of HH 41/42, HH 128/129 and HH 295. Given the size of the "blown-out cavity", it is reasonable to suggest it is being created by a powerful outflow source. Both MMS7 and MMS9 display optical, H_2 and CO outflows with an east-west orientation and one or both of these may be responsible for the large-scale movement of dust and gas in the region.

In the vicinity of MMS7 and MMS9, the IVN image of the region (Figure 2.9) shows several of the 1300μm objects detected by Chini et al. (1997). Faint sources can be seen at the positions of MMS5, MMS9, MMS10 and F3. As outlined in Yu et al. (1997), these sources appear to drive a combination of CO, optical and H_2 outflows. No source is seen at the position of MMS7 nor in the 2.12μm images of Yu et al. (1997) which confirms a heavily embedded source which is clearly identified by its bipolar reflection nebula. What is interesting about MMS9 is its classification as Class 0 protostar (Chini et al. 1997).

[16]Image taken from AAO/UKST Hα plate of the Orion region. See chapter 4 for details.

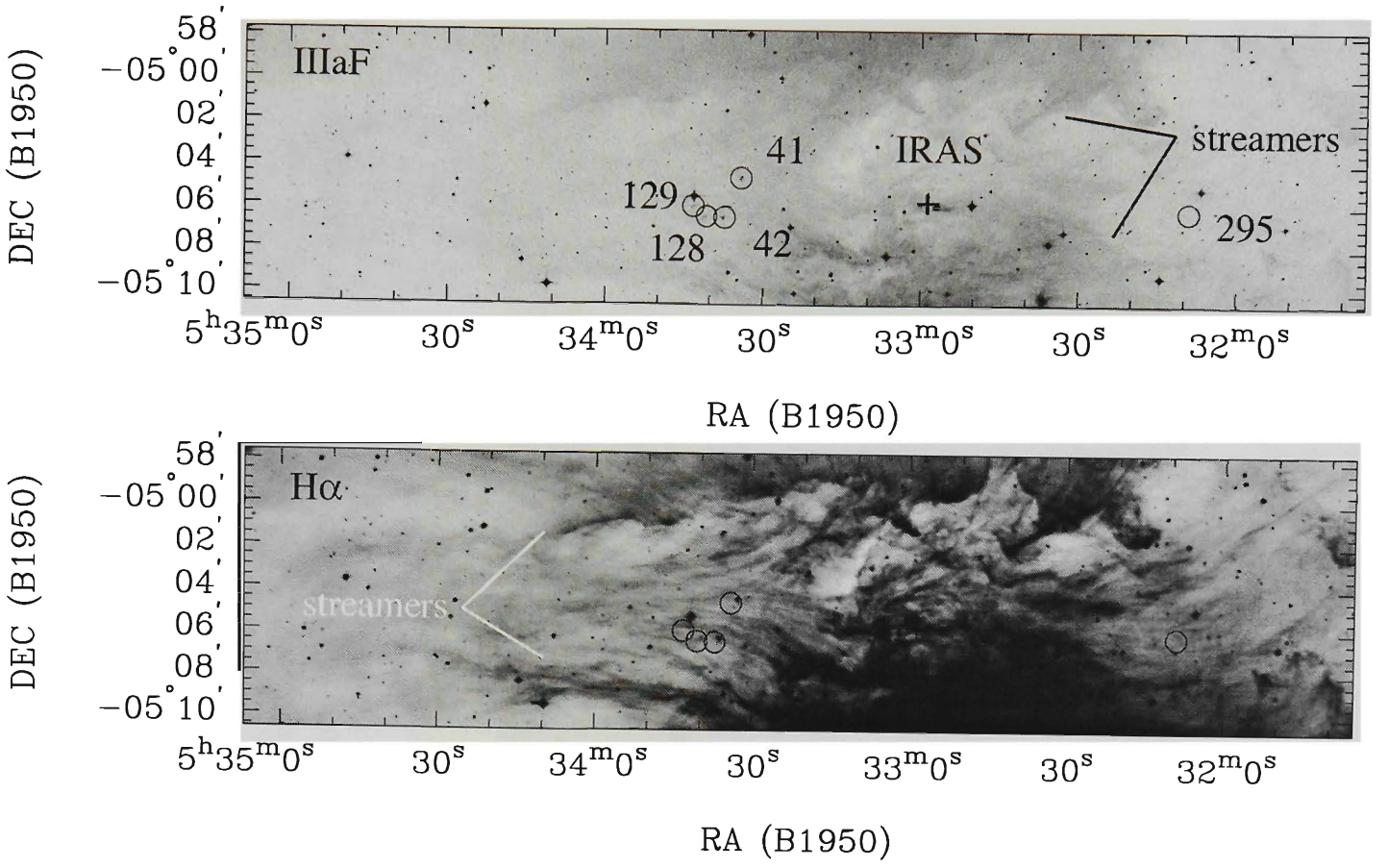

Figure 2.8: (top) IIIaF and (bottom) Hα images of steamers in OMC 2/3. Several HH objects in the region lie between the streamers which may have been created by the IRAS source 05329-0505/MMS7 (marked as IRAS in the IIIaF). See text for details.

Presently, the status of MMS5, MMS10 and F3 is unknown, but as they display peaks in the 1300μm map of Chini et al. (1997), they are most certainly young objects. Due to the considerable nebulosity seen in in the IIIaF, Hα and IVN images of the region, it is difficult to determine if the IVN emission is reflection or emission. However, the 2.14μm (continuum) image of Yu et al. (1997; their Figure 1) shows all objects have associated continuum emission which is most probably reflection emission associated with the embedded sources.

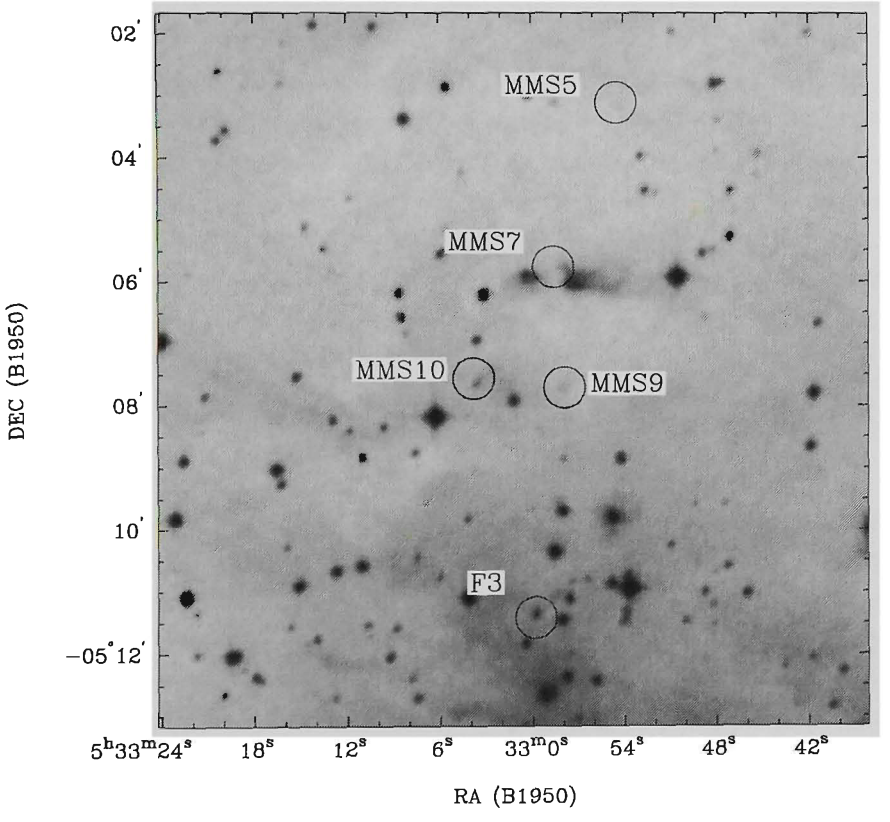

Figure 2.9: IVN image of the IRAS 05329-0505 region. Two Class 0 objects (MMS7 and MMS9) are identified by reflection nebulosities as are other embedded sources in the region. Source identifications are from Chini et al. (1997).

2.5 Summary

This chapter has shown the effectiveness of low cost video digitising in analysing ESO/SERC Sky Survey material in terms of identifying the main features associated with outflows from low mass stars. In conjunction with additional material such as Hα (i.e, HH 34 and IRAS 05329-0505) and near-infrared H_2 (i.e. HH 46/47) observations, the ESO/SERC material provides

us with a road-map of shock excited emission which can be used to identify excitation conditions along the length of an outflow. It has also been shown that the ESO/SERC material is capable of identifying HH energy sources by their reflection nebulosities (i.e. HH 46 IRS; IRAS 05329-0505) or alignment with HH emission in the form of a jet (HH 34IRS).

By comparing ESO/SERC survey plates with other wide-field observations, we do not have to resort to CCD cameras with small fields of view to study morphological properties of new and existing outflow features, although follow-up observations are vital for deeper studies. As we shall see in chapter 4, the AAO/UKST Hα and existing ESO/SERC survey material provide a unique tool by which we can identify, study and understand how outflows from low mass stars interact and modify their parental molecular clouds. A comparison between the ESO IIIaF and AAO/UKST Hα film material in Figure 2.8 shows the superior quality of the Hα compared to the broad-band IIIaF. The Hα clearly shows that one or several outflows in the OMC 2/3 region may be responsible for the large-scale movement of dust and gas in the region. Such features may have been missed using ESO/SERC material alone and may provide a way in which to identify giant HH flows in the future.

In the next chapter, we will use the ideas and techniques developed here and apply ESO/SERC material with deep CCD imaging and far-infrared data from IRAS to search for the energy sources of a sample of HH objects which have yet to have their energy source identified. Our aim is to identify which fraction of these objects are part of parsec-scale outflows such as HH 34, HH 46/47 and the objects associated with IRAS 05329-0505.

Acknowledgements

This research has made use of the SIMBAD data base, operated at CDS, Strasbourg, France, and the ESO/SERC Sky Surveys, based on photographic data obtained using the UKST which is currently operated by the AAO.

Chapter 3

Frequency of Giant Herbig–Haro Flows

3.1 Introduction

The abundance of nearby stellar outflow complexes accessible to observation from the southern hemisphere provides us with the opportunity to study highly supersonic outflows for comparison with theoretical models. Since the publication of the original catalogue of 43 HH objects (Herbig 1974), there has been a substantial increase in the number of known sources due to advances in imaging technology, especially in CCD imagery through narrow-band filters. Catalogues have been compiled by Schwartz (1977; deep red objective-prism survey of southern HH objects), Hartigan and Lada (1985; VRI and Hα images of suspected HH objects), Strom et al. (1986; VI, Hα and [SII] CCD images), von Hippel et al. (1988; literature survey up to 1988) and Reipurth (1999; extensive notes on individual HH objects with detailed references to the literature). The above catalogues show well over 450 HH objects are now known. However, about half still do not have their driving source positively identified. With the discovery that HH flows can attain sizes greater than 1 pc, it may well be that some fraction of these objects are themselves part of giant flows.

It is important to identify as many parsec-scale outflows from low mass stars as possible. As discussed by Eislöffel & Mundt (1997) and Reipurth, Bally & Devine (1997; hereafter RBD97), the increased scale length of giant HH outflows allows us to study (among other things), the behaviour of an outflow source over long periods of time. We can identify periods of enhanced activity, episodic outbursts and dormant phases by studying the distribution of HH

objects relative to the source. The question of episodic outbursts has recently become an issue when discussing HH outflow sources. It has been suggested by Reipurth & Aspin (1997) that HH flows are the result of repetitive FU Orionis (FUor) eruptions. Although the link between FUors and HH flows has been previously speculated (i.e., Dopita 1978; Reipurth 1989a), a near-infrared spectroscopic survey of 14 HH energy sources by Reipurth & Aspin showed the majority of high luminosity ($L_{bol} > 28\ L_{\odot}$) sources in their sample are in elevated FUor states. The issue of whether HH energy sources are FUor in nature can be addressed by identifying a large number of parsec-scale flows.

In this chapter, we set out to identify candidate giant HH flows by targeting a sample of HH objects without identified energy sources. As shown in chapter 2, the ESO/SERC material is extremely useful in identifying heavily reddened sources. Our initial survey was based on searching the ESO/SERC Southern Sky Atlas material for reddened sources in the vicinity of HH objects from Reipurth's catalogue. In some cases, candidate sources in the IVN were close to, or at the plate magnitude limit. In order to determine if such sources are real[17], deep CCD R and I band observations are needed to confirm their presence. In order to peer deeper into cloud cores, high resolution IRAS data at 12, 25, 60 and 100μm data can be used to identified heavily embedded objects not identifiable from the IVN material. Although IRAS data has long been used as a survey tool to identify candidate protostellar objects (i.e. Young, Lada & Wilking 1986; Beichman et al. 1986), HIgher RESolutiuon (HIRES) IRAS data, processed with the Maximum Correlation Method (see section 3.3) is able to identify extremely young protostellar objects with ages $< 10^4$ yr. In section 3.2, we present details on observations and data reduction. A classification scheme to identify candidate outflow sources is discussed in section 3.3. Results from individual HH complexes are discussed in section 3.4. Future directions and a summary are presented in sections 3.5 and 3.6 respectively.

3.2 Observations

3.2.1 Optical CCD Imaging

Narrow and broad-band CCD images of the HH complexes were obtained at the ANU 40inch telescope at Siding Spring Observatory during various periods shown in Table 3.1. Imaging was done with a 2048 $\times$ 2048 TEK CCD mounted at the f/8 Cassegrain focus. The 0.6″/pixel gave a field-

[17] i.e., not plate flaws!

of-view of $20.48' \times 20.48'$. The seeing conditions during usable time was typically less than $3''$. The narrow-band filters used consisted of Hα (6563Å; $\Delta\lambda$ 55Å), [SII] (6732Å; $\Delta\lambda$ 25Å) and red continuum (6676Å; $\Delta\lambda$ 55Å). We used Kron-Cousins R and I filters for the broad-band observations.

Table 3.1: Journal of CCD Observations.

Date	Filters
14/03/97 → 16/03/97	Hα, [SII], continuum
06/01/98 → 11/01/98	Hα, [SII], continuum, R, I
06/02/98 → 14/02/98	Hα, [SII], continuum, R, I
12/03/98 → 16/03/98	Hα, [SII], continuum, R, I
04/04/98 → 06/04/98	Hα, [SII], continuum

Typical exposure times were 10min. For narrow-band observations, multiple exposures were obtained for total exposure times ranging between 30min and 60min. Flat fields were obtained by illuminating the dome with a halogen lamp. All frames were reduced in a similar fashion with IRAF, where dark and bias frames were subtracted from source frames before flat fielding. Individual source frames were median combined to produce the final images.

3.2.2 IRAS High Resolution Data: HIRES

In order to peer deeper within molecular clouds beyond that possible with SERC IVN and deep I band observations, we turn to IRAS data processed via the Maximum Correlation Method (MCM; see Aumann, Fowler & Melnyk 1990 for a detailed discussion). With MCM, it is possible to produce HIgh RESolution (HIRES) images with a resolution better than an arc-minute, which is about a $\times 5$ improvement over the IRAS raw scan data and close to the diffraction limit of the telescope. The process of acquiring HIRES data consists of three steps. The first utilises a program called SNIPSCAN which retrieves the raw survey data. The second program, LAUNDR, cleans up the the IRAS raw scan data, and the third is YORIC, which actually applies the MCM algorithm to the LAUNDR'd data. For a full description of these steps, the reader is refereed to the HIRES WWW page at http://www.ipac.caltech.edu/ipac/iras/hires_proc.html. The data were obtained using the email retrieval service at IPAC[18] with the following parameters:

[18]See http://www.ipac.caltech.edu/ipac/iras/iras_data_requests.html

- The image and pixel sizes are $1^\circ \times 1^\circ$ and $15''$ respectively.
- All four bands (12, 25, 60 and 100μm) are processed.
- The raw scan data are de-striped with detector baseline removal and flux bias is applied.
- All three HCONs of survey data are CO-ADDED.
- Beam sample maps use specified spike positions/fluxes[19] on a highly smoothed background.
- The MCM algorithm is iterated a maximum of 20 times, with maps produced at the 1st, 5th, 10th and 20th iteration.

Once HIRES data was obtained, aperture photometry was performed on point sources using the *Skyview* image-processing software[20]. The aperture used were determined by averaging the point-source responses sampled on a rectangular grid throughout each image. This data is provided in the beam-width report ASCII files which lists the beam-width for each IRAS source at each iteration. The absolute uncertainty in HIRES-determined fluxes is $\sim$ 20% (Levine & Surace 1993). To check this, the IPAC program *Skyview* was used to sum fluxes over the beam-width at each wavelength with the error computed with $\sigma/\sqrt{N}$, where σ is the standard deviation of the sum and N is the number of pixels within the beam. For most sources, the 20% rule was found to be true although typical errors were found to be $\leq$ 5%. For sources included in the IRAS Point Source Catalogue, a comparison between HIRES-derived and IRAS PSC fluxes was found to be in agreement with the determined errors.

Recently, several studies have pushed the default number of HIRES iterations beyond 20 to achieve significant improvements in both resolution and image quality. In the paper of Aumman et al. (1990), the number of iterations of their 60μm image of the Pinwheel Galaxy M101 was set to 60 iterations, which allowed them to spatially resolve HII regions in the outer disk. In studies relevant to this discussion, Hurt & Barsony (1996), Barsony et al. (1998) and O'Linger et al. (1999) have pushed the number of iterations up to 150 to detect highly embedded Class 0 objects with extremely low luminosities (typically $< 10\ L_\odot$) which do not show any associated point source to K band (2.2μm) magnitudes < 18. In addition to data obtained with the default parameters, data where the number of iterations have been increased have been obtained and will be discussed in the text.

[19]Taken from the IRAS Point Source Catalogue.

[20]Available from http://www.ipac.caltech.edu/Skyview/

3.3 Source Classification

In order to classify young stellar objects from observed fluxes, many studies have used the infrared spectral index,

$$\alpha_{\lambda_1-\lambda_2} = \frac{log\lambda_1 F_{\lambda_1} - log\lambda_2 F_{\lambda_2}}{log\lambda_1 - log\lambda_2} \quad (1)$$

where λ_1 and λ_2 represent the most blue-ward and red-ward wavelengths for which fluxes (F_λ) can be obtained which are not upper limits. Equation 1 was first applied to young stellar objects for wavelengths between 2.2μm-10μm (i.e., Lada & Wilking 1984; Adams, Lada & Shu 1987). As circumstellar material is dispersed from the immediate environment of a young stellar object by action of its outflow, the spectral index is expected to decrease due to the decrease in the amount of material (infrared excess) surrounding the object. The above studies have listed Class I objects with $\alpha_{IR} > 0$ and Class II and Class III objects with $\alpha_{IR} < 0$. The difference between Class II and Class III is that the former have spectral energy distributions (SEDs) broader than a single temperature blackbody and evidence of a circumstellar disk (infrared excess), while Class III objects have SEDs similar to single temperature blackbodies, little infrared excess and are optically visible. The recently defined Class 0 objects (André, Ward-Thompson & Barsony 1993) are generally not identifiable for wavelengths $< 10\mu$m (Bachiller 1996) and so their classification at longer wavelengths is discussed below.

For the majority of cases presented here, 2.2μm observations are not available, but it is possible to classify infrared sources into Classes 0, I, II and III using IRAS data. For example, Margulis, Lada & Young (1993) used IRAS 12, 25, 60 and 100μm observations to classify sources in the Monoceros OBI molecular cloud. Using equation 1, Margulis et al. defined the dividing line between Class III and II objects at α = -2.5, whereas the dividing line between Class II and I objects is at $\alpha = 0$. A rough division between Classes I and 0 was obtained by computing α from those Class 0 objects in the list of Bachiller (1996) which have IRAS counterparts. For twelve sources with clear detections in at least two bands, α was found to lie in the range 1.04 (IRAS08076) $\leq \alpha \leq$ 3.57 (IRAS16293) with an average value of 1.92. Therefore, as a division between Class I and 0 objects, we adopt a value of $\alpha = 2$. The classification from Class 0 to Class III sources based on 12, 25, 60 and 100μm data is summarised in Table 3.2. For cases where K band (2.2μm) observations exist, they will be used in conjunction with HIRES data to compute the spectral index.

Table 3.2: Source classification using HIRES fluxes.

Class	α
0	>2.0
I	$0 \leq \alpha \leq 2.0$
II	$-2.5 \geq \alpha \leq 0$
III	< -2.5

3.4 Selected Herbig-Haro Complexes

Table 3.3 lists a selection of poorly studied HH objects which have yet to have their energy source positively identified. For some cases, extensive searches for the exciting sources have resulted in negative results, but it should be noted such surveys have usually concentrated within the immediate vicinity of the HH object in question. For some of the objects listed in Table 3.3, candidate energy sources have been put forward (i.e., IRAS 09094-4522 and HH 75; Cohen 1990), but the association is primarily based on the presence of a reddened object in the vicinity of the HH emission. Given the fact that HH objects can now be located more than a parsec from their exciting sources, applying what we know about existing giant HH flows to the objects listed in Table 3.3 will gauge if they themselves are part of giant HH flows.

For those HH objects without kinematic information, a tentative association with a source can be given if there is a symmetrical distribution of HH objects on either side of the suspected energy source (i.e., Bally & Devine 1994). Another method is to identify faint emission linking HH objects previously thought to be unrelated (Eislöffel & Mundt 1997). Therefore, deep, wide-field [SII] and Hα images will enable one to identify new HH emission which may have been missed in previous small-scale surveys.

Listed in Table 3.3 are proposed energy sources that have either been re-confirmed and/or identified from the current survey of photographic (IIIaJ, IIIaF, IVN), CCD (Hα, [SII], R, I) and IRAS HIRES data. For HH 66, HH 94 and HH 95, we defer discussion of these objects until chapter 4 as these objects highlight the usefulness of deep Hα films acquired through the new Anglo-Australian Observatory (AAO) and United Kingdom Schmidt Telescope (UKST) Hα survey of the southern Galactic plane. Unless noted in the discussion, distances listed in Table 3.3 have been taken from Reipurth (1999) and references therein.

Table 3.3: Surveyed Herbig-Haro objects with suggested energy sources.

HH	α(1950)	δ(1950)	Suspected Source	Region	Dist
	h m s	° ′ ″			(pc)
58	05 28 22.7	-04 11 44	IRAS 05283-0412[1]	Orion	470
59	05 29 52.0	-06 31 09	HH83 IRS	L1641	470
60	05 30 11.4	-06 28 50	HH83 IRS	L1641	470
131	05 32 18.9	-08 30 03	LDN1641 S3?	L1641	470
66[2]	05 37 55.0	-02 04 04	NGC 2023 mms1	L1630	470
94[2]	05 40 56.3	-02 34 14	NGC 2023 mms1	L1630	470
95[2]	05 41 22.5	-02 39 03	NGC 2023 mms1	L1630	470
124	06 38 17.0	+10 17 58	IRAS 06382+1017[3]	NGC 2264	800
73	09 00 26.6	-44 39 25	IRAS 09003-4438C	Vela	700
133	09 09 02.4	-45 18 18	IRAS 09094-4522	Vela	700
75	09 09 50.7	-45 30 07	IRAS 09094-4522[1]	Vela	700
137	11 11 49.0	-60 36 17	HH 137/138 IRS1	Carina	990
138	11 12 01.5	-60 36 35	HH 137/138 IRS1	Carina	990
180	18 14 25.2	-19 52 55	HH 180 IRS	Sagittarius	1700

[1]Previously identified as a candidate energy source; see text.
[2]See chapter 4, section 4.6.
[3]Binary source with each component driving a parsec–scale flow (see section 3.4.6).

3.4.1 HH 58

Previous studies

First identified by Reipurth & Graham (1988; hereafter RG88), HH 58 consists of a southern and northern groups of knots (see their Figure 2). The northern group consists of a chain of knots orientated along PA = 340°, while 1.′11 to the south, HH 58S consists of two bright knots. Located 1.′1 to the south of HH 58N lies the IRAS source IRAS 05283-0412. Based on the similar PAs of HH 58N and the location of the IRAS source with respect to HH 58N (159°), Cohen (1990) suggested IRAS 05283-0412 is a candidate energy source for HH 58N only with the energy source for HH 58S yet to be identified. The IRAS source was mapped at 1300μm by Reipurth et al. (1993a), while Dent, Matthews & Ward-Thompson (1998; hereafter DMW98) set an upper limit at 800μm and did not detect any H_2CO or ^{18}CO emission.

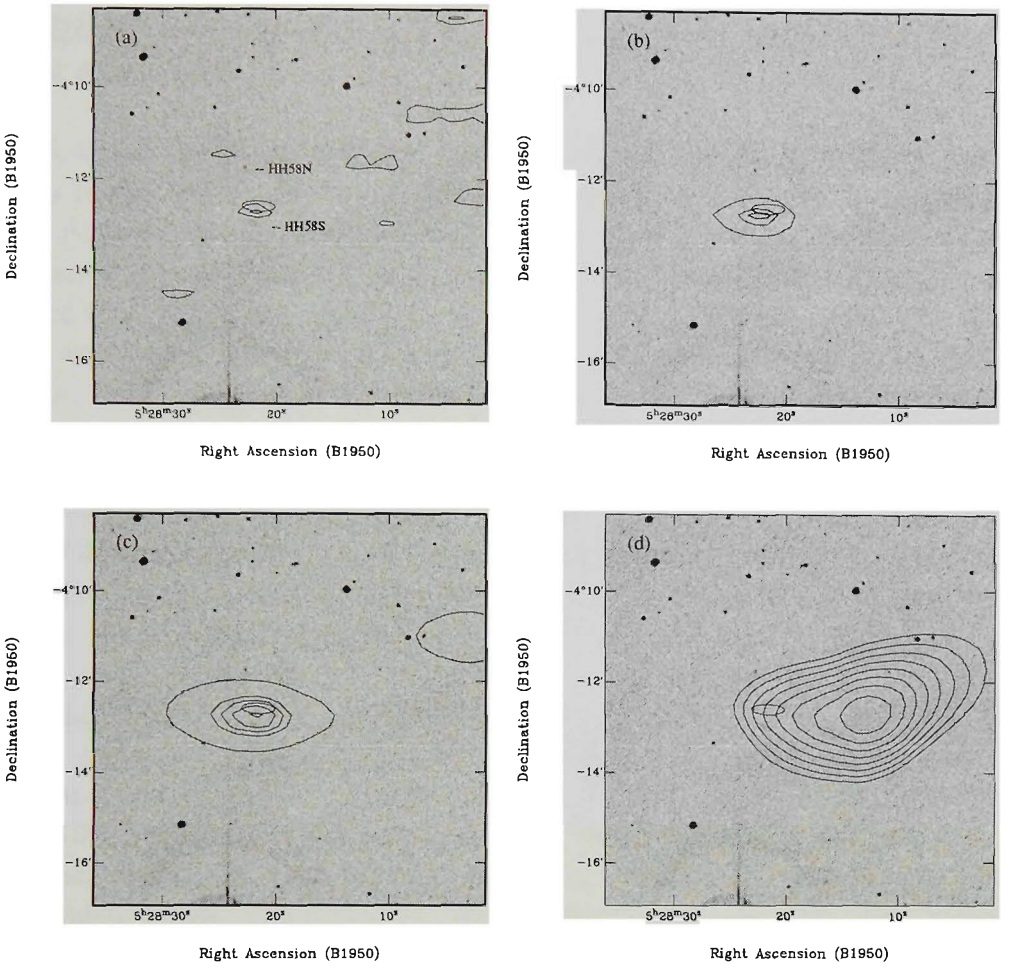

Figure 3.1: IIIaF image of the HH 58 region with contour overlays from IRAS HIRES images. The ellipse marks the position uncertainty of the IRAS source 05283-0412. (a) 12μm; contours at 2.93 and 3.22 MJy sr^{-1}, (b) 25μm; contours at 5.43, 16.30 and 21.74 MJy sr^{-1}, (c) 60μm; contours at 10, 20, 23, 26 and 29 MJy sr^{-1}, (d) 100μm; contours at 40 to 52 MJy sr^{-1} in steps of 2 MJy sr^{-1}.

New observational results

In Figure 3.1, the HIRES 12, 25, 60 and 100μm band images have been overlaid on the IIIaF image of the region. The IRAS source lies between HH 58N and HH 58S. In Figure 3.2, a magnified CCD I band image shows a faint reflection nebulosity associated with HH 58S and an enhanced image displays an inverted V-type structure with its apex close to the location of IRAS 05283-0412. Within the error ellipse and near the peak of the HIRES 12μm contours, Figure 3.2 shows a compact knot of reflection emission. The association of faint emission with HH 58S suggests the emission is scattered

light from a cavity surrounding the IRAS source and the shock-excited emission (HH 58S) has been created from the impact of the stellar wind with the western cavity wall.

Table 3.4 lists the fluxes obtained from the HIRES photometry. With the exception of the 100μm image, all HIRES images clearly detect a point source at the position of the IRAS source. However, the 100μm contours clearly shows an emission peak 160″ to the west of IRAS 05283-0412 where the majority of the 100μm flux is due to a distinct region separate from the IRAS source which may represent a cirrus condensation or heavily embedded Class 0 object. The peak flux of this new source (denoted hereafter as MZ 1) is located at α(B1950) = $05^h28^m12.67^s$ δ(B1950) = $-04°12'44''$. Using the 100μm beam-width (1.′36) and the relationship $I_{100\mu m} \approx 5A_V + 17$ MJy sr^{-1} mag^{-1} (Langer et al. 1989; Snell, Schloerb & Heyer 1989), the extinction associated with IRAS 05283-0412 and MZ 1 can be estimated[21]. Using the maximum values for $I_{100\mu m}$ at IRAS 05283-0412 (51 MJy sr^{-1}) and MZ 1 (55 MJy sr^{-1}) suggests $A_V > 7$ mag and > 8 mag respectively.

Using the HIRES fluxes, the spectral index for IRAS 05283-0412, $\alpha_{12-60\mu m}$ = 0.82, places the source in the Class I region. Due to the upper limits at 12, 25 and 60μm, a determination of α for MZ 1 is not possible, but André et al. (1993) suggested that the ratio $L_{bol}/(10^3 \times L_{1300\mu m})$ can be used as an evolutionary indicator of protostellar objects. During the accretion phase, the circumstellar mass of an object is proportional to $L_{1300\mu m}$, which is expected to decrease as the object moves toward the main sequence. Therefore, older objects will have higher values of $L_{bol}/(10^3 \times L_{1300\mu m})$. For Class 0 objects, $L_{bol}/(10^3 \times L_{1300\mu m})$ lies approximately between 2–15, whereas for Class I objects, the ratio lies in the range 30-200 (André et al. 1993). Therefore, to classify sources with $L_{bol}/(10^3 \times L_{1300\mu m})$, we need to model the source SED and integrate it to extract L_{bol} and $L_{1300\mu m}$. For this purpose, the following modified greybody is used:

$$S_\lambda = \Omega B(\lambda, T_d)(1 - e^{-\tau_\lambda}) \tag{2}$$

where Ω is the solid angle of the emitter, $B(\lambda, T_d)$ is the Planck function and τ_λ is the optical depth approximated by $(\lambda/\lambda_o)^\beta$; λ_o is the critical frequency where $\tau_\lambda = 1$. β is the dust grain opacity (or dust emissivity index). The $(1 - e^{-\tau_\lambda})$ factor accounts for the finite optical depth of a dust cloud at all wavelengths. For wavelengths $> 100\mu$m, theoretical models expect β to lie in

[21]It should be noted that $I_{100\mu m}/A_V \sim 5$ MJy sr^{-1} was found to be valid for diffuse (unresolved) clouds. Here it is clear that much of the region where the extinction is going on is not resolved at 100μm, and values for A_V should be considered as lower limits.

the range 1–2 where $\beta = 1$ defines amorphous carbon grains (Hanner 1988; Ossenkopf, Henning & Mathis 1992) and $\beta = 2$ defines crystalline grains typical of that seen in molecular clouds (Hildebrand 1983; Draine & Lee 1984). As the long wavelength shape of the SED is determined by T_d and β, IRAS and millimetre observations combined can provide tighter constraints on these values which in turn define L_{bol} and $L_{1300\mu m}$. However, for objects without fluxes greater than 100μm (like MZ 1), estimating the above parameters by fitting equation 2 to reliable IRAS 60 and/or 100μm data points gives us a crude estimate of L_{bol}[22] and $L_{1300\mu m}$[23] so that $L_{bol}/(10^3 \times L_{1300\mu m})$ can be used to estimate the evolutionary status of a source.

For IRAS 05283-0412 and MZ 1, the closest fit parameters (T_d, Ω, β and $\tau_{250\mu m}$) and SEDs are shown in Figure 3.3. For IRAS 05283-0412, the SED can be modelled by a two-component greybody comprising photospheric (T_d = 65 K) and dust emission (T_d = 29.5 K). The 1300μm flux is overestimated by a factor $\sim$ 1.5. Table 3.5 lists the fit properties for both sources. Table 3.5 shows $L_{bol}/(10^3 \times L_{1300\mu m}) \geq 21.24$ for IRAS 05283-0412, which suggests a Class I object. In addition, the low sub-millimetre fluxes for IRAS 05283-0412 and absence of H_2CO and ^{18}CO emission (DMW98) suggests it is a rather evolved object. In contrast, MZ 1 falls way under with $L_{bol}/(10^3 \times L_{1300\mu m}) \sim 4$, a candidate Class 0 object? A defining characteristic of Class 0 objects is a large amount of dust residing in the circumstellar envelope. The circumstellar dust mass surrounding a source can be estimated from the equation (Hildebrand 1983):

$$M_{env} = \frac{F_{1300\mu m} D^2}{\kappa_{1300\mu m} B(T_d)} M_\odot \tag{3}$$

where $F_{1300\mu m}$ is the observed flux at 1300μm, D is the distance to the source (in pc) and $B(T_d)$ is the Planck function B_λ at 1300μm for the dust temperature T_d. The mass opacity $\kappa_{1300\mu m}$ has values $\sim$ 0.01 cm^2 g^{-1} for Classes 0/I and $\sim$ 0.02 cm^2 g^{-1} for Class II/III sources (André & Montmerle 1994 and references therein).

[22]Integrated from 10 to $10^4\mu$m.

[23]Determined over a frequency bandwidth of 50GHz.

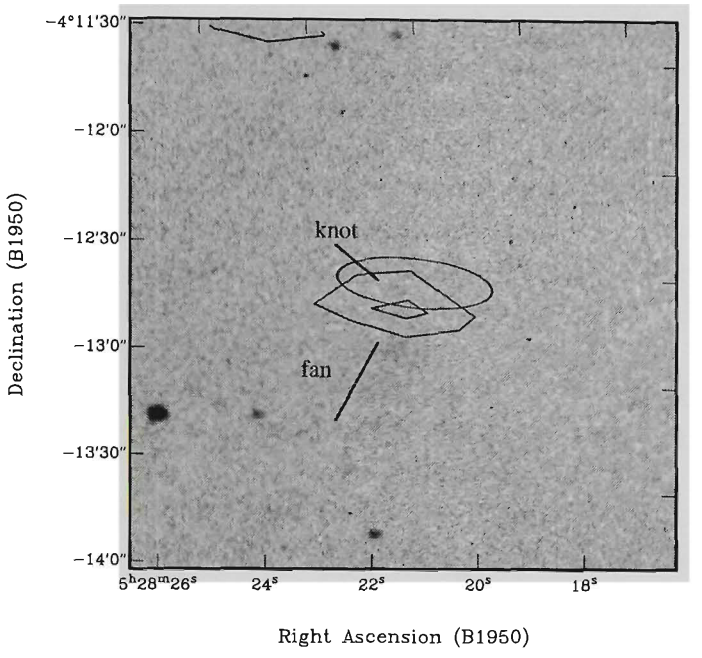

Figure 3.2: CCD I band image of the IRAS 05283-0412 and HH 58S region with HIRES 12μm contours at 2.93 and 3.22 MJy sr^{-1}. A compact knot is seen near the peak of the HIRES 12μm emission. The eastern wall of a faint fan-type structure is outlined and extends to the south. This feature is interpreted as scattered light from an outflow cavity. The positional error ellipse of the IRAS source is also shown.

Table 3.4: Fluxes for IRAS 05283-0412 and MZ 1.

Source	λ (μm)	Beam ($''$)	HIRES Flux (Jy)	Previous Flux (Jy)	Refs
IRAS 05283-0412:	12	58×30	<0.07 ± 0.01	<0.1	1
	25	65×35	1.28 ± 0.20	1.2	1
	60	82×55	5.58 ± 0.29	4.3	1
	100	95×70	20.18 ± 0.32	26.8	1
	800	16×16		<0.173	2
	1300	23×23		0.032	3
MZ 1:	12	58×30	<0.06 ± 0.01		
	25	65×35	<0.13 ± 0.01		
	60	82×55	<2.27 ± 0.1		
	100	95×70	25.46 ± 0.19		

REFERENCES: (1) Cohen (1990); (2) DMW98; (3) Reipurth et al. (1993a).

For IRAS 05283-0412, using the 1300μm flux from Reipurth et al. (1993a; Table 3.4), $\kappa_{1300\mu m}$ = 0.01 cm^2 g^{-1} and T_d = 29.5 K gives equation 3 a value of M_{dust} = 0.14 $M_\odot$. In comparison, Reipurth et al. (1993a) used $\kappa_{1300\mu m}$ = 0.003 and 0.02 to derive dust masses of 0.21 and 0.032 $M_\odot$ respectively for a volume-averaged T_d = 36 K. Bontemps et al. (1996) showed the (L_{bol},M_{env}) diagram (their Figure 1) can be used as an evolutionary diagram for embedded young stellar objects. For IRAS 05283-0412 ($L_{bol} \sim 5\ L_\odot$, M_{env} = 0.14 $M_\odot$), the source is again located in the Class I range. As there are no submillimetre observations of MZ 1 available, extrapolating the fit to 1300μm yields a value of 0.57 Jy. Placing MZ 1 in the L_{bol} versus M_{env} diagram suggests MZ 1 (M_{env} = 2.59 $M_\odot$, L_{bol} = 8.54 $L_\odot$) displays characteristics of a deeply embedded ($A_V > 8$ mag) Class 0 source.

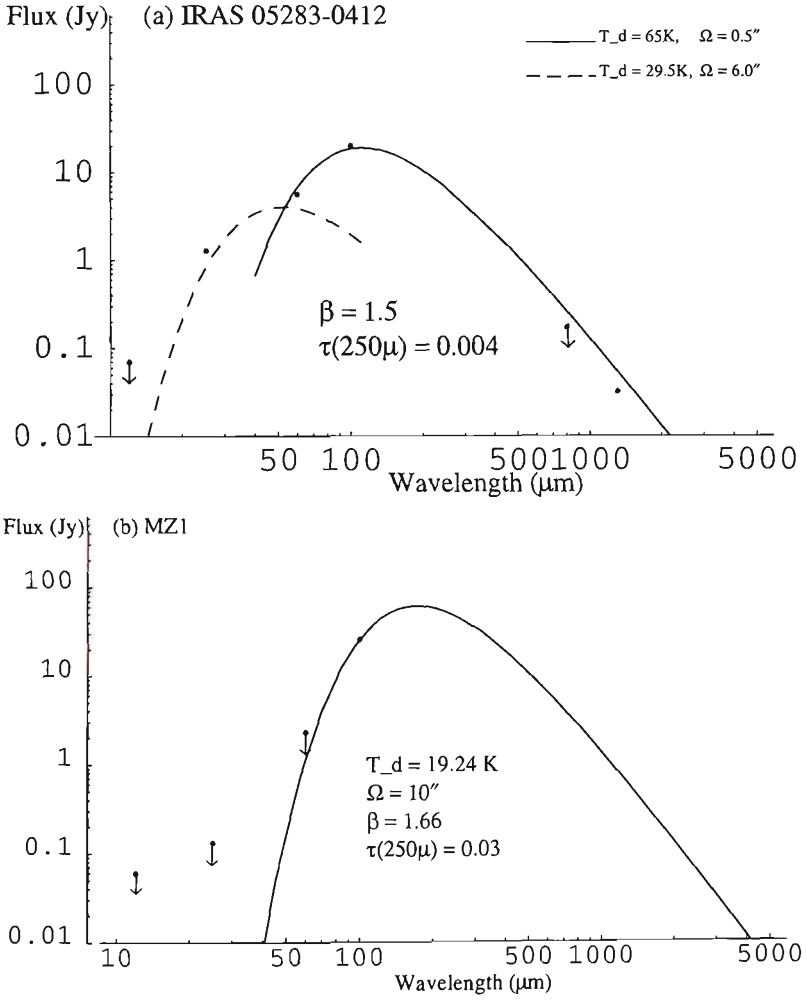

Figure 3.3: SEDs for the (a) Class I source IRAS 05283-0412 and (b) candidate Class 0 object, MZ 1. For IRAS 05283-0412, the two component fit can be explained by contributions from photospheric (T_d = 65 K) and dust (T_d = 29.5 K) components. For both sources, fit parameters are listed and upper limits are indicated.

Table 3.5: Derived properties for IRAS 05283-0412 and MZ 1.

Parameter	IRAS 05283-0412	MZ 1
Ω	0.5-6″	10″
T_d	29.5-65 K	19.24 K
L_{bol}	5.08 $L_\odot$	8.54 $L_\odot$
$L_{1300\mu m}$	0.0002 $L_\odot$	0.002 $L_\odot$
$L_{bol}/(10^3 \times L_{1300\mu m})$	$\geq$21.24	4.26
M_{dust}	0.14 $M_\odot$	2.59 $M_\odot$
$\alpha_{12-60\mu m}$	0.82	-
Class	I	0?

3.4.2 HH 59/60

Previous studies

Originally identified by RG88, HH 59 and HH 60 are located to the west of the main L1641 cloud in Orion. The IIIaJ and IIIaF images of HH 59 and HH 60 are shown in Figure 3.4[24]. HH 59 displays strong emission in the IIIaF, faint emission in the IIIaJ and none in the IVN which suggests an emission nebulosity. HH 60 displays very faint emission in the IIIaF and none in the IIIaJ or IVN. Although RG88 pointed out that there are several Hα emission-line stars and faint IRAS sources in the vicinity of these objects, they do not give a preference for a particular energy source. Using IRAS CO-Added scans, Cohen (1990) identified a faint 60μm source IRAS 05299-0627C[25] 3.′5 (0.47 pc) to the north-west of HH 60 as shown in Figure 3.5. Based on the position angle of this source with respect to the elongation of HH 60 (PA $\sim$ 304°), Cohen (1990) suggests this source as the energy source for HH 60. No CO-Added source was identified for HH 59. Due to the upper limits of the 12, 25 and 100μm fluxes, it is not possible to characterise the source. DMW98 obtained spectra at 800μm for IRAS 05299-0627C and found negligible flux (-0.002 Jy) in the direction of the source.

[24]IVN image not available at time of writing.

[25]Coordinates from Cohen (1990): α(B1950) = $05^h29^m59.9^s$, δ(B1950) = $-06°27'01''$

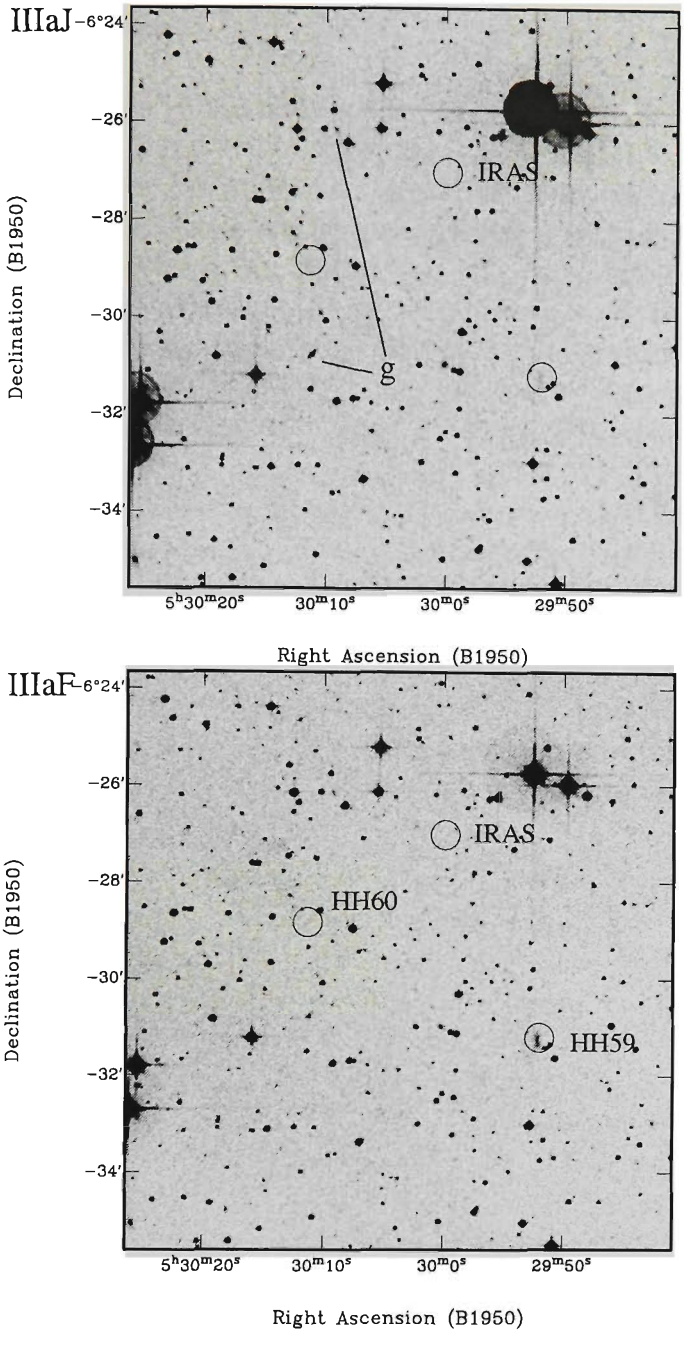

Figure 3.4: IIIaJ and IIIaF images of HH 59/60. HH 59 displays emission in both the IIIaJ and IIIaF, but not in the IVN (not shown). This suggests a true emission nebulosity. HH 60 displays faint IIIaF emission. The positions of each HH object and a (former) candidate energy source for HH 60 (IRAS 05299-0627C; marked as IRAS) are indicated. IRAS 05299-0627C may be a reddened galaxy of which several (labelled "g") are seen in the IIIaJ.

New observational results

For HH 59/60 and IRAS 05299-0627C, an ESO R band extinction map of the region (Cambrésy 1999) shows that $A_R < 0.5$ mag. Using $A_R/A_V = 0.748$ (Rieke & Lebofsky 1985), we find $A_V < 0.67$ mag and so IRAS 05299-0627C may in fact represent a background galaxy (several are seen in the vicinity of HH 59 and HH 60; see Figure 3.4). Located several arc-minutes to the east of HH 59 and HH 60 is the parsec-scale flow HH 83/84, identified as such by RBD97. The HH flow is driven by the embedded Class I object HH 83IRS/IRAS 05311-0631 (see RBD97 and references therein). Using long-slit spectroscopy, Reipurth (1989b) found HH 84 displays positive velocities in the range 100-200 km s^{-1} which places the HH object in the red-shifted lobe of the giant flow. For the knots associated with HH 83, those which extend towards HH 59/60 display decreasing negative velocities. Although no velocity information is available for HH 59/60, if they are associated with the HH 83/84 flow, long-slit spectroscopic studies should show they display negative velocities consistent with them lying in the blue-shifted lobe of the HH 83/84 giant flow. The distance from HH83 IRS to HH 59 is 18.′21, or 2.5 pc at a distance of 470 pc to Orion. Therefore, under our assumption, the addition of HH 59/60 to the HH 83/84 giant outflow increases the length from 1.46 pc to $\sim$ 4 pc in projection.

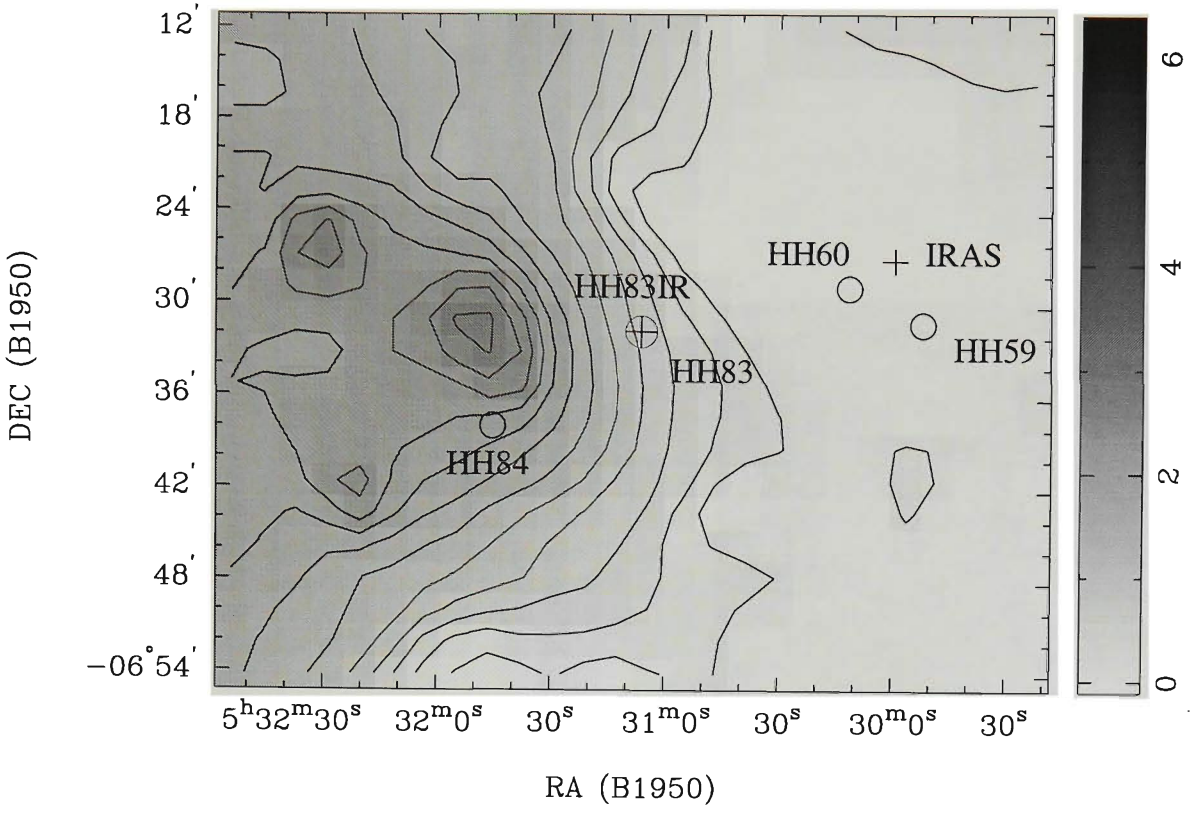

Figure 3.5: Extinction map (ESO R band counts; from Cambrésy 1999) showing the position of HH 59/60 in relation to the giant HH flow HH 83/84, to which HH 59/60 may be related. HH 83/84 are driven by the embedded T Tauri star HH83 IRS (identified by the cross). The positions of each HH object and a (former) candidate energy source for HH 60 (IRAS 05299-0627C; marked as IRAS) are indicated. The wedge shows units of A_R and contours range from 0.5 to 6 mag in steps of 0.5 mag.

3.4.3 DC266.1+01.1

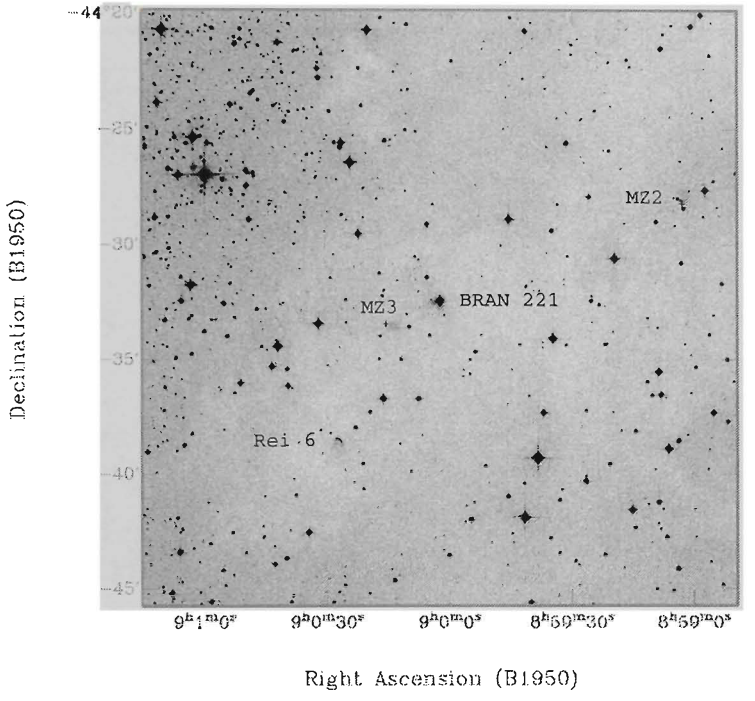

Figure 3.6: IIIaF image of the dark cloud DC266.1+01.1. The reflection nebulosities Bran 221 and Rei 6 are indicated. Two previously unknown objects, MZ 2 and MZ 3, are also labelled.

Previous studies

Lying in the direction of the Gum Nebula, the dark cloud DC266.1+01.1 (Hartley et al. 1986; Figure 3.6) is projected against the Vela Molecular Ridge (VMR) C region (Murphy & May 1991). In a CCD survey for HH objects in southern molecular clouds, RG88 found two HH objects in the direction of DC266.1+01.1. HH 73 consists of a chain of HH knots $\sim 29''$ in length and HH 74, $\sim 1.5''$ north-east of HH 73, is a stellar-like knot. Both objects lie in the vicinity of the reflection nebulosity Rei 6 (Reipurth 1981) which has been associated with red-shifted ^{12}CO emission (de Vries et al. 1984). The source is also a binary with separation $\sim 1\farcs5$ (Reipurth & Zinnecker 1993). Also located nearby is the nebulous object Bran 221 (Brand, Blitz & Wouterloot 1986). Two previously unknown objects were found $11\farcm3$ north-west of Bran 221 (MZ 2) and $5\farcm7$ NNW of Rei 6 (MZ 3). Both are labelled in Figure 3.6 and will be discussed later on. Following Liseau et al. (1992), a distance of 700 pc is adopted as the distance to the cloud.

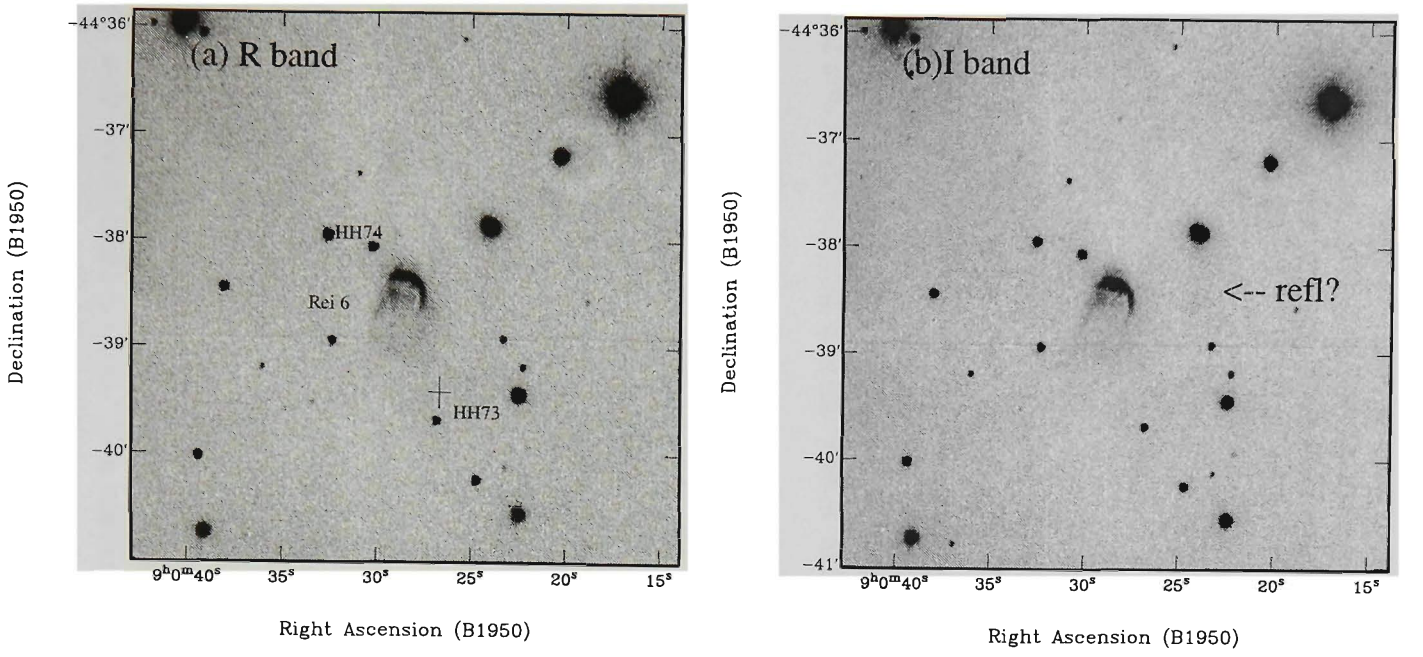

Figure 3.7: CCD (a) R and (b) I band images of the HH 73/74 region. The locations of HH 73 and the arcuate object Reipurth 6 are indicated. HH 74 is seen as a faint knot in the R band image. A faint reflection nebulosity, possibly from the exciting source of HH 73, is shown in the I band image.

Using IRAS CO-Added images, Cohen (1990) identified a faint point source, IRAS 09003-4438C (hereafter IRAS 09003C) $\sim$ 1.'0 from HH 73 and suggests it is a candidate energy source for that object. RG88 suggest HH 74 is associated with Rei 6. At the position of IRAS 09003C, DMW98 set an upper limit at 800μm with an absence of ^{18}CO gas and only a weak detection in H_2CO ($\leq$ 0.2 K km s^{-1}). As explained below, the coordinates given by Cohen (1990) for IRAS 09003C are incorrect, which explains these non-detections.

New observational results

IRAS 09003C and HH 73

In the vicinity of HH 73, the ESO/SERC images do not show any reddened sources which could be considered as a candidate energy source. Deep CCD R and I band images of the HH 73/74 region are shown in Figure 3.7. A comparison between these images shows the prominent reflection nebulosity associated with Rei 6. HH 73 is not visible in the R band image[26], while HH 74 is seen as a faint knot just above Rei 6. The I band image reveals a faint reflection nebulosity almost a minute west of Rei 6.

Overlaid on the CCD I band image, the HIRES images of the HH 73/74 region are shown in Figure 3.8. Rei 6 displays peaks in the 12μm and 25μm images while IRAS 09003C shows peaks at 60 and 100μm only. The HIRES fluxes for both sources are presented in Table 3.6. It was noted above that the coordinates given by Cohen (1990) for IRAS 09003C were incorrect. He gives α(B1950) = 09^{h}00^{m}23^s, δ(B1950) = $-$44°38′56″. An examination of the HIRES images reveal no source at this location although the 60μm image shows a peak at α(B1950) = 09^{h}00^{m}22.6^s, δ(B1950) = $-$44°37′59″. A difference of nearly a minute between the two positions is why DMW98 did not detect a source with their 16″ beam at 800μm.

Cohen (1990) noted the position of IRAS 09003C lies close to a double stellar source (star1 in Figure 3.8a), which when blinked in the ESO/SERC IIIaJ, IIIaF and IVN images, shows no evidence of extinction and therefore lies in front of the molecular cloud. As IRAS 09003C is detected only at 60 and 100μm, we conclude the apparent coincidence is just that with IRAS 09003C representing a more embedded source. The reflection nebulosity identified in Figure 3.7b extends from IRAS 09003C towards HH 73. As its position angle is similar to the knots that define HH 73, the reflection nebulosity may represent scattered light escaping from a cavity surrounding IRAS 09003C.

[26]Most probably due to the short integration time of the image (10min). The [SII] image of RG88 was 60min.

This scenario suggests IRAS 09003C as a candidate energy source for HH 73. The only difficulty with this interpretation is the alignment of the HH flow in PA $\sim$ 135°; the position of IRAS 09003C with respect to the centre of HH 73 is in PA $\sim$ 160°. However, this difficulty can be avoided if one thinks of HH 73 as the result of a grazing flow such as HH 110/270 (Reipurth, Raga & Heathcote 1996), where the flow angle bends 58° from HH 270 to HH 110. The change for HH 73 is less dramatic with a flow direction change $<$ 25°. The [SII] image of RG88 (their Figure 19a) shows a slither of emission bending from the line of HH 73 towards the reflection nebula and position of IRAS 09003C. A true test of this scenario requires high resolution millimetre observations to identify a dense molecular clump in the vicinity of HH 73.

With the HIRES fluxes listed in Table 3.6, the greybody fit to the SED for IRAS 09003C is shown in Figure 3.9. The fitted parameters and derived properties (Table 3.7) suggest a cold (T_d = 24.13 K) and low luminosity ($\sim$ 9 $L_\odot$) source. From the 60 and 100μm fluxes, $\alpha_{60-100\mu m}$ = 2.25, which places the source in the Class 0 range. Extrapolating the fit to 1300μm, a value of 0.14 Jy is obtained and using equation 3, the mass of the envelope is $\sim$ 1 $M_\odot$. In the (L_{bol},M_{env}) diagram of Bontemps et al. (1996; their Figure 1), IRAS 09003C is again located in the Class 0 region.

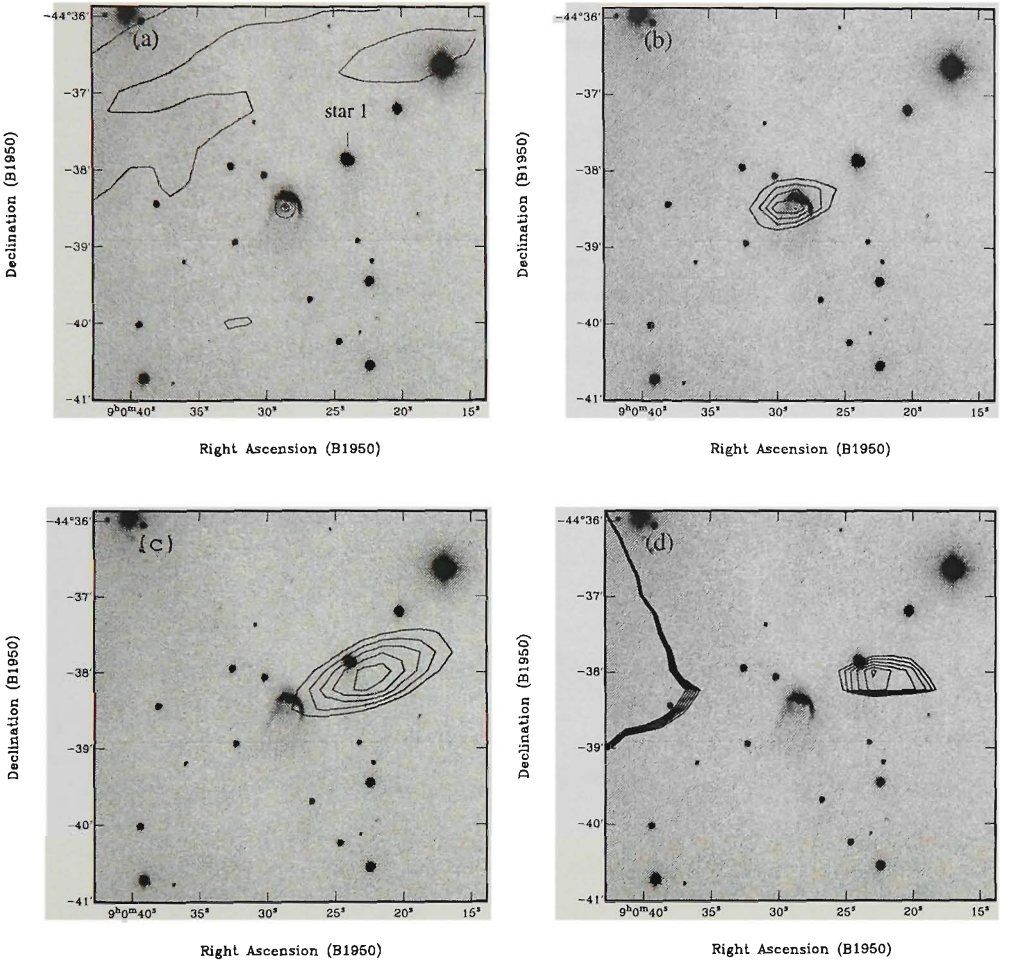

Figure 3.8: HIRES contours overlaid on the I band image of the HH 73/74 region. Rei 6 is detected at 12μm and 25μm, with IRAS 09003C detected at 60μm and 100μm. (a) 12μm contours at -0.1, 0.001 and 0.01 MJy sr^{-1} (peak = 395.74 MJy sr^{-1}); (b) 25μm contours at 1.2-2% in steps of 0.2% of peak (307.57 MJy sr^{-1}); (c) 60μm contours at 7-11% in steps of 1% of peak (175.26 MJy sr^{-1}); (d) 100μm contours at 44.2-44.7% in steps of 0.1% of peak (60.50 MJy sr^{-1}). The object marked "star 1" in (a) is a double source previously identified by Cohen (1990). See text for details.

Table 3.6: Fluxes for IRAS 09003C

λ (μm)	Beam ($''$)	HIRES (Jy)	Previous (Jy)	Refs
12	77×39	<0.04 ± 0.01	< 0.12	1
25	74×36	<0.15 ± 0.03	0.39	1
60	100×58	3.27 ± 0.25	2.60	1
100	136×106	17.17 ± 0.23	13.2	1

REFERENCE: (1) Cohen (1990).

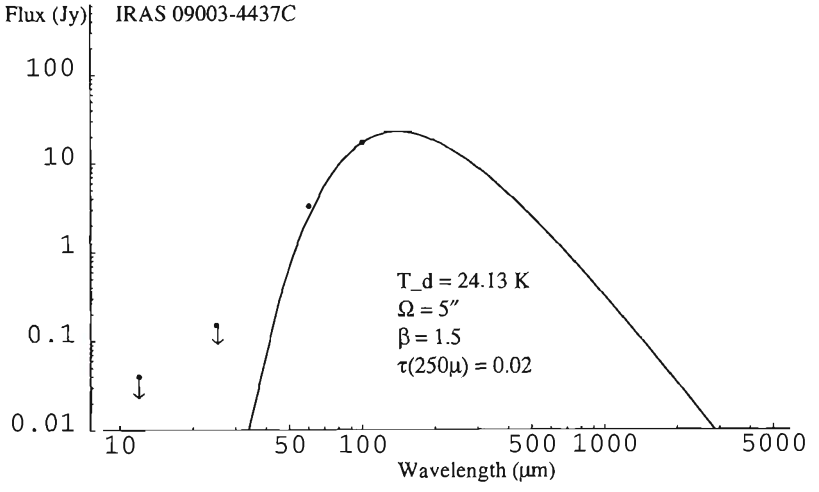

Figure 3.9: SED of the Class 0 candidate, IRAS 09003C. Parameters used to constrain the fit are listed. Upper limits are indicated.

Table 3.7: Derived properties for IRAS 09003C

Parameter	Value
Ω ($''$)	5
T_d (K)	24.13
L_{bol} ($L_\odot$)	9.14
M_{env}($M_\odot$)	1.04
$\alpha_{60-100\mu m}$	2.25
Class	0

As mentioned earlier and shown in Figure 3.6, two interesting objects, MZ 2 and MZ 3, were identified from the ESO/SERC plates.

MZ 2

Deep CCD R and I band images of MZ 2 are shown in Figure 3.10 which show it to be an optically visible star surrounded by several overlapping loops. To the south-west, there appears to be an increase in brightness in one of the loops. By blinking the ESO/SERC IIIaJ, IIIaF and IVN images, faint IIIaJ emission can be seen with the IVN emission brighter than both the IIIaJ and IIIaF. This suggests the loops are mainly reflection emission, but we do not rule out the possibility the emission seen in the IIIaJ image is not shocked [OIII] emission. Narrow-band CCD images of the source will confirm the presence of shock-excited emission. By blinking the ESO/SERC images, there appears to be significant extinction in the line of sight as the source size in the IVN image increases by a factor of two as compared to the size in the IIIaJ. This suggests MZ 2 may be associated with the molecular cloud. In addition, most of the stellar sources in Figure 3.10 do not display any change in brightness in the IIIaJ, IIIaF and IVN images which suggests they lie in front of the molecular cloud.

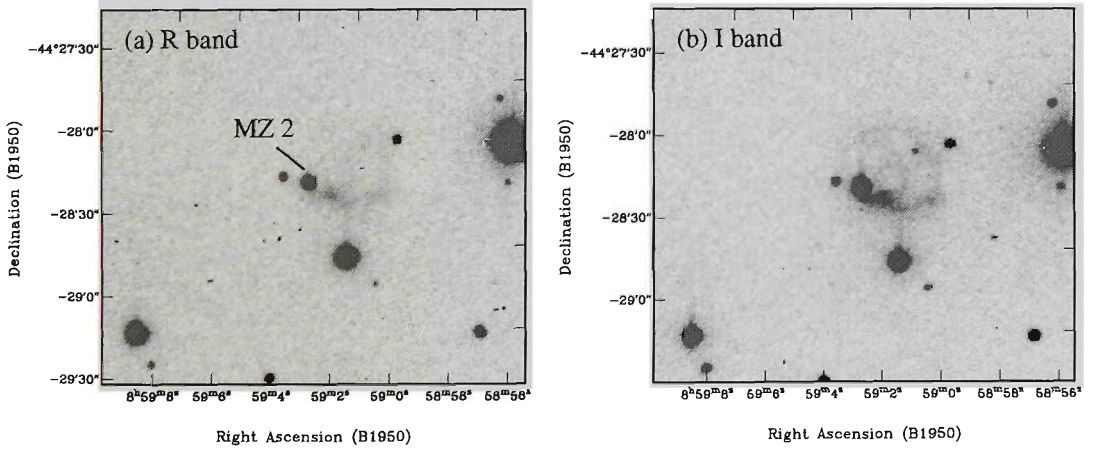

Figure 3.10: Magnified CCD (a) R and (b) I band images of MZ 2.

As shown in Table 3.8, the source, located at α(B1950) = $08^h59^m03.59^s$, δ(B1950) = $-44°28'10.96''$, displays HIRES emission in the 12, 25 and 60μm bands with an upper limit at 100μm. The HIRES contours are overlaid on the CCD I band image in Figure 3.11 where photospheric (12μm) emission coincides with the position of the optically visible source. The 25 and 60μm peaks are offset a few arc-seconds to the east of MZ 2 which can be explained

by shocked emission from an embedded cavity (see below).

From the HIRES fluxes listed in Table 3.8, the spectral index, $\alpha_{12-60\mu m}$ = -0.48, which places the source in the Class II region. Figure 3.12 shows a two-component fit to the SED with contributions from photospheric (T_d = 140 K) and dust (T_d = 65 K) emission. The derived properties in Table 3.9 indicate a low luminosity source (15.22 $L_\odot$), and extrapolating the fit to 1300μm, we derive a flux of 0.01 Jy and upon application of equation 3, the envelope mass is $\sim$ of 0.01 $M_\odot$. In the (L_{bol},M_{env}) diagram of Bontemps et al. (1996; their Figure 1), MZ 2 is placed beyond their sample of Class I objects which generally have $M_{env} > 0.01\ M_\odot$.

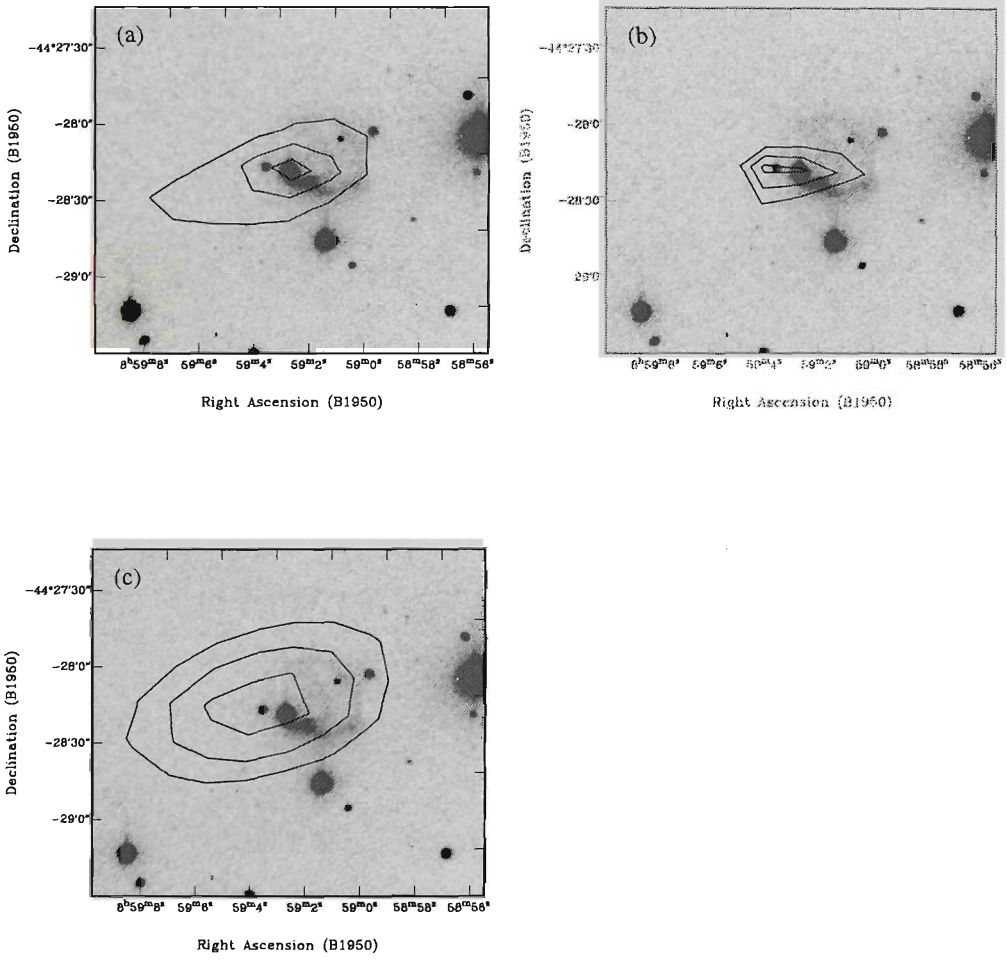

Figure 3.11: HIRES contours overlaid on the I band image of MZ2. (a) 12μm contours at 2-6% in steps of 2% of peak (395.74 MJy sr^{-1}); (b) 25μm contours at 6-10% in steps of 2% of peak (307.57 MJy sr^{-1}); (c) 60μm contours at 5-7% in steps of 1% of peak (175.26 MJy sr^{-1}). An upper limit is seen at 100μm, suggesting a lack of cold dust.

Table 3.8: HIRES fluxes for MZ 2

λ (μm)	Beam ($''$)	HIRES (Jy)
12	77×39	0.86 ± 0.03
25	74×36	1.24 ± 0.04
60	100×58	1.99 ± 0.02
100	136×106	<9.27 ± 0.01

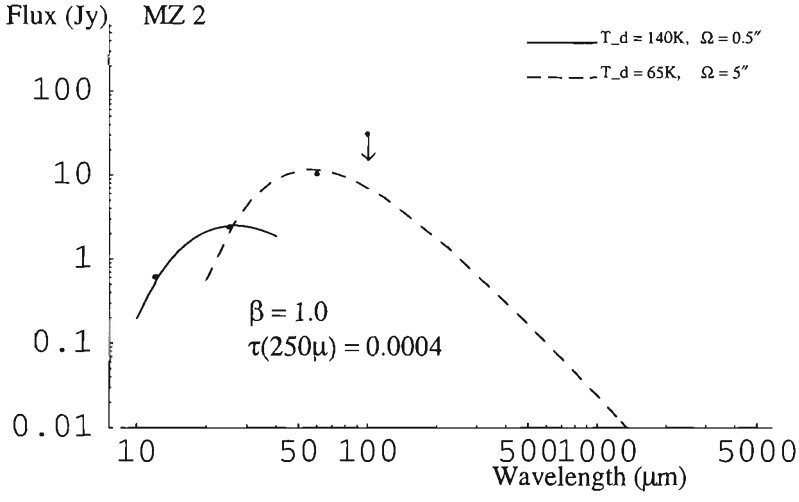

Figure 3.12: SED for the Class II source, MZ 2. The source is modelled with hot photospheric (T_d = 140 K) and cooler (T_d = 65 K) dust components. Parameters used to constrain the fit are listed and upper limits are indicated.

Table 3.9: Derived properties for MZ 2

Parameter	Value
Ω	0.5-5$''$
T_d	65-140 K
L_{bol}	15.22 $L_\odot$
M_{env}	0.01 $M_\odot$
$\alpha_{12-60\mu m}$	-0.48
Class	II

MZ 3

Lying in the vicinity of the nebulous object Bran 221 (see Figure 3.6), Figure 3.13 shows MZ 3 consists of an elliptical-type structure. The region was imaged with narrow-band Hα, [SII] and red continuum filters, but due to the poor seeing ($> 3''$), only extremely weak [SII] emission was found associated with MZ 3. By comparing the ESO/SERC IIIaJ, IIIaF and IVN images, the majority of emission appears to be reflection, with the emission becoming stronger with increasing wavelength. By comparing the CCD R and I band images, a bright section, or lane can be seen at the south-western edge of the ellipse.

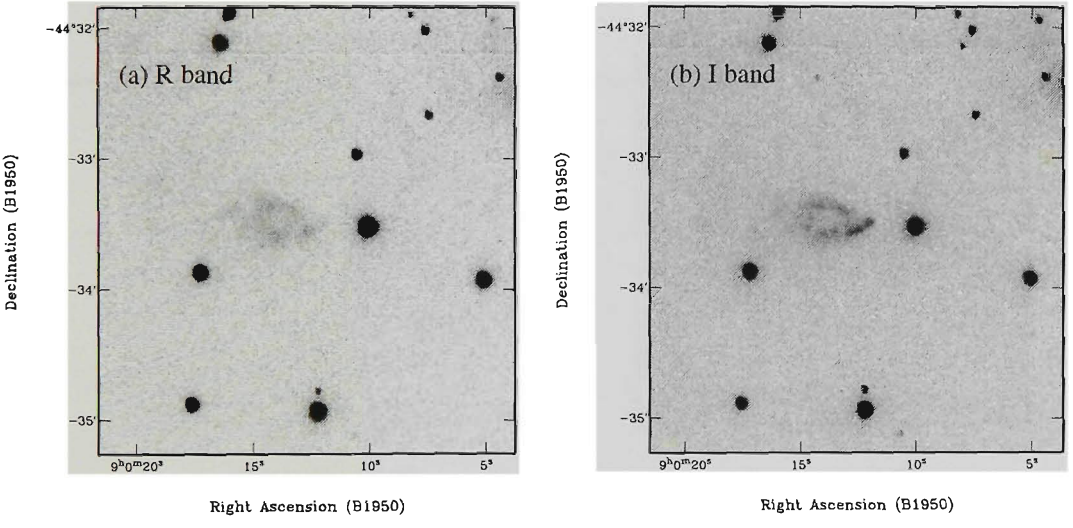

Figure 3.13: Magnified CCD (a) R and (b) I band images of MZ 3.

As shown in Figure 3.14, the 12 and 25μm HIRES contours detect a source at the western apex of the ellipse where the bright lane is located. The 60μm peak appears coincident with an optical star, but by blinking the ESO/SERC images shows this object (or any other star in the immediate vicinity) displays no variation in brightness which places them as foreground objects. The HIRES peaks in the 60 and 100μm maps are spatially offset from the 12 and 25μm maps. For the 12 and 25μm peaks, it is most likely the emission has originated from MZ 3 and is being reflected by the cavity which we see as the optical ellipse. As the 60 and 100μm images are capable of tracing regions of colder dust, the 60 and 100μm peaks in Figure 3.14c and 3.14d are most likely tracing the more immediate region surrounding the protostar itself.

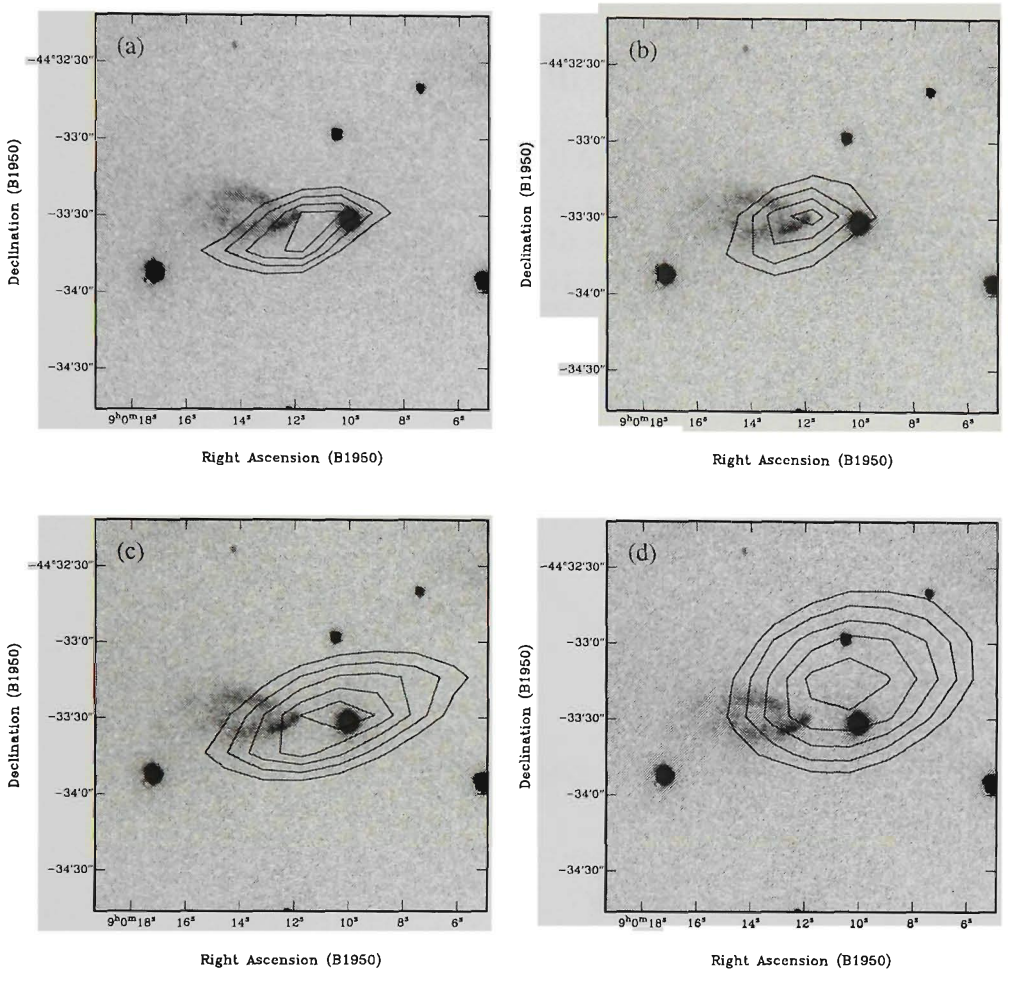

Figure 3.14: HIRES contours overlaid on the I band image of MZ 3. (a) 12μm contours at 2-3.5% in steps of 0.5% of peak (395.74 MJy sr^{-1}); (b) 25μm contours at 10-25% in steps of 5% of peak (307.57 MJy sr^{-1}); (c) 60μm contours at 30-50% in steps of 5% of peak (175.26 MJy sr^{-1}); (d) 100μm contours at 80-92% in steps of 3% of peak (60.5 MJy sr^{-1}).

Using the position α(B1950) = 09$^{\rm h}$00$^{\rm m}$11.64$^{\rm s}$, δ(B1950) = $-44°33'32.4''$, the HIRES fluxes for MZ 3 are listed in Table 3.10. As shown in Figure 3.15, the SED is modelled using a two-component greybody with photospheric (T_d = 147 K) and dust (T_d = 33 K) components. The derived properties in Table 3.11 suggests MZ 3 is a low-luminosity ($\sim$ 22 $L_\odot$) source with a spectral index $\alpha_{12-100\mu m}$ = 0.86, which places the source in the Class I range. At 1300μm, the extrapolated flux is $\sim$ 0.2 Jy, and using equation 3, an estimate of the surrounding envelope mass is $M_{env} \sim 1\ M_\odot$. In the (L_{bol},M_{env}) diagram of Bontemps et al. (1996; their Figure 1), MZ 3 is located near the Class 0/I boundary.

Table 3.10: HIRES fluxes for MZ 3

λ (μm)	Beam ($''$)	HIRES Flux (Jy)
12	77×39	0.62 ± 0.14
25	74×36	2.42 ± 0.66
60	100×58	10.37 ± 1.16
100	136×106	31.67 ± 0.88

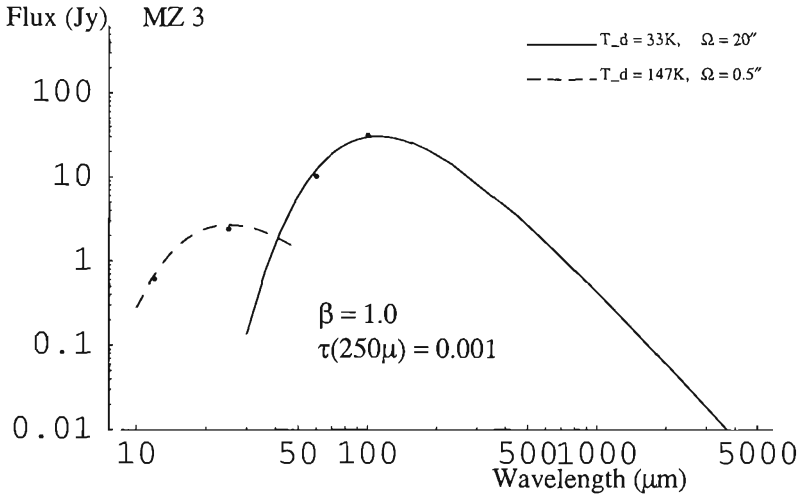

Figure 3.15: SED for the Class I source, MZ 3. The source is modelled with a hot photospheric component (T_d = 147 K) and a cooler (T_d = 33 K) dust component. Parameters used to constrain the fit are listed.

Table 3.11: Derived properties for MZ 3

Parameter	Value
Ω	0.5-20″
T_d	33-147 K
L_{bol}	22.34 $L_\odot$
M_{env}	1.06 $M_\odot$
$\alpha_{12-100\mu m}$	0.86
Class	I

3.4.4 HH 75/133

Previous studies

Located in direction of the Vela Molecular Ridge (VMR), the dark cloud complex Sa 114/DC268.0+01.0 (Sandqvist 1977; Hartley et al. 1986) contains the nebulous objects vdB 29a/b/c (van den Bergh & Herbst 1975). The UBV photometry of Herbst (1975a,b) identified the objects as young B-type stars belonging to the Vela R2 association at a distance between 450 to 870 pc. The cloud is projected against the VMR A/C regions[27] (Murphy & May 1991) which are located at a distance of 700 pc (Liseau et al. 1992) and is the distance adopted here.

On the southern outskirts of the cloud, RG88 identified HH 75, which is made up of a large grouping of knots which give the object a complex and chaotic appearance. The object extends $\sim 2'$ along PA = 295° from the southernmost knot back towards the dark cloud. From long-slit spectroscopy, RG89 found the object displays blue-shifted velocities (-127 to -75 km s^{-1}) which decrease with increasing distance from the cloud. About 14′ to the north-west of HH 75, Ogura (1990) identified another object, HH 133, which consists of several interconnecting knots aligned along PA $\sim$ 115°. No velocity information is available for this object. The IIIaJ, IIIaF and IVN images of the region are shown in Figure 3.16. HH 75 displays emission in the IIIaJ which suggests shocked [OIII] (5009Å), but the optical spectroscopy of RG88 does not extend blue-wards of 6175Å. The HIRES 12 and 25μm images show emission at $\sim$ 0.5 MJy sr^{-1} in both bands.

Cohen (1990) suggested IRAS 09094-4522 may be the energy source for HH 75, which is 8.′2 to the north-west and is visible in the IIIaJ, IIIaF and IVN images. In a survey of IRAS-bright Class I sources in the Vela region, Liseau et al. (1992) obtained NIR $JHKLM$ observations of IRAS 09094-4522 (their IRS47) while Massi, Lorenzetti & Vitali (1997) performed a K band and H_2 (2.12μm) survey of the HH 75/IRAS 09094-4552 region and did not detect any evidence for a molecular hydrogen outflow linking HH 75 to the IRAS source. At the IRAS position, DMW98 placed an upper limit at 800μm and also found low-level H_2CO emission (T_a^* dv $\leq$ 0.15 K km s^{-1}), but no evidence of ^{18}CO gas. Table 3.12 lists fluxes for IRAS 09094-4522 from 1.24 to 800μm. As for HH 133, the nearest IRAS source is IRAS 09092-4516, $\sim$ 2.′5 to the north-east of the HH group but its position with respect to the PA of the HH flow suggests it is an unlikely energy source. There appear to be no reddened IVN sources aligned along the PA of the flow.

[27]Not the VMR B region as indicated by Liseau et al. (1992).

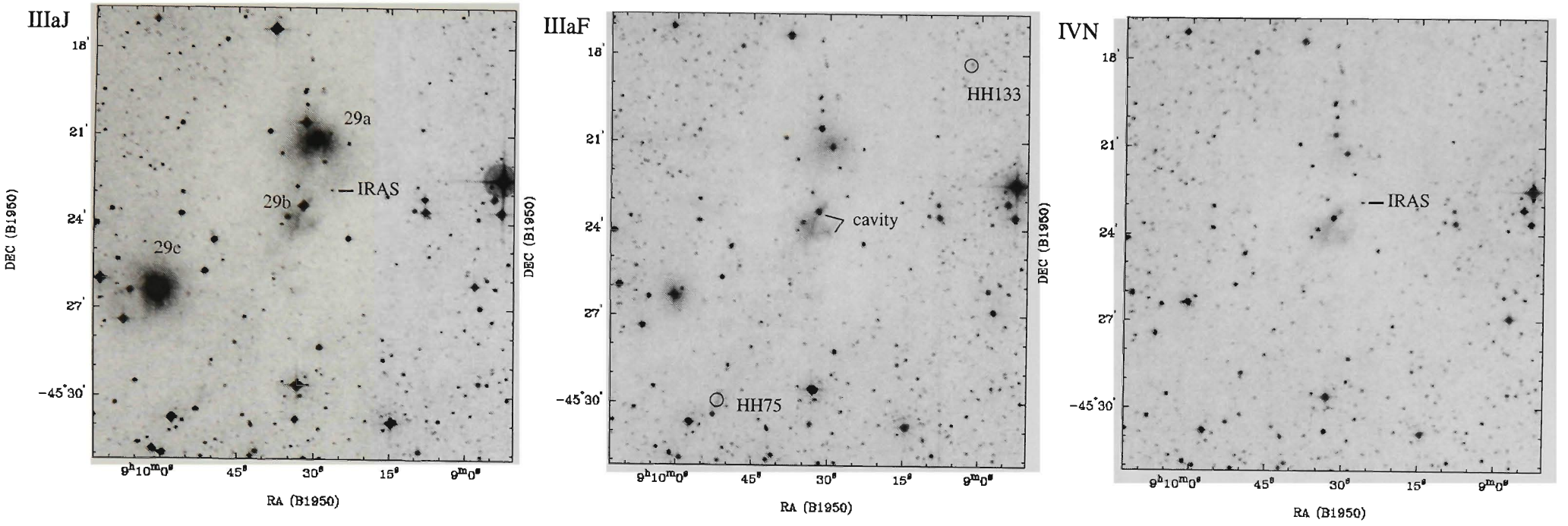

Figure 3.16: IIIaJ, IIIaF and IVN images of the HH 75/133 region. Along with HH 75 and HH 133, the nebulous B-type stars (vdB 29a/b/c) and IRAS 09094-4522 (labelled IRAS) are marked. The feature marked "cavity" in the IIIaF image may represent a relic cavity associated with the IRAS source. See text.

New observational results

Figure 3.17 shows HIRES contours overlaid on a deep CCD I band image of the region surrounding IRAS 09094-4522. The HIRES contours peak at the location of an optically visible source which also lies within the IRAS uncertainty ellipse. The position of the near-infrared source detected by Liseau et al. (1992) also lies close to both the error ellipse and optical source and so we will assume the optical, near-infrared and IRAS source correspond to the same object. Apart from the B-type stars vdB 29 a-c, IRAS 09094-4522 is the only other object within the region which could be considered as a possible HH energy source. Although the deep CCD R and I band images show numerous reddened sources, most are located near the cloud edges which suggests background sources.

A possible scenario is that IRAS 09094-4522 is the driving source for both HH 75 and HH 133. There are several lines of evidence which point towards this conclusion. The first is the emission seen to the south-east of the IRAS source. The ESO/SERC images (Figure 3.16) show the emission is mostly reflection, with decreasing brightness in the IIIaF, IVN and IIIaJ bands respectively. Although the emission overlaps the B-type star vdB 29b, the brighter part of the emission opens away from this star and the emission can be fitted with an ellipse with major and minor axes 6′.6 and 2′.4 respectively (1.35×0.49 pc for $D = 700$ pc) with the IRAS source located at the apex. The orientation of the ellipse is in PA $\sim 140°$. This emission could represent the remains of a cavity that has been blown out by the outflow from the IRAS source. The extension of this cavity towards HH 75 suggests the emission is part of the blue-shifted lobe which is in agreement with the blue-shifted velocities RG 88 found for HH 75.

The fact that the cavity does not appear symmetrical about the IRAS source suggests the red-shifted lobe is boring into the cloud with HH 133 just now appearing from its far side. Therefore, long-slit spectroscopy of HH 133 should show positive velocities consistent with it lying in the red-shifted lobe. RG88 noted that in addition to the multitude of knots that make up HH 75, fainter emission extends a further arc-minute to the north-west where the IRAS source lies. The overall PA of the elongated cavity and HH 75 display similar values (PA $\sim 140°$ and $150°$ respectively).

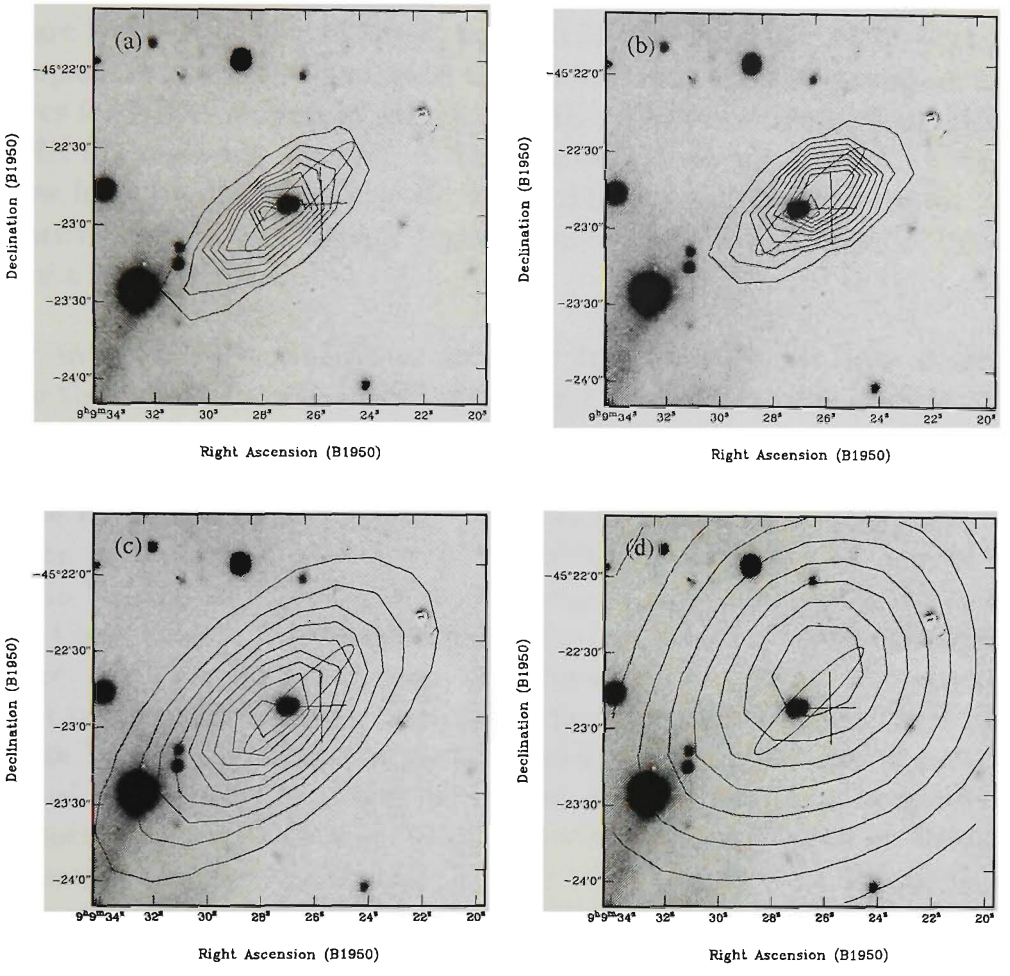

Figure 3.17: HIRES contours on an I band image of the IRAS 09094-4522 region. The ellipse marks the IRAS positional error while the cross marks the position of the near-infrared source identified by Liseau et al. (1992). (a) 12μm contours at 10-90% of peak (534.7 MJy sr^{-1}) in steps of 10%. (b) 25μm contours at 10-90% of peak (1713.99 MJy sr^{-1}) in steps of 10%. (c) 60μm contours at 10-90% of peak (1315.57 MJy sr^{-1}) in steps of 10%. (d) 100μm contours at 10-90% of peak (510.69 MJy sr^{-1}) in steps of 10%.

A second piece of evidence lies in the morphologies of both HH 75 and HH 133. A notable property of bow shocks associated with known giant HH flows (RBD97; Eislöffel & Mundt 1997) is the further they are from their exciting source, the more fragmented they become. The projected distance between the southern most part of HH 75 and the IRAS source is $\sim$ 8.'86, or 1.78 pc at a distance of 700 pc. Similarly, HH 133 is $\sim$ 6.'36, or 1.30 pc in projection from the IRAS source. Together, HH 75/133 would constitute an outflow with projected length $\sim$ 3 pc. Assuming a initial velocity of 150 km s^{-1} (HH 75 shows lower values due to de-acceleration), the dynamical ages of HH 75 and

HH 133 are estimated at 1.13×10^4 yr and 8.24×10^3 yr respectively. If we compare HH 75/133 with the giant flow HH 34 (Devine et al. 1997), both are of comparable length (~ 3 pc), with the terminal blue and red-shifted working surfaces for HH 34 defined by HH 88 and HH 33/40 respectively, while HH 75 and HH 133 represent the blue and red-shifted(?) terminal shocks from an outflow from IRAS 09094-4522. Given the different star forming regions, the similarity between their morphologies again suggests HH 75 and HH 133 are part of a giant HH flow.

Apart from HH 75 and HH 133, no other HH emission has been detected within the cloud. Assuming both objects are part of the same outflow, then their dynamical ages as derived above place a lower limit on the age of the driving source as the lack of other HH emission suggests the outflow phase is close to, or has ceased. This brings us to the IRAS source itself. In addition to published photometry, the HIRES fluxes[28] for the source are listed in Table 3.12. The spectral index $\alpha_{2.1-25\mu m} = 1.30$ places the source in the Class I range, but another index, $\alpha_{12-100\mu m} = 0.17$ places the source close to the Class I/II boundary. For wavelengths $<60\mu$m, the observed fluxes cannot be modelled by a single-temperature greybody. As the HIRES maps in Figure 3.17 show compact emission at both 12μm and 25μm, the observed SED can be modelled by a series of higher-temperature greybody components. However, in order to characterise the source based on the mass of its surrounding envelope, data for $\lambda \geq 60\mu$m are used for the greybody fit shown in Figure 3.18. Here we assume there is very little mass associated with the hot ($\lambda < 60\mu$m) component of the SED (see Hunter et al. 2000 and references therein). The derived properties and fit parameters are listed in Table 3.13.

Extrapolating the greybody fit to 1300μm, a value of 0.026 Jy is obtained and using equation 3, the envelope mass is estimated to be $\sim 0.12\ M_\odot$ (using $\kappa_{1300\mu m} = 0.01$ cm^2 g^{-1} for Class I objects; André & Montmerle 1994). Placing the source in the (L_{bol},M_{env}) diagram of Bontemps et al. (1996; their Figure 1), the source is located in the Class I region. However, as the greybody fit in Figure 3.18 is constrained to the upper limit at 800μm, M_{env} should also be considered an upper limit. Given that (a) $L_{bol}/(10^3 \times L_{1300\mu m}) = 405$ is greater than that for Class I objects, (b) the source appears to be optically visible and (c) there are no HH ejection events within $\sim 8 \times 10^4$ yr, we suggest the source lies well within the Class II phase of evolution.

[28]Using the IRAS position: α(B1950) = $09^h09^m26.57^s$, δ(B1950)$-45°22'55.10''$

Table 3.12: Fluxes for IRAS 09094-4522.

λ (μm)	Mag	Beam ($''$)	HIRES Flux (Jy)	Other (Jy)	Refs
1.24	11.82				1
1.63	10.10				1
2.19	8.90				1
3.79	5.94				1
4.64	4.80				1
12		59×29	13.62 ± 3.90	14.2	2
25		57×28	49.19 ± 13.33	48.6	2
60		85×45	108.54 ± 13.85	107.0	2
100		130×88	161.26 ± 7.84	141.0	2
800			<0.218		3

REFERENCES: (1) Liseau et al. (1992); (2) Cohen (1990); (3) DMW98.

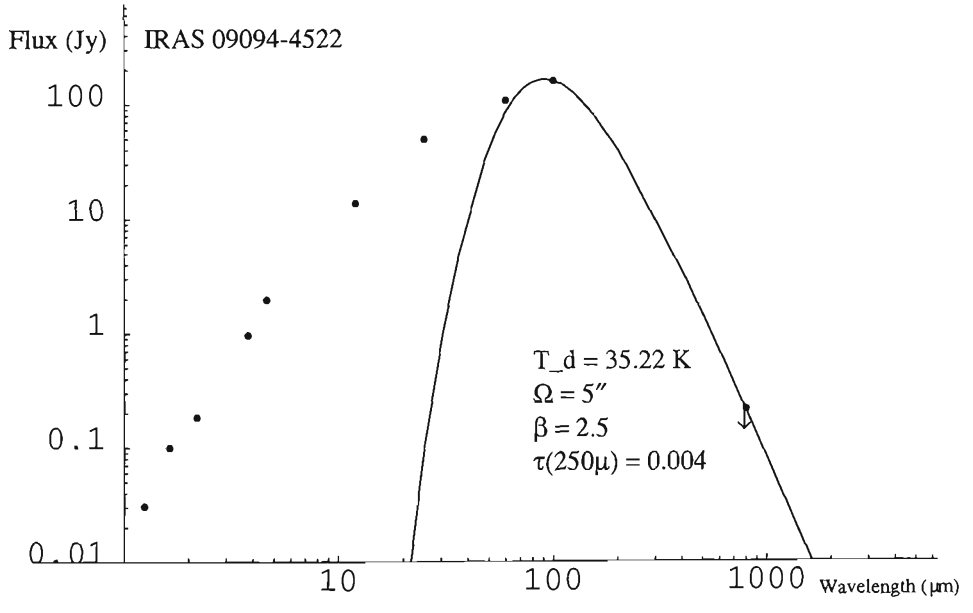

Figure 3.18: SED of the Class II object, IRAS 09094-4522. In order to estimate the amount of circumstellar dust associated with the source, the greybody fit is constrained to wavelengths $\geq 60\mu$m (see text for details). Parameters of the fit and upper limits are indicated.

Table 3.13: Derived properties for IRAS 09094-4522.

Parameter	Value
Ω	$5''$
T_d	35.22 K
L_{bol}	85.63 $L_\odot$
$L_{1300\mu m}$	0.0002 $L_\odot$
$L_{bol}/(10^3 \times L_{1300\mu m})$	405.26
M_{env}	$<$0.12 $M_\odot$
$\alpha_{2.1-25\mu m}$	1.30
$\alpha_{12-100\mu m}$	0.17
Class	II

3.4.5 HH 131

Previous studies

Located $\sim$ 3° south-west of the Orion Nebula (M 42), Ogura (1991) found this object consists of several bright knots (HH 131 A-H) and large optical filaments (features a-l) which he suggests are associated with HH 131. The IIIaF image in Figure 3.19 shows the string of knots HH 131 A-H and the large, extensive filaments which make up objects a-l. Although the nebulosities a-l have not been identified as genuine HH objects, they are brighter in the IIIaF than in the IIIaJ, with no emission in the IVN. This suggests they are emission-line (HH) in nature and may have been excited by the same source that has produced HH 131. The length of the HH 131 A-H group is $\sim$ 6′ (0.8 pc), and the span of the largest arc (consisting of nebulosities a, b, c, d and h) is $\sim$ 15′ (2 pc) across. Using an Hα objective-prism plate of the region, Ogura (1991) found no emission-line stars in the immediate vicinity of HH 131. Although there are several IRAS sources in the vicinity, the low-dispersion spectroscopy of Ogura (1991) does not identify them as T-Tauri stars.

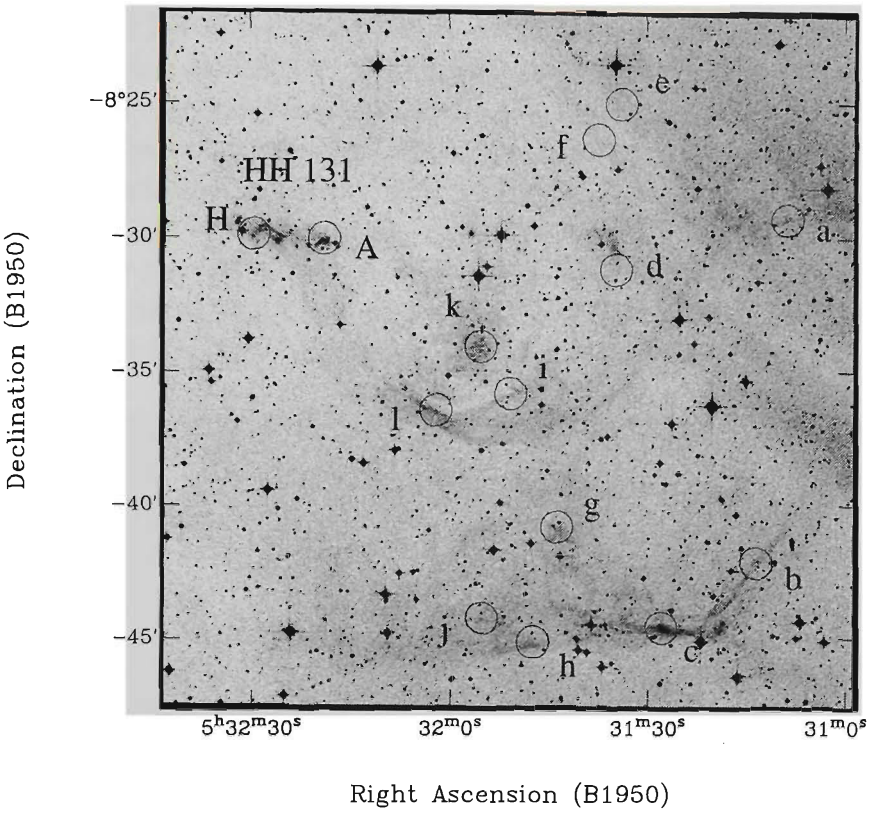

Figure 3.19: IIIaF image of HH 131. Only the end knots (HH 131 A/H) associated with the jet-like part of the flow are shown while the features a-l of Ogura (1991) outline several bow shock structures. See text for discussion.

Given the large size of the arc-like filaments a-l and their distance from the nearest portion of L1641 (1.°6, or 13.2 pc for D = 470 pc), it is tempting to suggest they comprise a large fragmented bow shock structure which is tracing a stellar outflow originating from L1641. To put things into perspective, the position of HH 131 and nebulosities a-l with respect to the southern portion of L1641 is shown in Figure 3.20. The morphology of HH 131 and nebulosities a-l point back towards the star forming regions L1641-S2 (IRAS 05403-0818), L1641-S3 (IRAS 05375-0731) and L1641-S4 (IRAS 05384-0808). If the driving source of HH 131 is located in these regions, what kind of properties should it posses? From the projected distance of HH 131 to L1641-S2/S3/S4 ($\sim$ 13 pc) and assuming the knots of HH 131 are moving at 50 km s^{-1}, typical for radial velocities of shocks located many parsecs from their sources (Bally et al. 1995, 1997; Devine et al. 1997; Reipurth et al. 1997), the dynamical age of HH 131 is $\sim 10^5$ yr.

Although there are a large number of pre-main sequence stars in the southern region of L1641 (Strom, Margulis & Strom 1989a,b; Hodapp 1994; Chen & Tokunaga 1994), known CO outflows in this region include L1641-S, L1641-

S2, L1641-S3 and L1641-S4 (Fukui et al. 1989; Wouterloot, Henkel & Walmsley 1989; hereafter WHW89). Morgan & Bally (1991) and Morgan et al. (1991) identified an outflow associated with MB 61 (IRAS C05383-0807), which is very close to L1641-S4. Recently, Stanke, McCaughrean & Zinnecker (2000) performed an near-infrared H_2 (2.12μm) survey of the region and identified a 2.6 pc string of H_2 emission associated with L1641-S and L1641-S3. They suggest L1641-S and L1641-S3 are part of the same flow originating from the Class I source, IRAS 05375-0731, which considering its luminosity ($\sim$ 70 $L_\odot$), is probably an intermediate-mass protostar.

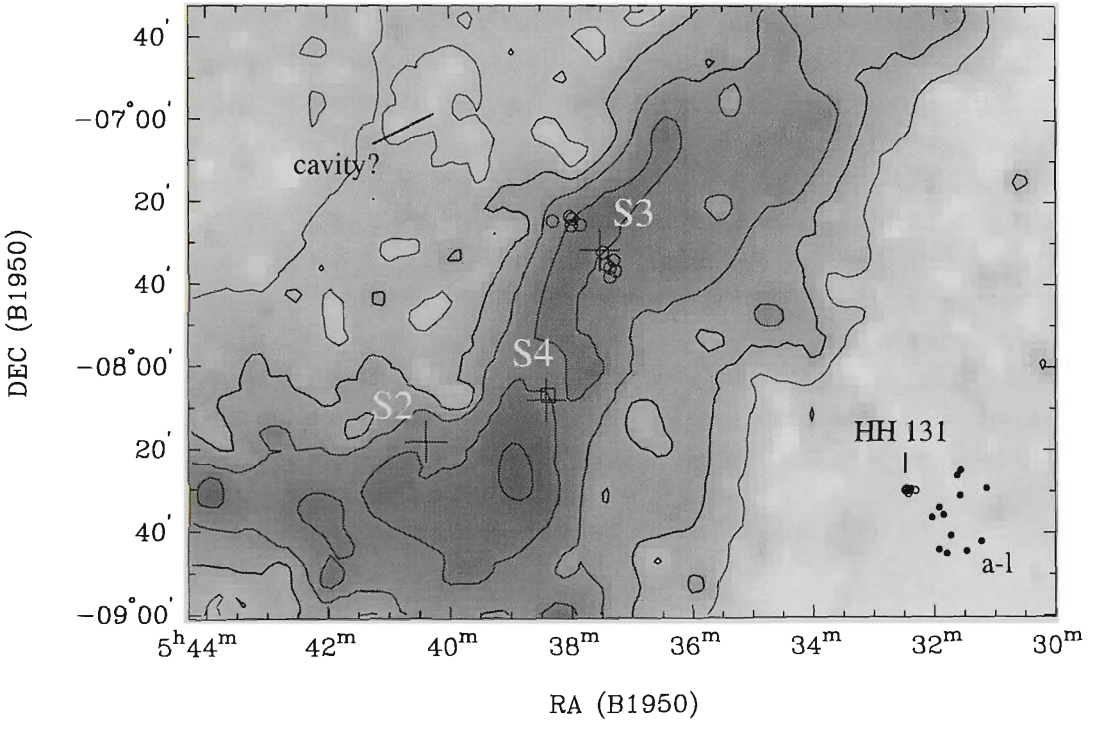

Figure 3.20: Extinction map (ESO R band counts) of the southern part of L1641 (from Cambrésy 1999). The position of HH 131 and features a-l are shown relative to the CO outflows L1641-S2, L1641-S3 and L1641-S4. An additional CO outflow, MB 61 (Morgan & Bally 1991; Morgan et al. 1991) is located close to L1641-S4 and is marked by the box. The circles identify the 2.6 pc H_2 flow identified by Stanke et al. (2000) and the feature marked cavity? may be a cavity resulting from the L1641-S3 flow punching out of the low-level emission. Contours range from A_R = 1 to 5 in steps of 1 mag. See text for details.

New observational results

It is interesting to note that in Figure 3.20, the extinction map shows a cavity in the low-level ($A_R < 2$ mag) emission to the north-east of L1641-S3. This cavity is well aligned with the axis defined by the H_2 flow identified by Stanke et al. (2000) and HH 131. This cavity may have been created by the flow as it punches out of the southern part of the L1641 GMC (as in HH 34; Bally & Devine 1994; see also chapter 4, section 4.7.2). In Table 3.14, properties of known southern L1641 CO outflows are listed. In order to compare ages of the CO outflows with that of HH 131, the dynamical time scales (τ) of the former can be calculated using the projected length and observed maximum CO velocity. However, considering that τ can be influenced by how an outflow interacts with the surrounding cloud environment, estimates of τ in Table 3.14 should be considered unreliable (see discussions in Yu, Billawala & Bally 1999 and Knee & Sandell 2000). As a result, either IRAS C05383-0807, L1641-S3 or L1641-S4 can be thought of as a candidate point of origin for HH 131, but considering the orientation of L1641-S3, HH 131 and a cavity (Figure 3.20) along PA $\sim 60°$, the L1641-S3 outflow at this stage represents the prime suspect. To date, no large-scale Hα and/or [SII] surveys of the southern portion of L1641 have been undertaken. With the new AAO/UKST Hα survey of the southern Galactic plane and selected regions (see chapters 4 and 5), it will be possible to map shock-excited emission and perhaps trace HH 131 back to its point of origin.

Table 3.14: Properties of the CO outflows L1641-S2, L1641-S3, L1641-S4 and MB 61.

Source	Size (pc)	Velocity† (km s^{-1})	Age (τ) (10^5 yr)	Orientation	Refs
L1641-S2 (IRAS 05403-0818)	0.6	25	0.23	E-W (blue-red)	1,2
L1641-S3 (IRAS 05375-0731)	0.6	23	0.25	NE-SW (red-blue)	1,3,4,5
L1641-S4 (IRAS 05384-0808)	0.8	8	0.98	E-W	1
MB 61 (IRAS C05383-0807)	0.4	6	0.65	E-W (blue-red)	3,4

†Maximum velocity relative to cloud.
REFERENCES: (1) Fukui et al. (1989), (2) WHW89, (3) Morgan & Bally (1991); (4) Morgan et al. (1991), (5) Stanke et al. (2000).

3.4.6 IRAS 06382+1017

Previous studies

First identified by Walsh, Ogura & Reipurth (1992), Figure 3.21 shows a deep red Palomar Sky Survey image of HH 124 which lies within a cometary globule. It consists of a long bipolar chain of bright knots emanating from the bright ($L_{bol} = 89\ L_{\odot}$) Class I object, IRAS 06382+1017. At the time, HH 124 was one of the largest HH flows known with an angular extent of 125″, which for a distance of 800 pc to NGC 2264 (Reipurth 1999), corresponds to a linear projected length of 0.48 pc. From their long-slit spectroscopy, Walsh et al. (1992) found the western knots HH 124A-C display negative radial velocities (up to -150 km s^{-1}), while the most eastern knot, HH 124E displaying a blue-shifted velocity $\sim$ 100 km s^{-1}. In HH 124D, they found the knot displayed both negative and positive velocities which they explain by suggesting the IRAS source is located within the knot and the observed velocities are due to bipolar motion. By noting the presence of giant bow shocks (HH 124-E and HH 124-W) placed symmetrically about the IRAS source (see Figure 3.22), Ogura (1995) found that the true extent of HH 124 was not 0.48 pc, but 5.4 pc. The HH nature of these bow shocks was provided by his narrow-band Hα, [SII] and red continuum observations.

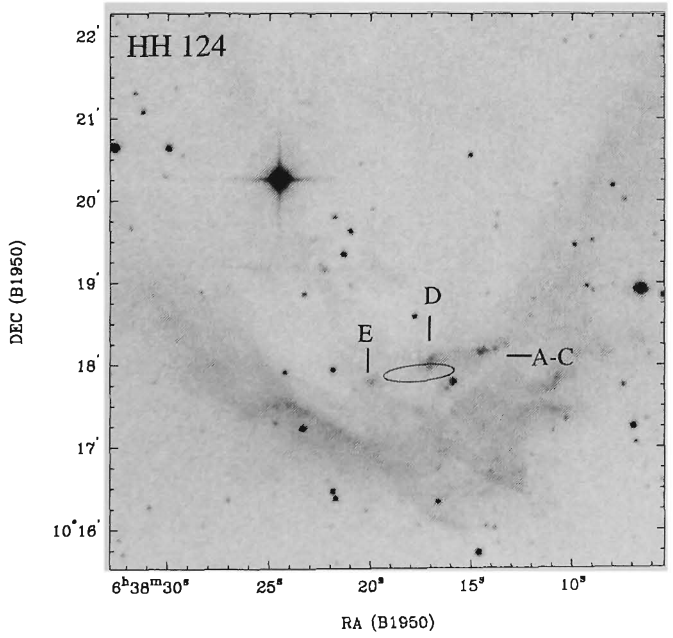

Figure 3.21: The HH 124 jet as seen on a deep red Palomar Sky Survey image. Clearly seen is the opaque cometary globule, in which the outflow source is embedded. Comprised of knots HH 124A-E, the flow is presumed to be driven by IRAS 06382+1017, for which the IRAS positional uncertainty ellipse is shown.

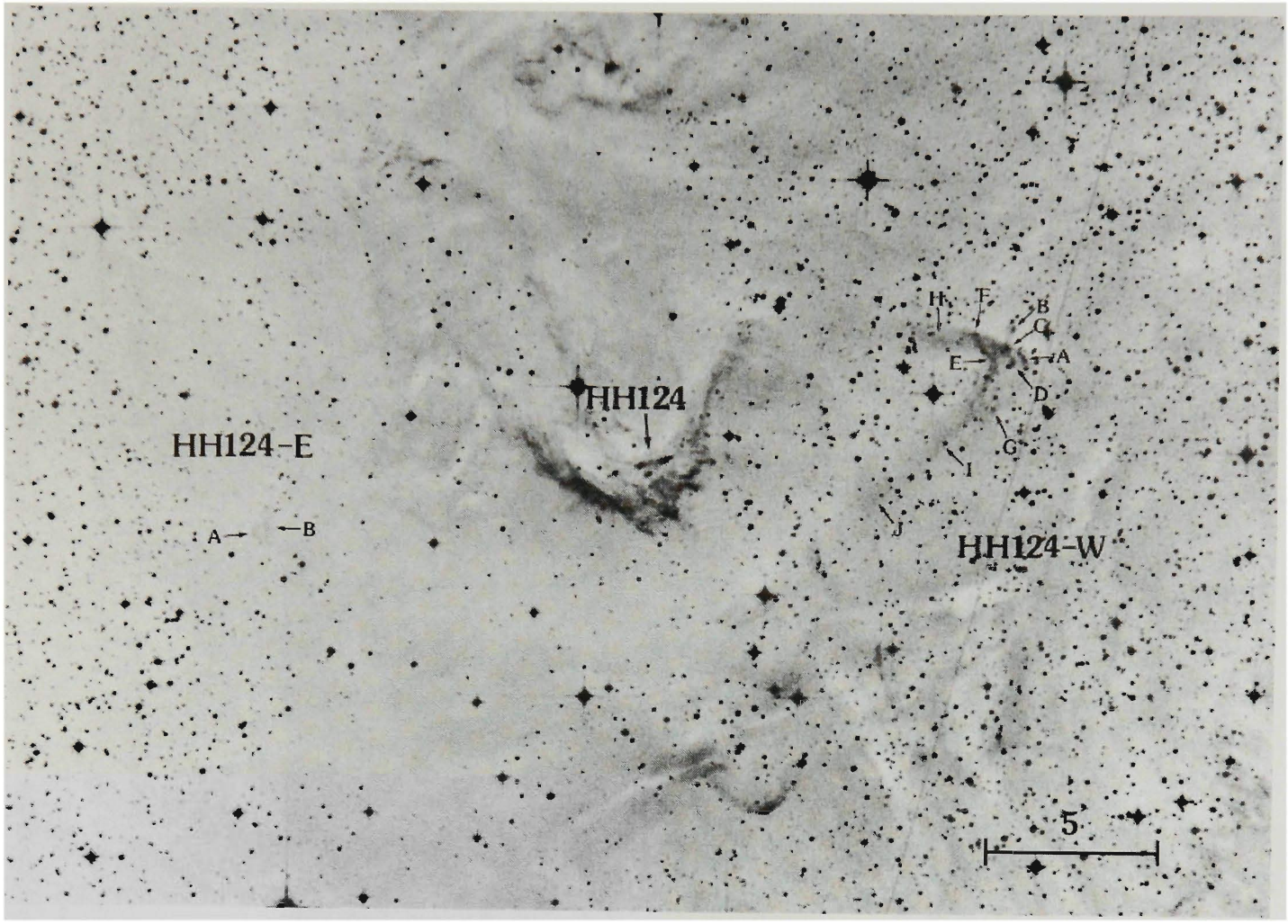

Figure 3.22: Deep red UKST IIIaF image of the HH 124 region. Located in an opaque cometary globule, the HH 124 jet powers a giant HH outflow which terminates at two large bow shocks to the east and west (HH 124-E and HH 124-W respectively). From Ogura (1995).

In their near-infrared study of the HH 124 region, Pichè, Howard & Pipher (1995) found the IRAS source is deeply embedded ($A_V \sim 35$ mag) with their K band image showing emission about the IRAS source elongated in PA $\sim 45°$, which is not along the axis defined by the optically visible HH knots (PA $\sim 105°$). In addition, their continuum-subtracted 2.12μm image of the HH 124D region shows several H_2 knots again aligned at PA $\sim 45°$. Piché et al. (1995) suggest the emission orientated at PA $\sim 45°$ represents a second outflow originating from the secondary component of a binary system within IRAS 06382+1017. Direct evidence of a binary system within the IRAS source was provided by Reipurth & Rodríguez (1998), who imaged the region with the VLA at 3.6cm. Within the IRAS positional uncertainty ellipse (see Figure 3.23), they found two sources with one (their source HH 124 #1) spatially coincident with the near-infrared source identified by Piché et al. (1995). The radio source HH 124 #2 of Reipurth & Rodríguez (1998) lies along the axis defined by the HH objects whereas the near-infrared source and radio source HH 124 #1 are located off-axis.

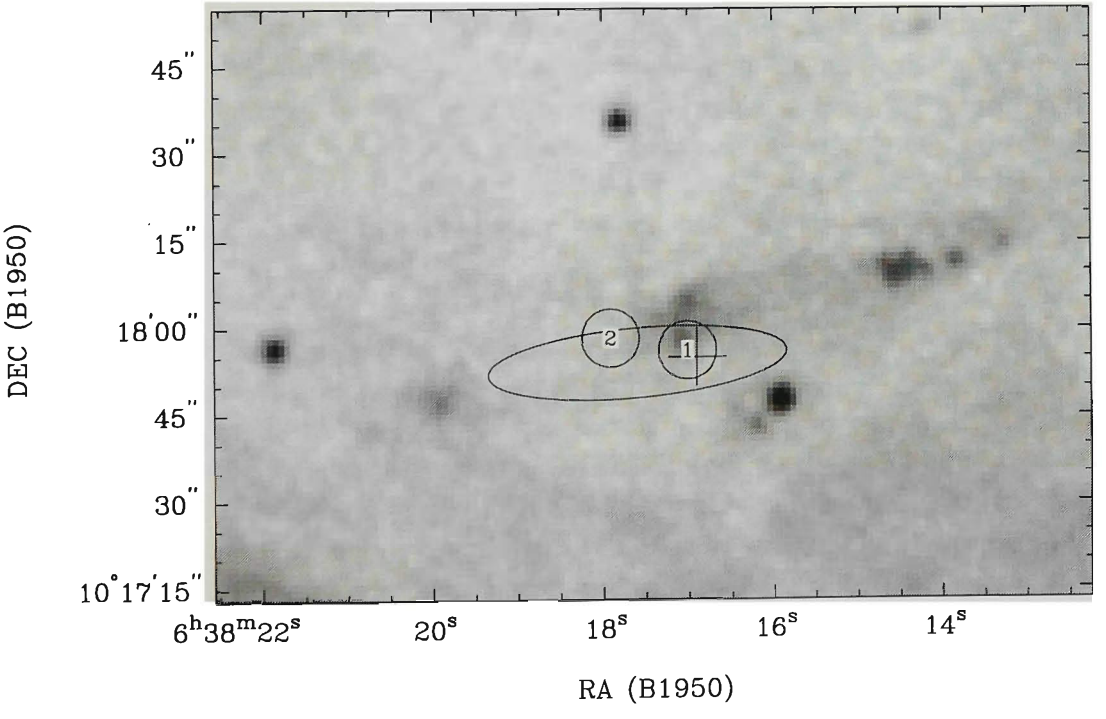

Figure 3.23: Deep red Palomar Sky Survey image showing two 3.6cm sources (Reipurth & Rodríguez 1998) located within the positional error ellipse of IRAS 06382+1017. One (HH 124 #1) corresponds to a highly reddened source (marked by the cross) which Piché et al. (1995) identify as the IRAS source. A second source (HH 124 #2), lies along the axis defined by the HH 124 jet. As both sources lie within the error ellipse, IRAS 06382+1017 may be a binary system with each source driving its own parsec-scale outflow. See text for discussion.

New observational results

As Piché et al. (1995) found both K band and H_2 emission extending almost orthogonal to the HH 124 jet, the presence of a second source within the IRAS error ellipse suggests IRAS 06382+1017 is a binary system. As HH 124 #1 and the near-infrared source (Piché et al. 1995) lie off-axis from the jet axis, these two sources most probably represent the same source which drives the H_2 emission orthogonal to the HH 124 jet. For HH 124 #2, the on-axis position make this an ideal candidate for the HH 124 flow. Given that HH 124 is a giant HH flow, do we see a flow of similar dimensions originating from HH 124 #1? Upon close examination of a deep red Palomar Sky Survey image of the region, several HH-like objects (A–G in Figure 3.24) are aligned along the axis defined by the H_2 knots identified by Piché et al. (1995; PA $\sim$ 45°). Incidently, these HH-like objects are clearly present in Figure 3.22, but Ogura (1995) does not make any mention of the objects in his discussion. Fortuitously, the south-western knots are present in his Hα, [SII] and red continuum images. From the observed intensities, all knots are [SII]-bright with no continuum emission. These are characteristics of low-excitation HH objects. Unfortunately, the north-eastern knots are not present in his narrow-band images, but by comparing deep blue and red Palomar Sky Survey images (not shown), they do appear to be brighter in the red. The emission seen in the blue could be due to [OII] (3727Å) and/or [OIII] (5007Å) emission (both lines are seen in the HH 124 jet; Walsh et al. 1992).

In Figure 3.24, the location of the HH-like knots with respect to the HH 124 #1 VLA source are shown. It is clear that all knots (A-G) lie along the axis of the H_2 knots in PA = 45°, but there is an apparent wandering of the observed emission beyond the opaque core of the cometary globule. Knots D and E may be the optical counterpart of the highly-collimated H_2 jet. The distribution of outer knots could be due to a precessing jet, which provides the S-shaped point symmetry also seen in HH 34 (see chapter 2, Figure 2.3) and RNO 43 (see chapter 1, Figure 1.1b). Another interesting feature is a wandering trail of emission which extends from knot E, right up to knots F and G. In the CCD images of Ogura (1995), this trail appears Hα-bright and is reminiscent of Hα emission seen in the HH 47 jet (Heathcote et al. 1996). In fact, the trail of Hα emission and knots G and H appear to form a large bow shock structure similar in appearance to HH 124-W (see Figure 3.22).

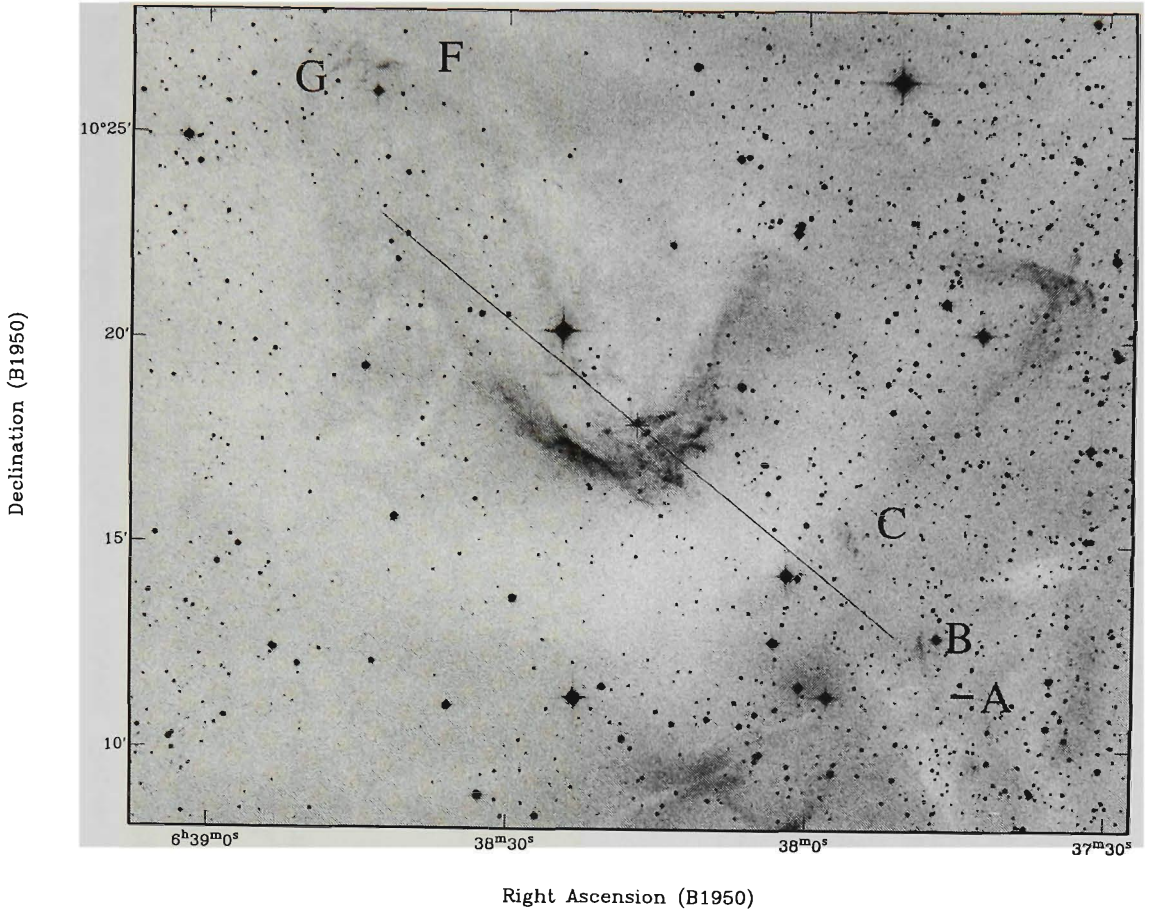

Figure 3.24: Contrast-enhanced deep red Palomar Sky Survey image of the HH 124 region. Knots A, B, C, F and G represent candidate HH objects possibly driven by the radio source HH 124 #1 (marked by the cross). The line defines the PA (= 45°) of the K band and H_2 emission identified by Piché et al. (1992). The optical knots display an S-shaped point symmetry about HH 124 #1. See text for discussion.

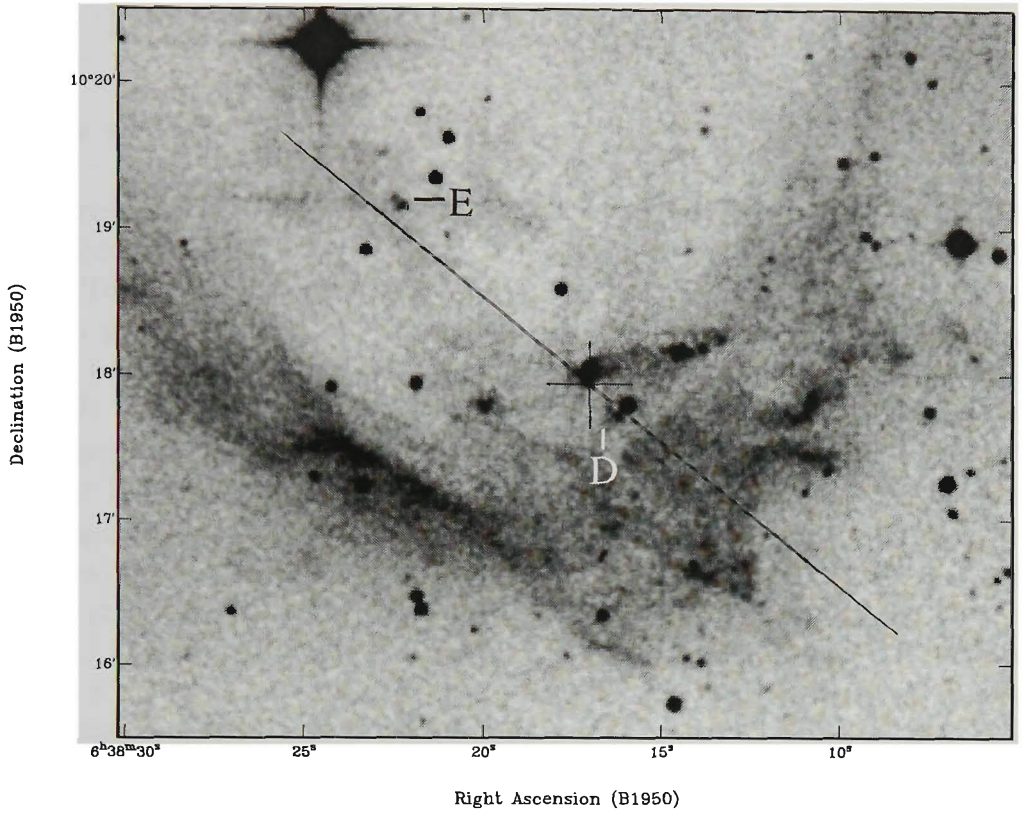

Figure 3.24 - continued: Knots D and E in the inner region of the cometary globule. Unlike knots A–C, F and G, D and E lie directly along the axis of the H_2 flow identified by Piché et al. (1992) and may represent the optical counterpart of a highly-collimated jet emanating from HH 124 #1. See text for discussion.

Assuming that knots A–G are part of a flow originating from HH 124 #1, the projected linear length between knots A and G is $\sim 1394''$, which for a distance of 800 pc corresponds to 5.43 pc in projection. Deep Hα, [SII] and red continuum images of knots A–G will be extremely valuable in characterising these objects. In conclusion, the binary system in IRAS 06382+1017 appears to be another example of an orthogonal outflow system. Other examples include HH 111/121 (Gredel & Reipurth 1994) and HH 1/2/144 (Reipurth et al. 1993b).

3.4.7 HH 137/138

Previous studies

Discovered by Ogura (1993), HH 137/138 are located in the dark cloud DC291.4-0.2 in Carina. The Hα+[SII] image in Figure 3.25 shows an overview of the region. To the north-west of the image, the open cluster NGC 3590 is seen, while to the south-west, the arc of nebulosity is associated with the massive HII region NGC 3603. In their UBV and Hβ photometry of NGC 3590, Moffat & Vogt (1975) identified two pre-main sequence stars in the cluster which they determine to be at a distance of 2060 pc. Similarly, Steppe (1977) obtained RGU photometry of the cluster and found a distance of 2360 pc. Subsequently, Ogura (1993) adopted a value of 2210 pc (mean of the above distances) as the distance to DC291.4-0.2. In a recent ^{12}CO survey of the Hartley et al. (1986) dark cloud catalog, Otrupcek (1999, private communication) found DC291.4-0.2 displays two velocity components at -5.6 and -7.9 km s^{-1}. In order to derive distances, the entire Hartley et al. catalog was employed using two different methods as outlined by Fich, Blitz & Stark (1989). Using a flat fit to her data, the -5.6 km s^{-1} component (T_A = 7.0 K) corresponds to a distance of 700 pc, while using R_0 = 8.5 kpc, Θ_0 = 220 km s^{-1} and the best fit of Fich et al. (see their equation 21), a distance of 960 pc was obtained. For the -7.9 km s^{-1} component (T_A = 4.5 K), the corresponding distances were 1000 and 1300 pc respectively. Here an average distance of $\sim$ 990 pc is assumed.

New observational results

As no IRAS sources are located within the optical boundary of the cloud, Ogura (1993) suggested an energy source could be located between the knots 137J and 138A. However, by blinking the IIIaJ, IIIaF and IVN images shown in Figure 3.26, a reddened source was found towards the centre of the cloud. Other reddened sources are found, but these are located at the cloud edges and are considered to be background objects. The newly identified reddened source, hereafter defined as IRS1, displays faint emission in all three images which suggests we are seeing reflection emission, possibly scattered light escaping from a cavity surrounding IRS1.

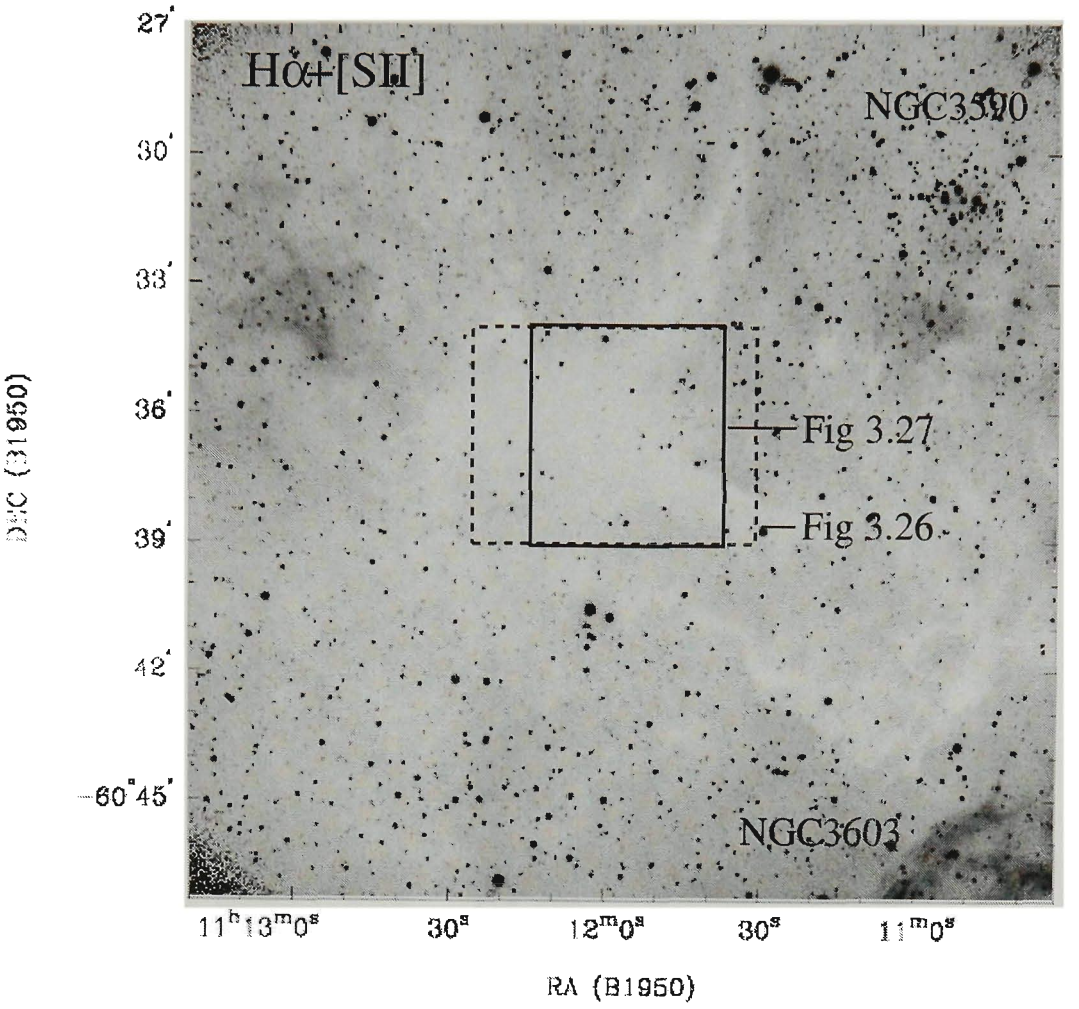

Figure 3.25: Combined CCD Hα+[SII] image of the filamentary dark cloud DC291.4-0.2. The location of the open cluster NGC 3590 to the north-west and an arc from the massive HII region NGC 3603 to the south-west are indicated. The dashed and solid lines approximate the inner regions of the cloud as seen in Figures 3.26 and 3.27 respectively.

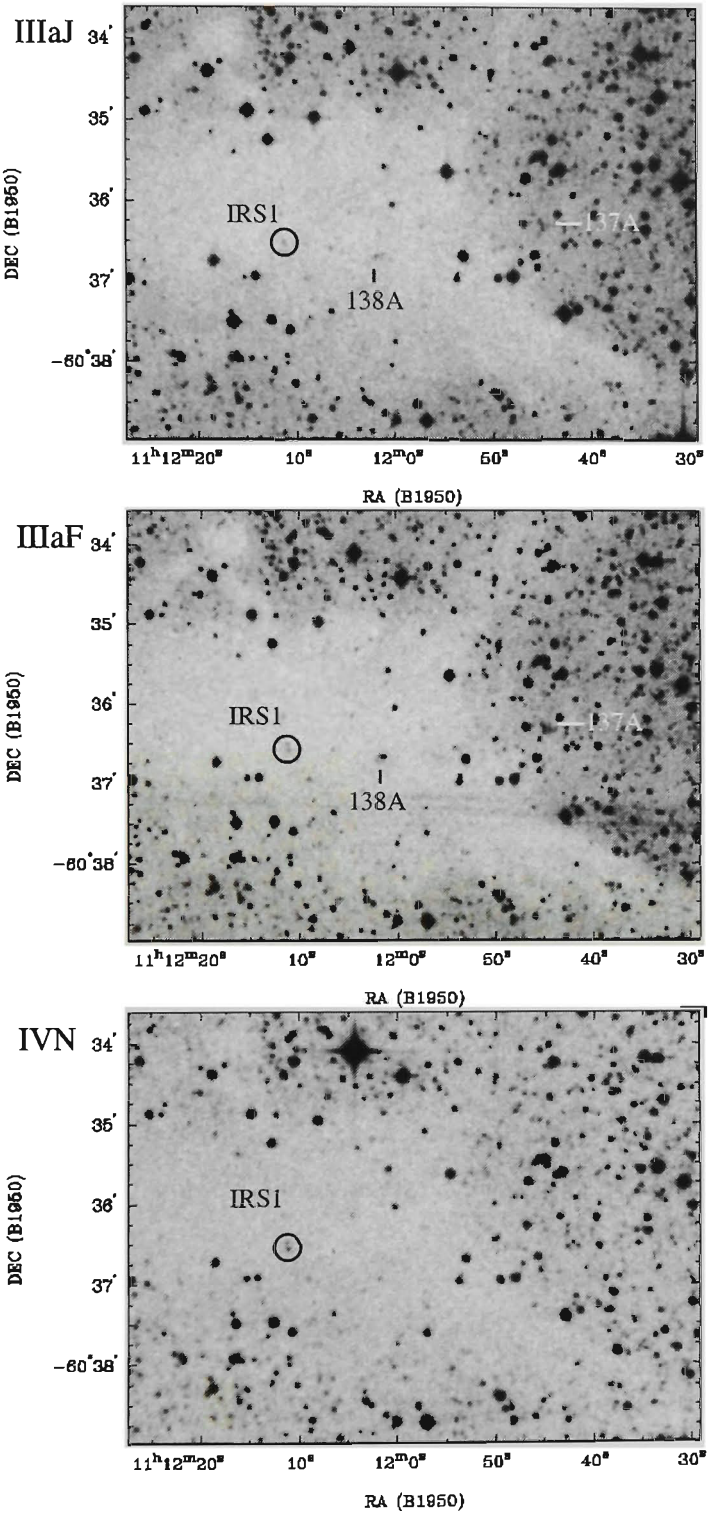

Figure 3.26: ESO/SERC images of DC291.4-0.2 and HH 137/138. The new source labelled IRS1 is proposed as the driving source for both HH objects. Some of the more visible HH objects are labelled.

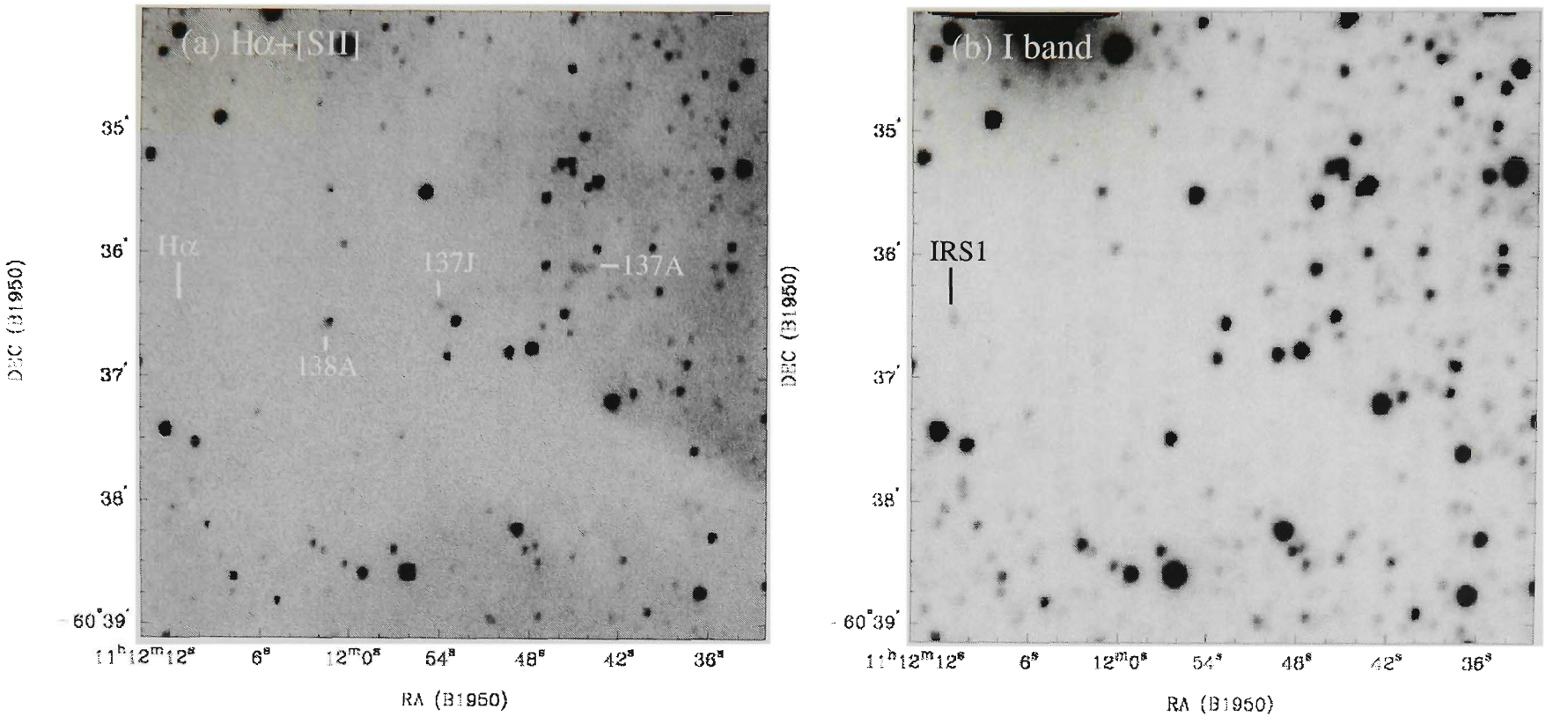

Figure 3.27: Corresponding (a) Hα+[SII] and (b) I band images of the HH 137/138 region. Faint Hα emission is seen associated with the reflection nebulosity associated with IRS1, which is the proposed energy source for HH 137 and HH 138. The location of various knots in the HH 137/138 flow are indicated.

Figure 3.27 shows Hα+[SII] and I band images of the inner region of DC291.4-0.2. The I band image (Figure 3.27b) confirms the presence of IRS1 by the presence of a reflection nebulosity. In addition, the presence of a faint nebulosity in the Hα+[SII] image is spatially coincident with the I band source/reflection nebulosity. This suggests it contains a component of scattered Hα emission. The coordinates of IRS1 are α(B1950) = $11^h12^m11.11^s$, δ(B1950) = $-60°36'31.30''$. As seen in Figure 3.27a, the PA of HH 138A with respect to the position of IRS1 is $\sim 275°$, while the PA of the HH 137 knots with respect to HH 138A is $\sim 280°$. This represents a deviation of $\sim 15°$. As discussed in section 3.4.3 for HH 73, such a deviation can be explained by a collision with an obstruction of some sort, perhaps a dense condensation within the molecular cloud. Another possibility is that the jet associated with IRS1 is precessing, although a combination of cloud interaction and precession is in evidence with the strong emission seen in the IIIaJ and IIIaF images at the positions of HH 138 A/B.

From the above discussion, we suggest IRS1 as the driving source for both HH 137 and HH 138. The HH 137/138 group represents the western lobe of the outflow with the counterflow moving into the cloud to the east of IRS1. The length of the western flow from IRS1 to HH 137A is $\sim 3'.36$, which at a distance of 990 pc corresponds to a projected length of 0.97 pc. Assuming the eastern counterflow is of similar dimensions, the total length of the HH flow is 1.94 pc and constitutes another example of a parsec-scale HH flow. Given that typical HH emission arises from shock with velocities ~ 150 km s^{-1}, the dynamical ages of individual knots in HH 137/138 are listed in Table 3.15.

From the distribution of knots, it appears that IRS1 has produced approximately three separate outbursts: the first produced the fragmented bow shock HH 137 A-I, the second HH 137J and the final and latest outburst has produced knots HH 138 A-D. Therefore, IRS1 appears to undergo an eruption every 2000 years or so with a flow dynamical age $\sim 0.64 \times 10^4$ years, or 6% of the time attributed to the outflow phase associated with low-mass young stellar objects ($\sim 10^5$ yr). The frequency of eruptions (~ 2000 yr) is similar to that seen in other outflows that are driven by FUor objects (i.e., Hartmann & Kenyon 1996; Reipurth & Aspin 1997) and HH 137/138 IRS1 may itself be a FUor candidate.

As the default HIRES images at 20 iterations failed to detect a source within the confines of DC291.4-0.2, further processing at 50, 150, 180 and 200 iterations still did not reveal a point source. This suggests IRS1 may be an extremely young source. For an object located at 990 pc, the IRAS survey limits at 12, 25, 60 and 100μm (see IRAS Explanatory Supplement, Section IV.A.1), would be able to detect a source with a minimum luminosity of 1.67 $L_\odot$ and spectral index $\alpha_{12-100\mu m} = 1.81$. These values suggest that a

Class I object, if present, should be observable by IRAS/HIRES which does not seem to be the case here. Therefore, HH 137/138 IRS1 may in fact be a Class 0 protostar which has been identified by its reflection nebulosity in the ESO/SERC and CCD images. The next stage in the study of the HH 137/138 flow is to obtain deep H_2 (2.12μm) images of the entire eastern part of the cloud which should identify the counterflow. Sub-millimetre photometry will be useful to characterise IRS1, while spectroscopic studies of individual HH knots in Table 3.15 should show decreasing velocities with increasing distance from IRS1.

Table 3.15: Properties of the HH 137/138 knots[†].

	Knot	Distance from IRS1 (arcsec)	Projected Distance (pc)	Dynamical Age ($\times 10^4$ yr)
HH 137	A	201.26	0.97	0.64
	B	196.46	0.95	0.62
	C	191.65	0.92	0.61
	D	189.27	0.91	0.60
	E	182.04	0.88	0.58
	F	174.86	0.84	0.55
	G	162.83	0.79	0.51
	H	146.03	0.70	0.46
	I	135.36	0.65	0.43
	J	125.60	0.61	0.40
HH 138	A	70.92	0.34	0.22
	B	69.13	0.33	0.22
	C	56.51	0.27	0.18
	D	51.70	0.25	0.16

[†]Assuming a distance of 990 pc to DC291.4-0.2.

3.5 Future Directions

Observations in the spectral regions 1–12μm and >100μm (sub-millimetre wavelengths) will be needed to confirm the results presented here. For observations between 1-12μm, the usage of large-scale near-infrared surveys such as DEep Near-Infrared Survey of the southern sky (DENIS; Gunn-i [0.82μm]; J [1.25μm] and K_s [2.15μm]) and the 2 Micron All-Sky Survey (2MASS; J [1.25 μm], H [1.65μm], and K_s [2.17μm]) will provide an unbiased tool to search for energy sources associated with those HH objects without identified energy sources and determine what fraction are part of parsec-scale outflows.

In addition to DENIS and 2MASS, a third infrared survey has recently been released to the astronomical community. The Mid-course Space Experiment (MSX) is a Ballistic Missile Defence Organisation satellite that was launched in April 1996 (see Mill et al. 1994 for a complete description). The infrared telescope on MSX, SPIRIT III, is an off-axis, aspheric re-imaging optical system with an unobscured primary aperture of about 33 cm diameter. With a spatial resolution of 18.3″/pixel ($\sim$ 0.01 and 0.04 pc for regions such as Chameleon and Orion respectively) and high sensitivity (0.1 Jy at 8.3μm), the SPIRIT III instrument imaged the Galactic plane ($|b| \leq 5°$) to a resolution $\sim 30\times$ greater than IRAS. SPIRIT III consisted of six different sensors which are listed in Table 3.16. Bands C and E are narrower analogs of the 12 and 25μm filters used by IRAS.

Table 3.16: SPIRIT III passbands.

Band	Passband (μm)	Central λ (μm)
B1	4.22-4.36	4.29
B2	4.24-4.46	4.35
A	6.03-10.91	8.28
C	11.1-13.24	12.13
D	13.5-15.9	14.65
E	18.3-25.0	21.34

Through the Infrared Processing and Analysis Centre (IPAC)[29] and the NASA/IPAC Infra-Red Science Archive (IRSA)[30], the release of Version 1 of

[29]See http://www.ipac.caltech.edu/ipac/msx/msx.html
[30]See http://irsa.ipac.caltech.edu/applications/MSX

the MSX Point Source Catalog (PSC) provides an extremely useful database of over 300,000 infrared sources to search for candidate protostellar objects. In combination with DENIS and 2MASS, the MSX survey will provide a powerful database to search for and characterise the energy sources of not only sources associated with parsec-scale HH outflows, but all pre-main sequence stars. In order to show the usefulness of the MSX PSC, we have identified a candidate energy source of a poorly studied object. Reipurth (1999) lists HH 180 as a faint HH knot associated with a small reflection nebula in the L291 cloud in Sagittarius. No other information is available on this object. In Figure 3.28, the IIIaF image of the region shows the object consists of a compact knot with a tail of emission extending to the north-east. There are no known Hα emission-line or IRAS sources in the immediate vicinity of the object.

By scanning the MSX PSC, a candidate energy source has been found for HH 180. Listed as MSX5C_G011.4569-01.7786 (hereafter HH 180IRS), the source is detected at 8.28μm (Band A), 12.13μm (Band C), 14.65μm (Band D) and 21.34μm (Band E). Given the detections at 12.13 and 21.34μm, we have used HIRES data to search for the source at 12, 25, 60 and 100μm. At the position given in the MSX catalogue[31], HIRES data of the source at 20 iterations shows it is drowned out from emission associated with the nearby reflection nebulosity IC 4700: higher iterations may isolate HH 180IRS. The MSX and HIRES fluxes for the source are listed in Table 3.17 and the SED is shown in Figure 3.29. Although the HIRES fluxes are upper limits, the MSX data clearly shows the source displays an increasing SED. By computing the spectral index from 8.28 to 21.34μm, i.e., $\alpha_{8.28-21.34\mu m}$, we find a value of 0.34 which indicates a Class I object. Higher iterations of HIRES data and/or sub-millimetre data are needed to constrain the SED at higher wavelengths.

We have made a cursory scan of the MSX PSC to see if any of candidate energy sources listed in Table 3.3 and new objects (MZ 2, MZ 3) have counterparts in the MSX catalogue. Unfortunately, the Orion region was not covered by the MSX survey and so we cannot search for sources associated with IRAS 05283-0412 (HH 58), HH 59/60, HH 131 and MZ 1. Our initial findings are presented in Table 3.18 where all sources have been identified in at least one band of the MSX survey. Interestingly enough, there are no MSX counterparts to IRAS 09003C and HH 137/138 IRS1. The non-detection of these sources at mid-infrared wavelengths affirms our earlier assumptions that these sources are extremely young (Class 0) protostars which should be identifiable with high-resolution sub-millimetre observations.

[31] α(B1950) = $18^h14^m25.28^s$, δ(B1950) = $-19°53'05.69''$

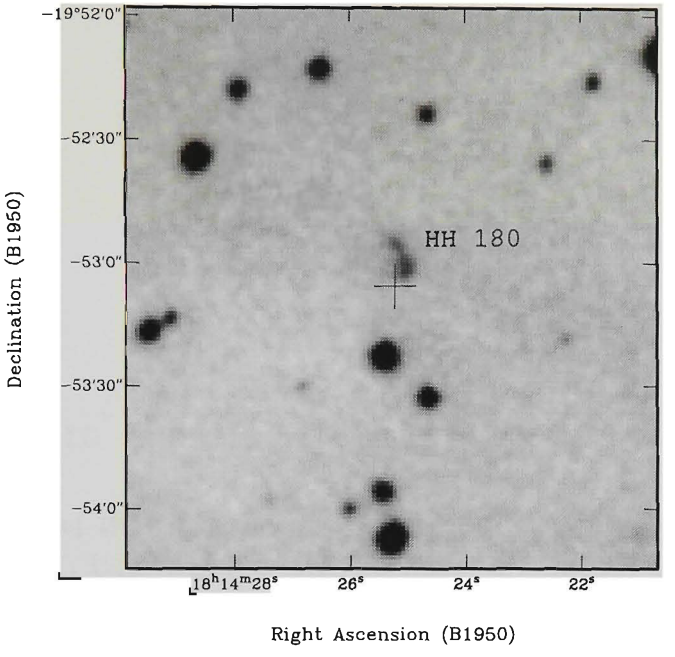

Figure 3.28: IIIaF image of HH 180. The location of the Class I object, HH 180 IRS, is indicated by the cross.

Table 3.17: Fluxes for HH 180IRS.

λ (μm)	Beam ($''$)	MSX (Jy)	HIRES (Jy)
8.28		0.74	
12	60×29		<0.85 ± 0.12
12.13		1.52	
14.65		1.19	
21.34		2.62	
25	58×30		<1.39 ± 0.18
60	90×58		<23.99 ± 2.33
100	121×93		<280.52 ± 11.70

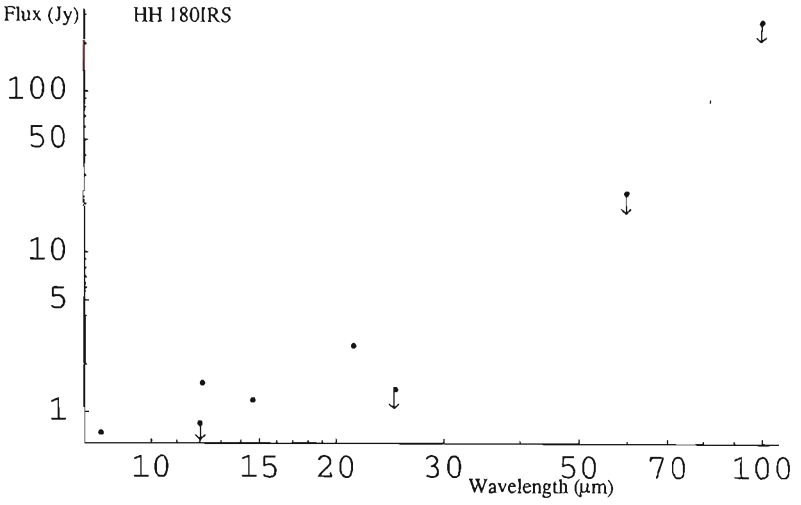

Figure 3.29: SED of the Class I source, HH 180IRS. Mid-infrared data are from the MSX PSC. Upper limits (HIRES data) are indicated.

3.6 Summary

In this chapter we have used CCD narrow and broad-band observations, existing ESO/SERC and IRAS HIRES data to identify candidate giant sized HH flows which consist of HH objects previously thought to be unrelated. It should be noted that we have only touched the tip of the iceberg in terms of associating energy sources with those HH objects without an energy source. With new HH objects continuously being identified, applying the method presented here for each object provides a way to identify candidate energy sources and provide some constraints on which may be related to the HH object in question. The DENIS, 2-MASS and MSX surveys will undoubtedly be used to identify candidate energy sources of Class I and above, but to identify the youngest (Class 0) protostars, HIRES and/or sub-millimetre observations must be used. We have used HIRES data to identify MZ 1, IRAS 09003C and HH 137/138 IRS1 as candidate Class 0 protostars of which two (IRAS 09003C and HH 137/138 IRS1) appear to be driving HH flows. As we will see in chapter 4, HIRES data will again be used to identify candidate driving sources of new HH flows which have not been previously identified with shorter wavelength observations.

Although optical spectroscopy is needed to confirm our conclusions, we have identified HH 59/60, HH 131, HH 75/133 and HH 137/138 as candidate parsec-scale outflows from low-mass stars. IRAS 06382+1017 appears to be a binary with both components driving parsec-scale flows. For HH 59/60 and HH 131,

Table 3.18: Sources detected by MSX.

Source	MSX Catalog Name	Band B1 Flux (Jy)	Band B2 Flux (Jy)	Band A Flux (Jy)	Band C Flux (Jy)	Band D Flux (Jy)	Band E Flux (Jy)
IRAS 09094-4522	MSX5C_G267.9108+01.7810	(0)	(0)	5.9979(4)	15.251(3)	21.449(4)	39.906(4)
MZ 2	MSX5C_G265.9967+01.0407	(0)	(0)	0.75388(4)	(0)	(0)	3.2290(3)
MZ 3	MSX5C_G266.1975+01.1334	(0)	(0)	0.61909(3)	(0)	(0)	3.8945(1)
HH 180IRS	MSX5C_G011.4569-01.7786	(0)	(0)	0.73681(4)	1.5167(4)	1.1913(4)	2.6233(1)

Numbers in brackets denotes the Band quality flag in the MSX PSC, with 4 = excellent, 3 = good, 2 = fair, 1 = limit, 0 = not detected.

their inclusion into the parsec-scale class is almost obvious due to their location well away from the L1641 giant molecular cloud. For HH 75/133, our multi-wavelength observations have shown that apart from IRAS 09094-4522, there is no other candidate energy source within the molecular cloud which can be considered as a potential energy source. Similarly, for HH 137/138, our observations have identified a reddened source which lies both within the molecular cloud and along the axis defined by the HH objects.

Due to the regular spacing of HH objects relative to HH 137/138 IRS1, we have suggested this source may be a candidate FUor-type object. With the possible exception of IRAS 09003C and HH 137/138 IRS1[32], the majority of suggested energy sources listed in Table 3.3 display characteristics of older, more evolved sources which are close to the termination of the outflow phase[33]. In the terminology of Reipurth & Aspin (1997), these sources are considered to be in low-level FUor-type states. Our findings cannot either confirm or contradict the Reipurth & Aspin theory that all high-luminosity HH energy sources are in elevated FUor states. As the dynamical time-scales for HH outflows exceed the time-scale by which HH energy sources decay from elevated to low FUor states, it may be better to target a sample of younger outflows from Class 0 and Class I objects where the outflows are still extremely powerful.

As there does not appear to be any HH emission observed beyond that already seen, our results for the energy source of HH 58 suggests it does not drive a parsec-scale outflow. However, this may just be due to the evolutionary status of the energy source. IRAS 05283-0412 appears to be close to the Class II phase of evolution, and as a source evolves from the Class 0 to III stage, the stellar outflow clears away circumstellar material to the point where the star becomes optically visible (the Class III stage). Due to the lack of material for the stellar wind to impact with, we no longer see shocked emission in the form of HH objects and the observed HH objects (i.e., HH 58) represent some of the last ejection events to be seen before the energy source enters the Class III evolutionary phase. Previous ejection episodes have long since dissipated from view, but deep Hα and [SII] imaging in excellent seeing conditions may still be able to identify remnant bow shocks. The HH 75/133 system represents an evolved outflow as the objects are located far ($\sim$ 1.5 pc) from the proposed driving source and no other HH emission lying in their wake. As the source migrates from a Class II to Class III source, the HH flow will cease altogether.

[32]The source NGC 2023 mms1 is also included here, but see chapter 4, section 4.6 for a more detailed discussion.

[33]Although the precise nature of MZ 1, MZ 2 and MZ 3 is unknown, they do not appear to drive obvious HH outflows.

We have also shown not all HH energy sources drive parsec-scale outflows. We have speculated that HH 73 is part of a grazing flow like that seen in HH 110/270 where the presence of an obstacle such as a molecular cloud fragment hinders the outflow from extending to parsec-scale lengths. Although HH 137/138 is a candidate parsec-scale outflow, it also shows signs of an outflow-cloud interaction at the position of HH 138A. However, the outflow has not been deflected by a great amount since previous ejections have ploughed through the cloud and cleared the path so that future ejection events will only graze the sides of the cavity. As will be seen in chapter 4, giant HH outflows in the Orion star forming region have a more dramatic effect on the surrounding molecular cloud with the creation of large-scale cavities which may support the molecular cloud against further collapse and regulate future star formation.

Acknowledgements

Many thanks go to the staff at the Infrared Processing and Analysis Center (IPAC) for their efforts in processing the IRAS HIRES data. Without their help, much of the research presented in this chapter would not have been possible. Also, thanks go to the Mount Stromlo Time Allocation Committee for the generous allocation of time on the 40-inch telescope. This research has made use of the SIMBAD data base, operated at CDS, Strasbourg, France, and the ESO/SERC Sky Surveys, based on photographic data obtained using the UKST which is currently operated by the AAO. Palomar Sky Survey material used is based on photographic data of the National Geographic Society – Palomar Observatory Sky Survey (NGS-POSS) obtained using the Oschin Telescope on Palomar Mountain. The NGS-POSS was funded by a grant from the National Geographic Society to the California Institute of Technology. The plates were processed into the present compressed digital form with their permission. The Digitised Sky Survey was produced at the Space Telescope Science Institute under US Government grant NAG W-2166.

Chapter 4

The AAO/UKST Hα Survey I: L1630/L1641

4.1 Introduction

A large number of giant HH flows (and their small-scale counterparts) may have dramatic effects on the stability and chemical composition of a giant molecular cloud (GMC). It has been suggested that outflows may provide a mechanism for self-regulated star-formation and large-scale bulk motions within GMCs (Foster & Boss 1996). It is therefore important to gain information on the distribution of outflows and particularly giant flows within SFRs. The new Anglo-Australian Observatory (AAO) and United Kingdom Schmidt Telescope (UKST) Hα Survey of the Southern Galactic Plane (Parker & Phillipps 1998a) will be beneficial for such studies as it provides an unbiased search for new HH objects over entire SFRs with its wide-field and high resolution capabilities.

In this chapter we concentrate on a search for new HH objects in the first, deep Hα film of the Orion SFR. The distance to the Orion region lies between 320 to 500 pc (Brown, De Geus & De Zeeuw 1994). Here we adopt a distance of 470 pc based on the distance of H_2O masers in Orion-KL (Genzel et al. 1981). Strong emission and reflection nebulosity in the region makes searching for HH objects difficult. Previous attempts at surveys for faint red nebulosities in L1630 and L1641 have used standard broad-band IIIaF R plates (IIIaF emulsion and RG630 filter), which were limited to subregions clear of high background emission (Reipurth 1985; Malin, Ogura & Walsh 1987; Reipurth & Graham 1988; Ogura & Walsh 1991; 1992). The new, deep fine resolution Hα films enable us to conduct a more complete survey for

emission-line nebulosities for consequent follow-up observations.

In Section 2 we present a brief introduction to the specifics of the Hα survey and details on observations and data reduction. Results are presented in Sections 3, 4, 5 and 6 where individual objects are discussed. In Section 7 we make some general conclusions about giant HH flows and finally in section 8, we make references to future work.

4.2 Observations and Data reduction

4.2.1 The AAO/UKST Hα survey

Under the auspices of the AAO, the UKST has recently embarked on a new Hα survey of the Southern Galactic Plane, Magellanic Clouds and selected regions. No systematic high resolution Hα survey has been carried out in the southern hemisphere since the pioneering work of Gum (1955) and Rodgers, Campbell & Whiteoak (1960). With the increase in resolution and sensitivity of differing wavelength technologies, there has been the need to perform an Hα survey with similar attributes.

The unusually large, single-element Hα interference filter is centred on 6590Å with a bandpass of 70Å. It is probably the largest filter of its type in use in astronomy. Coated onto a full field 356mm $\times$ 356mm RG610 glass substrate, the 305mm clear circular aperture provides a 5.5° field-of-view. Further details of the filter properties and specifications are given by Parker & Bland-Hawthorn (1998). The detector is the fine grained, high resolution Tech Pan film which has been the emulsion of choice at the UKST for the last 4 years. This is due to its excellent imaging, low noise and high DQE (i.e. Parker, Phillipps & Morgan 1995; Parker et al. 1998). Tech Pan also has a useful sensitivity peak at Hα as it was originally developed for solar patrol work. Though electronic devices such as CCDs are the preferred detector in much of modern astronomy, they cannot yet match the fine resolution and wide-field coverage of the Tech Pan film and UKST combination.

Typical deep Hα exposures are of 3 hours duration, a compromise between depth, image quality and survey progress as the films are still not sky-limited after this time. The Southern Galactic Plane survey requires 233 fields on 4 degree centres and will take 3 years to complete. Initial survey test exposures have demonstrated that the combination of high quality interference filter and Tech Pan film are far superior for the detection and resolution of faint

emission features near the sky background than any previous combination of filter and photographic plate used for narrow-band observations (Parker & Phillipps 1998a). It is the intention that the original films will be digitised using the Royal Observatory Edinburgh's SuperCOSMOS facility (Miller et al. 1992; Hambly et al. 1998). It is planned to release a calibrated atlas of digital data to the wider astronomical community as soon as possible.

Table 4.1: Plates used in the current survey.

Plate	α_{1950}	δ_{1950}	Date	Emulsion	Filter	Exp (min)
R3816	05^h32^m	-04°00'	77-12-11	IIIaF	RG630	90
J3828	05^h32^m	-04°00'	77-12-16	IIIaJ	GG395	70
I3869	05^h32^m	-04°00'	78-01-13	IVN	RG715	60
HA17828	05^h36^m	-04°00'	97-12-02	4415	HA659	180
R7462	05^h36^m	-09°00'	82-01-26	IIIaF	RG630	90
J8235	05^h36^m	-09°00'	82-11-14	IIIaJ	GG395	65
I7406	05^h36^m	-09°00'	81-12-19	IVN	RG715	90

4.2.2 Photographic Astrometry and image reduction

For the Orion region, a deep 3-hour Hα exposure was obtained on 1997 December 2nd during a period of good seeing. The plate (HA 17828) was centred at 05^h36^m, -04°00' (1950) and designated grade A based on standard UKST visual quality control procedures by resident UKST staff. Three independent visual scans of the film were carefully made by QAP, SLM and WJZ using an eyepiece and later a 10× binocular microscope. HH objects display a wide range of morphologies including knots, arcs and jets. A combined list of such features was produced and served as the basis for subsequent astrometry. The new Hα images were then compared with deep non-survey UKST IIIaJ, IIIaF and IVN broad-band copy plates of the same field to confirm the objects as true emission-line sources. The plates used and their characteristics are presented in Table 4.1.

Crude positions for each object were first determined using simple XY positions from the film and transformed to B1950 coordinates by use of the UKST program PLADAT. Accurate positions were then obtained by using *SkyView* FITS files of the surrounding region. This resulted in a positional accuracy within 2″ for each object. Digitised images of each source were then made using a video digitising system (Zealey & Mader 1997; 1998). This enabled

us to process images via un-sharp masking and histogram enhancement to recover the original detail as seen on the TechPan film.

4.2.3 Optical CCD Observations

As the Orion region shows highly structured background emission, it is important we distinguish between photo-ionized filamentary structures and bona fide HH objects. This can be accomplished with Hα and [SII] images by noting that HH objects usually have [SII]/Hα ratios > 0.3 compared to [SII]/Hα $\sim$ 0.1-0.3 for emission associated with HII regions. We obtained narrow and broad-band images of HH candidates at the Australian National University 1.0m telescope at Siding Spring Observatory during various periods in January-April 1998. Imaging was done with a 2048 $\times$ 2048 TEK CCD mounted at the f/8 Cassegrain focus. The 0.″6 per pixel gave a field-of-view of 20.′48 $\times$ 20.′48. The seeing conditions during usable time was typically $< 3''$. Narrow-band filters used were [OIII] (λ5016; $\Delta\lambda$ 25Å), Hα (λ6565; $\Delta\lambda$ 15Å), [SII] (λ6732; $\Delta\lambda$ 25Å) and red continuum (λ6676; $\Delta\lambda$ 55Å). The Hα filter also transmits the [NII] ($\lambda\lambda$6548/6584) lines. We used a standard Kron-Cousins filter for the I-band observations.

Typical exposure times were 300s and 900s for broad and narrow-band frames respectively. Flat fields were obtained by illuminating the dome with a halogen lamp. All frames were reduced in a similar fashion with IRAF[34], where 25 median combined bias frames were subtracted from source frames prior to flat fielding. Individual source frames were median combined to produce the final images. In several instances, we were not able to obtain corresponding continuum frames to our CCD Hα and [SII] images. As major HH emission-lines do not fall within the spectral response curve of the RG715 + IVN filter/emulsion combination ($\Delta\lambda$ = 6900Å-9100Å), we use photographic IVN images to serve as continuum images where needed.

4.2.4 Near-infrared Observations

In January 1993 several HH complexes (including Ori I-2) were imaged using IRIS, the AAO infrared camera and low resolution spectrograph. The 128 $\times$ 128 format array has 60μm pixels which when used in the f/15 imaging mode provided a spatial resolution of 1.″94 per pixel and a 4.′1 $\times$ 4.′1 field-of-view.

[34]IRAF is distributed by the National Optical Astronomy Observatories, which are operated by the Association of Universities for Research in Astronomy, Inc., under cooperative agreement with the National Science Foundation.

Each source was observed through a 1% bandpass filter centred on the H_2 $v = 1 - 0$ $S(1)$ transition at 2.12μm. Continuum images were made using a 4% bandpass filter at 2.24μm. Individual frames were linearised, flat fielded against a dome flat and sky subtracted before being combined and calibrated using the IRIS image reduction package known as YOGI-FIGARO. A mosaic of twelve frames, each of five minutes in length were combined to form the final images.

4.2.5 IRAS HIRES Data

IRAS HIRES data (see chapter 3 for details) was obtained to search for candidate energy sources for newly discovered HH objects. For the majority of cases, the default parameters (see chapter 3, section 3.2.2) were used, but in some cases, the data were processed beyond 20 iterations. This data will be discussed were appropriate.

4.3 Results

Table 4.2 lists new HH objects identified by our narrow-band CCD imaging of candidates identified from the Orion Hα plate. Several objects were identified by Reipurth (1985) as candidate HH objects from his ESO R film survey of the Orion region. Objects independently discovered by the CCD imaging of Reipurth, Bally & Devine (1998; hereafter RBD98) are indicated. In addition to brief comments about their nature and location, Table 4.2 also suggests possible energy sources based on evidence presented.

4.4 New objects in L1630

Our survey region of the southern portion of L1630 is shown in Figure 4.1. A diffuse shell of Hα emission and network of bright-rimmed cometary globules surrounds the multiple OB system σ Ori. Ogura & Sugitani (1998) list many of these globules as remnant clouds which may be sites of retarded star formation. The bright HII regions NGC 2024 and IC 434 (which includes The Horsehead Nebula) outline an ionization front between the southern portion of L1630 and σ Ori. This ionization front extends towards the open cluster NGC 1981 which approximately marks the division between L1630 and L1641. The position of the new HH flows in the region are indicated.

Table 4.2: New Herbig-Haro flows in Orion.

HH	α_{1950}	δ_{1950}	Former Designation[c]	Region	Comment	Energy Source
289A	$05^h35^m32.4^s$	$-01°46'52''$		Ori I-2; L1630	large bow shocks	IRAS 05355-0416
292A[a]	$05^h34^m30.7^s$	$-06°36'03''$		L1641; NGC 1999	one-sided jet?	BE Ori
301 [a]	$05^h34^m12.6^s$	$-06°23'06''$	Rei 43	L1641; cluster	cup-shaped object	N23?[b]
302 [a]	$05^h34^m22.3^s$	$-06°22'31''$	Rei 44	L1641; cluster	bright object	N23?[b]
303B[a]	$05^h33^m52.7^s$	$-06°21'24''$	Rei 36	L1641; cluster	VLA jet	VLA source
304A[a]	$05^h34^m10.6^s$	$-06°16'42''$	Rei 41	L1641; cluster	working surfaces	HH 304IRS
305F[a]	$05^h33^m58.7^s$	$-06°21'31''$		L1641; cluster	symmetric group	PR Ori B?
306B[a]	$05^h33^m40.9^s$	$-06°10'33''$	Rei 34	L1641; cluster	bow shock	VLA source
307A[a]	$05^h33^m39.7^s$	$-06°04'46''$		L1641; cluster	large bow shocks	VLA source
308A[a]	$05^h33^m51.4^s$	$-06°04'42''$		L1641; cluster	linear features	VLA source
309A[a]	$05^h33^m35.9^s$	$-05°51'29''$	Rei 33	L1641; cluster	fragmented	VLA source
403 [a]	$05^h34^m36.9^s$	$-05°55'01''$		L1641; cluster	fragmented	L1641-N
404 [a]	$05^h34^m46.6^s$	$-05°46'14''$		L1641; cluster	sickle-shaped	L1641-N
405 [a]	$05^h34^m57.7^s$	$-05°45'20''$	Rei 46	L1641; NGC 1980	faint	HH 405IRS
406 [a]	$05^h35^m11.7^s$	$-05°41'05''$		L1641; NGC 1980	diffuse	HH 405IRS
407A	$05^h32^m43.2^s$	$-06°00'32''$		L1641; NGC 1980	fragmented	V380 Ori?
444D[a]	$05^h37^m18.6^s$	$-02°31'52''$		IC 434; L1630	one-sided jet	V510 Ori

[a] Independently identified by RBD98.

[b] Chen et al. (1993).

[c] Reipurth (1985).

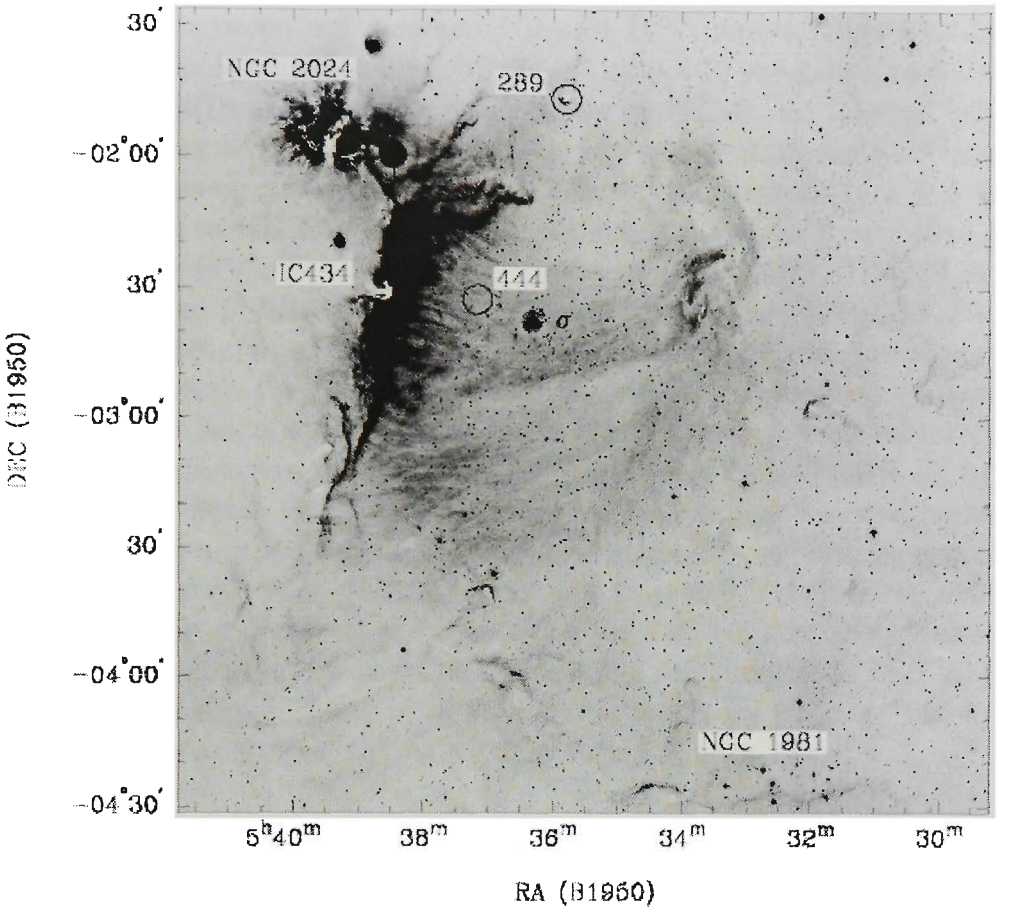

Figure 4.1: The L1630 survey region. The image was derived from an unsharp-mask print of the Hα plate. The upper north-east of the image shows the IC 434 and NGC 2024 HII regions. Surrounding the σ Ori OB system is a diffuse shell of Hα emission in addition to numerous cometary globules and ionization fronts which extend from NGC 2024 to the open cluster NGC 1981. The location of new HH flows are indicated by their numbers. North is up and east is left in all images.

4.4.1 HH 289

Located on the north-western outskirts of IC 434, the bright rimmed cometary globule Ori I-2 is host to the low-luminosity (L_{bol} = 13 $L_{\odot}$) IRAS source 05355-0416, which drives both a bipolar CO and near-infrared molecular hydrogen outflow (Sugitani et al. 1989; Cernicharo et al. 1992; Hodapp 1994). The IRAS source is also associated with a H_2O maser (Wouterloot & Walmsley 1986; Codella et al. 1995). Using the classification scheme outlined in chapter 3, section 3.3, the spectral index derived from the IRAS 12μm (0.44 Jy) and 100μm (46.35 Jy) fluxes gives $\alpha_{12\mu m-100\mu m}$ = 1.20, which places the source in the Class I category.

A comparison between our scanned Hα and IVN images (Figures 4.2a,b) identifies a chain of emission-line objects (objects 2-5) extending to the east of the globule. To the west, we see another emission-line feature (object 1) which appears as an extension of faint emission seen in the IVN image. The Hα+[SII] images (Figures 4.3a,b) confirms the presence of a HH flow, designated here as HH 289. In the central part of the globule, our Hα+[SII] and H_2 images (Figures 4.3b,c) show two faint [SII] knots (HH 289 A/B) which mirror the position of the H_2 emission. With the exception of knot C, all knots appear [SII]-bright. Knots D-F show large arc-like morphologies which open towards the IRAS source. This gives the impression of a bubble surrounding the eastern side of the globule which may represent an interface between the outflow and the UV radiation field from ζ Ori, which is 42′ to the east of Ori I-2. From the distribution of optical and near-infrared emission about the IRAS source (Figures 4.3b,c), we suggest it is the driving source of the HH 289 outflow. The chain extends 551″ from the IRAS source making the lobe 1.23 pc in projection. This puts the Ori I-2 flow in the class of parsec-scale flows from low-mass stars (Eislöffel & Mundt 1997; R97). It is only the second such outflow to be found in a cometary globule. The other is HH 124, a 5.4 pc flow in the NGC 2264 region (Ogura 1995)[35].

As HH objects typically display tangential velocities in the order of 150 km s^{-1} (i.e., Mundt 1988), the age span of the optical knots ranges from 530 yr (knot A), to 8100 yr (knot F). The projected lengths of the (red-shifted) CO, H_2 and optical HH flows are 40″ (0.09 pc), 80″ (0.18 pc) and 551″ (1.23 pc) respectively. Apart from knot A, we do not see any evidence of HH emission associated with the blue-shifted CO lobe, which we expect will be very faint due to the tenuous medium on the western side of the globule. Deeper [SII], [OII] and/or [OIII] images of the western side of the globule may reveal fainter emission.

In Figure 4.3b, we note the appearance of a tube-like feature extending out of the western side of the globule (object 1 in Figure 4.2a). It is well aligned and mirrors the inner [SII] and H_2 knots with respect to the IRAS source. As this feature is visible on our Schmidt images, the emission is most probably scattered light reflected off the walls of the cavity formed by the outflow as it bores its way out of the globule. Using AAO/UKST Hα material, we have identified a similar feature associated with the cometary globule and outflow complex CG30/HH 120 (Zealey et al. 2000). The Hα streamer extends to the south-west of the globule and appears to be similar to an extensive H_2 filament associated with the infrared source CG30-IRS1. The tube-like feature in Ori I-2 and the streamer in CG30 may represent limb-brightened cavities.

[35]See Chapter 3, section 3.4.6.

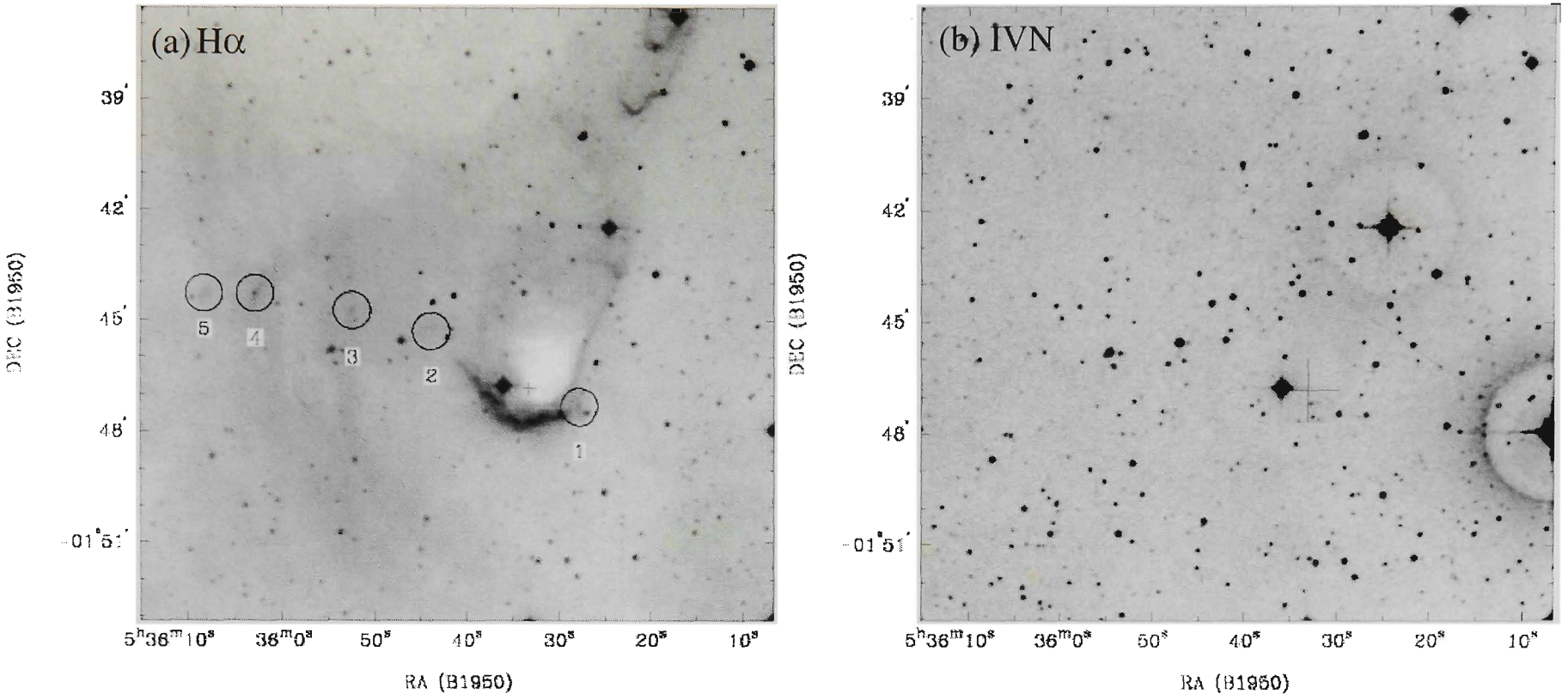

Figure 4.2: Scanned (a) Hα and (b) IVN images of the HH 289 outflow in the Ori I-2 cometary globule. The chain of emission-line objects (1-5) are shown with respect to the embedded IRAS source (marked with a cross). Note the bubble-like structure surrounding the eastern side of the globule (see text for details).

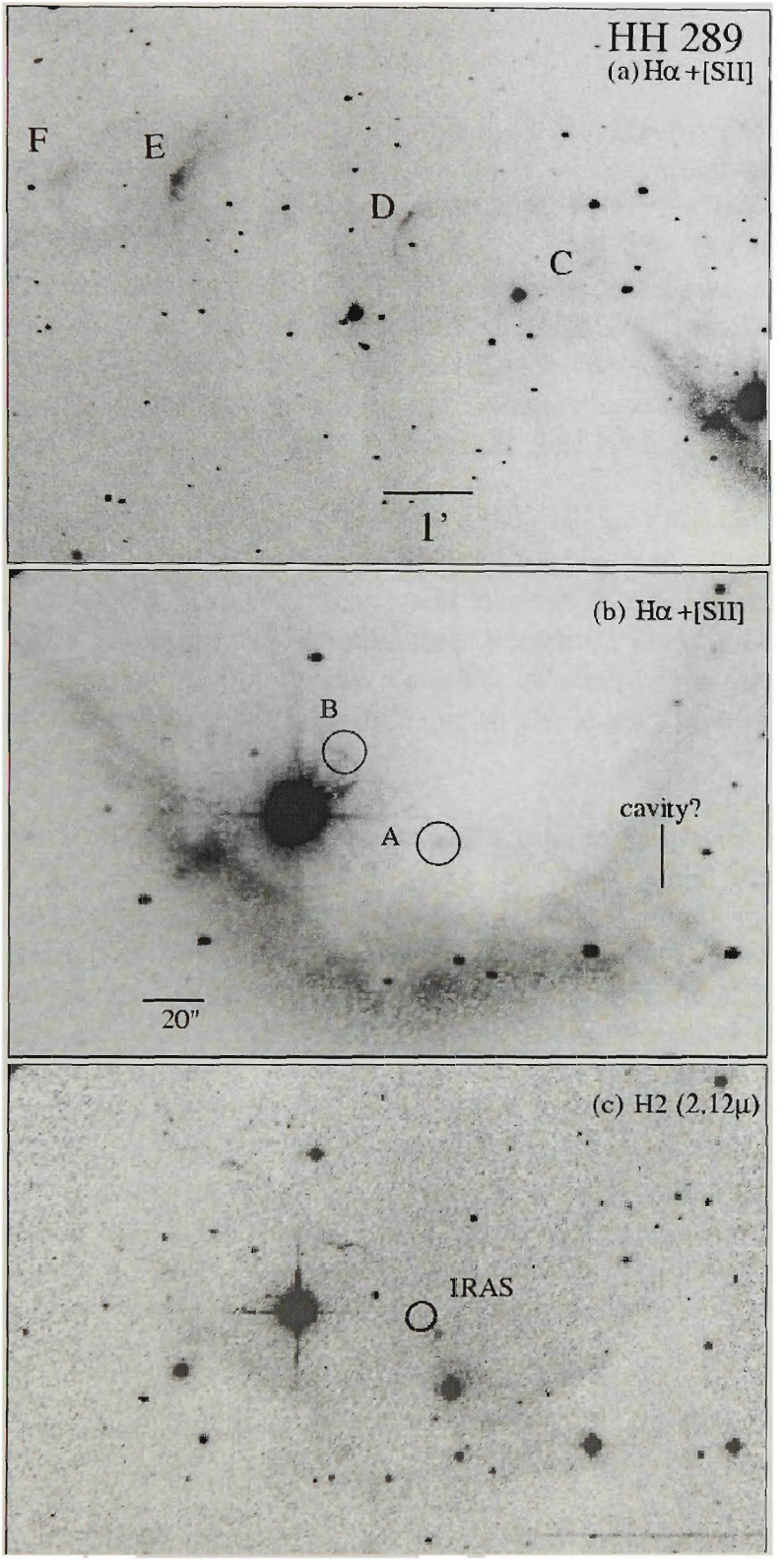

Figure 4.3: (a) Combined Hα+[SII] image of the HH 289 outflow showing the outer knots C-F. The inner region of the globule seen in (b) Hα+[SII] and (c) H_2 clearly show knots A and B have both optical and near-infrared emission. The position of the IRAS source is marked by the circle in the H_2 image. The feature marked "cavity" may represent a cavity evacuated by the outflow as is propagates out of the globule.

4.4.2 HH 444

Located in the vicinity of σ Ori (Figure 4.1), V510 Ori (= HBC 177) was first classified as a T-Tauri star based on an objective-prism survey of the Orion region by Sanduleak (1971). Cohen & Kuhi (1979) list the star as a classical T-Tauri star (cTTs) with W(Hα) > 10Å. The Hα emission-line survey of Wiramihardja et al. (1991) found the source to be a strong Hα emitter with $V = 14.6$ mag as opposed to $V = 13.54$ mag found by Mundt & Bastian (1980). Outflow activity associated with the source was suggested by high–velocity emission seen in long-slit spectroscopic studies (Jankovics, Appenzeller & Krautter 1983; Hirth, Mundt & Solf 1997).

By use of Hα material, the first optical detection of the V510 Ori jet (Parker & Phillipps 1998b; this chapter) is shown in Figure 4.4a. Reipurth et al. (1998) also present a Hα+[SII] image and spectra of the jet and source in which the latter shows a rich emission–line spectrum. Their spectroscopy of the HH 444 jet shows strong Balmer emission relative to the [OII] and [SII] lines. They also detect a faint counter-jet to the main (blue–shifted) lobe seen in Figure 4.4a.

The scanned Hα image (Figure 4.7a) reveals a highly collimated jet. Several faint knots (A-C) are located 57″, 84″ and 194″ from V510 Ori. The flow terminates at the large bow shock structure HH 444D, which displays wide wings sweeping back towards to position of V510 Ori. The Hα+[SII] image (Figure 4.4b) clearly identifies the HH 444 jet extending from V510 Ori. Due to the seeing conditions at the time ($\sim$ 3″), we can only confirm the presence of knots B and D in the Hα+[SII] image. For the continuum frame (Figure 4.4c), conditions were slightly better and based on the scanned Hα and continuum image, knots A-C are considered as pure emission-line features. The jet appears as two separate parts, with the first section appearing as a bright region extending 10″ from V510 Ori, while a second, more fainter part extends a further 6″. This change may represent several individual condensations not resolved by our images. The total projected length of the observed optical flow is 0.6 pc in length.

The small separation between V510 Ori and its jet implies the jet is still active today and coupled with the fact that we do not see an obvious counter flow suggests an evolved case of a one-sided jet (Rodríguez & Reipurth 1994). Reipurth et al. (1998) argue that since the optical jet is directed away from the σ Orionis group of OB stars, the counter-jet is being exposed to strong ultraviolet radiation which in turn impedes normal jet formation. High resolution optical and near-infrared studies of the jet and energy source will be beneficial in determining the nature of this unusual outflow complex.

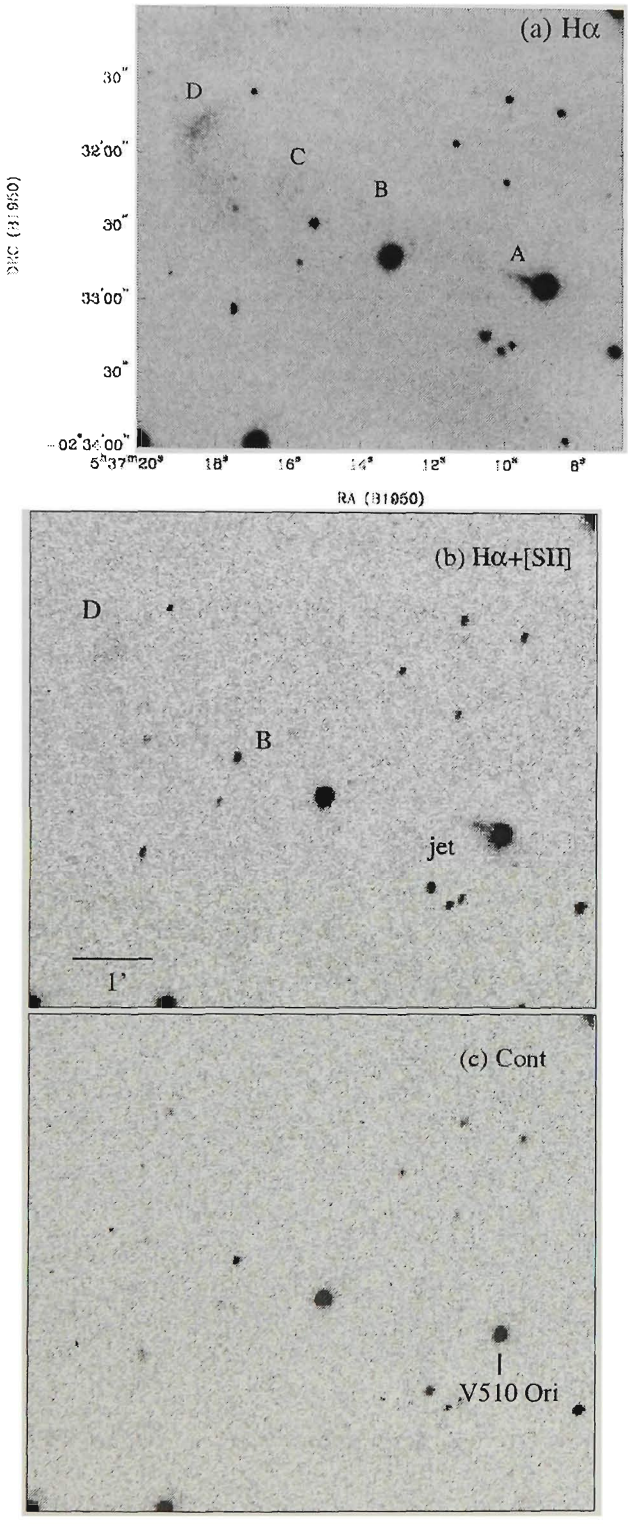

Figure 4.4: (a) Scanned Hα, (b) Hα+[SII] and (c) continuum images of the HH 444 outflow. The Hα and Hα+[SII] images clearly show the jet from V510 Ori. The large bow shock structure, HH 444D, sweeps back towards V510 Ori. Note the absence of a counter-jet the the south-west.

4.5 New objects in L1641

As shown in Figure 4.5, the northern border of L1641 is approximated by the bright ionization front near the open cluster NGC 1981. The cloud extends several degrees south of the figure. The Hα emission surrounding the bright HII region M42 shows remarkable substructure. The southern portion of the image is bounded by the bright reflection nebulosity NGC 1999. In contrast to the L1630 region, we have identified 15 HH complexes within the outlined region shown in Figure 4.5. The region is shown in more detail in Figure 4.6, where the new objects and features of note are indicated. Several strings of objects appear to extend to the north and north-east of the figure. The outlined region towards the centre of Figure 4.6 contains a cluster of objects surrounding the high-luminosity source IRAS 05338-0624 ($L_{bol} \sim 220\ L_{\odot}$).

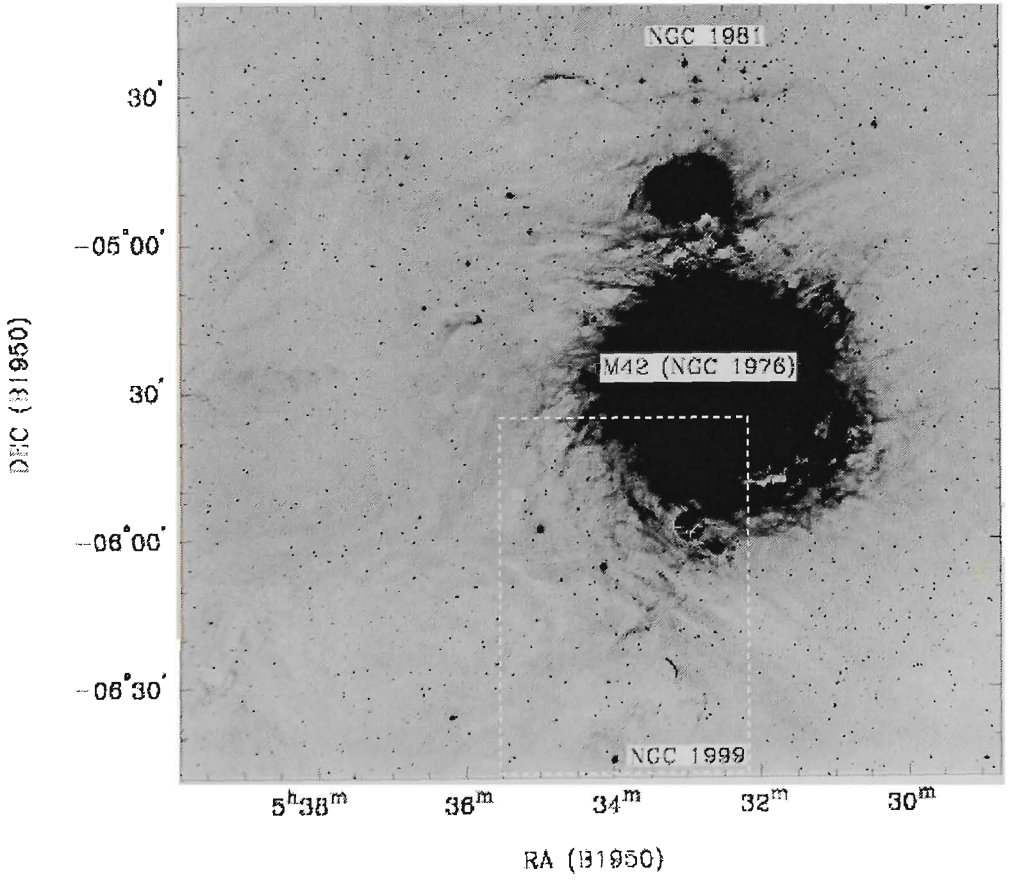

Figure 4.5: Unsharp-mask Hα scan of the L1641 survey region. The northern extent of L1641 is indicated by the bright ionization rim near the open cluster NGC 1981. The bright HII region M42 (NGC 1976) is surrounded by highly structured filaments with several cometary globules seen to the east. The southern portion of the image is bounded by the reflection nebulosity NGC 1999. The box outlines the region shown in Figure 4.6 where a large number of HH objects have been identified.

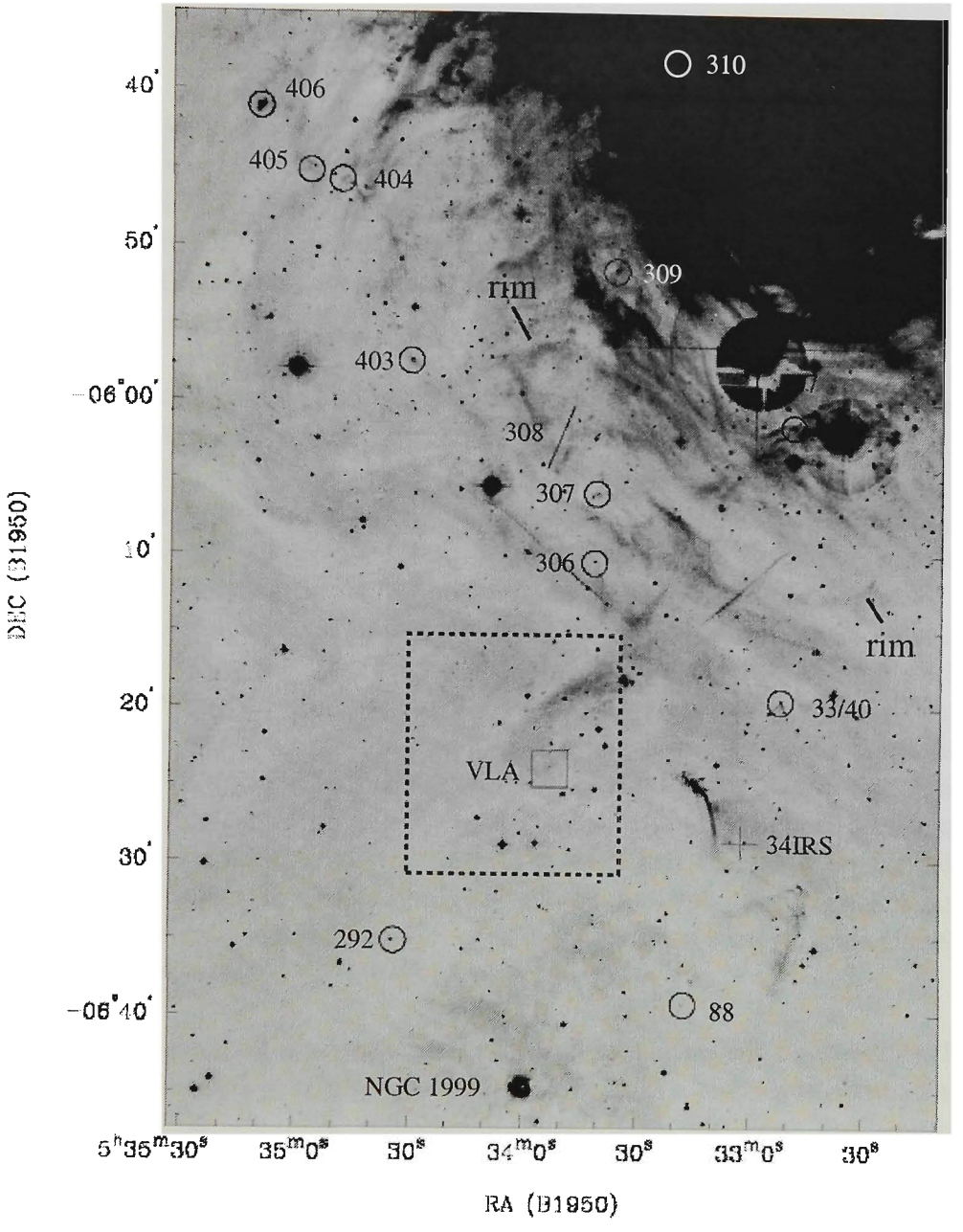

Figure 4.6: Scanned Hα image of the L1641-N region outlined in Figure 4.5. The HII region M42 (NGC 1976) is seen to the north-west with the reflection nebulosity NGC 1999 seen to the south. New objects are numbered and indicated by a single circle to avoid confusion. Delineated by the dashed ellipse, a large rim of Hα emission appears to surround the HH 306-309 and HH 407 group. To the north of HH 309, RBD98 identified several bow shocks (HH 310) in the main nebulosity of M42. As a scale reference, the 3 pc flow HH 34 is shown with its northern (HH 33/40) and southern (HH 88) terminal working surfaces. The central source (34IRS) is indicated by the cross. The bordered region (see Figure 4.8) contains a cluster of objects surrounding the bright IRAS source 05338-0624 (marked as VLA).

4.5.1 HH 292

Located in the south-east portion of Figure 4.6, BE Ori (= HBC 168; IRAS 05345-0635) is a classical[36] T-Tauri star of luminosity $\sim$ 10 $L_{\odot}$ and W(Hα) > 10Å (Cohen & Kuhi 1979; Strom, Margulis & Strom 1989a). No molecular outflow was detected by Levreault (1988a,b). The near-infrared photometry of Strom et al. (1989a) indicates excess emission suggesting the presence of a remnant circumstellar disk.

In Figure 4.7, our scanned Hα and CCD images clearly show a highly collimated flow originating from BE Ori. The flow has also been identified by Reipurth (1999; private communication). On the Hα scan (Figure 4.7a), knots B-D appear to be linked by a stream of Hα emission which could be interpreted as a jet. BE Ori itself is surrounded by diffuse Hα emission which extends towards knot A, which is to the south-west of the source. All these features are confirmed by our Hα+[SII] and continuum images (Figures 4.7b,c). All knots appear Hα-bright with knot B displaying a combination of emission and continuum emission. Designated HH 292, the flow extends along PA = 225° with knot A located 114.″7 to the south-west and knots B-D located 21.″2, 47.″3 and 64.″4 to the north-east of BE Ori respectively, making the total flow length 0.4 pc. In their survey of L1641, Stanke, McCaughrean & Zinnecker (1998; hereafter SMZ98) identified compact H_2 emission associated with knots A and D (SMZ 25 B and A respectively), which may represent the terminal working surfaces of the flow where the wind is encountering dense material.

It is interesting to note the asymmetry in HH emission with respect to BE Ori. The lack of optical counterparts to knots B-D to the south-west of the source suggests BE Ori may have undergone highly irregular outbursts in the past. Assuming a tangential flow velocity of 150 km s^{-1}, knots B-D have ages approximately 300, 700 and 1000 yr respectively, suggesting periodic outbursts every 300-400 yr whereas knot A has an age of 1700 yr. As the seeing during our observations of BE Ori was $\sim$ 3″, deeper imaging may reveal further HH emission and constrain the ejection history of the source.

[36]Using the fluxes in Strom, Margulis & Strom (1989a), and using the classification scheme described in Chapter 3, section 3.3, the spectral index, $\alpha_{2.19\mu m-12\mu m}$ = -0.46 which also places the source as a Class II (≡ classical T Tauri) object.

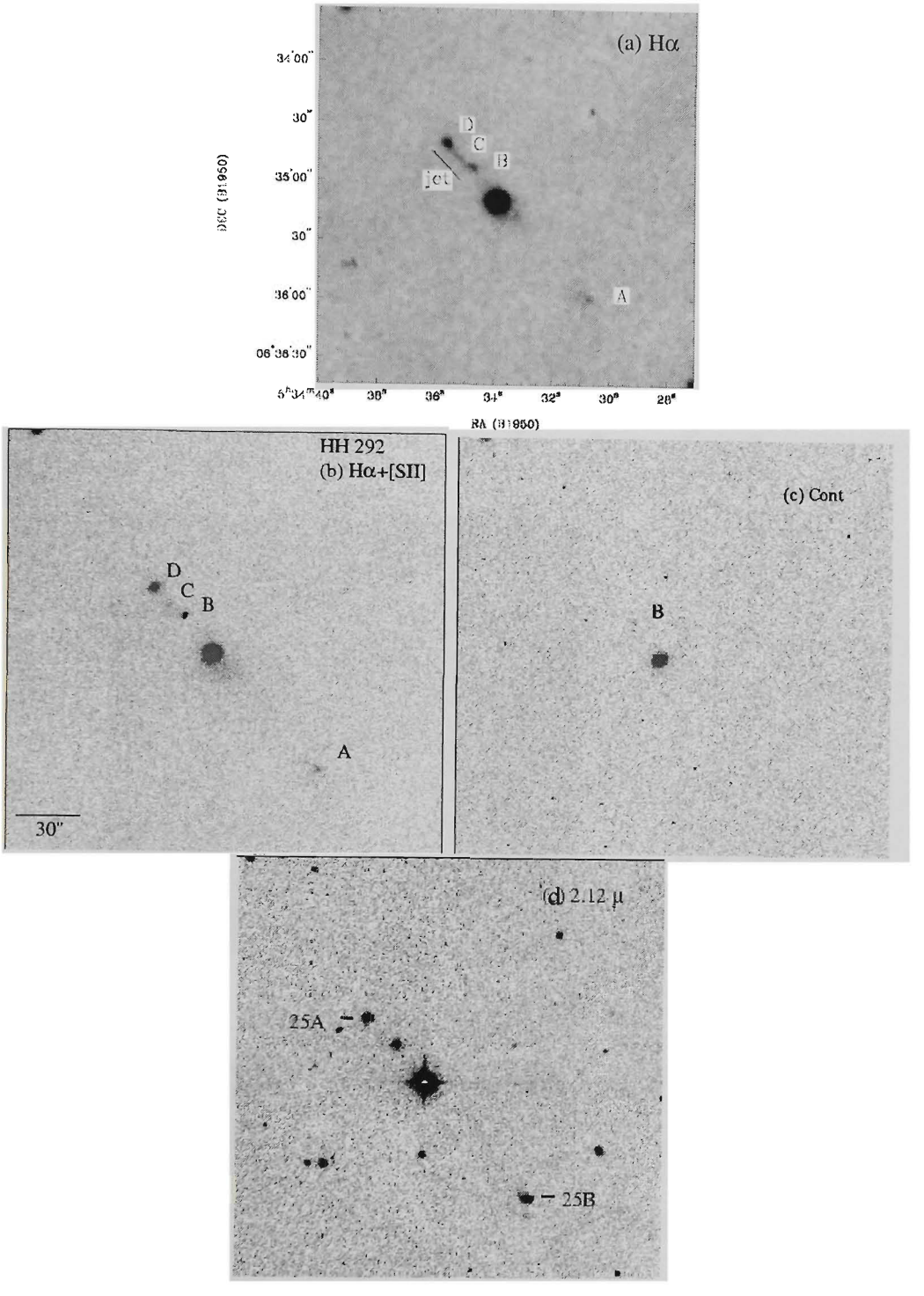

Figure 4.7: The BE Ori/HH 292 outflow. (a) A stream of Hα emission, or jet, links three knots (B-D) to the north-east, while a further Hα knot (A) is seen to the south-west. (b) CCD Hα+[SII], (c) continuum and (d) H_2 (2.12μm; SMZ98) images. HH 292B comprises of both emission and continuum emission in the optical and near-infrared images while HH 292 A and D correspond to the H_2 (2.12μm) features SMZ 25B and SMZ 25A respectively.

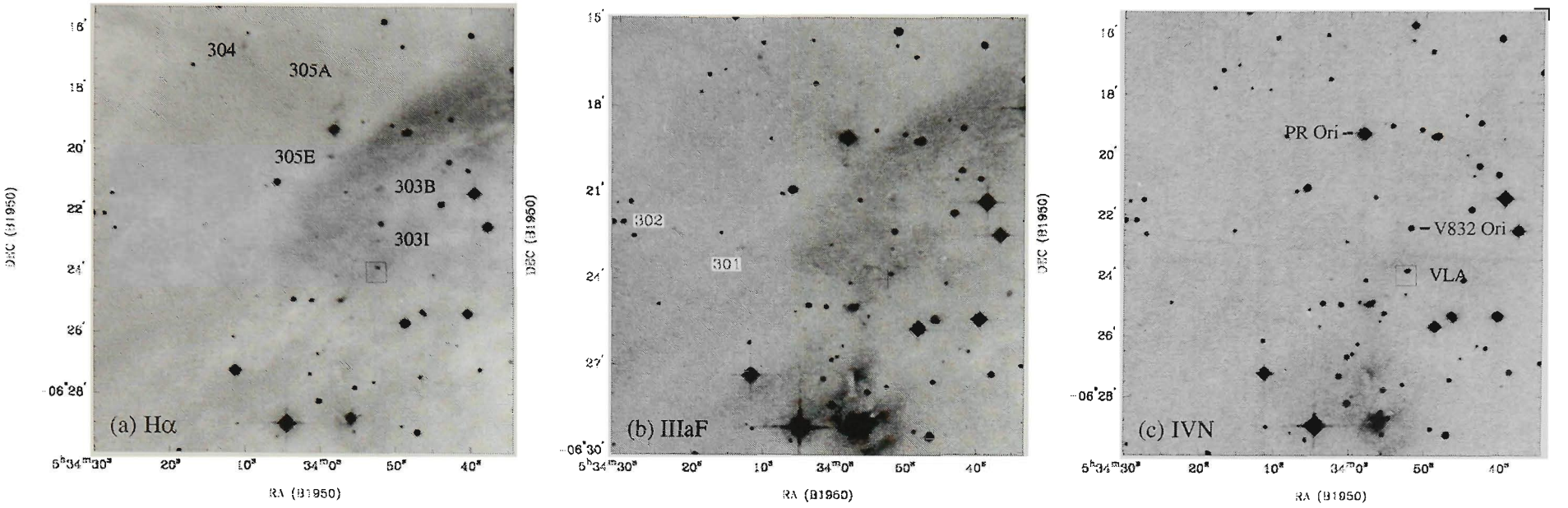

Figure 4.8: Scanned (a) Hα, (b) IIIaF and (c) IVN images of the region outlined in Figure 4.8. Note that many of the nebulosities on the IIIaF are rather faint in comparison to their appearance in Hα. The indicated nebulosities are absent from the IVN image, confirming they are pure emission-line objects. The emission-line stars PR Ori and V832 Ori are indicated with the location of VLA outflow source indicated by the box in all images.

The L1641-N region

In Figure 4.8, we present scanned Hα, IIIaF and IVN images of the outlined region in Figure 4.6 where a cluster of faint red nebulous objects was found by Reipurth (1985). The region has been mapped in ^{12}CO by Fukui et al. (1986, 1988) who found a bipolar outflow, L1641-N, centred on the bright (220 $L_{\odot}$) far-infrared Class I source IRAS 05338-0624. Near-infrared imaging of the region by Strom, Margulis & Strom (1989b), Chen et al. (1993) and Hodapp & Deane (1993), revealed a dense cluster of approximately 20 members surrounding the IRAS source. Davis & Eislöffel (1995; hereafter DE95) and SMZ98 identified a multitude of H_2 (2.12μm) emission which outlines a cavity bored out by the CO outflow and multiple jet and bow shock features which extend at least 2 pc to the south of the embedded cluster. In the following, we present our CCD images of the region shown in Figure 4.8 which confirm many of the Reipurth nebulosities as bona fide HH objects. Scanned Hα images for several of these objects are also presented in Parker & Phillipps (1998b). Independent CCD imaging of the region has also been presented by RBD98. Candidate energy sources for these flows are presented based on their location with respect to the optical and near-infrared emission (DE95, SMZ98).

4.5.2 HH 301/302

Extending to the east of Figure 4.8, the combined Hα+[SII] image of these two objects (Figure 4.9a) shows HH 301 consists of three bright knots (A-C) which form an U-like structure with several fainter knots (D-F) trailing to the south-west. Likewise, HH 302 consists of one bright knot (A) with a fainter one (B) extending to the south-west. Both objects are brighter in [SII] with faint Hα emission. This property is apparent from Figures 4.8a and 4.8b, where HH 301/302 are prominent on the IIIaF, but faint in the Hα image. RBD98 suggest HH 301/302 are related based on their elongation towards the L1641-N embedded cluster where the presumed driving source is located. A line of [SII] emission can be seen to the south which mirrors the position of HH 301/302 and coincides with H_2 emission (SMZ 17/18). The southern part of the Hα+[SII] image shows a string of faint knots which together with HH 301/302, produces a V-type structure with the apex pointing back towards the infrared cluster.

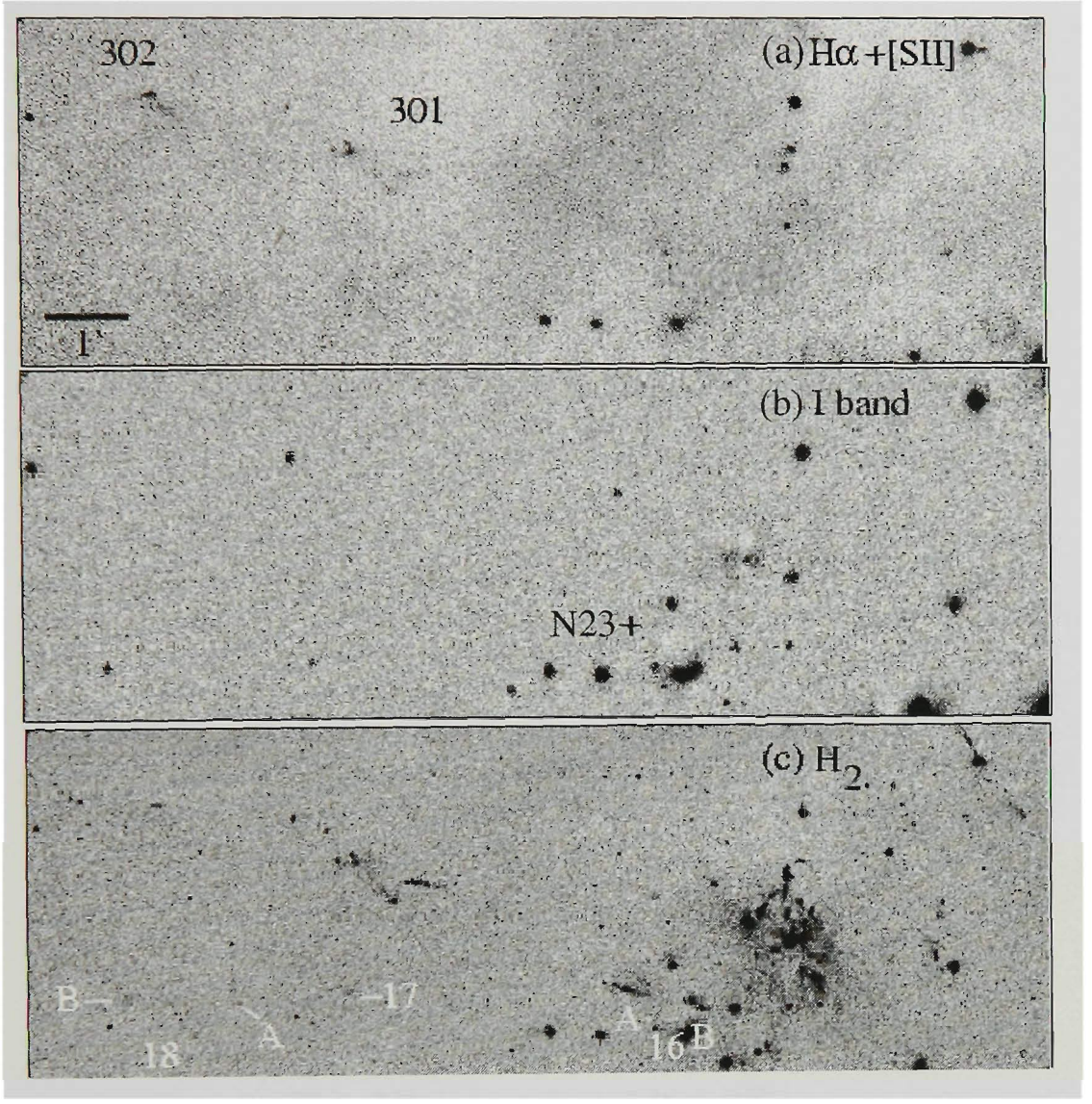

Figure 4.9: (a) Hα+[SII], (b) I-band and (c) H_2 (2.12μm) images of the HH 301 and HH 302 outflows identified from Figure 4.8. The cross in the I-band image marks the location of the presumed energy source (N23 of Chen et al. 1993) for HH 301/302. The H_2 (2.12μm) image clearly shows the jet-like feature (SMZ 16A/B) which is possibly a jet originating from N23. In the Hα+[SII] image, several faint knots correspond to the faint H_2 (2.12μm) features SMZ 17, SMZ 18A and SMZ 18B.

DE95 and SMZ98 identified a chain of H_2 knots (I/J and SMZ 16 A/B respectively) which extend east from the embedded cluster with a morphology reminiscent of a jet. As HH 301/302 and SMZ 17/18 contain both optical and near-infrared emission, we suggest they are tracing the walls of a cavity outlined by the V-type structure. The presence of a jet (SMZ 16A) and counterflow (SMZ 16B) suggests we are seeing a single outflow complex. As the jet extends directly between SMZ 17/18 and HH 301/302, we do not rule

out the possibility of 3 separate flows, although we draw a comparison with the outflow source L1551-IRS5, where HH 28/29 are not located along the jet axis, but close to the walls of a cavity identified by optical, near-infrared and CO observations (see Davis et al. 1995 and references therein).

Chen et al. (1993) identified a K′ band source (their N23) in the direction of DE95 I/SMZ 16B which is not visible in our I band image (Figure 4.9b). However, using HIRES images, processed to 150 iterations, Figure 4.10 shows a point source at the position of N23 at 12 and 25μm only. At 60 and 100μm (not shown), the emission becomes blended with the strong emission associated with L1641-N. The HIRES fluxes for N23 are listed in Table 4.3. Calculated from the 2.1μm data of Chen et al. (1993) and HIRES fluxes, the spectral index[37] for N23, $\alpha_{2.1-25\mu m}$ is 2.80 which places it in the Class 0 range[38]. However, by definition, Class 0 objects have at most weak emission for wavelengths $< 10\mu$m (Bachiller 1996) and due to the contribution of emission from L1641-N at all wavelengths, the spectral index for N23 should be considered an upper limit and the source is most likely a Class I object. Although the separation between the K' position of N23 and the 12μm peak is $\sim 8''$, based on the alignment of optical and near-infrared emission, we propose N23 as the driving agent for both SMZ 17, SMZ 18A/B and HH 301/302. Further spectroscopic studies are needed to clarify its nature.

Table 4.3: HIRES fluxes for N23

λ (μm)	Beam ($''$)	Mag	HIRES (Jy)
2.1[†]		16.1	
12	38×21		0.24 ± 0.02
25	37×22		2.51 ± 0.48
60	67×48		<26.62 ± 3.92
100	95×83		<121.56 ± 14.50

[†]From Chen et al. (1993).

[37]See chapter 3, section 3.3

[38]$\alpha_{12\mu m-25\mu m} = 2.20$, which also places the source in the Class 0 category.

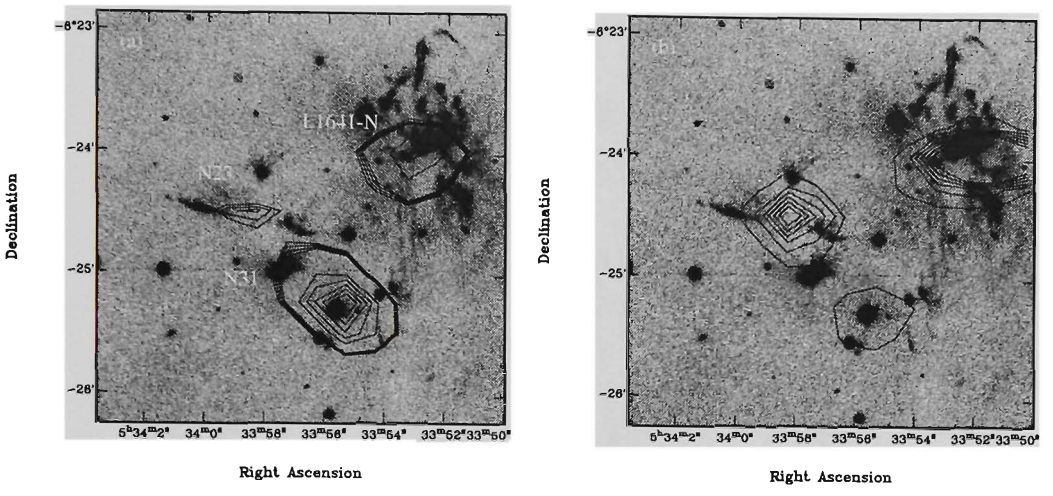

Figure 4.10: Narrow-band H_2 (2.12μm) image (from SMZ98) of the SMZ 16 A/B jet overlaid with HIRES contours at (a) 12μm with contours from 2 to 2.3% and 4 to 8% of the maximum (556.54 MJy sr^{-1}) and (b) 25μm with contours at 5 to 30% in steps of 5% of the maximum (823.62 MJy sr^{-1}). N23, the candidate energy source for SMZ 17/18 and HH 301/302 is shown along with contours for L1641-N and source N31 in the list of Chen et al. (1993).

An additional piece of evidence that favours our interpretation of the SMZ 17/18 and HH 301/302 outflow is seen in Figure 4.11 where IRAS HIRES contours are overlaid on the H_2 (2.12μm) image of SMZ98. Clearly, 100μm emission delineates a cavity outlined by HH 301/302 to the north and SMZ 17/18 to the south. The peaks in the 100μm emission are not associated with any known embedded object, although there is a star close to the 100μm emission peak near HH 301. A scan through the literature shows it has not been identified as a young stellar object. The association between shocked H_2 and 100μm dust emission suggests a strong interaction between the outflow and the molecular cloud.

4.5.3 HH 303

The HH 303 flow consists of two groupings of knots aligned along a north-south direction. The Hα+[SII] image in Figure 4.12a shows the northern-most group (knots A-F) outlines a bow-shock with a sheath of Hα emission overlaying clumpy [SII] emission. Several more [SII]-bright knots (I-K) extend towards the south.

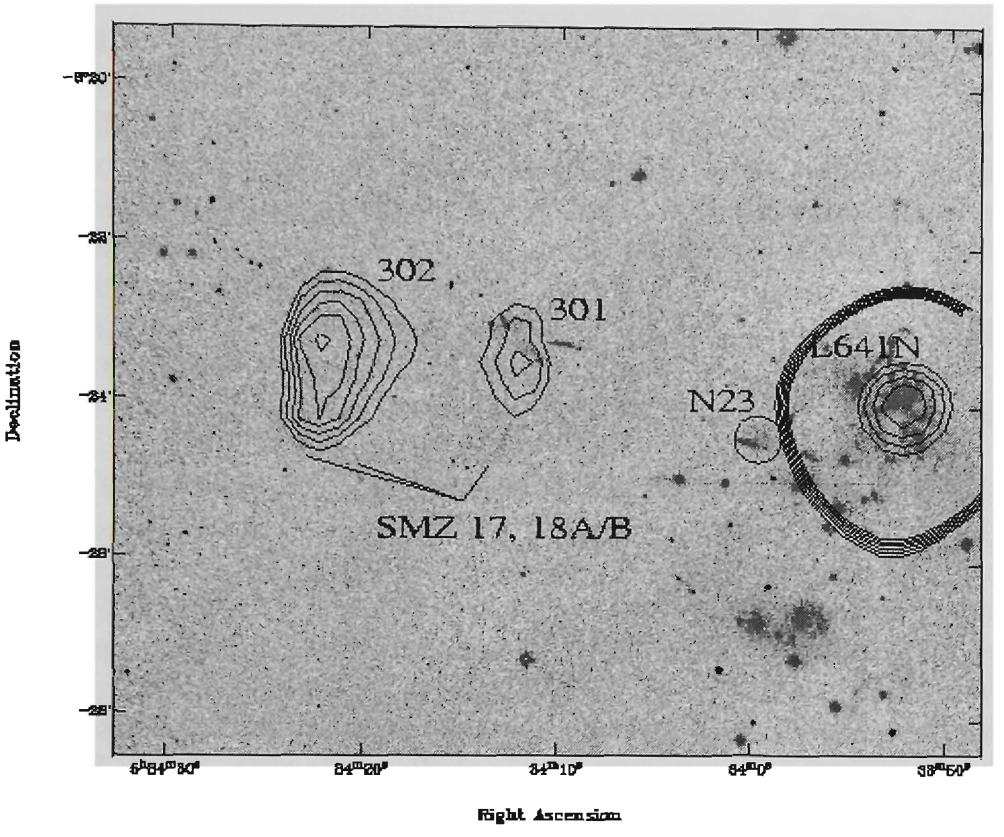

Figure 4.11: Narrow-band H_2 (2.12μm) image of HH 301/302 (from SMZ98) overlaid with 100μm HIRES contours. The position of the candidate energy source, N23, is indicated by the circle. The correspondence between the H_2 and 100μm emission suggests the outflow is strongly interacting with its surroundings. The outer contours of the HIRES emission fit within a cavity delineated to the north by HH 301/302 and SMZ 17/18 to the south (see Figures 4.9a,c). Due to the intensity range, contours for HH 301/302 and the outer annulus surrounding L1641-N are at 30-35% in steps of 1% of the maximum (1168 MJy sr^{-1}), while the inner contours for L1641-N are at 80-100% in steps of 5% of the maximum.

At first glance, HH 303 could be interpreted as a highly collimated flow originating from the variable star V832 Ori (Figure 4.12b). The optical and near-infrared photometry of this source (source N2 of Chen et al. 1993) shows a spectral energy distribution which declines rapidly for $\lambda > 1\mu$m, suggesting a lack of circumstellar material. A comparison of our optical images with the near-infrared data of SMZ98 shows the majority of HH 303 displays both optical and H_2 emission, thereby suggesting HH 303 is behind V832 Ori and unrelated to the star. Knots HH 303 B, F and I are coincident with the H_2 knots SMZ 8A, 8B, and 14P respectively, with the H_2 emission displaying bow shock morphologies which open towards the south in the direction of L1641-N.

As knots HH 303 I-K lie within the blue lobe of L1641-N, it has been suggested the CO, near-infrared and optical flows derive from a common source (Strom et al. 1989b; SMZ98; RBD98). Chen et al. (1993) identified a bright M band source (their N15) $\sim 8''$ to the east of the IRAS position. Chen, Zhao & Ohashi (1995) detected this source with the VLA at 2.0mm, 7.0mm and 1.3cm, while SMZ98 identified a 10μm source coincident with N15 and the VLA source. As N15, the 10μm source and the 1.3cm source represent the same object, we follow RBD98 and label it as the "VLA source" which they suggest is the driving source for HH 303 and the illuminator of the reflection nebulosity seen to the north-east in our I band image (HD93; Figure 4.12b).

However, it is important to mention that the L1641-N region is a highly clustered environment where identifying outflow sources requires the highest resolution possible. Anglada et al. (1998) identified two radio continuum sources, VLA2 and VLA3, which are 0.″8 and 0.″2 to the west and east respectively from the nominal position of the VLA source. Further observations of the region reveal a fainter source within 1″ of VLA2 (Anglada 1998, private communication). The CO data of Fukui et al. (1986; 1988) clearly indicates the L1641-N molecular outflow is more complex than a simple bipolar outflow. Higher resolution studies of these sources are needed to determine which source is driving the optical and H_2 emission. In particular, it would be interesting to see if the VLA source displays an elongated radio jet with its long axis pointing in the direction of HH 303.

In addition to HH 303, RBD98 suggest the VLA source also drives HH 61/62, which are located 46.′8 (6.5 pc) to the south of L1641 (see Figure 4.21). If their assumption is correct, the HH 61/62/303 flow is 7 pc in length, with the northern lobe only 5% the length of the southern lobe. Any shocks associated with the northern lobe will be extremely faint due to the lack of molecular material as the flow moves away from L1641.

4.5.4 HH 304

Located to north-east of the VLA source, the [SII] image of HH 304 (Figure 4.13a) shows several compact knots which are [SII]-bright. Knot B is compact with a bow shock structure (knot A) extending towards the north-east and then curls back to the north-west. Knots C and D display an opposing bow shock structure, with knots C and D connected by faint [SII] emission. The overall morphology of the system suggests the energy source is located between knots A/B and C/D. The I-band image (Figure 4.13b) shows a compact reflection nebulosity with a tail which mimics part of the [SII] emission associated with knots A and B. A reddened source (which we denote as

HH 304IRS) appears where the reflection emission is most compact.

The HH 304 complex is also seen in the H_2 mosaic of SMZ98, who label it SMZ 5. HH 304A is seen as a bright bar which extends 6″ along an east-west direction. At the position of the compact reflection nebulosity, a bright H_2 knot is seen, with a trail of H_2 emission extending from HH 304IRS towards HH 304C. The appearance of the optical and near-infrared emission suggests we are seeing two lobes with knots A and C representing the north-eastern and south-western working surfaces respectively. HH 304IRS appears midway between these two opposing working surfaces. There are no IRAS or Hα emission-line stars at the location of the reflection nebulosity.

Using IRAS HIRES images, processed to 150 iterations, a source has been detected close to the position of the I-band reflection nebulosity. As shown in Figure 4.14, a point source is detected at 25μm only with a flux of 0.04 $\pm$ 0.02 Jy. The 12 and 100μm HIRES images (not shown) do not show a point source, while at 60μm, the emission becomes blended with that of another source $\sim$ 5″ to the west which displays a point source at 60μm (0.03 $\pm$ 0.07 Jy) only. Using the relationship $I_{100\mu m} \approx 5A_V + 17$ MJy sr^{-1} mag^{-1} (Langer et al. 1989; Snell, Schloerb & Heyer 1989), a lower limit[39]. to the extinction in the line of sight towards HH 304IRS is 4 mag ($I_{100\mu m} = 37.6$ MJy sr^{-1}), indicating a highly obscured source. The non-detection at 12μm and the blending of emission at 60 and 100μm suggests HH 304IRS is either a Class 0 or Class I object. Further observations in the near-infrared and sub-millimetre regimes will help clarify the nature of the source.

[39]It should be noted that $I_{100\mu m}/A_V \sim 5$ MJy sr^{-1} was found to be valid for diffuse (unresolved) clouds. Here it is clear that much of the region where the extinction is going on is not resolved at 100μm, and values for A_V should be considered as lower limits.

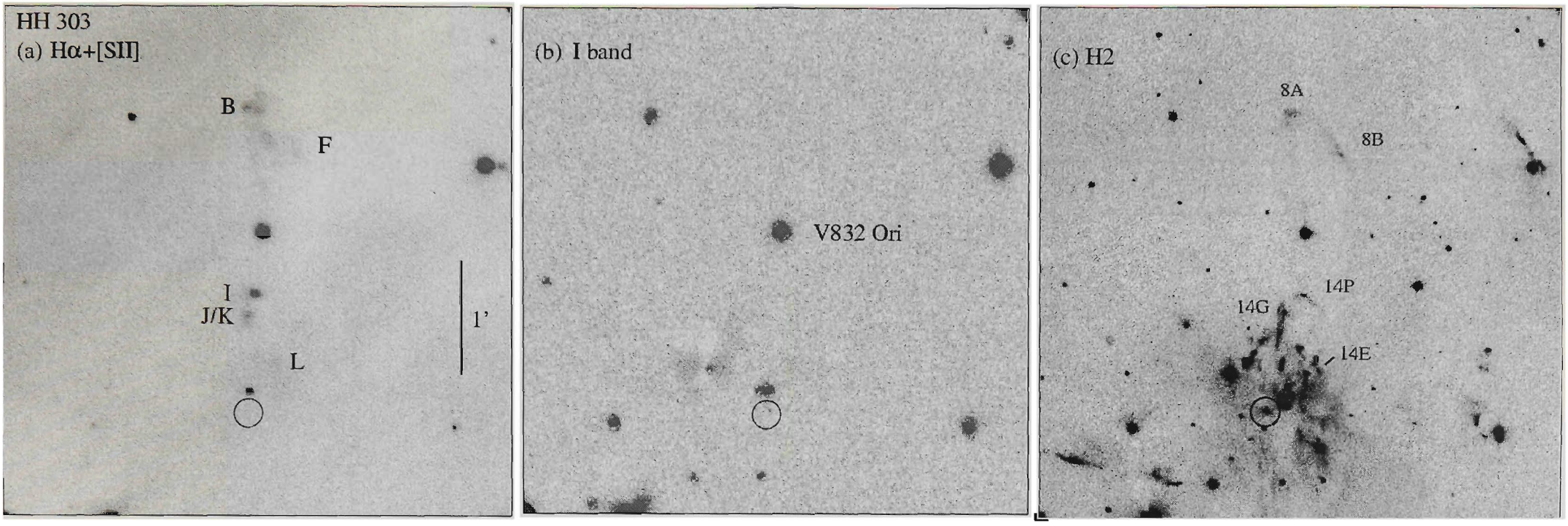

Figure 4.12: (a) Hα+[SII], (b) I-band and (c) H_2 (2.12μm) images of the HH 303 complex identified from Figure 4.8. The circle marks the location of the VLA source, which RBD98 propose as the driving source for HH 303. Both the Hα+[SII] and 2.12μm images show that a number of HH knots show corresponding structures.

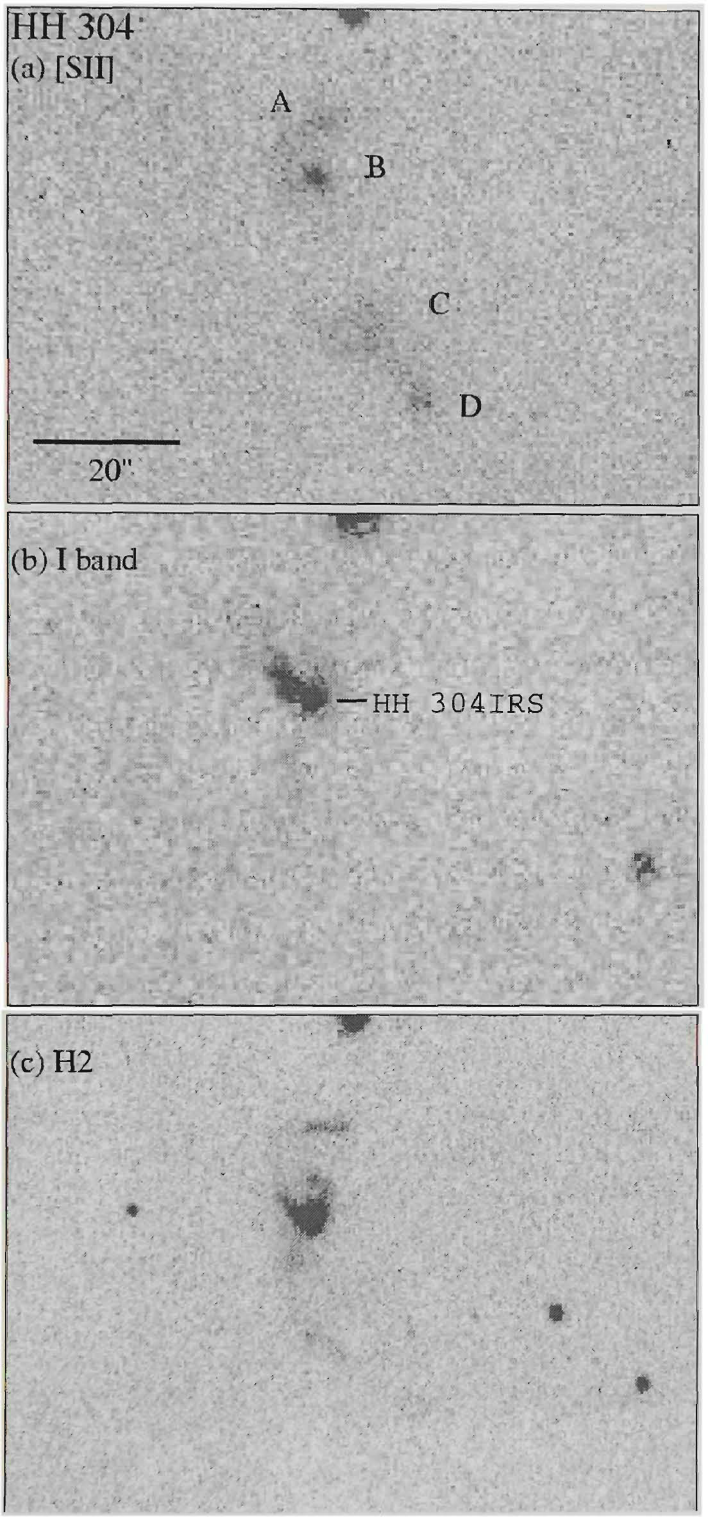

Figure 4.13: (a) [SII], (b) I-band and (c) 2.12μm images of the HH 304 outflow located in the north-east of Figure 4.8. Knots A/B and C/D represent opposing bow shocks with a reddened source located at knot B. The candidate energy source (HH 304IRS) displays a fan of reflection nebulosity extending to the north-east.

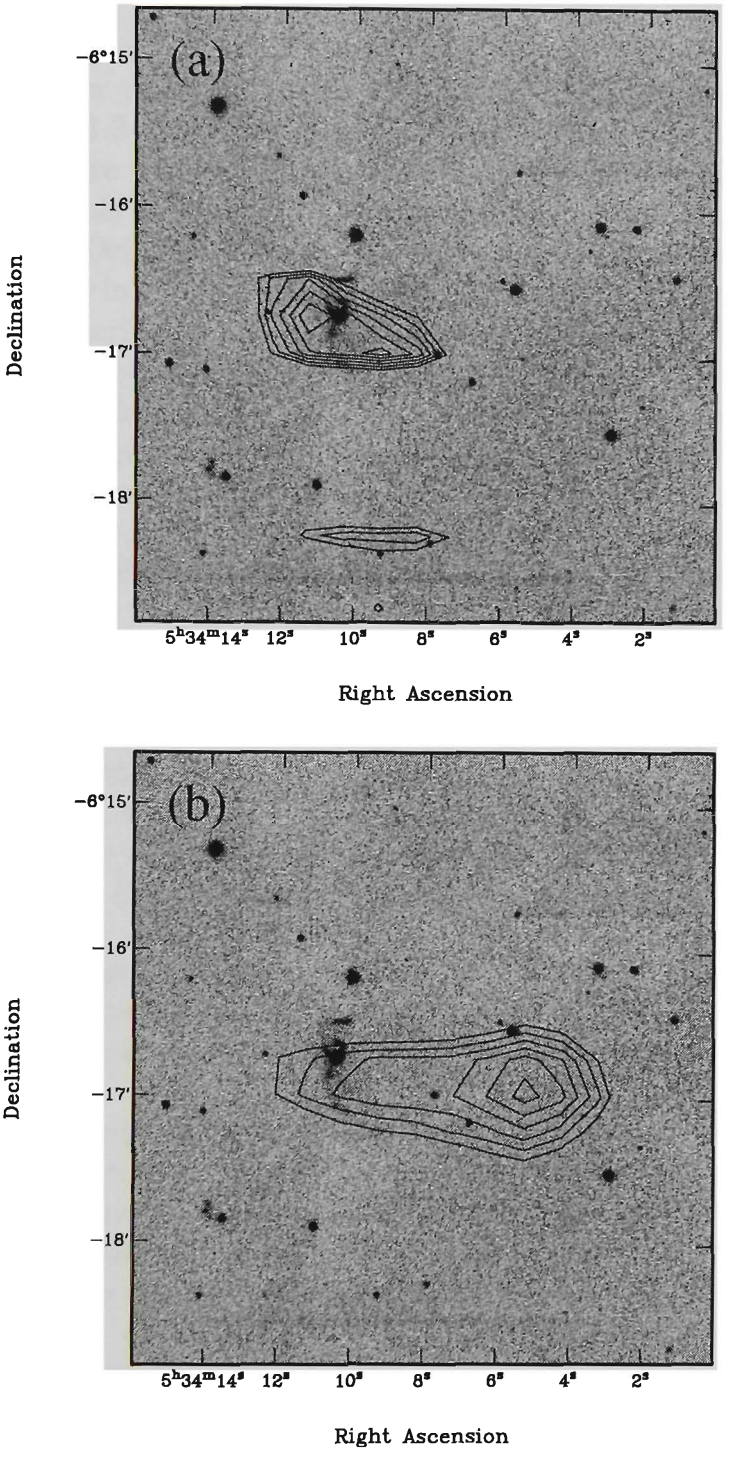

Figure 4.14: HIRES contours (iterations = 150) of HH 304IRS overlaid on the H_2 image from SMZ98. (a) 25μm with contours at 0.4 to 1.4 MJy sr^{-1}, in steps of 0.2 MJy sr^{-1}. (b) 60μm with contours at 1 to 3.5 MJy sr^{-1}, in steps of 0.5 MJy sr^{-1}.

4.5.5 HH 305

The HH 305 outflow appears aligned along a north-south axis centred on the bright ($V \sim 11.3$ mag) star PR Ori. With the exception of knots A and F, all objects are Hα-bright, with knot B displaying an inverted V-type structure only visible in Hα. Knot A shows a bow shock structure which opens towards PR Ori. It is interesting to note that HH 305E represents the brightest nebulosity in the flow. The increased brightness could be attributed to the flow encountering an obstacle of some sort, perhaps in the form of a molecular clump. The dark lane seen in Figures 4.6, 4.8 and 4.15 represents a change in the molecular distribution in this part of L1641. At the position of HH 305E, the flow impacts the molecular cloud and then deflects to where we see HH 305F. Based on their separation from PR Ori, RBD98 suggest knots C/D represent an HH pair located 16″ from the source. Similarly, knots B/E and A/F represent HH pairs located 65″ and 108″ from PR Ori respectively, making the total flow length 0.54 pc.

At present, it is unknown if HH 305 is being driven by PR Ori or a more embedded source behind it (RBD98). In a major study of *Einstein* X-ray sources in L1641, Strom et al. (1990) identified PR Ori as a low-luminosity (13 $L_{\odot}$) source with a spectral type of K4e and W(Hα) = 0.5Å. Their *JHKLM* photometry indicates a lack of infrared colour excess normally attributed to a circumstellar disk. Based on their data, PR Ori appears to be a weak-lined T-Tauri star (wTTs). Its location with respect to the L1641 molecular cloud shows it lies in a region of low obscuration and in addition to the fact that SMZ98 did not detect any H_2 emission associated with HH 305 rejects the notion of an embedded, more younger source located behind PR Ori.

If PR Ori is the energy source of HH 305, it would present a major discrepancy in star formation theory as wTTs are not thought to be associated with circumstellar disks and/or outflow phenomenon. Magazzu & Martin (1994) identified what was thought to be a HH flow associated with the wTT, HV Tau. Woitas & Leinert (1998) suggested the HH object is actually a companion T-Tauri star with strong forbidden emission lines whose presence originally led Magazzu & Martin to their conclusions. How do we reconcile the fact that PR Ori is a wTTs with an outflow? The answer may lie in Table 2 of Strom et al. (1990), who list PR Ori as an optical double. Our CCD images also show PR Ori as an extended source, in which case it seems more plausible the companion (PR Ori-B) is the driving source of HH 305. Clearly, further studies of this HH complex are needed.

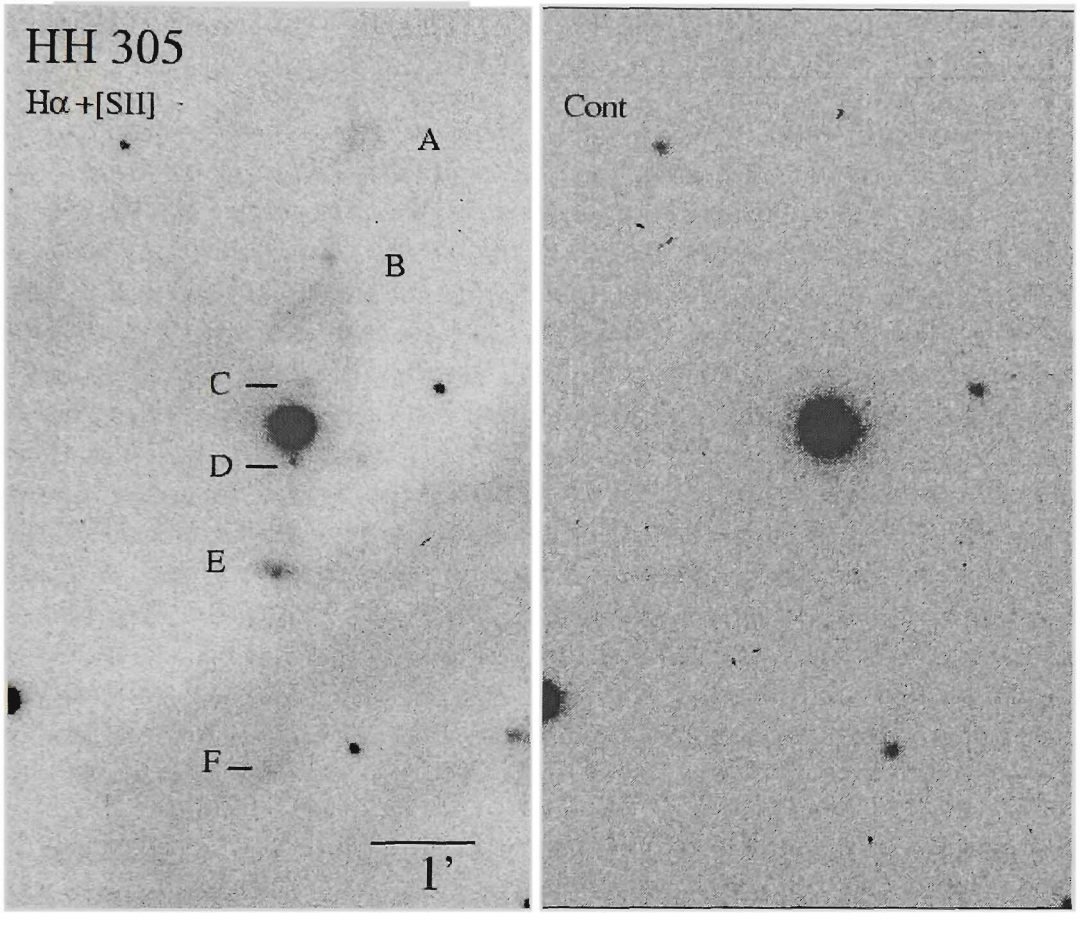

Figure 4.15: (left) Hα+[SII] and (right) continuum images of the HH 305 flow identified from Figure 4.8. Knot E marks the location where the flow may be deflected by a dense region indicated by the darkened strip seen to the south of the image. Note that PR Ori appears slightly extended and is in fact an optical double, where the companion is the proposed energy source for HH 305 (see text).

4.5.6 HH 306-309

Figures 4.6 and 4.16 show scanned Hα and IVN images of a string of emission-line objects (HH 306-309) extending away from the VLA source and up into the main emission nebulosity of M42. A large arcuate structure (HH 407) can be seen near the bright stars towards the western border. The large rim of Hα emission identified in Figure 4.6 is orientated along PA = 55° and appears to surround all objects in the figure. A comparison of the Hα and IVN images confirms all objects are pure emission-line features.

The HH flows

In conjunction with the IVN image (Figure 4.16b), our Hα+[SII] images confirm all as bona fide HH objects. In Figure 4.17, the Hα+[SII] image shows HH 306 consists of two bright compact knots (B and F) with a trail of emission extending to the south. A further knot, HH 306G, lies to the west which may be unrelated, or part of an older fragmented shock. HH 307 consists of several bright knots which mark the apexes of large arcs or wings which sweep out and open towards L1641-N. RBD98 suggest HH 308 appears as a fragmented bow shock with knots A and B representing the eastern and western wings respectively. Located between HH 308A and B, we note the presence of a third knot not identified by RBD98 which we denote here as HH 308C. HH 309 (Figure 4.18) shows a similar structure to HH 308, with knots A and B representing the first fragmented bow shock, knot C the second and knots D/E the third. The reverse bow shock morphology of HH 309B can be explained by noting the distribution of Hα emission on the scanned Hα and CCD Hα+[SII] images. The knot appears to have curled around the background emission which may have been responsible to creating the fragmented appearance of HH 309.

In searching for further emission north of HH 309, RBD98 discovered several bow shock structures, designated HH 310, within the main nebulosity of M42 (see Figure 4.6). The objects are brighter in [SII] than in Hα, thus discounting the possibility they might be photo-ionized rims. We have also imaged these structures and for completeness, present our Hα, [SII] and continuum images in Figure 4.19. Our [OIII] frame (not shown) does not detect the bow shocks associated with HH 310, thereby suggesting the flow is moving with a velocity less than 100 km s^{-1}. Our [SII] and continuum images (Figures 4.19a,b) identify several bow shock structures to the north-west of HH 310 which are [SII]-bright and absent in the continuum frame. Assuming for the moment these features are bona fide HH objects, their apparent deviation from the axis defined by HH 310 can be explained if the flow is being redirected by an obstacle, possibly the long tongue-like feature which extends from the top of the images. An alternative explanation is that they form part of a separate flow, perhaps from the L1641-N region. Spectroscopic observations of these features are needed to determine if they are HH shocks.

The embedded counterflow

To the south of L1641-N, SMZ98 discovered a long chain of bow shocks. Designated SMZ 23, the 9.′8 (1.35 pc) chain consists of at least 7 bow shocks (A-G) which may represent the red-shifted counterflow to HH 306-310 (this

chapter, RBD98). Stanke, McCaughrean & Zinnecker (2000) found further large-scale H_2 emission features which may be related to SMZ 23. These bow shocks, SMZ 6-2 and SMZ 6-4A-C, extend south of the SMZ 23 chain and increase the chain from 1.35 pc to 2.78 pc. From the ^{13}CO data of Bally et al. (1987; hereafter B87), the integrated moment map (Figure 4.20) shows evidence of a cavity created by SMZ 23/6-2/6-4A-C. What is interesting about this cavity is its size and orientation with respect to L1641-N, HH 306-310 and the large cavity dubbed by RBD98 as the "L1641-N chimney", which they suggest has been excavated by the repeated passage of bow shocks associated with HH 306-310. The location of individual knots associated with SMZ 23/6-2/6-4A-C appears to trace the western wall of the southern cavity, suggesting the flow impacts with the cavity wall which produces the observed emission. We suggest this southern cavity is being excavated by SMZ 23, SMZ 6-2 and SMZ 6-4A-C as the red-shifted flow propagates into the cloud and away from L1641-N. The ^{13}CO velocity structure of the southern cavity is evident from 5-8 km s^{-1}, with the L1641-N molecular core and the "L1641-N chimney" appearing around 8 and 8-11 km s^{-1} respectively. This gives further evidence that the southern cavity and the "L1641-N chimney" represent expanding red and blue-shifted lobes centred on the L1641-N region.

Following similar arguments in RBD98, the dimensions of this southern cavity to be $5' \times 12'$ in length, giving a total area of $\sim 1 \times 10^{37}$ cm^2. Assuming the intensity in the cavity lies within 3-5 K.km s^{-1}, the total mass excavated by the SMZ 23/6-2/6-4A-C flow is $\sim$ 37-62 $M_\odot$. RBD98 find HH 306-310 has removed $\sim$ 190 $M_\odot$ of gas from L1641. Apart from obvious errors in estimating the ^{13}CO intensity and cavity size, we should point out we have not taken into account the possibility the southern cavity may have been formed by the combined action of more than one outflow.

SMZ 23/6-2/6-4A-C, HH 306-309 and HH 310 all display large bow shock structures which open towards the L1641-N region where the presumed energy source lies. As mentioned for HH 303, the high degree of clustering about the VLA source confuses identifying specific energy source(s). However the principal components HH 306B, HH 307A, HH 308C and HH 309A are located 806″, 1152″, 1331″, 1955″ away from the position of the VLA source. In addition to HH 310A (2764″), the HH 306-310 lobe is 6.3 pc in length. The geometry of HH 306-310 and SMZ 23/6-2/6-4A-C about the VLA source and VLA2/VLA3 strongly favours at least one of them as the energy source of the optical and near-infrared emission. Whichever of these sources is responsible for the observed emission, the combined length of HH 306-310 and SMZ 23/6-2/6-4A-C lobes is $\sim$ 10.5 pc. High-resolution radio studies will be beneficial for identifying radio jets and their orientation with respect to the optical and near-infrared emission.

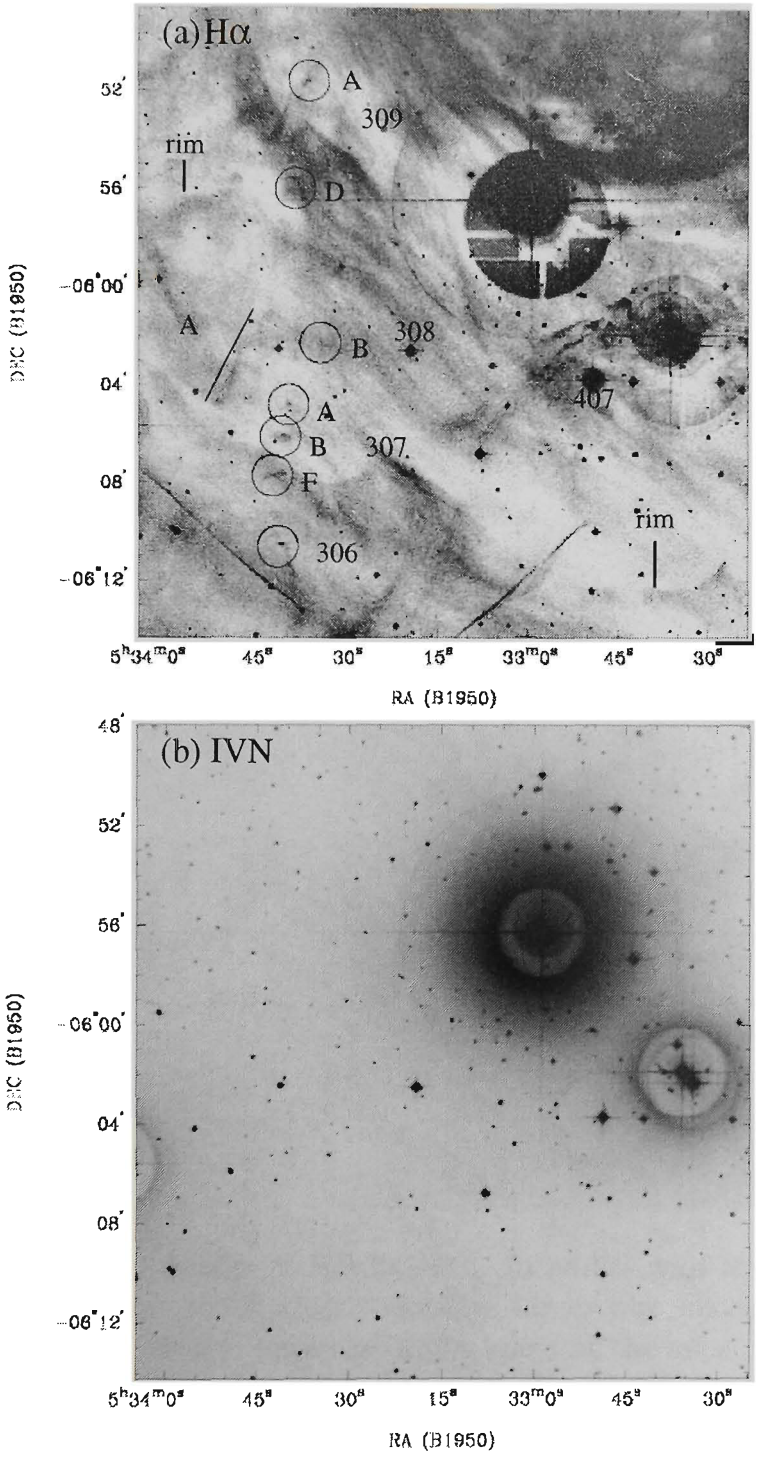

Figure 4.16: Scanned (a) Hα and (b) IVN images of the northern objects HH 306-309 and HH 407 identified in Figure 4.6. The large rim of Hα emission is clearly visible and as no emission is seen in the IVN image, the rim is identified as a pure emission-line feature.

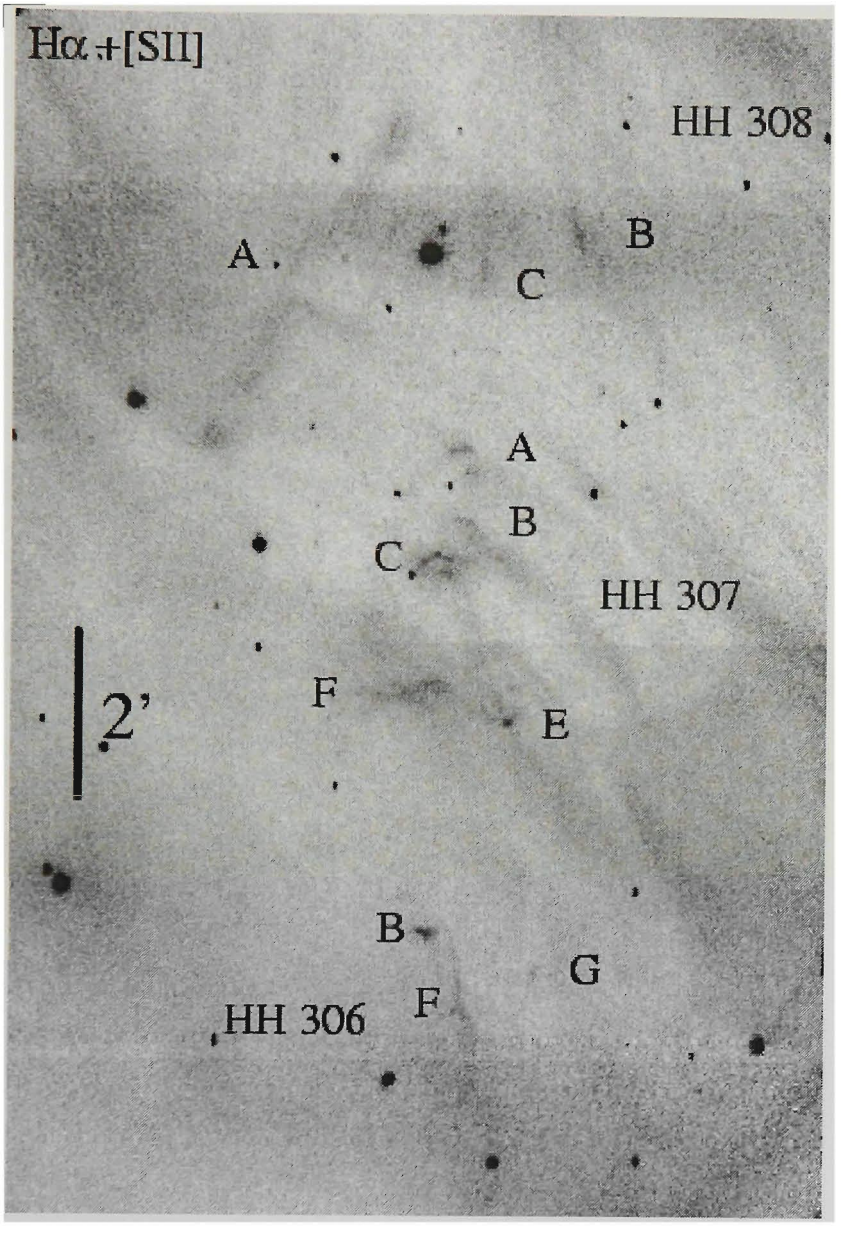

Figure 4.17: Hα+[SII] image of HH 306-308. In addition to several bright knots, the HH 307 bow shock clearly displays larger bow shock structures which open to the south and have the bright knots at the apex of the bows. HH 308 appears as a highly fragmented bow shock with HH 308A displaying an elongated structure (see text for details).

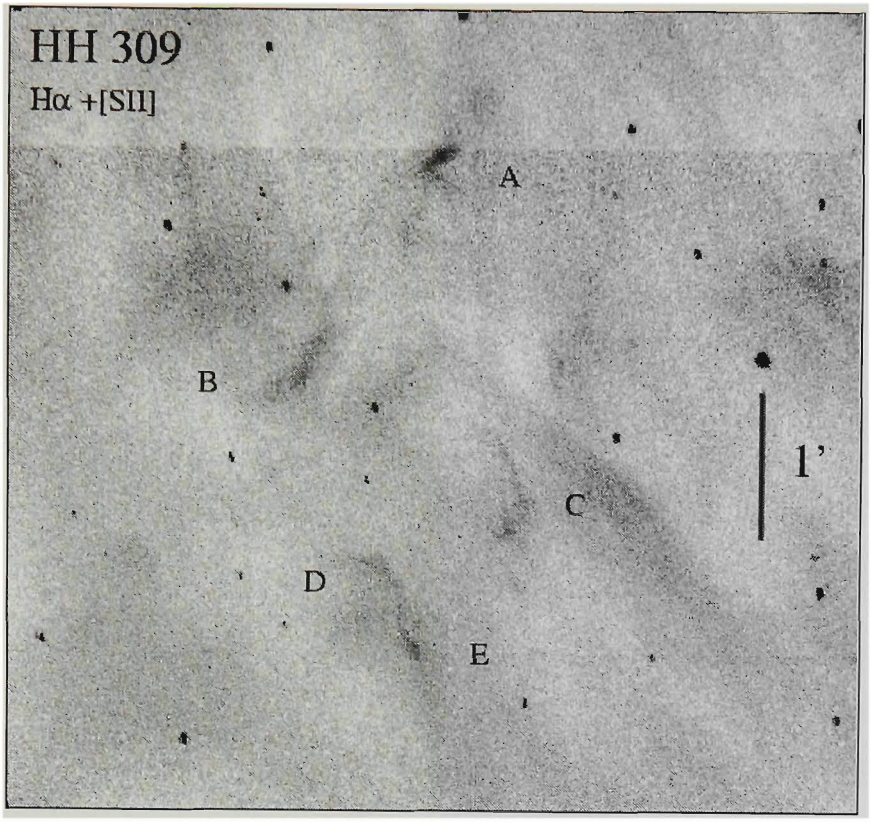

Figure 4.18: Hα+[SII] image of the HH 309 bow shock. The reverse morphology of knot B can be explained as the flow passes over the background Hα emission which extends from the north-east to the south-west of the figure.

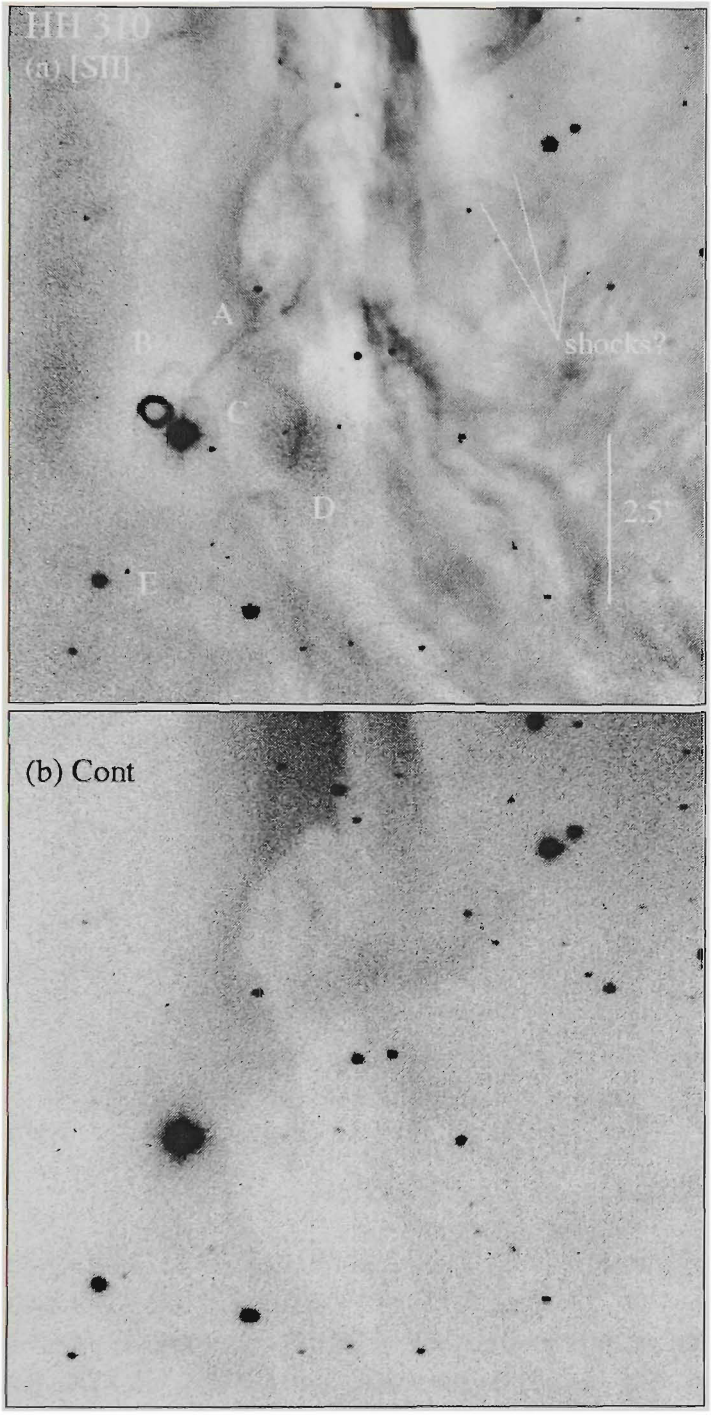

Figure 4.19: (a) [SII] and (b) continuum images of the HH 310 region (see Figure 4.6 for location). To the north-west we see several "bow shocks" which may be genuine HH objects associated with HH 310. They may be deflected from the flow axis by the tongue-like feature which extends from the top of the figure.

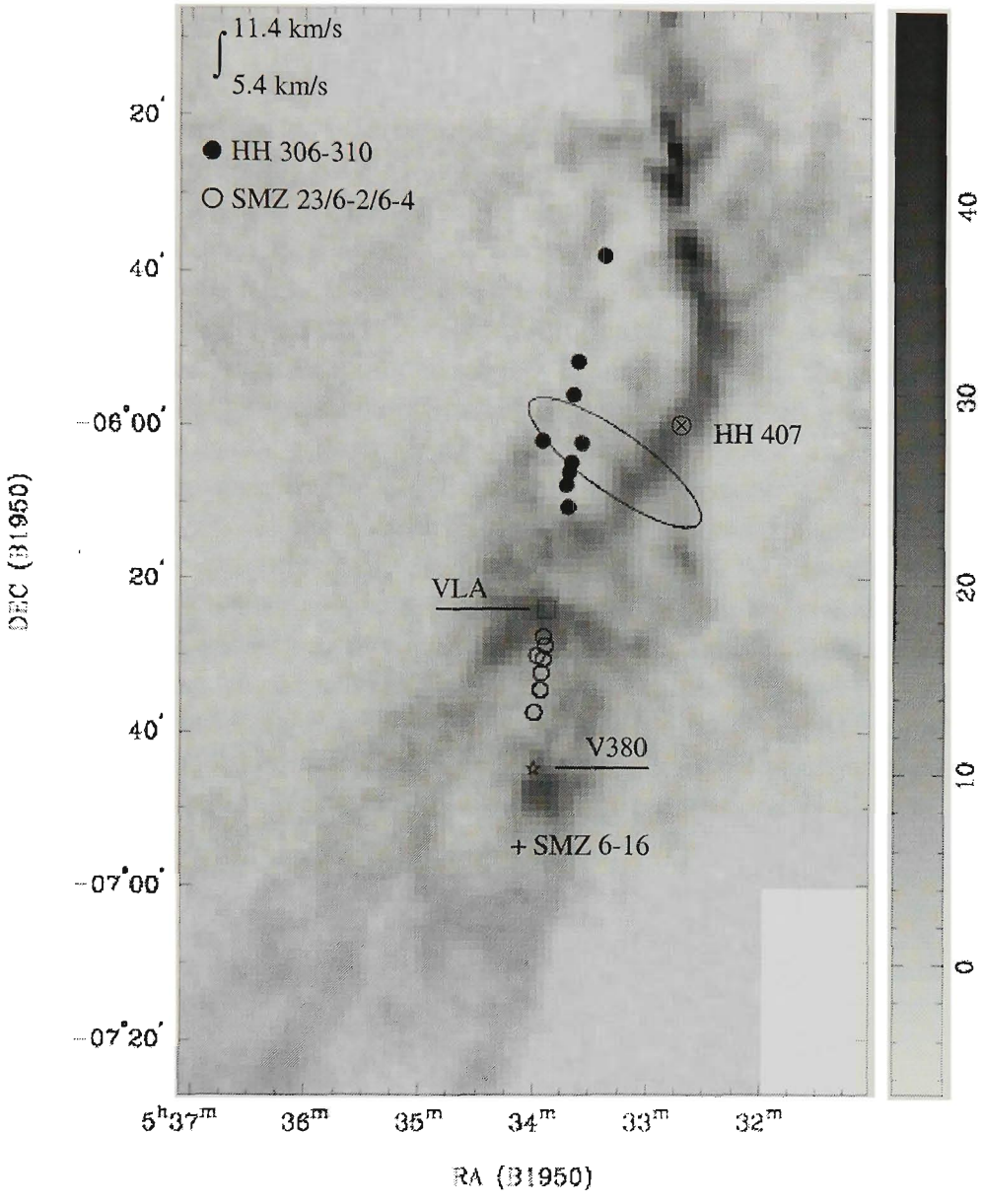

Figure 4.20: Integrated ^{13}CO map of the L1641 cloud from B87. The emission has been integrated from 5.4 km s^{-1} to 11.4 km s^{-1} with respect to the L1641-N cloud velocity (8.4 km s^{-1}). Filled and open circles represent the HH 306-310 and SMZ 23/6-2/6-4A-C flows respectively. The western wall of the southern cavity is traced by the SMZ 23/6-2/6-4A-C flow. A H_2 feature (SMZ 6-16; Stanke et al. 2000) may represent the embedded counterflow to HH 407 ($\otimes$). Both are proposed to be driven by V380 Ori ($\star$). Also shown is the position of the proposed driving source for HH 306-310 and SMZ 23/6-2/6-4A-C (the VLA source, shown by a box). The location of the Hα rim with respect to HH 306-310 and HH 407 is indicated by the ellipse. The $\int$-shaped filament (B87) is seen to the north and approximates the western wall of the "L1641-N chimney." The wedge shows intensity in units of K.km s^{-1}.

The southern L1641 region

In a search for optical counterparts to HH 306-310, our deep IIIaF plate of the southern region of L1641 identifies several features reminiscent of large bow shocks. The IIIaF image of these features in relation to L1641-N and HH 306-310 is shown in Figure 4.21, and a zoomed image of these features is shown in Figure 4.22. Object A appears as a diffuse feature and object B appears as a bright nebulosity with a long curve which extends 16′ to the north near object A. At first glance, object B and HH 61/62 (the counter-lobe to HH 303; RBD98) appear to outline the eastern and western wings of a large fragmented bow shock structure. Objects C and D appear as large arc-like structures which open to the north and are 3-4′ in extent. As C and D are located well away from the main cloud, our line-of-sight increases which may suggest they are not physically associated with L1641. We should also note that many of the terminal bow shocks associated with parsec-scale HH flows show substantial substructure which is lacking from the IIIaF image. In order to resolve the nature of features C and D, we obtained Hα and [SII] images, but due to variable cloud cover, we were not able to classify these objects as bona fide HH objects. Deeper images and/or spectra of objects A-D are required to determine if they are photo-ionized regions or HH objects.

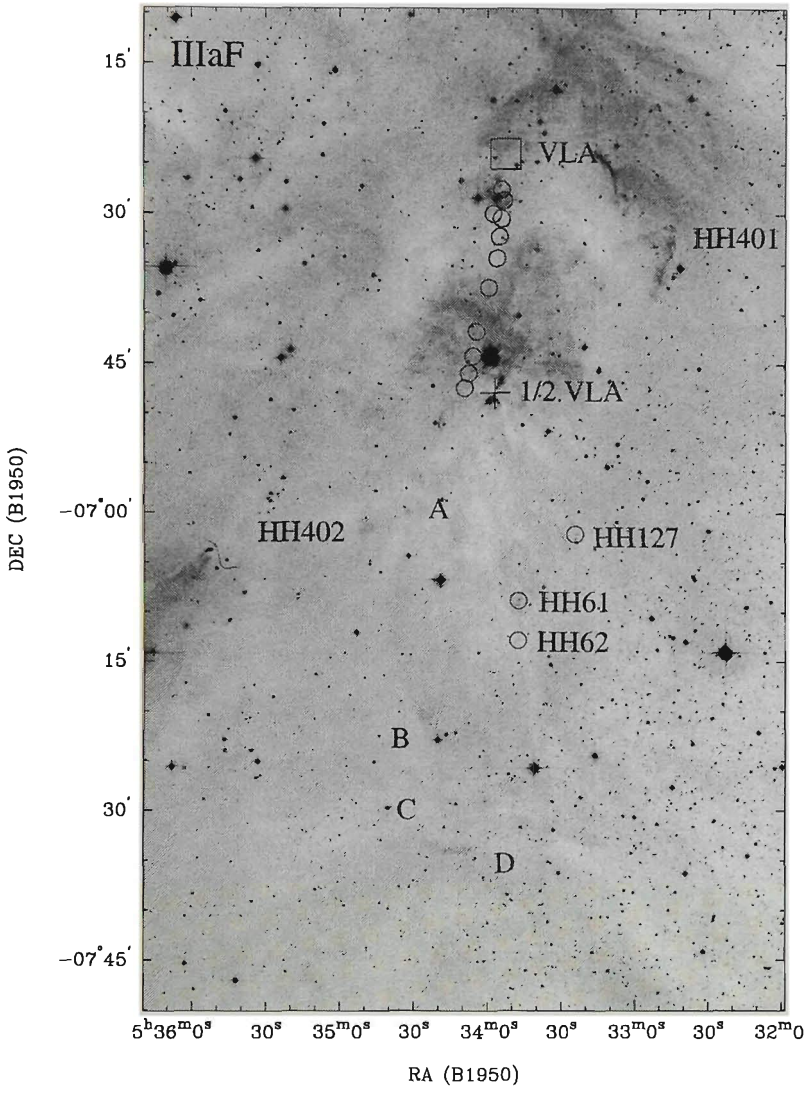

Figure 4.21: Scanned IIIaF image of features A, B, C and D to the far south of L1641-N. To the south-west the cloud boundary is clearly seen with respect to the background star field. These features are not visible on IIIaJ and IVN plates which suggests they are emission-line objects, possibly HH objects originating from the L1641-N region. The position of the VLA source is marked by a box for reference and comparison with Figure 4.6. The near-infrared counter-lobe to HH 306-310, SMZ 23/6-2/6-4A-C, is indicated by open circles. HH 61/62 are thought to be associated with HH 303, while HH 127 represents a possible counter-lobe HH 403/404 (RBD98). Also seen is the 5.9 pc flow HH 401/402 (Ogura 1995), which is driven by the deeply embedded source HH 1/2 VLA (marked as 1/2 VLA).

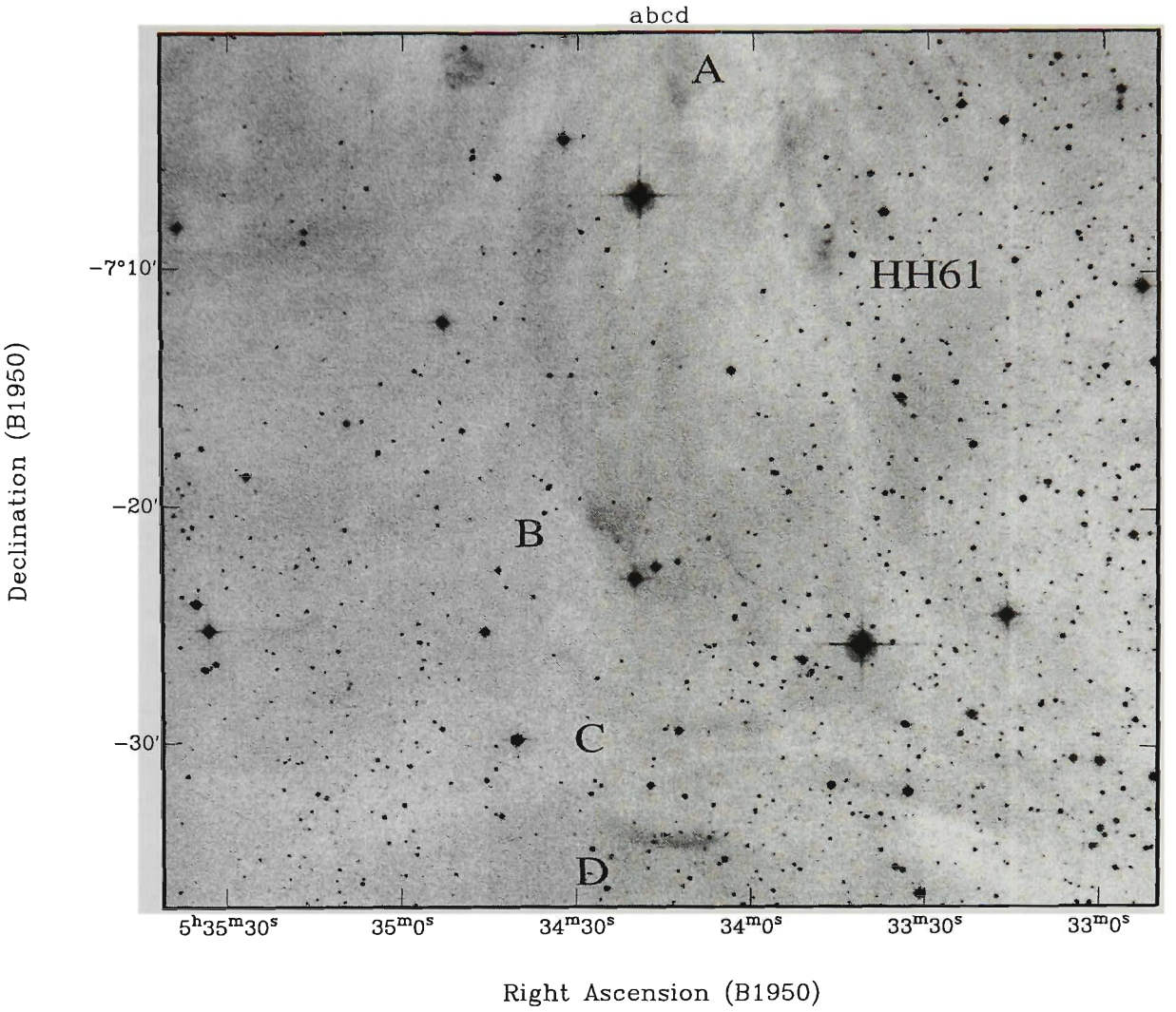

Figure 4.22: Zoomed IIIaF image of large-scale features, A-D. Also shown for reference is HH 61.

4.5.7 HH 403-406

To the north-east of Figure 4.6, a second string of objects extends away from the L1641-N cluster. HH 403 and HH 404 are located well clear of the eastern edge of the L1641 molecular cloud. Although seeing at the time of observing was $> 3''$, our Hα and [SII] CCD images (not shown) did allow us to classify these features as genuine HH objects. In Figure 4.24, the scanned Hα and IVN images show HH 403 consists of a large number of emission-line knots in addition to a curved (HH 403G) and amorphous feature (HH 403H) to the south-west. The CCD images of RBD98 clearly shows HH 403 as a highly fragmented object which is very similar in appearance to HH 262 (López et al. 1998). A further $9'$ to the north-east, HH 404 displays a sickle-like structure not too dissimilar from the HH 47 jet (Heathcote et al. 1996). As these features are Hα-bright, RBD98 raised the question as to whether or not HH 403/404 are bow shocks or bright rims. However, based on morphological grounds, they suggest HH 403/404 are highly fragmented bow shock structures which point back towards L1641-N where the presumed energy source lies. Our contrast-enhanced scanned Hα image of the region (Figure 4.24a) appears to confirm their suspicion as we see a lack of background Hα emission in the direction of HH 403/404 which has probably been removed by the action of the flow as it propagates away from L1641.

The scanned Hα image identifies several large-scale bow shocks with HH 403 and HH 404 at their apexes. RBD98 do not detect these features on their CCD images. Originally thought to be bright rims, comparison of the Hα emission with the ^{13}CO data of B87, indicates these "rims" do not outline the L1641 molecular cloud, or any other well-defined ^{13}CO ridge. The first bow shock is defined by the arc-like object HH 403G and HH 404H representing the eastern and western wings respectively. The eastern wing trails $7'$ to the south before it blends into the background Hα emission. The second bow shock appears as an extended feature similar in appearance to HH 403G. The third bow shock only displays the western wing which extends northward from the second bow to the apex of HH 404, which shows a bright arc with faint Hα emission which combine to form an inverted U-type structure.

North-east of HH 404, a faint object HH 405 displays Hα emission extending along PA = 45°. RBD98 suggest the emission is reminiscent of a jet. A further $6'$ to the north-east, HH 406 is a large diffuse object. Are HH 405 and HH 406 related to HH 403/404? The IVN image (Figure 4.24b) shows a reddened source (denoted HH 405IRS) at the position of HH 405. A reflection nebulosity is also seen nearby. The position of the nearest IRAS source, 05347-0545, is shown in our IVN image. It is a 60 and 100μm source only, indicating it is heavily obscured and may be related to HH 405 and/or

HH 406. Overlaid on the IIIaF image of HH 405, the HIRES images (processed to 300 iterations) in Figure 4.23 show a point source at 25, 60 and 100μm only. However, it is uncertain as to whether th emission is entirely from HH 405IRS, or if there is a contribution from the nearby star V992 Ori. The emission peak in the 60 and 100μm images does shift toward V992 Ori. Although there is no point source of such at the position of HH 405IRS, the 25μm image, shows two peaks either side of the source with a bridge of emission parallel to the HH 405IRS jet.

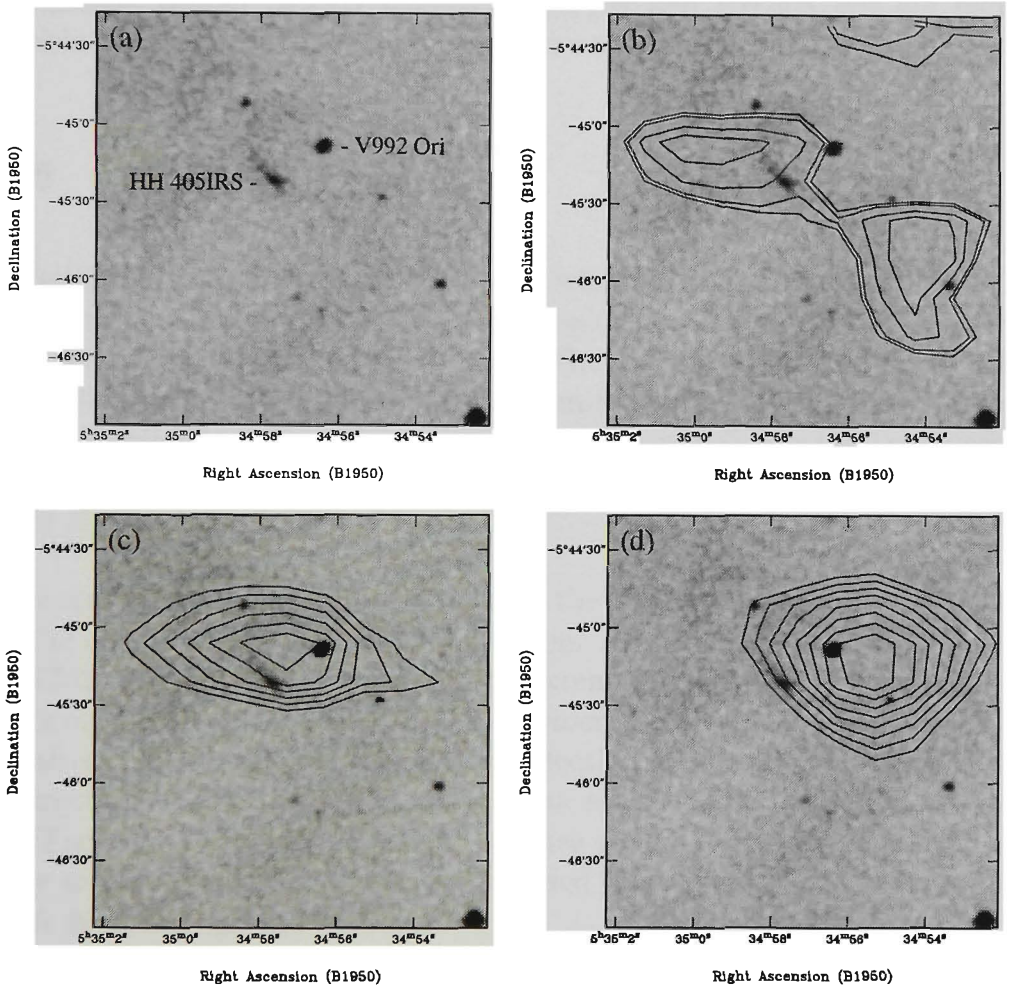

Figure 4.23: HIRES images of HH 405IRS. (a) IIIaF image of HH 405 and V992 Ori. (b) 25μm HIRES contours at 1.2, 1.4, 2 and 2.5 MJy sr^{-1}. (c) 60μm HIRES contours at 8 to 13 MJy sr^{-1} in steps of 1 MJy sr^{-1}. (d) 100μm HIRES contours at 15 to 22 MJy sr^{-1} in steps of 1 MJy sr^{-1}.

Based on the location of HH 405IRS with respect to HH 405/406 and the reflection nebulosity, we suggest this source is the driving agent for HH 405 and HH 406 thereby making the flow length 0.78 pc in extent. Near-infrared

polarimetry and imaging will be useful for determining if HH 405IRS or IRAS 05347-0545 is the illuminator of the reflection emission.

Located to the far south-west of L1641-N, RBD98 noted HH 127 mirrors the position of HH 404 with L1641-N positioned at the centre (see Figure 4.21). Although HH 127 lies at an angle of 10° from the HH 403/404 and L1641-N axis, they suggest HH 403/404 and HH 127 represent the blue and red-shifted lobes respectively of a 10.6 parsec-scale flow centred on the VLA source. Given the clustered nature of potential outflow sources about the VLA source, proper motion studies of HH 127 and HH 403/404 are highly desirable to constrain the location of their energy source(s).

4.5.8 HH 407

Located 28.'3 north-west of L1641-N and within close proximity to HH 306-310, Figures 4.6 and 4.16 identify a large, highly fragmented structure located in the direction of several bright stars. The Hα+[SII] image (Figure 4.25) confirms it as a bona fide HH object as it emits predominately in [SII]. Knots A and B display bow shock structures with a streamer (knots C/D) extending to the south-east. In Figures 4.6 and 4.16, fainter Hα emission extends a further 6′ to the south-east of knots C/D.

As the streamers of HH 407 point towards the L1641-N region, it seems probable the energy source lies in that direction. An examination of the H_2 data of SMZ98 does not reveal any emission extended towards HH 407. After re-examining our Hα plate, we noticed the presence of a large loop-like structure (hereafter loop A) extending out of the reflection nebulosity NGC 1999 and in the direction of HH 407. Comparison of our scanned Hα, IIIaF and IVN images (Figure 4.26) indicates loop A is a pure emission-line feature. Although faintly seen on the IIIaF image, the scanned Hα image clearly distinguishes loop A from background emission.

In a recent study of the NGC 1999 region, Corcoran & Ray (1995; hereafter CR95) discovered a second loop (hereafter loop B) of Hα emission extending west of the NGC 1999 which delineates a poorly collimated outflow associated with HH 35 and represents the counterflow to the red-shifted molecular CO outflow discovered by Levreault (1988a,b; see Figure 4.26). CR95 suggest the Herbig Ae/Be star V380 Ori (which illuminates NGC 1999) drives HH 35, loop B and the molecular outflow. The presence of loops A and B suggests the presence of a quadrupole outflow in NGC 1999. Using similar arguments as CR95, we suggest loop A delineates an optical outflow which, in conjunction with HH 407, represents a 6.2 pc lobe at PA = -23° with respect to V380 Ori.

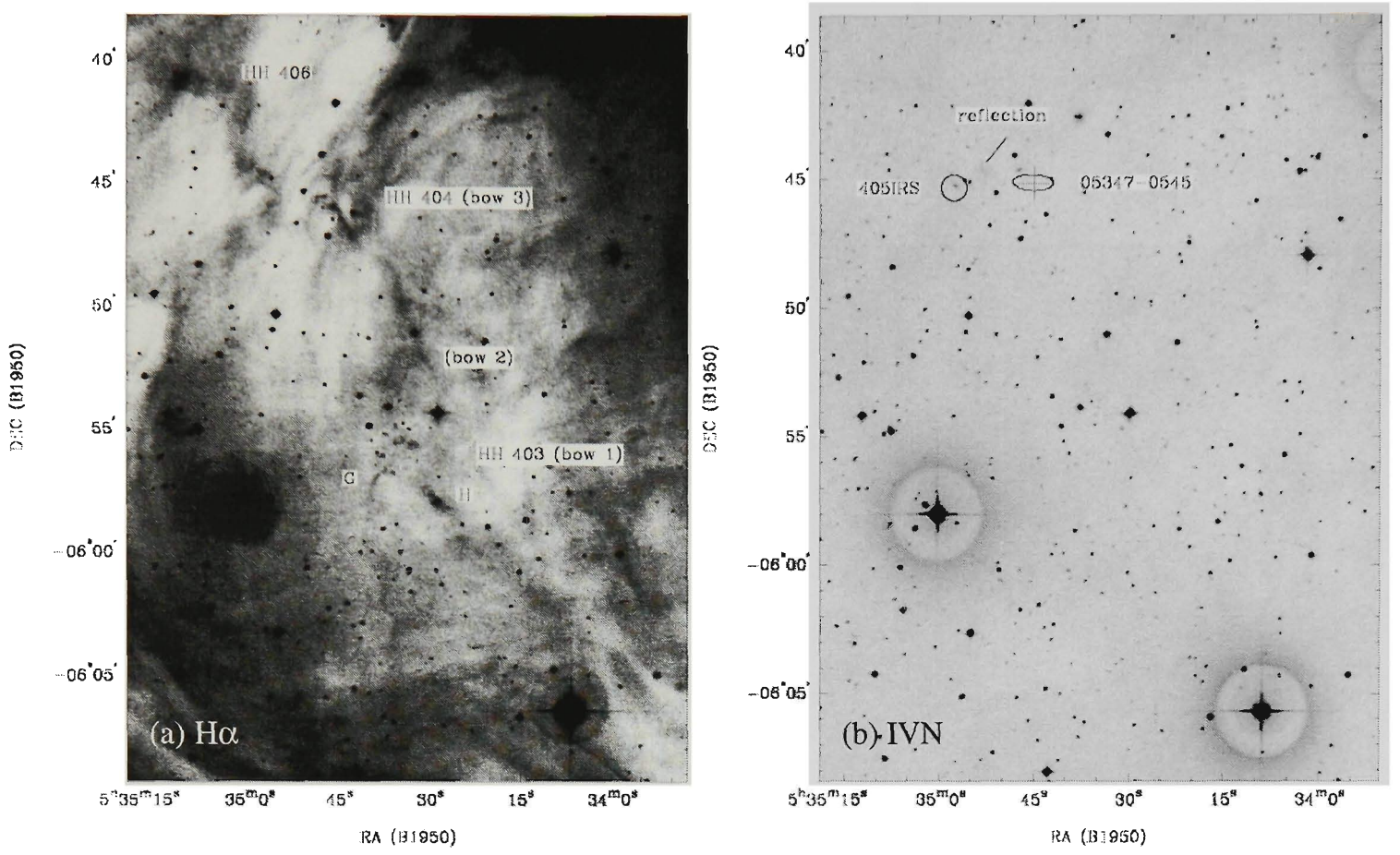

Figure 4.24: Scanned (a) Hα and (b) IVN images of the HH 403/404 and HH 405/406 complexes identified in Figure 4.6. The Hα image has been enhanced so as to show the HH 403/404 outflow has cleared away a significant portion of dust in the region as it propagates away from the L1641-N region. HH 403/404 are located at the apexes of two large bow shocks (bow 1 and bow respectively). The IVN image identifies a reddened source with associated reflection nebulosity at the position of HH 405, which is the proposed energy source for HH 405/406. The nearby IRAS source 05347-0545 (labelled 05347) may be related to HH 405/406 and/or the reflection nebulosity between it and HH 405IRS. The major and minor axes of the IRAS error ellipse have been multiplied by two for clarity.

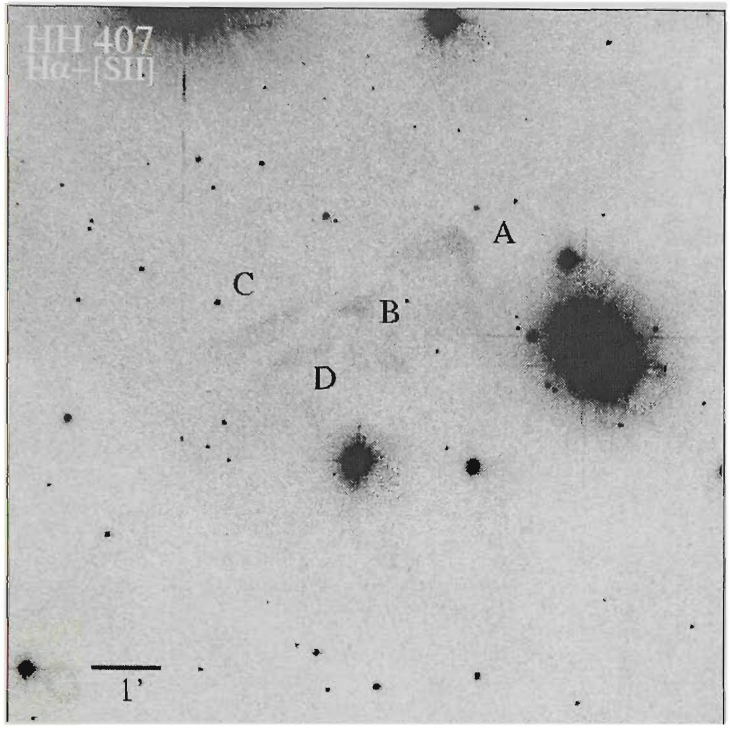

Figure 4.25: Hα+[SII] image of the fragmented bow shock HH 407 identified in Figures 4.6 and 4.16. Knots A and B display arcuate morphologies. Objects C and D are part of a streamer which trails several arc-minutes to the south-east.

In a search for optical counterparts to HH 407, our deep IIIaF plates do not reveal any clear candidates, although if we assume loop A and HH 407 are propagating out and away from L1641, the southern counterflow may not yet have emerged from the far side of the molecular cloud. Stanke et al. (2000) have identified a large H_2 feature (SMZ 6-16) to the south of NGC 1999 which may represent an embedded counterflow to loop A and HH 407 (see Figure 4.20). HH 130 is a large bow shock structure located 8.'5 south-east of NGC 1999 and has been linked to HH 1/2 (Ogura & Walsh 1992) and V380 Ori (Reipurth 1999). CR95 suggest the energy source of HH 130 is located to the north-east of knot H (see Figure 4.26). If HH 130 and/or SMZ 6-16 represents the counterflow to loop A and HH 407, the outflow axis would be bent by up to 10°. A similar situation is seen in HH 127/403/404 (RBD98), HH 110/270 (Reipurth, Raga & Heathcote 1996) and HH 135/136 (Ogura et al. 1998). Under the assumption that V380 Ori drives both HH 407 and SMZ 6-16, the total flow length is projected at 8 pc. Proper motion and spectroscopic studies of HH 130, HH 407 and SMZ 6-16 are needed to determine if their motion and radial velocities are directed away from the V380 Ori region.

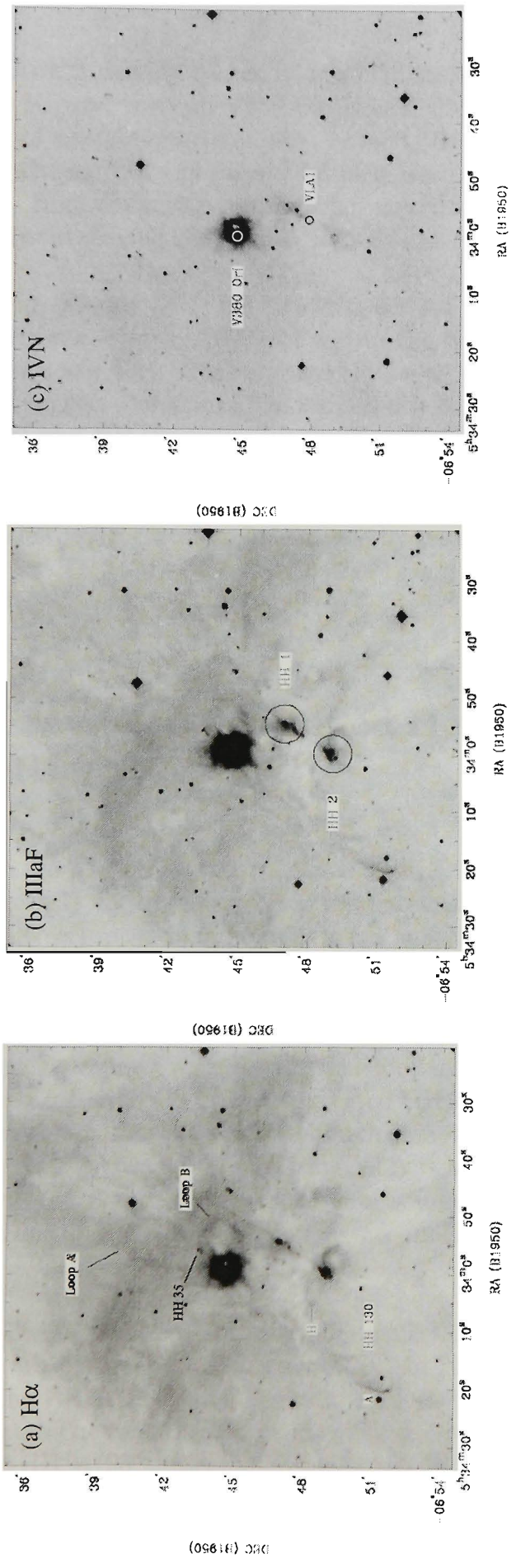

Figure 4.26: Scanned (a) Hα, (b) IIIaF and (c) IVN images of the NGC 1999 region. The Hα image clearly identifies two loops of emission extending out of NGC 1999. HH 35 is associated with loop B. HH 130 is a large arcuate object which extends from the bright bow shock HH 130A to HH 130H. The IVN image indicates the positions of V380 Ori and VLA1, which are the illuminating and driving sources of NGC 1999 and HH 1/2 respectively.

Is V380 Ori the driving source of loop A? In addition to V380 Ori, CR95 found two K band sources, V380 Ori-B and V380 Ori-C, within NGC 1999. By means of speckle-interferometry, Leinert, Richichi & Hass (1997) identified V380 Ori as a binary consisting of a Herbig Ae/Be (V380 Ori) and T Tauri star. High resolution mm-interferometry of NGC 1999 will help clarify which source is driving the optical emission associated with loop A.

As shown in Figure 4.20, HH 306-310, HH 407 and the $\int$-shaped filament (B87; Johnstone & Bally 1999) lie within the rim of Hα emission identified in Figures 4.6 and 4.16. Approximated by an ellipse $13'.6 \times 4'$ (3.6×0.54 pc) in size, we suggest the ellipse has formed due to the combined action of the HH 306-310 and HH 407 flows expelling molecular gas from the main cloud core. The UV radiation from the nearby bright stars excites the outer edge of the expanding molecular material which we see as the Hα ellipse. Such a large-scale movement of molecular gas by parsec-scale HH flows has been suggested for HH 34 (Bally & Devine 1994) and HH 306-310/SMZ 23/6-2/6-4A-C (RBD98; this work).

4.6 Previously-identified Herbig-Haro Flows: HH 94/95

Located in the southern outskirts of L1630, HH 94/95 were first identified by Reipurth (1985) during a search for red nebulosities on deep ESO R plates. Both display complex morphologies such that Reipurth (1989b) originally suggested HH 94 is a bent jet with HH 94D 65 km s^{-1} red-shifted relative to the beginning of the jet. $8'$ to the south-east of HH 94, HH 95 consists of several knots which give the object a chaotic appearance, with HH 95B displaying a bow shock morphology which opens to the north-west and it is for this reason Reipurth (1989b) suggested HH 94/95 may be related. IRAS and near-infrared observations of Reipurth (1989b) failed to detect a plausible energy source for either object. Using VLA 6cm observations, Curiel et al. (1989) detected a faint radio continuum source at the geometrical centre of the HH objects and suggested it as a candidate energy source for both objects.

Given the distance of HH 94/95 from the main L1630 cloud core, it is possible HH 94/95 are part of a much larger flow. In Figure 4.27, the scanned Hα image of the HH 94/95 region shows a large shell-like structure surrounding both objects. The shell displays a morphology similar to the Rosette Nebula with both HH 94/95 projected towards the inner, less ionized region. A comparison is drawn between HH 306-310 (section 4.5.6) and HH 407 (section

4.5.8), which have hollowed out a major part of the L1641 molecular cloud. For HH 94/95, a similar situation is evident, except that the outflow is moving away from the L1630 cloud and the stellar wind has created the Hα shell as it punches out of the low-level ionized gas, which we see as the optical Hα shell. Given that both HH 94/95 lie at the inner edges of this shell, is seems plausible the wind is interacting with low-level molecular gas (< 1-2 K.km s^{-1}; see Figure 4.30) to produce the observed HH emission.

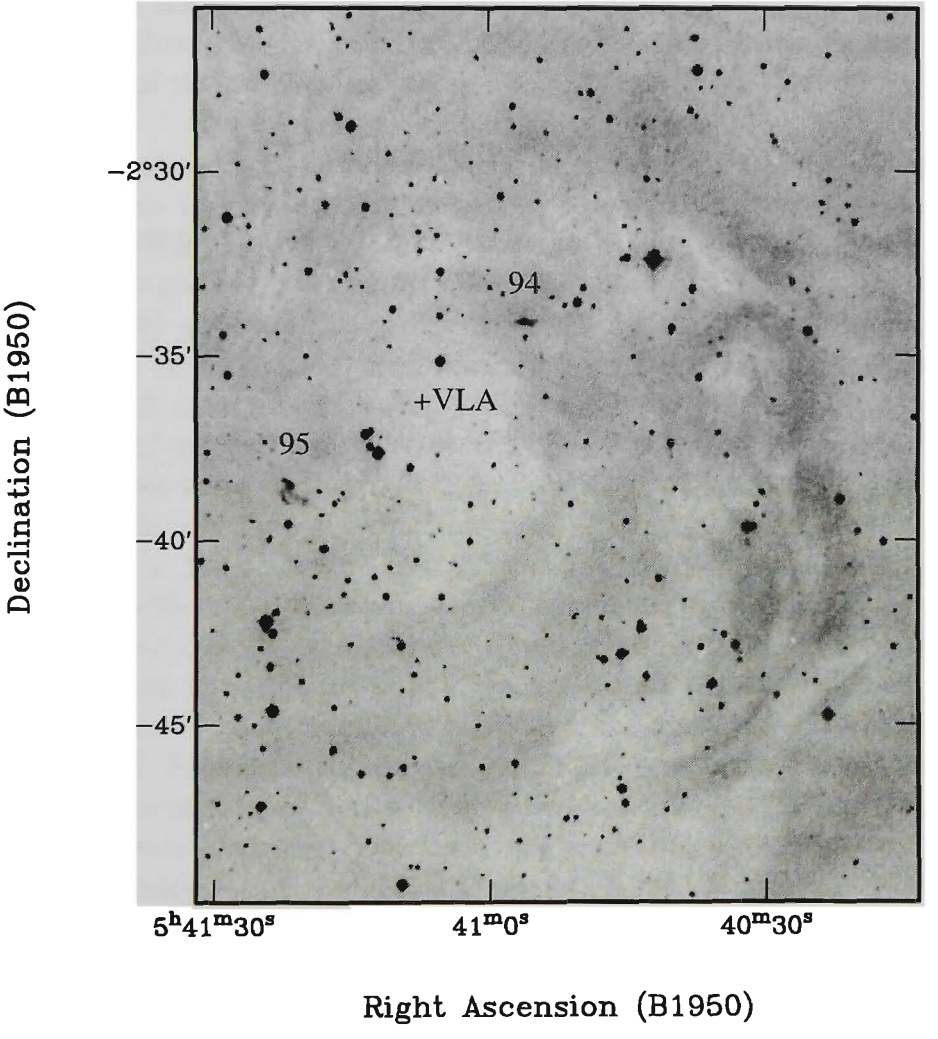

Figure 4.27: Scanned Hα image of HH 94/95. Both objects lie within the inner part of a shell-like feature, possibly an indication that both HH objects are part of a parsec-scale flow that is clearing dust in the region. The position of the VLA source detected by Curiel et al. (1989) is shown. See text for discussion.

If HH 94/95 are truly part of a giant HH flow, how can we account for the differences in velocities seen in individual knots? As mentioned briefly above, Reipurth (1989b) found knots HH 94 A-C have a blue-shifted velocity $\sim$ -34 km s^{-1}, but at knot D, the velocity abruptly changes to +30 km s^{-1}. For HH 95, knots A and C have blue-shifted velocities of -31 and -16 km s^{-1} respectively. Knots within highly fragmented bow shocks can display large variations in proper motions and position angles, particularly as seen in the rest frame of the bow shock (i.e., López et al. 1998). This leads to a chaotic appearance which has been seen in HH 403 (section 4.5.7). For the present case, we suggest HH 94/95 represent chaotic, terminal working surfaces of a parsec-scale outflow which, like HH 403-406 (section 4.5.7), is clearing away a large portion of the surrounding diffuse ionized medium.

The final piece of the puzzle for HH 94/95 is to identify a plausible energy source. Previous to this investigation, the 6cm VLA source detected by Curiel et al. (1989; see Figure 4.27) was the best candidate since it was positioned at the geometrical centre of the HH pair. Dent, Matthew & Ward-Thompson (1998) placed an upper limit of 0.022 Jy at 1100μm. With the identification of the large Hα shell surrounding the HH objects, it seems unlikely the VLA source can be responsible for it. Drawing a line through both objects and projecting back towards the L1630 molecular cloud, we see the line passes through the HII region NGC 2023. Like L1641-N (section 4.5.1), NGC 2023 contains an embedded cluster of $\sim$ 20 members (Sellgren 1983; Depoy et al. 1990; Lada et al. 1991) and HH objects (Malin, Ogura & Walsh 1987). With 1300μm observations, Launhardt et al. (1996) detected no dust condensations in the region which suggests the NGC 2023 cluster is more evolved than L1641-N. Although the driving source for HH 94/95 may still lie within the NGC 2023 cluster, a recent ^{12}CO survey of the Horsehead Nebula and NGC 2023 region by Sandell et al. (1999) identified an extremely high-velocity bipolar CO outflow with spatial extent $\sim$ 190″ (0.43 pc for D = 470 pc). Using sub-millimetre observations, they found the outflow is driven by a low luminosity ($\leq$ 10 $L_{\odot}$) Class 0 object, NGC 2023 mms1 (hereafter mms1). This object is embedded in a CS (J=1-0) core detected by Lada, Bally & Stark (1991; LBS 36) and corresponds to the 1300μm source LBS 36 SM1 detected by Launhardt et al. (1996).

As discussed by Sandell et al., the outflow from mms1 appears to be precessing. Figures 4.28a and b show the CO hot-spots, or bow shocks identified by Sandell et al. which clearly show four distinct but related lobes. The bow shocks be and rw represent blue and red-shifted bow shocks orientated at PA $\sim$ 120° with respect to mms1. The other blue and red-shifted lobes are defined by a series of bow shocks labelled b1-b4 and r1-r4 respectively and are in PA $\sim$ 145° with respect to mms1. As be and rw are closer to mms1, they may represent younger bow shocks compared to the working surfaces

of the main jet (r4/b4 in Figure 4.28). Given the compactness of the CO emission at be and rw, using AAO/UKST Hα and CO (J=3$\rightarrow$2)[40] data, we searched the region for evidence of shock excited HH emission. As shown in Figure 4.28c, we identified a bright Hα knot which corresponds to the be bow shock. The correspondence between Hα and CO emission suggests this knot is a high excitation HH object which has resulted from the outflow interacting with the surrounding medium. This interaction also suggests the current outflow orientation is in PA $\sim$ 120°, which is the PA of be/rw with respect to mms1.

Assuming the axis defined by the knot of Hα emission and the mms1 source represents the current PA of the outflow, Figure 4.29 shows both HH 94/95 also lie along this axis and may have originated from mms1. If we assume the PAs of the blue and red-shifted lobes b1-b4/be and r1-r4/rw define the opening angle of the outflow, we see that to the north-west, HH 66 also lies within this opening angle. To date, this object has not had its energy source identified. The [SII] image of RG88 (their Figure 13a), shows HH 66A displays a bow shock structure which opens towards mms1 and may be related. The distances of HH 94 and HH 95 from mms1 are $\sim$ 33.62′ and 41.32′ respectively which, at a distance of 470 pc to L1630, corresponds to distances of 4.62 pc and 5.67 pc in projection. Using a value of 90 km s^{-1} for the terminal velocity of the blue-shifted CO lobe, Sandell et al. estimate a dynamical age of $\sim$ 2500 yr, but if HH 94/95 are associated with the outflow, this extends out to 6 $\times$ 10^4 yr which agrees with typical ages of Class 0 objects ($\sim$ 10^4 yr) and provides further support for an association between HH 94/95 and mms1. Figure 4.30 shows ^{13}CO data (Bally et al. 1987; 1991) of the NGC 2023, HH 66 and HH 94/95 region. HH 66 and HH 94/95 are clearly located in regions with little or no emission ($<$ 1 K.km s^{-1}), a characteristic of HH objects associated with giant HH flows. It is interesting to note that the distribution of ^{13}CO gas in the vicinity of HH 94/95 almost surrounds the large Hα shell.

Based on the above evidence, we suggest mms1 as the energy source for HH 94/95. The CO outflow represents the inner jet which drives a parsec-scale HH flow (HH 94/95) which is moving through and clears away gas from the outer regions of L1630. This disruption is seen as the large Hα shell surrounding the HH objects and is also seen in HH 306/310 (section 4.5.1) and HH 403-406 (section 4.5.7). Proper motion studies of HH 66 will determine if it is moving away from mms1.

[40]Kindly provided by Goeran Sandell, NRAO.

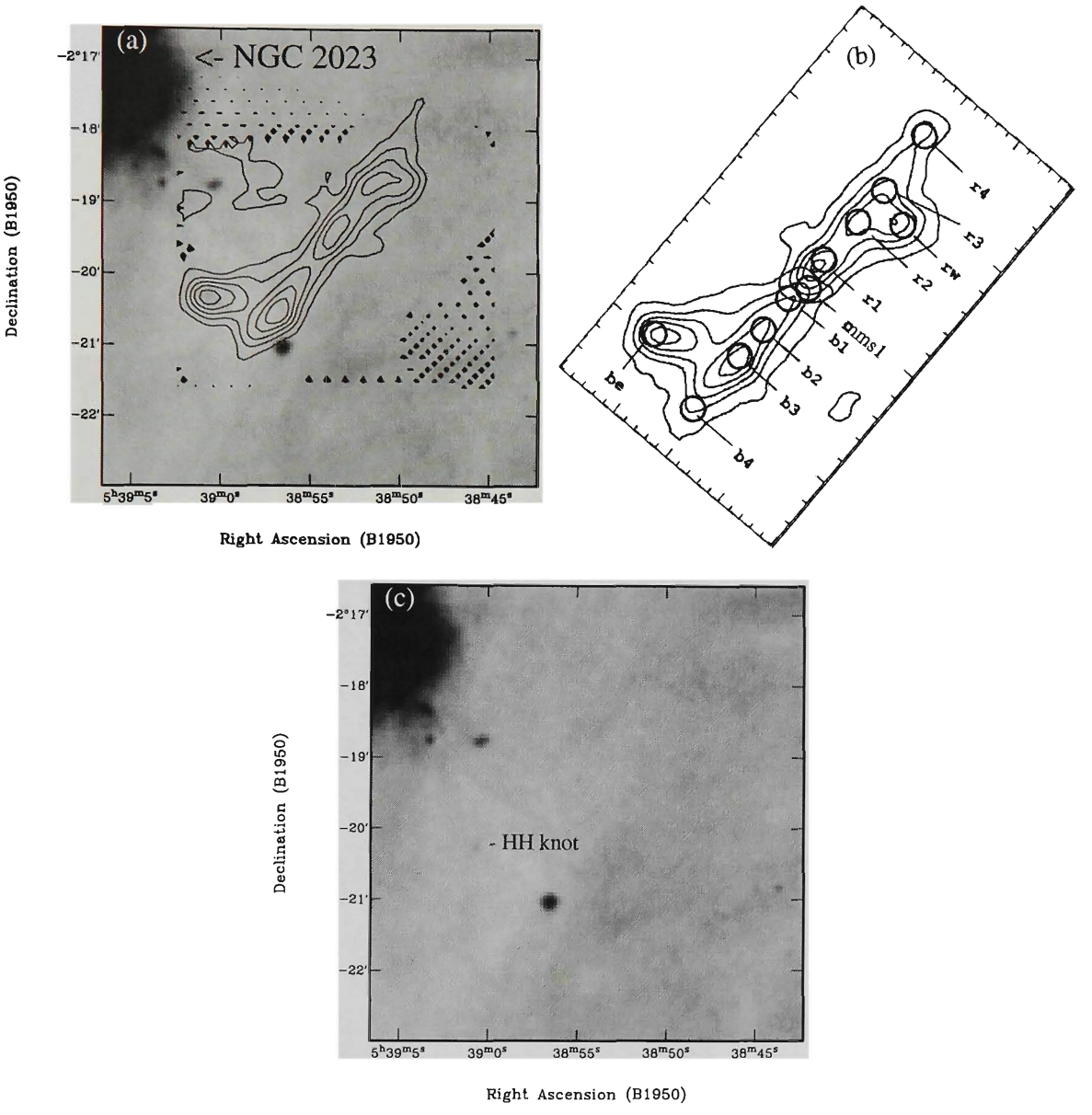

Figure 4.28: The NGC 2023 mms1 outflow. (a) CO ($J = 3 \rightarrow 2$) emission overlaid on the Hα image from the Orion plate. Contours are 120 to 200 K.km/s in steps of 20 K.km/s. (b) Nomenclature of the CO outflow. The blue-shifted (b1-b4) and red-shifted (r1-r4) positions are associated with the main jet, while the off-axis bow shocks be and rw are a result of precession in the jet from the embedded source (mms1). Each subdivision in (b) corresponds to 10″ (taken from Sandell et al. 1999). (c) Hα image of the region showing the location of a high-excitation HH object which corresponds to the be bow shock.

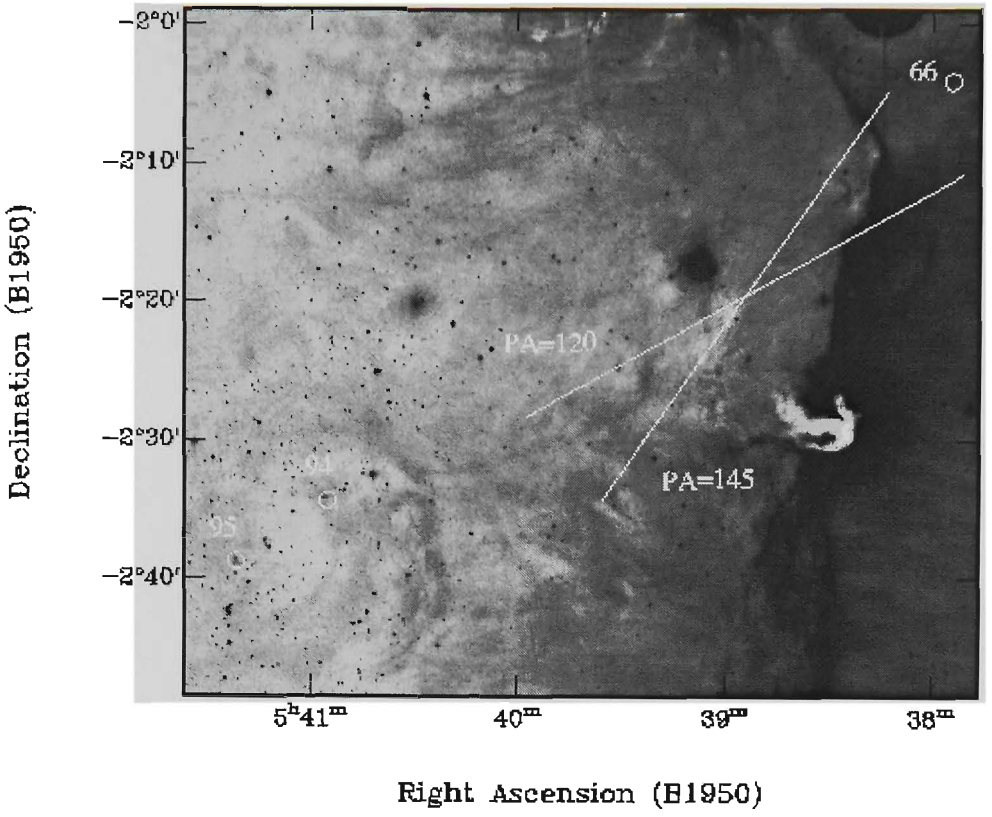

Figure 4.29: Hα image showing the positional relationship between HH 94/95, the outlying shell and mms1. The lines define the PA of CO lobes b1-b4/r1-r4 (PA = 145°) and be/rw (PA $\sim$ 120°) with respect to the outflow source mms1, which is located where the lines intersect. Both HH 94/95 lie along the 120° line while another object, HH 66, lies within the opening angle of the outflow defined by both lines. See text.

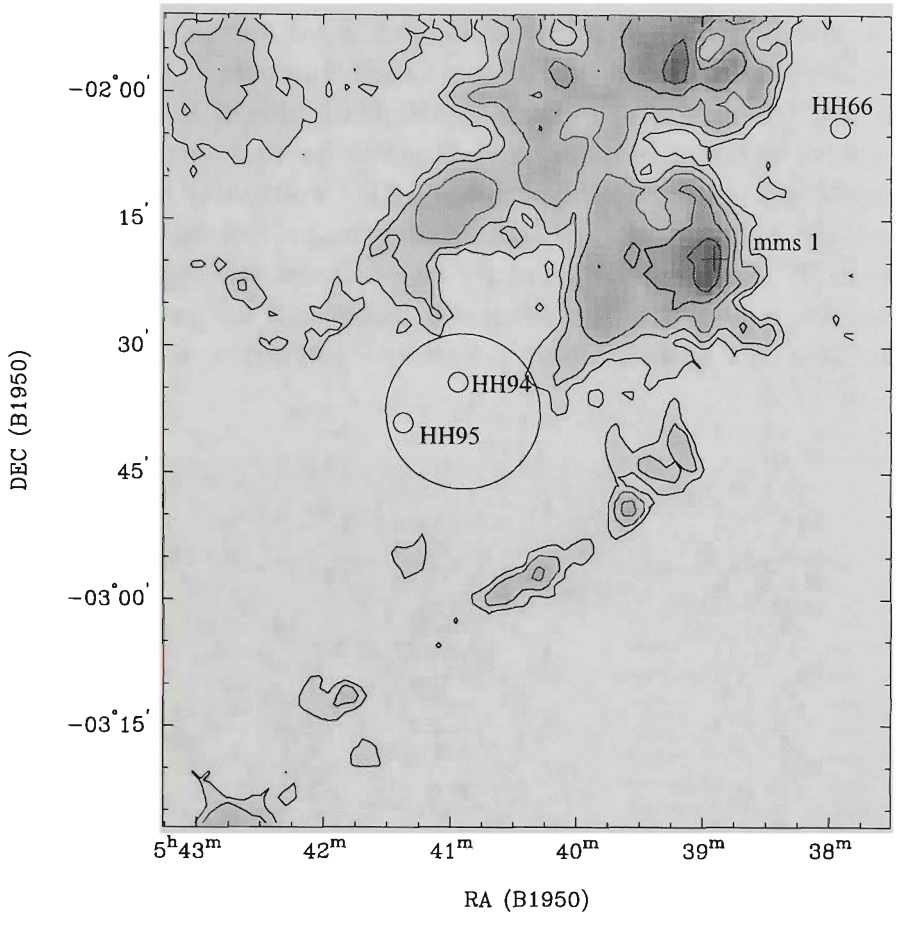

Figure 4.30: Integrated ^{13}CO map of the NGC 2023 and HH 94/95 region. The emission has been integrated from 8.1 km s^{-1} to 10.27 km s^{-1} with respect to the CS core LBS 36 ($\sim$ 9.1 km s^{-1}) which harbours the Class 0 protostar NGC 2023 mms1 (indicated by the cross). The positions of HH 66 and HH 94/95 are indicated. The large circle represents the position of the large Hα shell seen in Figure 4.27. Contour intervals are 1, 2, 4, 8 and 16 K.km s^{-1}.

4.7 Thoughts on Giant Herbig-Haro Flows

4.7.1 Outflow Models

It has long been a question of how fast, highly collimated optical jets can drive the less collimated and slower CO molecular outflows. In the two-wind models (Pudritz 1986), the optical HH and CO outflows are thought to be driven by two different kinds of wind which originate from the same source: the optical HH flow is driven by a collimated stellar wind, while

the CO outflow is driven by a less collimated wind being driven from the accretion disk which surrounds the young stellar object. In the case of unified models (Masson & Chernin 1993; Raga et al. 1993), the highly collimated HH jet drives an envelope of slower, less collimated material which is seen as the molecular CO outflow. The scenario is summarised in Figure 4.31, where we see the jet has numerous internal working surfaces (HH objects) which intercept material from the jet and eject it sideways. This sideways "splashing" leads to the formation of a turbulent envelope which surrounds the jet beam. The turbulent envelope is identified as the molecular CO outflow.

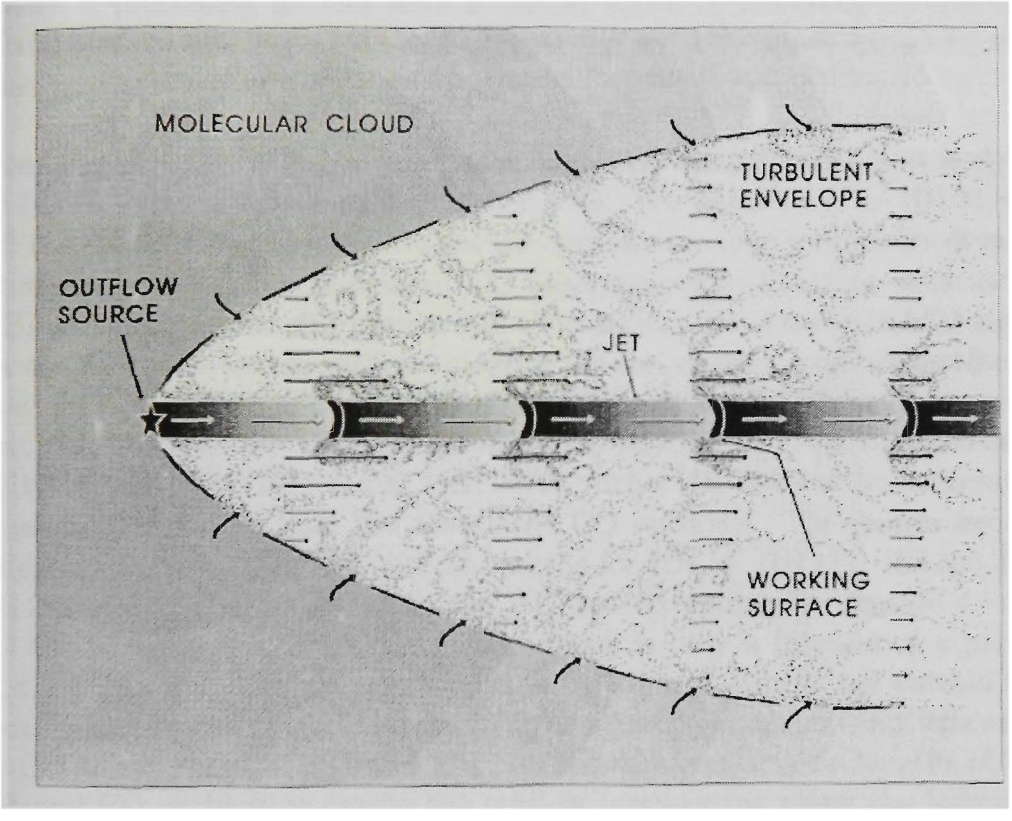

Figure 4.31: A unified jet/molecular outflow model. The outflow source ejects a jet with a number of internal working surfaces (HH objects) which intercept material from the jet and eject it sideways. This sideways ejection leads to the formation of a turbulent envelope which is equated with the molecular CO outflow. This model accounts for outflow complexes such as HH 289, HH 306-310/SMZ 23/6-2/6-4A-C and HH 444. From Raga et al. (1993).

A case for unified models is supplied by HH 289 and HH 306-310/SMZ 23/6-2/6-4A-C. For these complexes, the outflow source is driving a highly collimated H_2 and/or optical jet, has multiple working surfaces (HH objects) and drives a poorly collimated molecular CO outflow. Although no molecular CO outflow has yet been identified, the HH 444 complex also displays

similar features predicted by unified models. The large sweeping bow shocks in these complexes become progressively larger with increasing distance from the source. At the apex of each is a bright HH knot which represents the working surface where the incoming jet material is splashed sideways and distributed into the turbulent envelope. As the bow shocks increase in size, CO bearing gas can become entrained in the wake of the bow shock (Raga & Cabrit 1993). A direct result of this is that as the bow shocks broaden, so does the molecular CO outflow. However, the increase in size of bow shocks with increasing distance from the source is not the only factor which can create a broad molecular CO outflow. In the jet model of Masson & Chernin (1993), a precessing jet can have a similar effect by sweeping up different portions of the ambient cloud and carving out a cavity which broadens with time.

From Figure 4.31, it is expected that both the optical (HH) and molecular (CO) emission traces similar dimensions. For cases such as HH 34 and HH 111, RBD98 discuss how the optical outflows are nearly an order of magnitude larger than the associated CO outflows, while for cases such as B5 IRS1 and HH 243/244, the optical and CO outflows are of comparable length. For the new parsec-scale outflows identified in this chapter, combining the optical data presented here with CO observations from the literature suggests that the VLA source (HH 306-310/SMZ 23/6-2/6-4A-C), IRAS 05355-0416 (HH 289) and NGC 2023 mms1 (HH 94/95) drive HH flows at least an order of magnitude longer than the associated CO outflows. The reason for the difference between HH/CO outflow lengths for HH 34, HH 111, HH 306-310, HH 289 and HH 94/95 is due to the HH flow extending far beyond ($>>$ 1 pc) the parental molecular cloud core, which is only a fraction of a parsec ($<<$ 1 pc) in size. Beyond the cloud core, HH bow shocks do not entrain CO bearing gas, but more likely atomic and/or ionized gas which is not traceable by CO lines. For B5 IRS1 and HH 243/244, the comparable lengths of the HH and CO outflows is due to the outflow propagating along the long axis of the molecular cloud.

4.7.2 Effect on Molecular Clouds

Assuming the ^{13}CO cavities represent expanding bubbles, the energy needed to create the SMZ 23/6-2/6-4A-C and HH 306-310 bubbles is $\sim 2.3 \times 10^{47}$ ergs and $\sim 8.7 \times 10^{47}$ ergs respectively. In addition, the estimated amount of gas removed by SMZ 23/6-2/6-4A-C and HH 306-310 adds up to ~ 250 $M_{\odot}$, which is $\sim 0.5\%$ of the total mass of the L1641 molecular cloud ($\sim 5 \times 10^4$ $M_{\odot}$; B87). Although the HH 306-310/SMZ 23/6-2/6-4A-C outflow is a dominant feature in the L1641 GMC, what effect (if any) do other known giant

flows in L1641 have? Figure 4.32 shows ^{13}CO maps of regions surrounding known giant HH flows in L1641. For each, the emission has been integrated $\sim \pm$1-2 km s^{-1} with respect to the parental cloud core which harbours the driving protostar. Assuming that the ^{13}CO emission within such an interval reflects motions due to outflow, what is apparent from these maps is that the majority of giant flows display terminal bow shocks projected against large-scale cavities.

If giant outflows are important in the evolution of the L1641 GMC, for a ^{13}CO mass $\sim 5 \times 10^4$ $M_\odot$ (B87) and assuming a core line width $v_{turb} \sim$ 1.5 km s^{-1}, the total turbulent kinetic energy ($M_{cloud}v_{turb}^2/2$) for L1641 is 1.1×10^{48} erg. Wilking, Blackwell & Mundy (1990) found the kinetic energy of the L1641–N CO outflow to be 1.1×10^{46} erg. Assuming L1641–N and HH 306-310/SMZ 23/6-2/6-4A-C are driven by the same source, and if L1641–N represents the typical (giant) outflow power in L1641, we require $\sim$ 100 giant protostellar outflows to yield the turbulent kinetic energy of L1641. If we turn to momentum considerations, the approximate number of flows like L1641–N required to stir up the L1641 GMC can be estimated by dividing the radial component of the L1641 momentum by that of the momentum of the L1641–N outflow. For the former, we calculate the momentum within the turbulent line core ($M_{cloud}\Delta v_{turb}$) = 7.5×10^4 $M_\odot$ km s^{-1}. For L1641–N, Wilking et al. (1990) found the outflow has a momentum $\sim$ 50 $M_\odot$ km s^{-1}which implies $\sim$ 1500 L1641–N–like flows are required to drive turbulent motions in L1641.

For both energetic and momentum cases, the estimated number of giant flows can be reduced since Wilking et al. (1990) do not account for flow inclination which may underestimate momentum and energy calculations. Other areas of underestimation include possible mass contributions from low–velocity gas in the line core[41]. Another point to consider is shown in Figure 4.32. For known giant flows in L1641, the terminal bow shocks are located well away from the confines of the GMC. In these cases, the bow shocks are propagating into the intracloud medium and since they are no longer sweeping up ambient cloud material, it becomes difficult to trace energy and momentum. In addition, as these flows are still gaining momentum from the driving protostellar source, estimates of mass and momentum for a typical L1641 giant flow such as L1641–N should be considered as lower limits. Finally, we have neglected the effect of sub–parsec flows. If we assume a typical small–scale outflow produces a kinetic energy $\sim 4 \times 10^{43}$ erg[42], then on energetic grounds, an example combination of 90 giant flows with 2750 smaller outflows are required to yield the turbulent energy. Whether such numbers exist is presently unknown.

[41]For CO outflows in Circinus, Bally et al. (1999) estimate this "hidden mass" could increase momentum and kinetic energies of outflows by factors of 5 and 2.2 respectively.

[42]As for T Tau; Bally & Lada (1983).

For the L1641 GMC, it appears that rather large numbers of giant and sub–parsec flows are required to directly effect the stability of the GMC. This is the opposite to that seen in smaller molecular clouds host to giant protostellar outflows (L1448; Wolf–Chase, Barsony & O'Linger 2000, B18; Arce & Goodman 2001). However, we should consider what effect the L1641 giant flows have on the molecular cores which harbour the driving source. For example, Anglada, Sepúlveda & Gómez (1997) identified a 89 $M_{\odot}$ NH_3 core harbouring the L1641-N embedded cluster. With a size 0.32 $\times$ 0.63 pc, the core has a gravitational binding energy (GM^2/R) $\sim$ 3.33 $\times$ 10^{45} erg. This is a factor 3 times less the kinetic energy associated with the L1641–N outflow which is more than capable of unbinding and dispersing the parental core.

To summarize, the overall morphology of the L1641 GMC may be a direct result of the molecular gas interacting with the Ori OB Ic association, but the internal structure and dynamics are controlled by giant HH flows and to a lesser degree, their sub-parsec counterparts. The majority of giant flows in L1641 (Figures 4.20 and 4.32) show evidence of large expanding cavities/bubbles disrupting the surrounding molecular gas, which form highly compressed filamentary structures (cavity walls) which, after a time, collapse to form a new wave of star formation. After the effects of supernova remnants and OB winds, these flows may account for the fractal (hierarchal) structure of the interstellar medium on scales $\leq$ 10 pc.

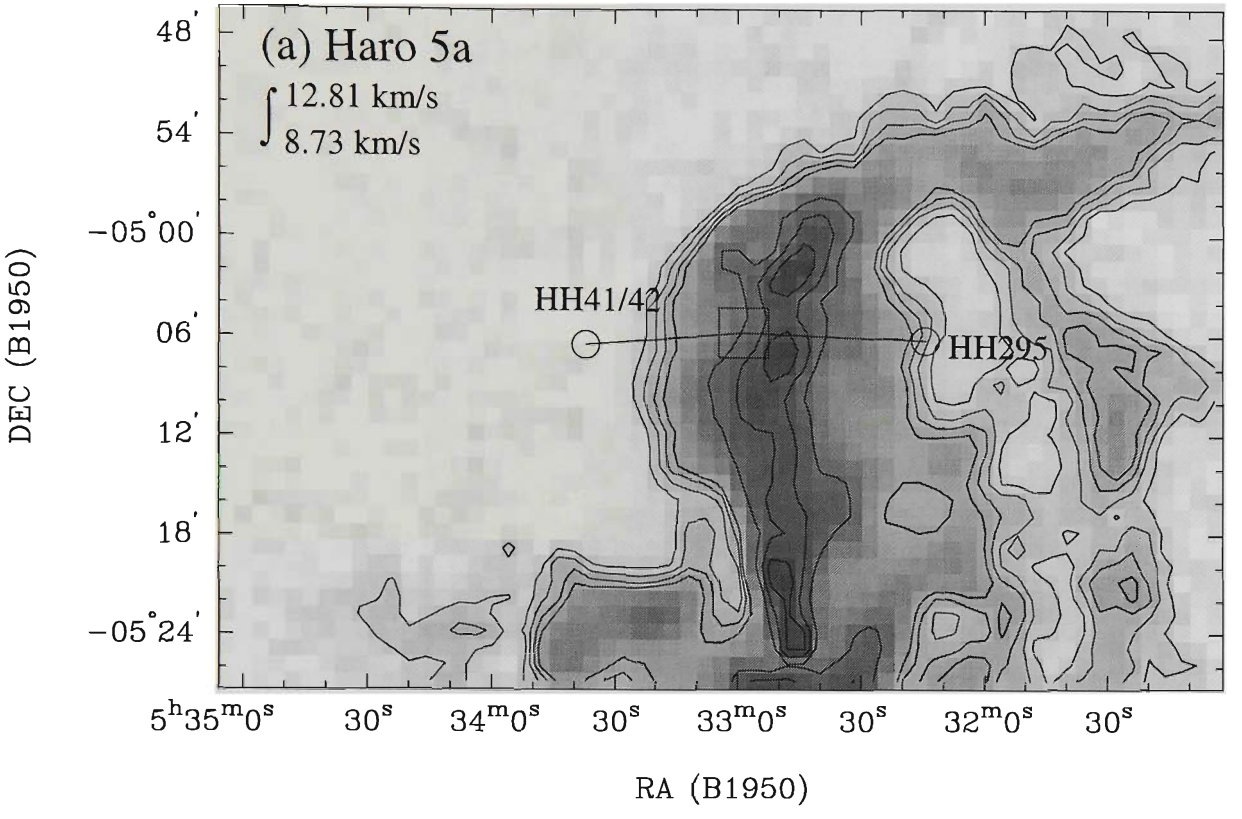

Figure 4.32: The effect of giant HH flows on the surrounding environment. For known giant flows in L1641, ^{13}CO maps are used to search for cavities projected against the terminal bow shocks. (a) Haro 5a (IRAS 05329-0505; see chapter 2, section 2.4.4): This source (centre of box) drives a 3 pc flow which terminates at HH 41/42 to the east and HH 295 to the west (R97). A cavity, also seen in optical images (see chapter 2, Figure 2.8), is clearly seen projected against the position of HH 295. Contour levels are at 3, 5, 7, 9, 20, 25 and 30 K.km s^{-1}.

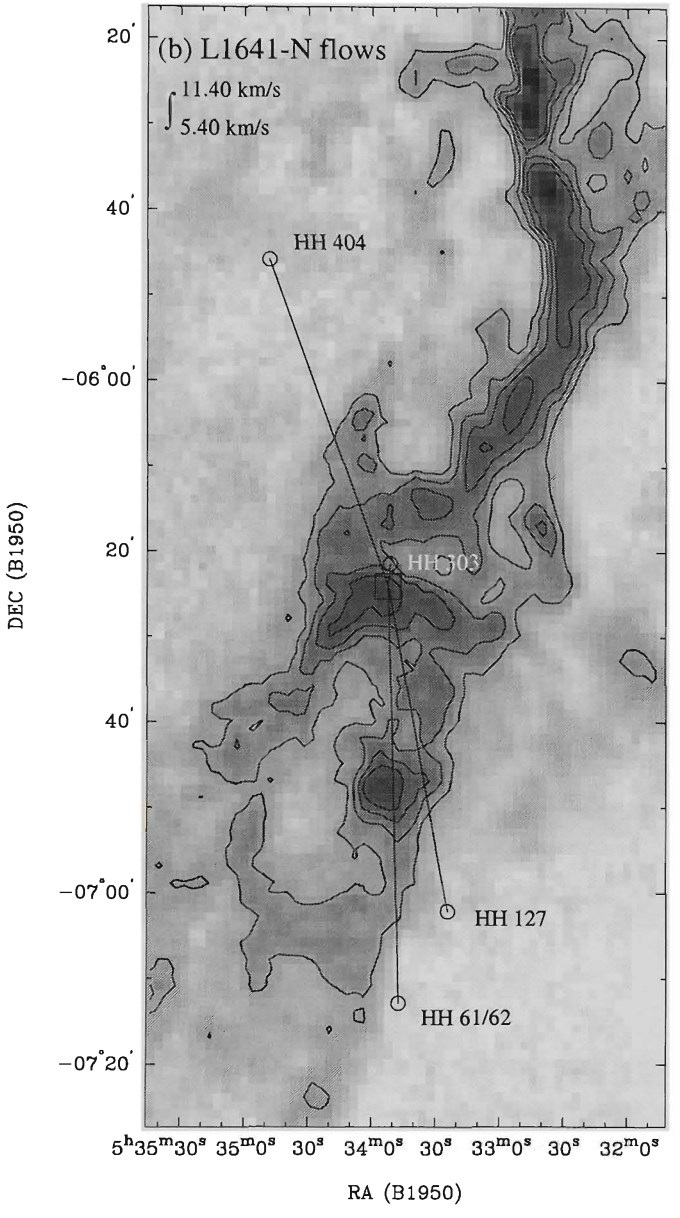

Figure 4.32 – continued: (b) L1641-N flows: A source within the L1641-N cluster (marked by the box) drives a 10.6 pc flow which terminates to the north-east at HH 404 and to the south at the position of HH 127 (RBD98). Similarly, The VLA source (centre of box) drives a 7 pc flow which is seen as the HH 303 jet to the north and ends to the south at HH 61/62 (RBD98). For both flows, there are no indications of cavities as both lobes have left the confines of the GMC. Contours at 10, 15, 20 and 25 K.km s^{-1}.

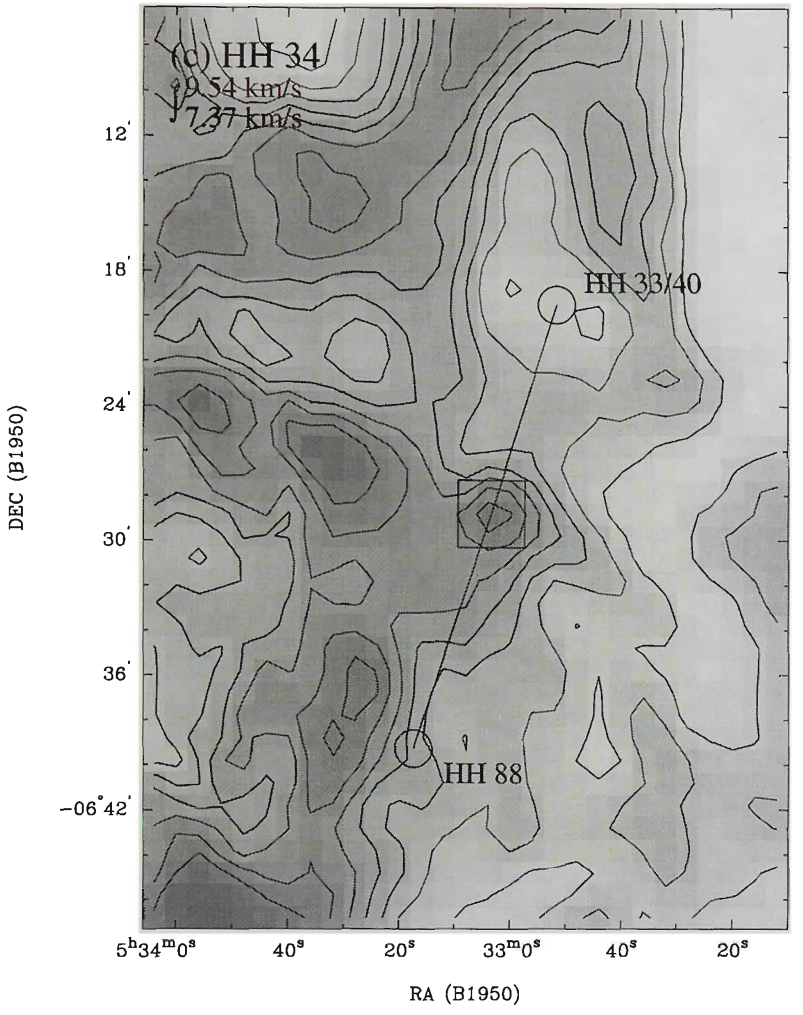

Figure 4.32 – continued: (c) HH 34IRS. Driven by the Class I protostar, HH 34IRS (centre of box), the 3 pc flow terminates to the south at HH 88 and to the north at HH 33/40 (see chapter 2, section 2.4.1). As found by Bally & Devine (1994), a large-scale cavity is spatially coincident with HH 33/40. The southern lobe of the outflow is moving away from the L1641 GMC and does not have as much influence as the northern lobe. Contours at 3, 5, 7, 9, 11, 13 and 15 K.km s^{-1}.

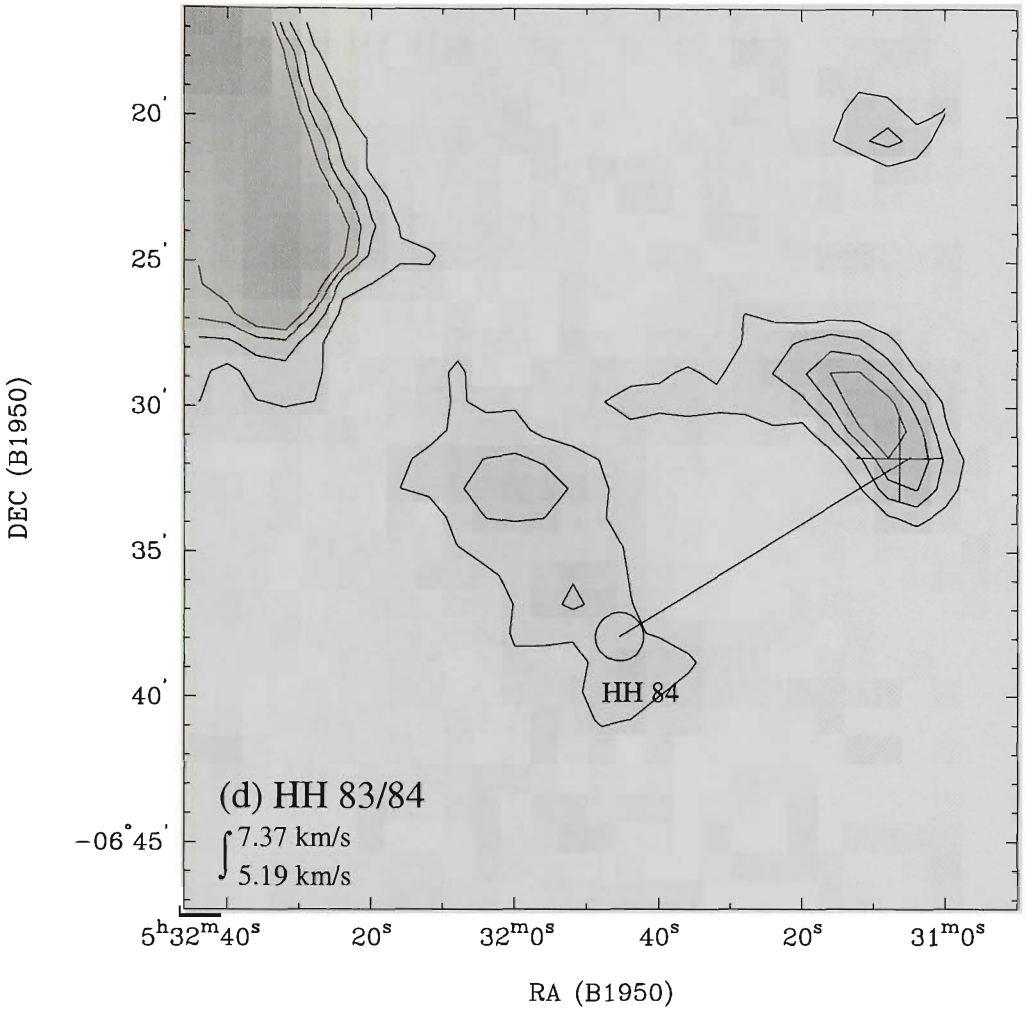

Figure 4.32 – continued: (d) HH 83IRS. The Class I object HH 83IRS (marked by the cross) drives a 1.46 pc flow which terminates to the south-east at HH 84[43] (R97). The ^{13}CO map shows evidence of a cavity between the cloud containing HH 83IRS and the cloud which lies along the same line of sight as HH 84. HH 84 may in fact be impinging upon this cloud. Contours at 1, 2, 3 and 4 K.km s^{-1}.

[43]This flow possibly includes HH 59/60 to the north-west (not shown); see Chapter 3, section 3.4.2. In this case, the outflow extends to 4 pc.

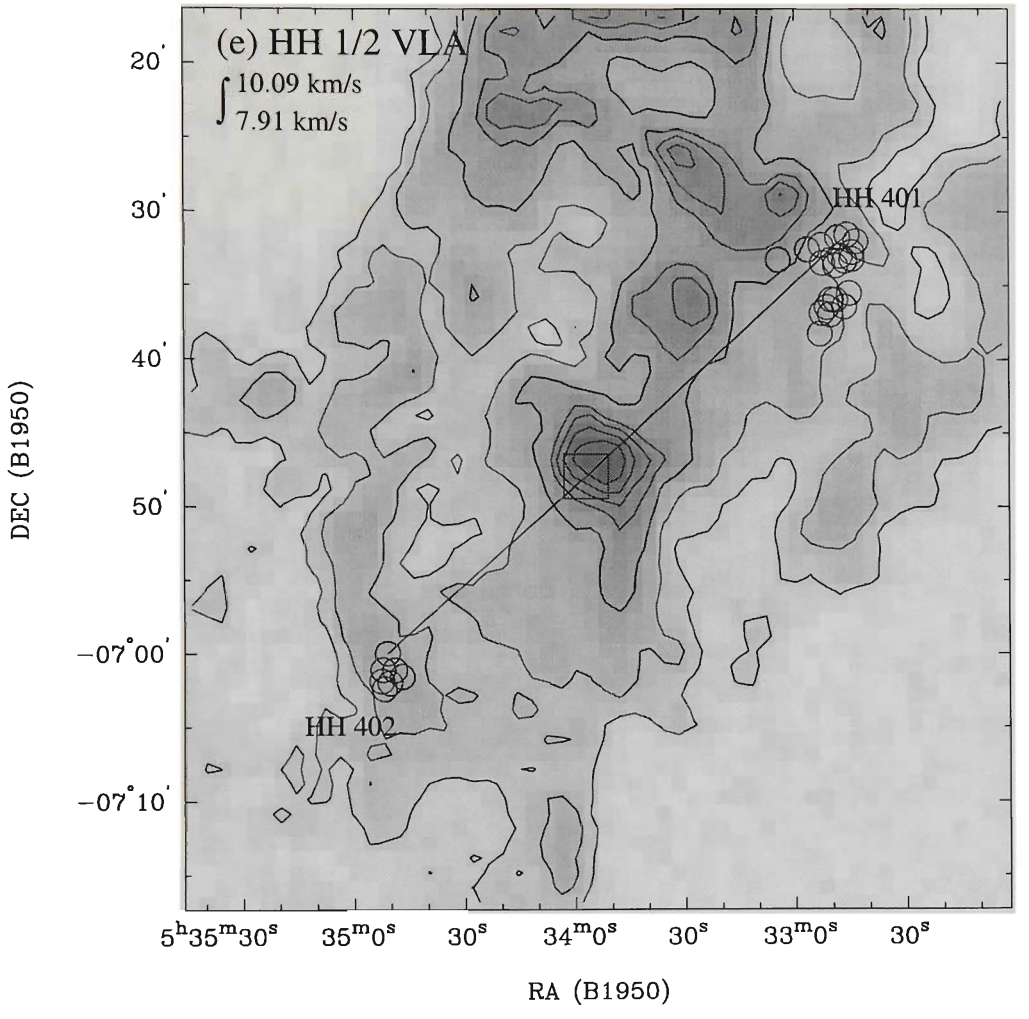

Figure 4.32 – continued: (e) HH 1/2 VLA. Driven by the deeply embedded source, HH 1/2 VLA (centre of box) drives a 6 pc flow which terminates to the north-west at HH 401 and to the south-east at HH 402 (Ogura 1995). A hint of a cavity is projected against the position of HH 401. Contour levels are 2, 4, 8 and 12 K.km s^{-1}.

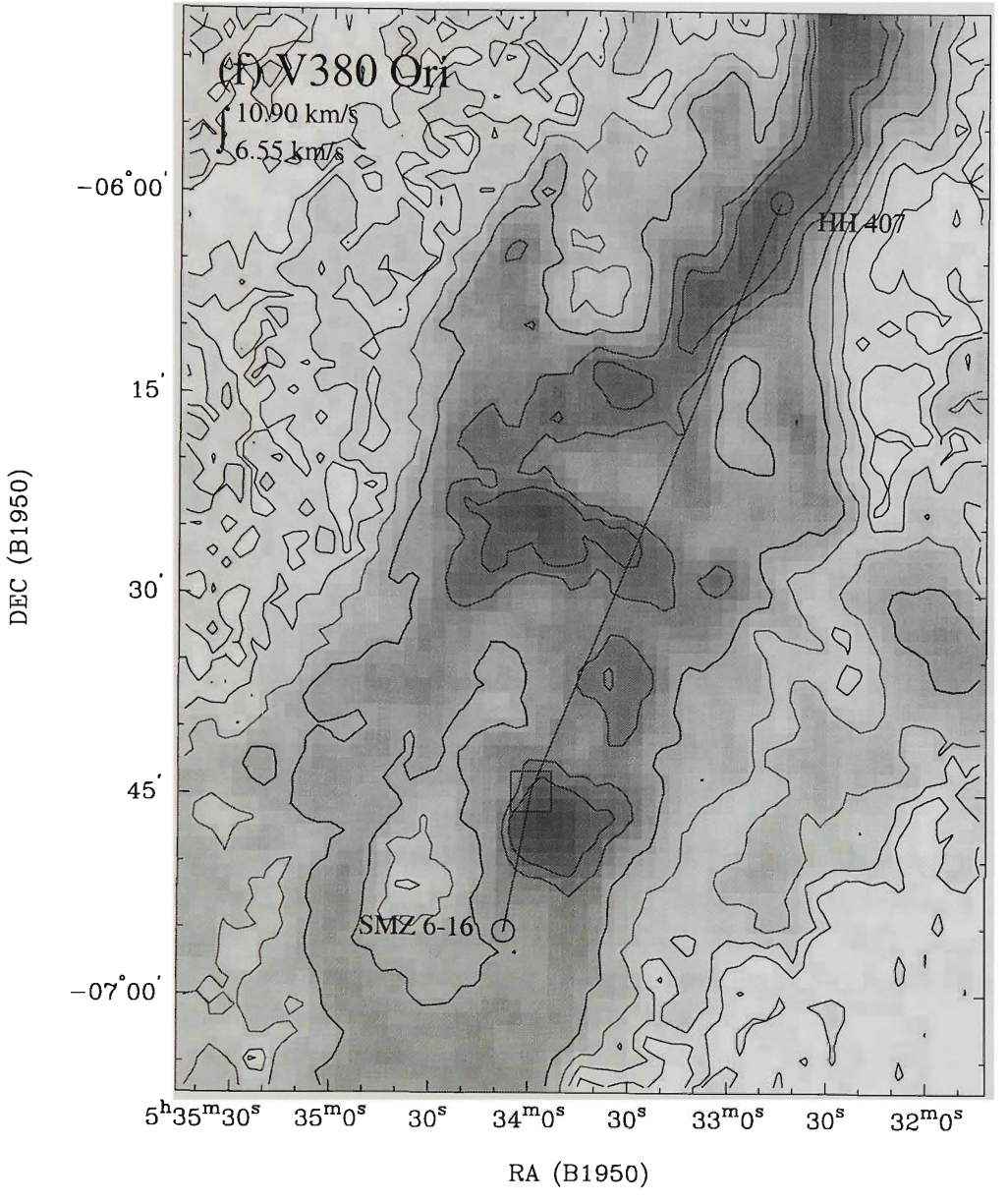

Figure 4.32 – continued: (f) V380 Ori. This source (centre of box) is proposed to be the driving source for the 8 pc flow containing HH 407 to the north-west and the large H_2 bow shock SMZ 6-16 south of V380 Ori. Although no cavities are seen towards HH 407, the object may be impacting with the western wall of the L1641-N chimney. As for SMZ 6-16, the bow shock is projected towards a cavity associated with the SMZ 23 outflow and may in fact contribute somewhat to the creation of this cavity. Contours at 1, 2, 4, 8, 16 and 20 K.km s^{-1}.

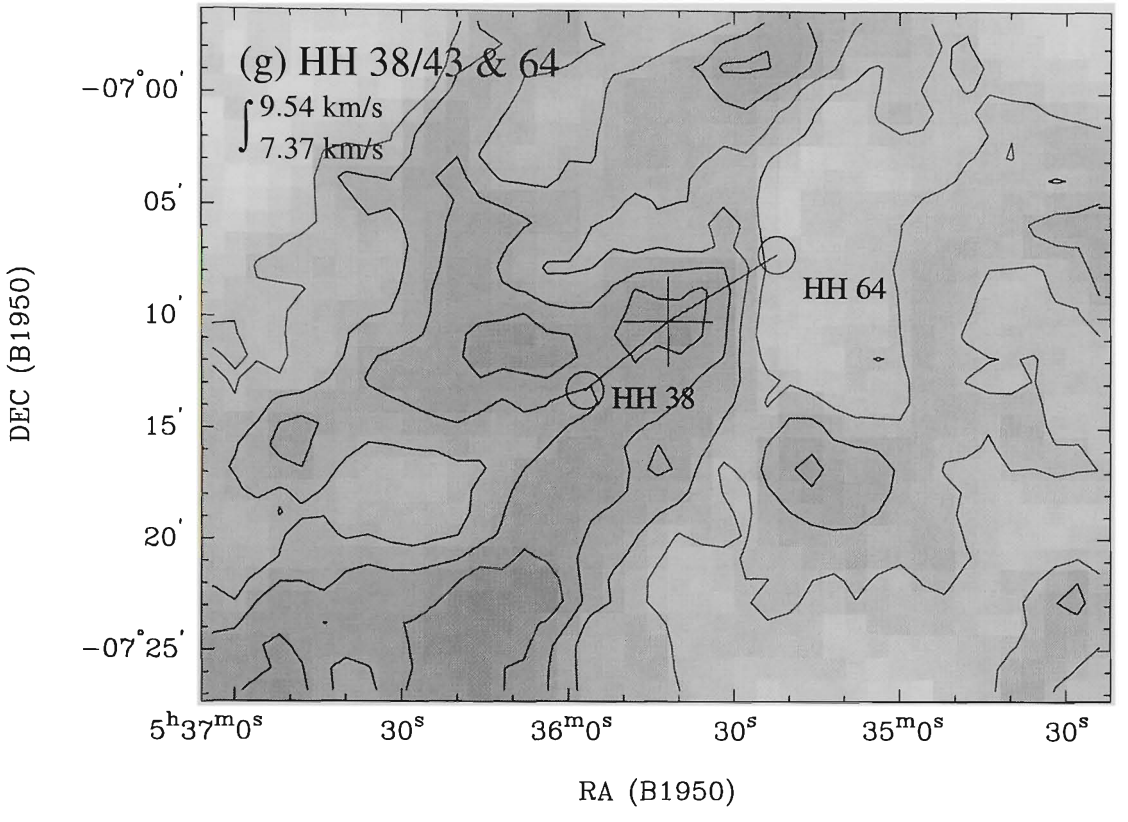

Figure 4.32 – continued: (g) HH 43 MMS1. Eislöffel & and Mundt (1997) and Stanke et al. (2000) have recently identified HH 38/43 & HH 64 as a 1.4 pc outflow. The driving source is the Class 0 object, HH 43 MMS1 (marked by the cross). In the ^{13}CO map, we see two large cavities projected towards HH 64 and HH 38. Contours at 4, 6, 8 and 10 K.km s^{-1}.

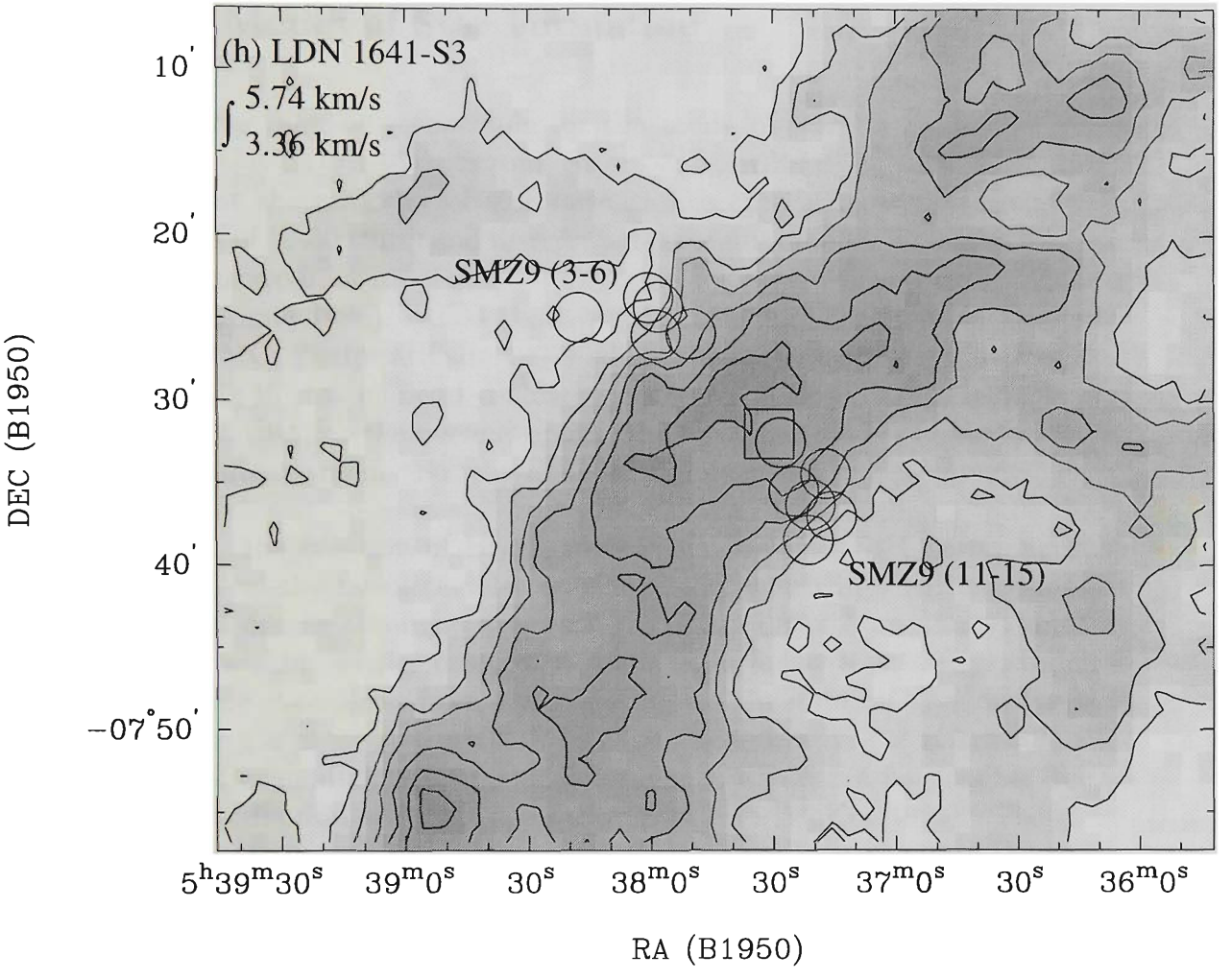

Figure 4.32 – continued: (h) L1641-S3. As suggested in chapter 3, section 3.4.5, L1641-S3 (centre of box) was suggested as a candidate energy source for HH 131. Circles represent individual H_2 knots of the 2.6 pc flow identified by Stanke et al. (2000). Both lobes are projected towards low density regions with a suggestive cavity seen towards SMZ 9 (11-15). As shown in a large-scale extinction map of the region, (see chapter 3, Figure 3.20), the L1641-S3 outflow may have created a cavity seen to the north-east beyond the SMZ 9 (3-6) lobe. Contours at 1, 3, 5, 7, 9 and 11 K.km s^{-1}.

4.7.3 Modes of Star Formation

Giant flows may be responsible for the mode of star formation occurring within a GMC. In L1641, Strom, Strom & Merrill (1993) and Allen (1996) found that the majority of star formation occurs in an aggregated (small groupings of 10-50 stars) and distributed (sporadic) mode. This is in contrast to the clustered nature of star formation in regions such as ρ Oph (Wilking, Lada & Young 1989), L1630 (Lada et al. 1991) and the Rosette Molecular Cloud (RMC; Phelps & Lada 1997) where the majority of stars are found to be forming in rich embedded clusters. The results from these regions tend to suggest that for the current epoch, the clustered mode of star formation is the dominant mode. So why is L1641 different?

In L1641, the creation of large-scale cavities by giant HH flows opens up the GMC to the far-ultraviolet radiation field which in turn, increases the ionization degree throughout the cloud. Future star formation is unlikely to occur within cavities created by giant flows for at least 10^5 yr, which is the lifetime of outflows from low-mass objects. In addition, the low levels of molecular gas associated with these cavities (generally < 3 K.km s^{-1}) suggests that even after this time, star formation would not be possible due to the low extinction and high ionization rate (i.e., McKee 1989). Therefore, a likely place to find new generations of star formation is within the highly compressed filaments which make up the cavity walls. In fact, the vast majority of CS cores identified in L1641 by Tatematsu et al. (1993; 1998) are located within these filamentary structures. This is shown in Figure 4.33.

After the removal of large amounts of molecular gas by giant HH flows ($\sim$ 250 $M_\odot$ for HH 306-310/SMZ 23/6-2/6-4A-C), the filaments will, after a time, start to collapse and form cores along their length. As these cores compete for a limited amount of molecular gas, they will tend to have lower masses than cores in regions such as L1630, ρ Oph and the RMC. As a result, they will not have sufficient gravity to merge and so continue to form in isolation. Such a scenario may account for the formation of the distributed mode found in L1641. It is interesting that the clustered mode in regions such as L1630, ρ Oph and the RMC may be triggered by ionization fronts from nearby HII regions. For L1641, regions south of δ = -5° are not under the direct influence of HII regions and/or ionization fronts and since this region contains a large number of giant HH flows, it appears that at least for this part of L1641, giant HH flows are the major influence on both its morphology and star forming capabilities.

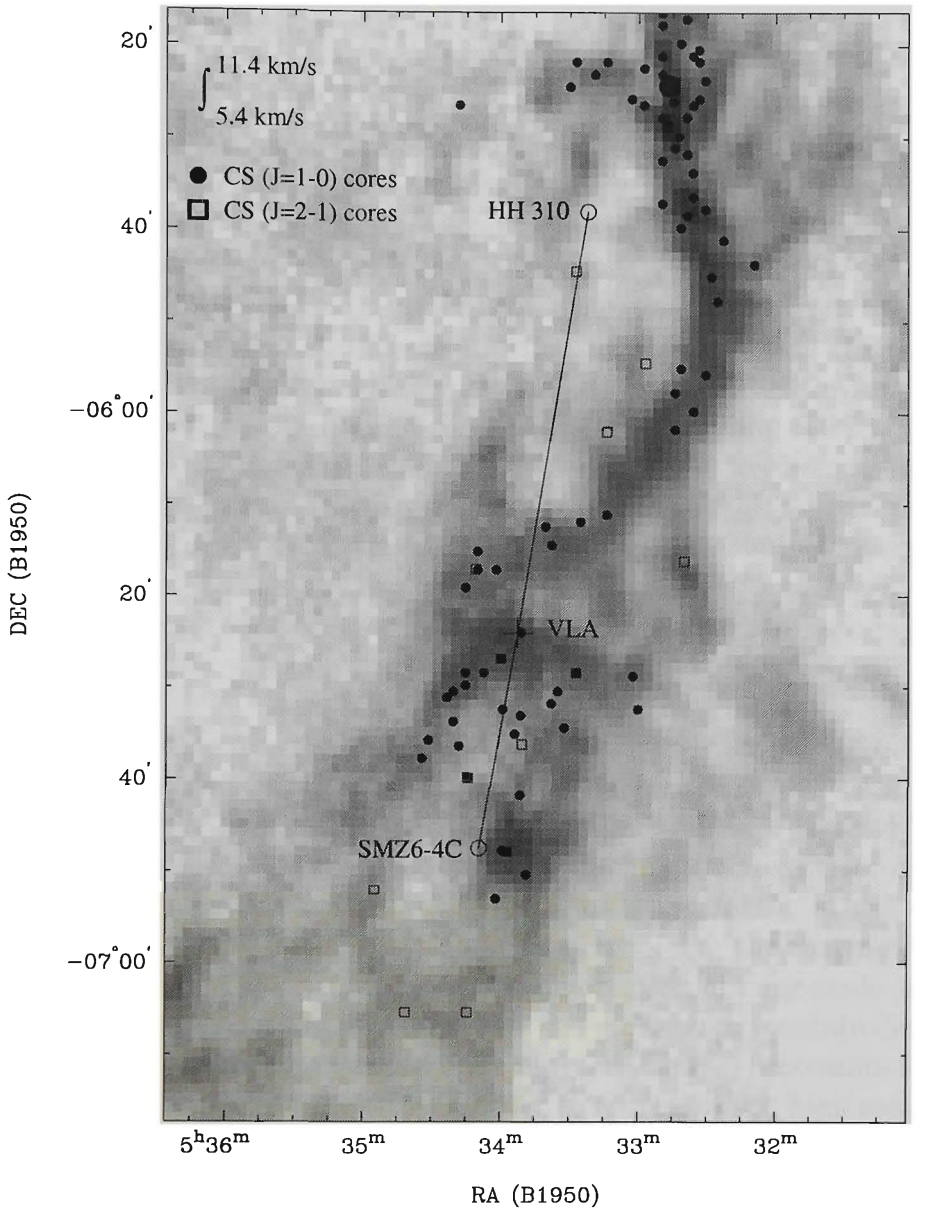

Figure 4.33: Figure 4.20 with the position of CS (J=1-0) (Tatematsu et al. 1993) and CS (J=2-1) (Tatematsu et al. 1998) cores. Only those cores with velocities within the integrated emission (5.4-11.4 km s^{-1}) are plotted. The majority of CS cores are located within the large-scale filaments which delineate the northern and southern cavities created from the passage of HH 306-310 and SMZ 23/6-2/6-4A-C bow shocks driven by the VLA source (for clarity, only the northern and southern-most terminal bow shocks (HH 310 and SMZ 6-4C respectively, are plotted). From the distribution of CS cores, it appears these flows have influenced the future star formation ability of L1641. See text for details.

4.8 Summary

By use of a single AAO/UKST Hα film of the Orion region, we have identified emission-line nebulosities which resemble bow shocks, jets and extensive alignments of arc-shaped nebulae indicating possible giant molecular flows. Subsequent narrow and broad-band CCD imaging has confirmed these features as genuine HH objects tracing outflows ranging in size from a fraction of a parsec to over 6 pc in length. In addition to the 3 pc wide Hα rim surrounding HH 306-310 and HH 407, the Hα loop (loop A) extending out of the NGC 1999 reflection nebulosity and the Hα shell surrounding HH 94/95 have not been identified in previous studies. Although these features are faintly visible in our IIIaF images, the excellent contrast of the Hα film with respect to IIIaF and published CCD images of these regions clearly distinguishes these features from background emission, thereby allowing a thorough investigation of how outflows from young stars affect the surrounding interstellar medium.

The lack of optical and molecular emission associated with HH 403/404, the presence of the Hα rim and the identification of large ^{13}CO cavities associated with HH 34 (Bally & Devine 1994), HH 306-310 (RBD98) and the SMZ 23/6-2/6-4A-C counterflow (this chapter) suggests that, in the absence of massive star formation, parsec-scale flows are the dominating factor in disrupting molecular gas in GMCs. They may also be responsible for the continuation of star formation beyond the current epoch. The creation of large-scale cavities seen in ^{13}CO maps produce highly compressed regions which contain dense ($\sim 10^5$ cm^{-3}) CS cores which may represent candidate Class 0 protostars formed as a result of the expanding cavities. In order to test this idea, high resolution sub-millimetre observations in conjunction with near-infrared H_2 (2.12μm) imaging will identify and determine the distribution of newly-forming Class 0 protostars with respect to the CO cavities.

Although we have suggested candidate energy sources for many of the new HH flows, only a few (Ori I-2, BE Ori and V510 Ori) can be considered as certain. The identification of at least 4 sources within an arc-minute of the VLA source warrants sub arc-second CO mapping of the region to determine which source is driving the optical and near-infrared emission associated with HH 306-310, HH 403/404, HH 407 and SMZ 23/6-2/6-4A-C. Near-infrared spectroscopy of proposed outflow sources for HH 301/302, HH 304, HH 305 and HH 405 will be useful in classifying their nature for comparison with other HH energy sources. To varying degrees, the optical sources BE Ori and V510 Ori exhibit optical variability and multiple-ejection events (HH objects). The fact these sources still posses highly collimated jets well after they have emerged from their parental molecular cloud may provide important

insights into jet evolution. In relation to the newly discovered parsec-scale flows, high resolution spectroscopy and proper motion studies of individual knots associated with HH 61/62/303, HH 306-310, HH 127/403/404, HH 407 and features A-D to the far south of L1641-N will determine velocities, excitation conditions and confirm points of origin.

Due to the success of the Orion Hα film, the Carina, Cha I/II, Sco OB1, ρ Oph, R Cra and CMa OB1[44] star-forming regions are to be surveyed in a similar fashion to that presented in this chapter. The majority of these cloud complexes lie within 500 pc and maximise the detection of faint, large-scale flows for comparative studies with the Orion region where we hope to address the following questions:

- What is the nature of the energy source? Parsec-scale flows are associated with Class 0, Class I and optically-visible T-Tauri stars. Is the parsec-scale phenomenon due to inherent properties of the energy source?
- How does the flow remain collimated over such large distances? Does the nature of the surrounding environment have a collimating effect?
- To what extent do parsec-scale outflows affect star formation within molecular clouds? Is there any evidence for self-regulated star formation?

[44]See Chapter 5.

Acknowledgements

Thanks go to the staff of the AAO and particularly the UKST for the teamwork which makes the Hα survey possible. Thanks also go to the Mount Stromlo Time Allocation Committee for the generous allocation of time on the 40-inch telescope. Thanks go to John Bally for use of the Bell Labs 7-m ^{13}CO data of the Orion A and B regions, and Thomas Stanke for supplying his H_2 (2.12μm) data of L1641-N. Thanks also go to David Malin at the AAO for providing unsharp-mask prints of the Orion film. This research has made use of the SIMBAD data base, operated at CDS, Strasbourg, France, and the ESO/SERC Sky Surveys, based on photographic data obtained using the UKST which is currently operated by the AAO. IRAF is distributed by the National Optical Astronomy Observatories, which are operated by the Association of Universities for Research in Astronomy, Inc., under cooperative agreement with the National Science Foundation.

Chapter 5

The AAO/UKST Hα Survey II: CMa OB1/R1

5.1 Introduction

Since the Orion Hα film was taken in 1997, the Anglo-Australia Observatory (AAO) and United Kingdom Schmidt Telescope (UKST) Hα survey of the southern Galactic plane is now more than 60% complete. In this chapter, we present preliminary results of a search for giant Herbig-Haro (HH) outflows in the Canis Major OB1/R1 region which is located at a distance of 1150 pc (Claria 1974). Figure 5.1 shows the CMa OB1/R1 region as seen on the SuperCOSMOS-scanned AAO/UKST Hα plate. The prominent arc of emission nebulosity is the HII region S296 (Sharpless 1959). The circular patch of Hα emission to the north-west is IC 2177, which is excited by the Be star HD 53367. S297 is another bright HII region to the south of the figure.

Although numerous B-type (van den Bergh 1966; Herbst, Racine & Warner 1978; Shevchenko et al. 1999) and Hα emission-line (Wiramihardja et al. 1986) stars are found in the CMa OB1/R1 region, only one HH outflow has been associated with the highly luminous, FU Orionis (FUor) star Z CMa (IRAS 07013-1128). In fact, only two HH outflows have been found in CMa. The other, HH 72 (Reipurth & Graham 1988), lies $\sim 13^{\circ}$ to the south of Z CMa. The low number of HH flows in this part of the Galactic plane is surprising since the region contains two giant molecular clouds, each with mass $\sim 10^5\ M_{\odot}$ (Blitz 1978; Machnik et al. 1980) and drawing a comparison with the similarly massed L1630 and L1641 giant molecular clouds in Orion (see chapter 4), we would expect to see more HH outflows.

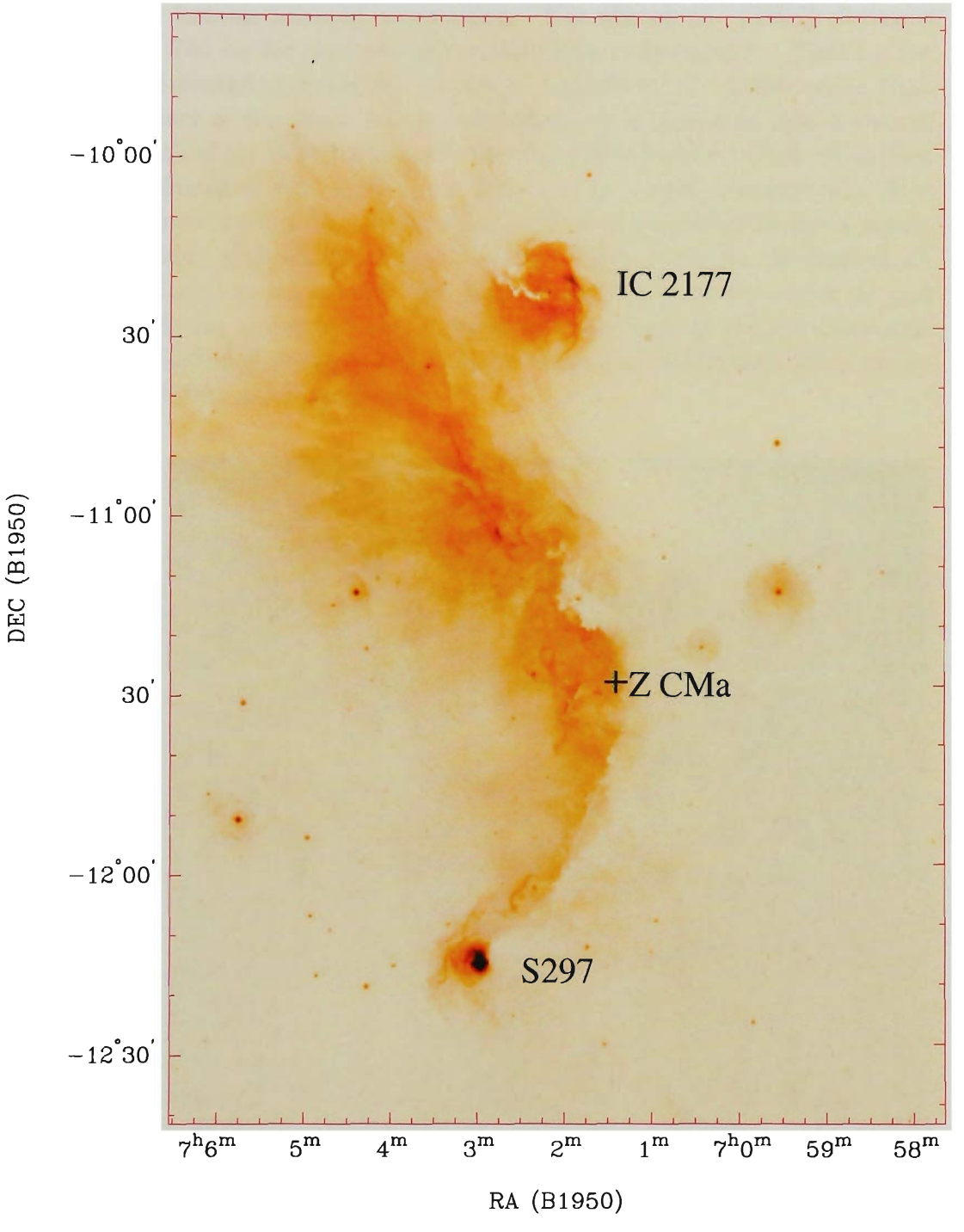

Figure 5.1: SuperCOSMOS-scanned Hα image of the CMa OB1/R1 region. The arc of nebulosity is S296. Along with Z CMa, the HII regions IC 2177 and S297 are identified.

Z CMa itself has an infrared companion. Koresko et al. (1991) derive a luminosity of 700 $L_{\odot}$ for the optically-visible FUor object and $\sim$ 2300 $L_{\odot}$ for the invisible infrared companion. However, Lamzin et al. (1998) argue that the FUor object is the more active component, it is unknown which source drives the optical jet (HH 160) and molecular CO bipolar outflow identified by Poetzel, Mundt & Ray (1989) and Evans et al. (1994) respectively. The HH flow consists of a highly collimated blue-shifted jet (HH 160) and a string of 15 HH objects aligned along the axis (PA $\sim$ 60°) of the jet. Poetzel et al. find that the total extent of the blue and red-shifted lobes are $\sim$ 1.6 pc and 2.0 pc respectively which combine to give a total extent of 3.6 pc. They also found that the radial velocities seen in the blue- and red-shifted lobes are $\sim$ -620 and +345 km s^{-1} respectively.

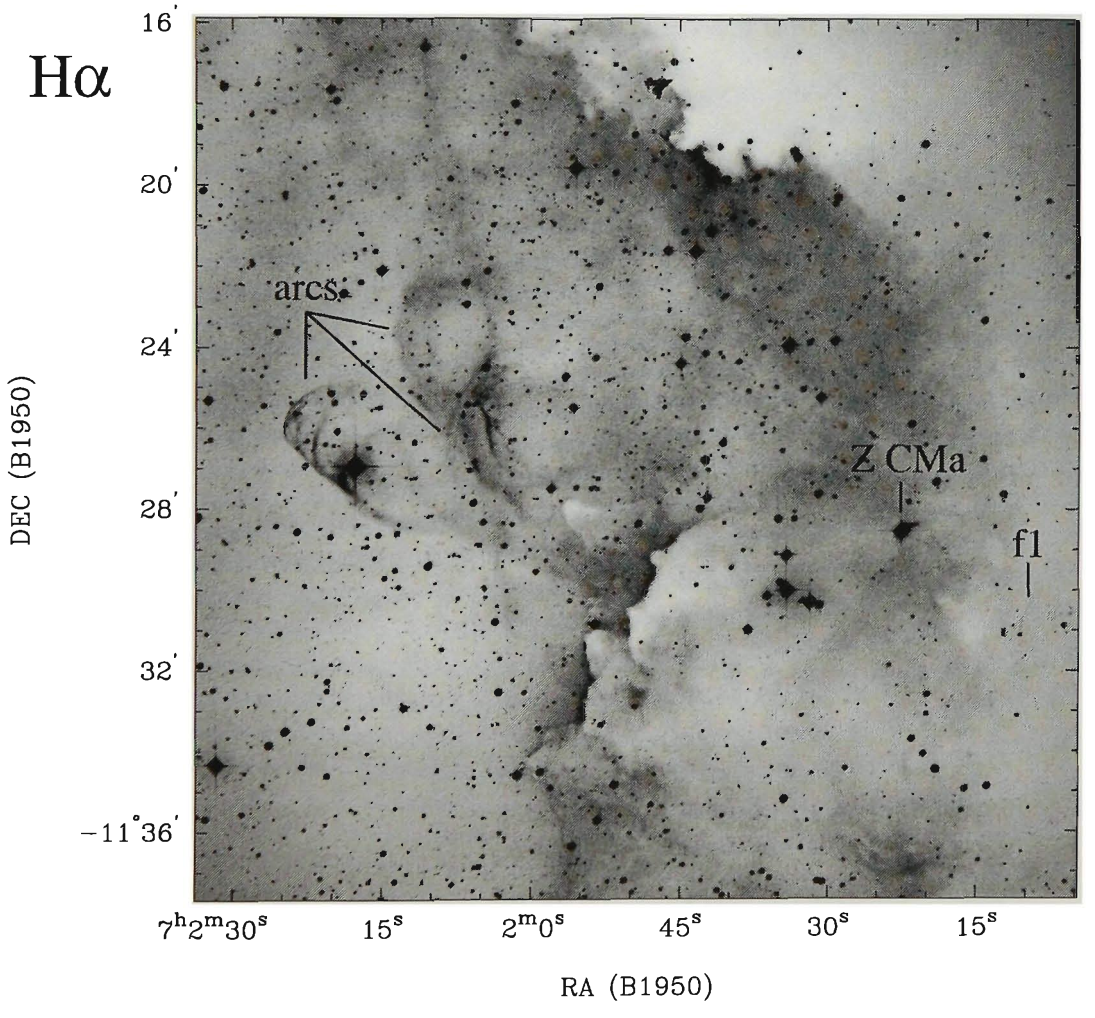

Figure 5.2: SuperCOSMOS-scanned AAO/UKST Hα image of the Z CMa region. The large arcs, possibly associated with Z CMa are shown along with the HH-like object f1 of Poetzel et al. (1989).

During a visual inspection of the AAO/UKST Hα plate of the Z CMa region, several large-scale arc-like objects were identified which may be related to the existing HH outflow. The SuperCOSMOS-scanned image of the Z CMa region is shown in Figure 5.2. Clearly seen in the Hα image are the large bow shock-type arcs to the east of Z CMa which show a similar morphology to HH 407 (see chapter 4, section 4.5.8). A literature search shows the arcs have not been investigated in terms of a relationship between them and the Z CMa/HH160 system, although their location with respect to the ionization front of S296 may have led investigators to think they were part of the HII region. We have obtained narrow-band Hα and [SII] images to determine if the large arc-like structures are associated with Z CMa and not part of the general HII region. In section 5.2, we present photographic material used, along with observations and data reduction of the CCD narrow-band data. Results and a summary are presented in sections 5.3 and 5.4 respectively.

5.2 Observations & Data Reduction

5.2.1 Schmidt Plate Material

The ESO/SERC and Hα plates used and their properties are listed in Table 5.1. Due to the large range of contrast in the region, each of the images in Figures 5.2 and 5.3 were "flat-fielded" by fitting a first or second order polynomial fit to the field and subtracting this from the original image.

Table 5.1: ESO/SERC Plates used for the Z CMa region.

Plate	α_{1950}	δ_{1950}	Date	Emulsion	Filter	Exp (min)
I5515	07^h00^m	-10°00'	79-12-09	IVN	RG715	90
J8384	07^h00^m	-10°00'	83-02-07	IIIaJ	GG395	65
OR12913	07^h00^m	-10°00'	89-01-08	IIIaF	OG590	63
HA18244	06^h56^m	-12°00'	99-02-05	4415	HA659	180

5.2.2 SuperCOSMOS data

The CMa OB1/R1 Hα film (UKST field HA1017) was scanned using the Royal Observatory of Edinburgh's precision micro-densitometer facility, SuperCOSMOS (Miller et al. 1992; Hambly et al. 1998). In the "mapping

mode", SuperCOSMOS digitises the 4×4° area of the Schmidt plate in ∼ 2.5 hours, with a resulting resolution of 10μm (0.67″) pixels. After scanning, the data was processed in the "image analysis mode" to detect astronomical objects, and for all these objects their positions, celestial coordinates, instrumental magnitudes, and other parameters were determined. In this presentation, we will only deal with the pixel data.

5.2.3 CCD Imaging

Narrow-band CCD images of the Z CMa region were obtained during the 4th-6th April 1998 at the Australian National University 40inch telescope at Siding Spring Observatory. Imaging was done with a 2048 × 2048 TEK CCD mounted at the f/8 Cassegrain focus. The 0.6″/pixel gave a field-of-view of 20.48′ × 20.48′. The seeing conditions during usable time was typically less than 3″. Narrow-band filters used consisted of Hα (6563Å; $\Delta\lambda$ 55Å), [SII] (6732Å; $\Delta\lambda$ 25Å) and red continuum (6676Å; $\Delta\lambda$ 55Å). Exposure times for each field are shown in Table 5.2. Flat fields were obtained by illuminating the dome with a halogen lamp. All frames were reduced in a similar fashion with IRAF, where dark and bias frames were subtracted from source frames before flat fielding. Individual source frames were averaged together to produce the final images. Remaining defects such as bad pixels and cosmic rays were removed by hand.

Table 5.2: CCD imaging log.

Region	Filter	Exposure Time (sec)
Z CMa:	Hα	2×900
	[SII]	2×900
	continuum	2×300
Arcs:	Hα	3×600
	[SII]	2×900
	continuum	2×300

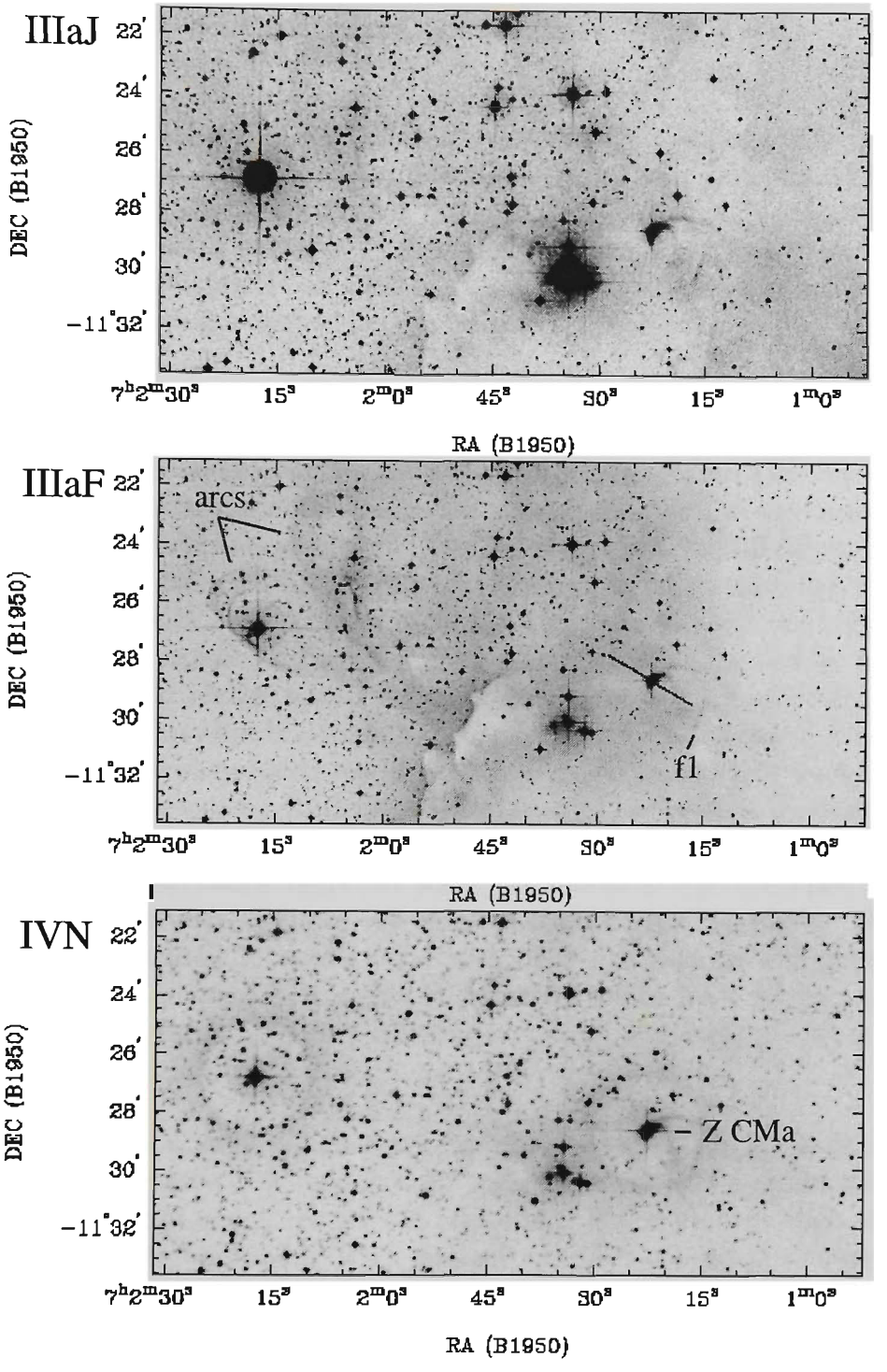

Figure 5.3: ESO/SERC images of the Z CMa region. Several large arcs are seen to the east of Z CMa and may be related to the HH 160 flow identified by Poetzel et al. (1989). The arcs are faint in the IIIaJ, strong in the IIIaF and absent in the IVN. The line in the IIIaF, centred on Z CMa, denotes the PA of the HH jet ($\sim$ 60°) of which the faint finger-like object f1 (from Poetzel et al.) lies in the red-shifted lobe. See text for details.

5.3 Results and Discussion

The ESO/SERC IIIaJ, IIIaF and IVN images of the Z CMa region are shown in Figure 5.3. By comparing the Hα, IIIaJ and IIIaF with the IVN, no continuum appears to be associated with the large bow structures, although the IIIaJ shows faint emission associated with the arcs. The needle-like HH object f1 of Poetzel et al. (1989) displays emission in all images which suggests it displays a combination of emission and reflection nebulosity.

Figure 5.4 shows the [SII] and Hα images of the giant arcs. In order to match the background brightnesses, the background of the Hα frame was estimated and scaled to match that of the [SII] frame. As the IVN and CCD continuum images do not show any emission associated with these structures, the continuum frame is not shown. Clearly, there is substantial substructure associated with some arcs. To ease the discussion, structures have been labelled as arcs A-F. A closer view of A, B, D, E and F is show in Figure 5.5. Arc A shows an almost straight line of emission which is flanked by fainter wings which open to the west. A bright compact knot lies almost at the centre of the brighter line of emission. The circular arc that is object B clearly appears to surround emission associated with arc A. In contrast to A, arc B displays no sign of substructure at the resolution of the present observations. Arc C is diffuse and Hα-bright. Arcs D, E and F appear as one large bow shock structure, although there are some peculiarities. For example, arc D displays a brightness enhancement close to the B5 star HD 53456. Arc E displays a bright knot located at the apex of a bow with its wings linking up to arc D. Finally, arc F is highly structured with at least six [SII]-bright knots located towards the tip of another bow with the wings merging with those of D and E.

With the exception of arc C, the majority of emission displays [SII]/Hα (relative intensity) ratios > 1, which is in accordance with low-excitation HH emission[45]. If these structures are not part of the HII region, are they part of the Z CMa/HH 160 outflow? There are several lines of evidence to suggest they are;

[45]The identification of arcs A-F as genuine HH objects has been independently found by Reipurth (2001; private communication). In the upcoming third edition of the Herbig-Haro catalogue, he labels the complex as HH 388.

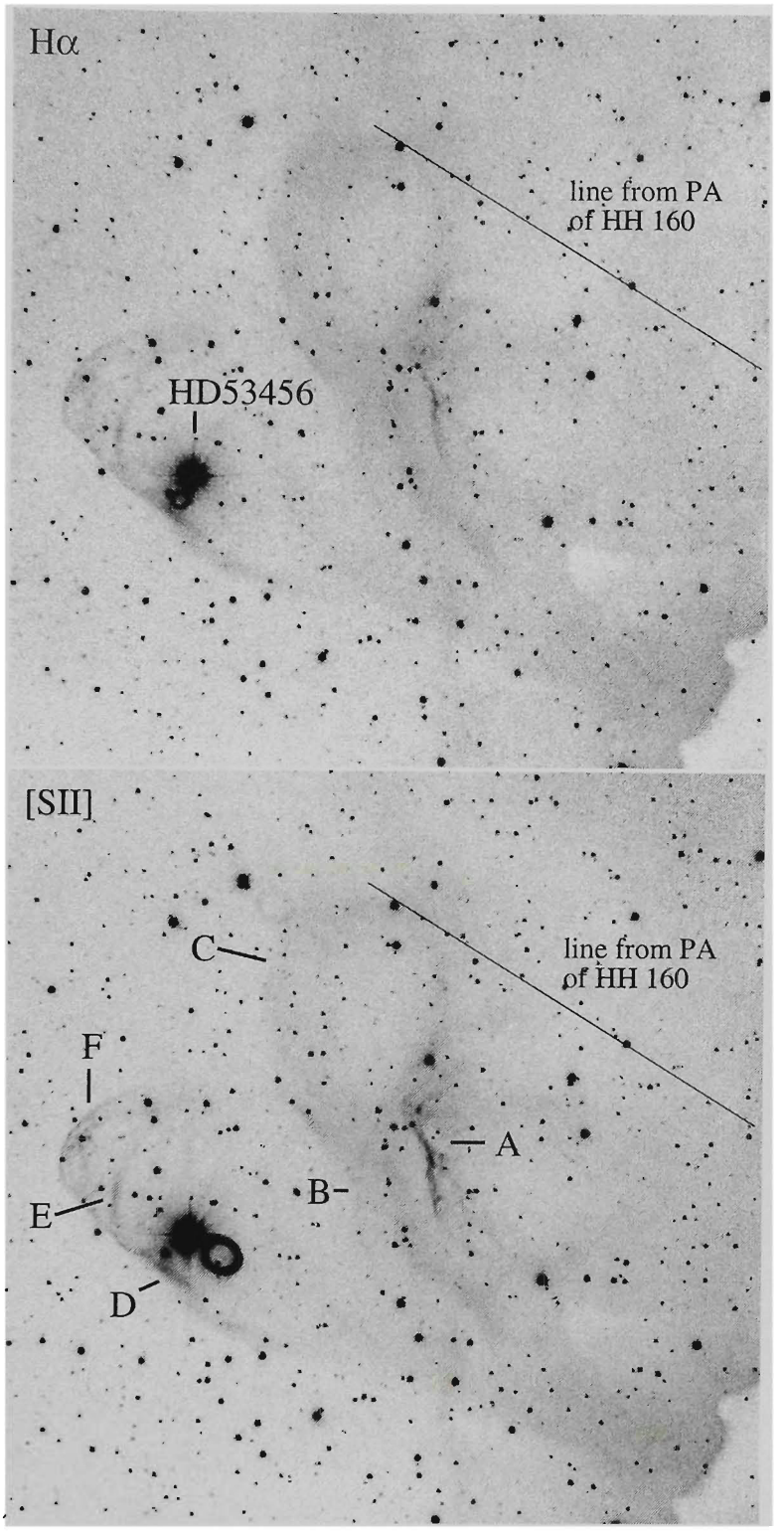

Figure 5.4: CCD Hα and [SII] images of the arcs. The images are 10.27′ on a side. The position of the B5 star HD 53456 and arcs relevant to the discussion are labelled and discussed in the text. The lines in both images represents the PA ($\sim$ 60°) of the HH 160 flow identified by Poetzel et al. (1989).

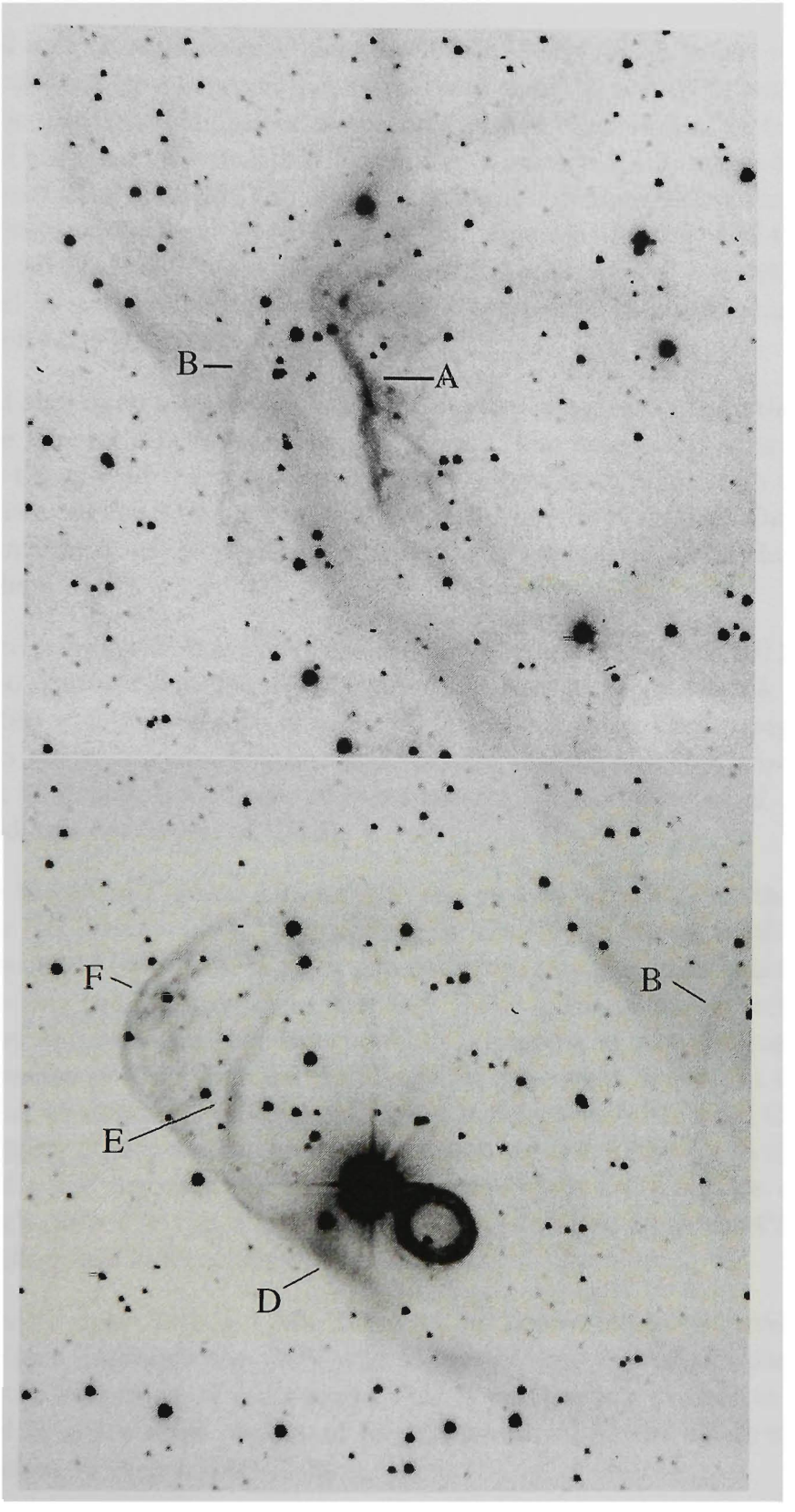

Figure 5.5: Magnified [SII] images of arcs (top) A and B and (bottom) D, E and F. The images are 5.12′ on a side.

1. All arcs show faint emission in the IIIaJ band which is not reflection as there is no corresponding emission in the IVN and CCD continuum. The apparent brightness of the arcs in the IIIaJ is similar to the IIIaJ emission seen in HH 47D (chapter 2, section 2.4.2) which has been detected in [OII](3727Å) and [OIII](5007Å). If the IIIaJ emission represents one or both of these lines, this suggests that like HH 47D (i.e., Morse et al. 1994), the shocks are moving with velocities $\sim$ 100 km s^{-1} and into a medium of pre-ionized gas excited by the same stars which excite the HII region.

2. All arcs open towards Z CMa and their morphologies are distinct from the general HII emission in the region. The brightness of arc A can be thought of the region where recent ejecta is colliding with material which was part of a previous ejection episode from Z CMa. Due to the faintness of arc C, we suggest it represents a bow shock predating the others.

3. The presence of knots at the bow of arc F can be likened to HH 2, which also displays a multitude of knots (i.e. Hester, Stapelfeldt & Scowen 1998) which represent a fragmented bow shock where the fragmentation is a result of hydrodynamic and thermal instabilities that arise as the arc is driven into dense ambient material (see Hester et al. for an in-depth discussion of HH 2).

4. As shown in Figures 5.3 and 5.4, the arcs do not lie along the PA of the HH flow ($\sim$ 60°). As discussed by Eislöffel & Mundt (1997), flows associated with giant HH flows do not propagate along a straight line all the way from the source to flow end. Some of the physical mechanisms they suggest why this is so include precession of the jet due to the presence of a companion. Evidence for precession is seen in the 6cm VLA observations of Cohen, Bieging & Schwartz (1982) and Cohen & Bieging (1986) where the PA of the outflow was found to be at $\sim$ 71° and $\sim$ 44° respectively. With such a large variation in outflow opening angle, arcs A-F can be thought as ejecta produced when the PA of the outflow was different to what it is today.

5. Finally, apart from Z CMa, there are no known outflow sources in the vicinity, although the BOV star HD 53456 may contribute somewhat to the ionization of some arcs. This is particularly evident at arcs D and E which show regions of brightness enhancement where they are in close vicinity to HD 53456.

Under the assumption arcs A-F are part of the HH 160 complex, the flow length increases to 5.89 pc, which is 1.6 times further that that found by Poetzel et al. (1989). The question arises whether there are HH objects in the south-western lobe which mirror the position of arcs A-F. Although we imaged regions west of Z CMa, the seeing was 2-3″, so were were not able to identify any such counterparts. However, the density of the medium in which the two outflow lobes are moving may be different such that the red-shifted lobe is moving into a less dense region compared to that of the blue-shifted lobe. Therefore, any shocked emission associated with the western lobe will be faint. Deeper, wide-field imaging will be useful to see if the flow extends further, while spectroscopy of arcs A-F will be able to discriminate between HH and HII emission.

5.4 Summary

This chapter has shown that Z CMa is still the only known HH outflow in the CMa OB1/R1 region. However, it should be noted that the large-scale arcs located near Z CMa were obvious whereas smaller-scale jets and outflows may yet be identified. Our initial survey of the region was only by naked eye whereas in the Orion region (chapter 4), the usage of a 10× microscope yielded a large number of new HH objects. To this end, we will use SuperCOSMOS data to conduct a more thorough search for HH nebulosities and identify what percentage of the Wiramihardja et al. (1986) Hα emission-line stars display evidence of optical jets like that seen for the Orion Hα emission-line objects BE Ori and V510 Ori.

Acknowledgements

Thanks go to Harvey MacGillivray and the SuperCOSMOS team at the Royal Observatory Edinburgh for their speedy delivery of the SuperCOSMOS data used in this chapter. This research has made use of the SIMBAD data base, operated at CDS, Strasbourg, France, and the ESO/SERC Sky Surveys, based on photographic data obtained using the UKST which is currently operated by the AAO.

Chapter 6

Conclusions and Future Work

The work in this thesis has been geared towards (a) identifying parsec–scale outflows from young stellar objects and (b) determining what effect these giant flows have on their parental molecular clouds. In both cases, wide–field optical (ESO/SERC, AAO/UKST Hα Survey) and infrared (IRAS) surveys continue to offer new and exciting advances into the star forming process.

In chapter 2, digital material from wide–field ESO/SERC plates was used to highlight the usefulness of such material in characterising Herbig–Haro (HH) outflows. By simple comparison of IIIaJ, IIIaF and IVN material, it is possible to distinguish between reflection and HH–type emission, estimate excitation conditions along a flows length, and most importantly, identify HH energy sources. In particular, the IVN material is capable of identifying heavily embedded Class 0 protostars by the presence of their faint reflection nebulosities.

In chapter 3, a multi-wavelength study of a sample of HH objects without an identified energy source was conducted to establish what fraction were part of giant HH outflows. By using a combination of SERC IVN, deep CCD R/I band imaging and reprocessed far–infrared IRAS HIRES data, potential energy sources were identified. For the majority of candidates, physical parameters such as T_d, L_{bol}, spectral index, class (0 $\rightarrow$ III) were derived from their spectral energy distribution. Not all surveyed HH objects were found to belong to giant flows. This is mostly due to the evolutionary status of the outflow source. As the source evolves towards the main sequence, there is a systematic decrease in terminal velocity of outflow ejecta. This slow–moving material produces at most very weak shocks with the surrounding interstellar medium, which is tenuous. Therefore, the likely-hood of detecting giant HH flows will be greatest when the outflow source is in the Class 0 or early

Class I stage of evolution. In searching for candidate energy sources, several interesting new pre–main sequence objects were identified from existing ESO/SERC plate material. These objects (MZ 2 and MZ 3), display ring–like nebulosities seen in many FU Orionis objects. With the combination of existing ESO/SERC and new AAO/UKST Hα material, it will be possible to identify many more of these objects so that we can create a large sample from which we can understand mass outflow from young stellar objects and identify its relationship to the overall process of star formation.

In chapter 4, first results obtained with the AAO/UKST Hα Survey of the Southern Galactic Plane were presented. With its large field of view ($4^\circ \times 4^\circ$) and superb imaging resolution (provided by the Hα filter and TechPan emulsion combination), the survey is particularly suited to identifying new HH objects and outflows where strong emission and reflection nebulosity have usually hindered such surveys. Using a single, wide–field Hα film of the Orion region, highly collimated jets and bow shock structures were identified. These objects have previously been seen only as faint nebulosities on deep ESO R plates. With a follow–up CCD narrowband [SII], Hα and red continnum survey, it was found that all objects display HH–type emission, while deep CCD I band imaging, IRAS HIRES images and exising near–infrared surveys revealed possible driving sources for each HH object.

Four parsec–scale flows have been found to originate from within the L1641–N infrared cluster in the Orion A (L1641) giant molecular cloud (GMC). The southern portion of the Orion B GMC (L1630) hosts the known objects HH 94/95. With Hα material, it has been shown these objects are possibly part of a 8.5 pc flow originating from the Class 0 protostar NGC 2023 mms1, while a 1 pc flow was associated with the Ori I–2 cometary globule. For many of the new giant HH flows, the co–existience of large arc–like bow shocks and highly collimated jets stronly favours the "unified" models of HH jet and molecular CO outflows. The knots observed at the apex of the large bow shocks correspond to internal working surfaces which intercept material from the jet and eject it sideways. This sideways ejection leads to a turbulent envelope which is seen as the slower–moving molecular CO outflow. In most cases, the CO outflow was not found to be co–existient with the optical HH flow. This can be understood by examining the size of the parental molecular cloud core which are only a fraction of a parsec in size. For distances less than the width of a parental core, the HH and CO flows are spatially coincident, but once the HH flow leaves the confines of the core, the HH flow does not entrain CO bearing gas, but more likely atomic and/or ionized gas not detectable in CO.

With Hα material alone, many of these giant flows have been shown to be significant contributors to the large–scale movement of gas and dust in the L1630 and L1641 molecular clouds. For a specific example, the 10 pc flow HH 306–310/SMZ 23 in L1641–N was shown to have have excavated a total mass of $\sim$ 250 $M_{\odot}$ from the L1641 molecular cloud. It may well be that the overall morphology of the northern Orion A GMC is a direct result of molecular gas interacting with the Ori OB I association (subgroups a, b, and c), but the internal structure of the southern half (δ below -6°) is determined by giant HH flows and to a lesser degree, their sub–parsec counterparts. With the AAO/UKST Hα survey, it has been possible to detect these flows and show how they are directly responsible for the disruption of molecular gas and dust which may provide a mechanism for self–regulated star formation. For the majority of giant HH flows in Orion, these highly compressed regions are sites of dense cores identidied by CS (J=1–0) and CS (J=2–1) observations. As the CS lines trace densities exceeding 10^5 cm^{-3}, these cores most probably represent sites where Class 0 protostars are just beginning to form.

Finally, in chapter 5, initial results of a survey for giant flows in the Canis Major OB1/R1 association reveals that the Z CMa/HH 160 outflow appears longer than previously expected. Coupled with AAO/UKST Hα material, narrowband [SII], Hα, and red continuum CCD imaging suggests this flow is 6.7 pc in length, or 1.9 times larger than previously thought. It is interesting this high–luminosity Class II source displays a highly collimated jet. For the low–luminosity HH outflow sources, it has been shown that when a source is close to, or within the Class II stage of evolution, there is no trace of a highly collimated jet or well–defined large–scale bow shocks several parsec from the driving source. With the AAO/UKST Hα Survey, it will be interesting to identify more sources like Z CMa so that we can understand if its observed properties are intrinsic to high–luminosity sources or some as yet, undefined property.

Bibliography

Adams, F.C., Lada, C.J., Shu, F.H., 1987, ApJ, 312, 865

Allen, L., 1996, Ph.D. thesis, Univ. Massachusetts

André, P., Montmerle, T., 1994, ApJ, 420, 837

André, P., Ward-Thompson, D., Barsony, M., 1993, ApJ, 406, 122

Anglada, G., Villuendas, E., Estalella, R., Beltrán, M.T., Rodríiguez, L.F., Torrelles, J.M., Curiel, S., 1998, AJ, 116, 2953

Anglada, G., Sepúlveda, I., Gómez, J.F., 1997 A&AS, 121, 255

Anglada, G., Rodríguez, L.F., Torrelles, J.M., 1996, ApJ, 473, L123

Arce, H.G., Goodman, A.A., ApJ, 554, 132

Aumann, H.H., Fowler, J.W., Melnyk, M., 1990, AJ, 99, 1674

Bacciotti, F., Eislöffel, J., 1999, A&A, 342, 717

Bachiller, R., 1996, ARA&A, 34, 111

Bachiller, R., Martin-Pintado, J., Planesas, P., 1991, A&A, 251, 639

Bachiller, R., Martin-Pintado, J., Tafalla, M., Cernicharo, J., Lazareff, B., 1990, A&A, 231, 174

Bally, J., Reipurth, R., Lada, C.J., Billawala, Y., 1999, AJ, 117, 410

Bally, J., Devine, D., Alten, V., Sutherland, R.S. 1997, ApJ, 478, 603

Bally, J., Devine, D., Reipurth, B., 1996, ApJ, 473, L49

Bally, J., Devine, D., Fesen, R.A., Lane, A.P. 1995, ApJ, 454, 345

Bally, J., Devine, D., 1994, ApJ, 428, L65

Bally, J., Langer, W.D., Liu, W., 1991, ApJ, 383, 645

Bally, J., Stark, A.A., Wilson, R.W., Langer, W.D., 1987, ApJ, 312, L45 (B87)

Bally, J., Lada, C.J., 1983, ApJ, 265, 824

Barsony, M., Ward-Thompson, D., André, P., O'Linger, J., 1998, ApJ, 509, 733

Beckwith, S., Gatley, I., Matthews, K., Neugebauer, G., 1978, ApJ, 223, L41

Beichman, C.A., Myers, P.C., Emerson, J.P., Harris, S., Mathieu, R., Benson, P.J., Jennings, R.E., 1986, ApJ, 307, 337

Bence, S.J., Padman, R., Isaak, K.G., Wiedner, M.C., Wright, G.S., 1998, MNRAS, 299, 965

Bence, S.J., Richer, J.S., Padman, R., 1996, MNRAS, 279, 866

Bessell, M.S., 1979, PASP, 91, 589

Blitz, L., 1978, Ph.D. thesis, Columbia University

Blondin, J.M., Königl, A., Fryxell, B.A. 1989, ApJ, 337, L37

Böhm, K.H., 1956, ApJ, 123, 379

Böhm, K.H., Solf, J., 1990, ApJ, 348, 297

Böhm, K.H., Mannery, E., Brugel, E.W., 1980, ApJ, 235, 137

Bontemps, S., André, P., 1997, in Poster Proc. IAU Symp. 182, *Herbig-Haro Flows and the Birth of Low Mass Stars*, eds. F. Malbet & A. Castets, Kluwer, p63

Bontemps, S., André, P., Terebey, S., Cabrit, S., 1996, A&A, 311, 858

Brand, J., Blitz, L., Wouterloot, J.G.A., 1986, A&AS, 65, 537

Brown, A.G.A., De Geus, J., De Zeeuw, P.T., 1994, A&A, 289, 101

Brugel, E.W., Mundt, R., Bührke, T., 1984, ApJ, 287, 73

Cabrit, S., Raga, A., Gueth, F., 1997, in IAU Symp. 182, *Herbig-Haro Flows and the Birth of Low Mass Stars*, eds. B. Reipurth and C. Bertout, Kluwer, p163

Cabrit, S., Bertout, C., 1992, A&A, 261, 274

Cabrit, S., Bertout, C., 1990, ApJ, 348, 530

Cambrésy, L, 1999, A&A, 345, 965

Cantó, J., Raga, A.C., 1998, MNRAS, 297, 383

Cernicharo, J., Bachiller, R., Duvert, G., Gonzalez-Alfonso, E., Gomez-Gomzalez, J., 1992, A&A, 261, 589

Chen, H., Grenfell, T. G., Myers, P. C., Hughes, J. D., 1997, ApJ, 478, 295

Chen, H., Zhao, J.-H., Ohashi, N., 1995, ApJ, 450, L71

Chen, H., Tokunaga, A.T., 1994, ApJS, 90, 149

Chen, H., Tokunaga, A.T., Strom, K.M., Hodapp, K.-W., 1993, ApJ, 407, 639

Chini, R., Reipurth, B., Sievers, A., Ward-Thompson, D., Haslam, C.G.T., Kreysa, E., Lemke, R., 1997, A&A, 325, 542

Claria, J.J., 1974, A&A, 37, 229

Codella, C., Palumbo, G.G.C., Pareschi, G., Scappini, F., Caselli, P., Attolini, M.R., 1995, MNRAS, 276, 57

Cohen, M., 1990, ApJ, 354, 701

Cohen, M., Schwartz, R.D., 1987, ApJ, 316, 311

Cohen, M., Bieging, J.H., 1986, AJ, 92, 1396

Cohen, M., Bieging, J.H., Schwartz, P.R., 1982, ApJ, 253, 707

Cohen, M., Kuhi, L.V., 1979, ApJS, 41, 743

Cohen, M., Schwartz, R.D., 1976, MNRAS, 174, 137

Corcoran, D., Ray, T.P., 1995, A&A, 301, 729 (CR95)

Cudworth, K.M., Herbig, G.H., 1979, AJ, 84, 548

Curiel, S., Rodríguez, L. F., Canto, J., Torrelles, J. M., 1989, RMxAA, 17, 137

Dent, W.R.F., Matthews, H.E., Ward-Thompson, D., 1998, MNRAS, 301, 1049 (DMW98)

Depoy, D.L., Lada, E.A., Gatley, I., Probst, R., 1990, ApJ, 356, 55

Devine, D., Reipurth, B., Bally, J., 1999, AJ, 118, 972

Devine, D., Bally, J., Reipurth, B., Shepherd, D., Watson, A., 1999, AJ, 117, 2931

Devine, D., Bally, J., Reipurth, B., Heathcote, S., 1997, AJ, 114, 2095

Davis, C.J., Eislöffel, J., 1995, A&A, 300, 851 (DE95)

Davis, C.J., Mundt, R., Eislöffel, J., Ray, T.P., 1995, AJ, 110, 766

de Vries, C.P., Brand, J., Habing, H.J., Israel, F.P., de Graauw, Th., Wouterloot, J.G.A., van de Stadt, H., 1984, A&AS, 56, 333

Dopita, M.A., 1978, ApJS, 37, 117

Dopita, M.A., Evans, R., Schwartz, R.D., 1982, ApJ, 263, 73

Draine, B.T., Lee, H.M. 1984, ApJ, 285, 89

Edwards, S., Snell, R.L., 1984, ApJ, 281, 237

Edwards, S., Snell, R.L., 1983, ApJ, 270, 605

Eislöffel, J., Mundt, R., 1997, AJ, 114, 280

Eislöffel, J., Smith, M.D., Davis, C.J., Ray, T.P., 1996, AJ, 112, 2086

Eislöffel, J., Mundt, R., 1994, ApJ, 284, 530

Elias, J.H., 1980, ApJ, 241, 728

Evans, N.J., II, Balkum, S., Levreault, R.M., Hartmann, L., Kenyon, S., 1994, ApJ, 424, 793

Fernandes, A.J.L., Brand, P.W.J.L., 1995, MNRAS, 274, 639

Fich, M., Blitz, L., Stark, A.A., 1989, ApJ, 342, 272

Foster, P.N., Boss, A.P., 1996, ApJ, 468, 784

Fukui, Y., 1989, in ESO Workshop on *Low Mass Star Formation and Pre-Main Sequence Objects*, ed. Bo Reipurth, p95

Fukui, Y., Iwata, T., Mizuno, A., Ogawa, H., Takaba, H., 1989, Nature, 342, 161

Fukui, Y., Takaba, H., Iwata, T., Mizuno, A., 1988, ApJ, 325, L13

Fukui, Y., Sugitani, K., Takaba, H., Iwata, T., Mizuno, A., Ogawa, H., Kawabaa, K., 1986, ApJ, 311, L85

Genzel, R., Reid, M.J., Moran, J.M., Downes, D., 1981, ApJ, 244, 884

Goodrich, R.W., 1987, PASP, 99, 116

Gredel, R., 1994, A&A, 292, 580

Gredel, R., Reipurth, B., 1994, A&A, 289, L19

Gueth, F., Guilloteau, S., 1999, A&A, 343, 571

Gum, C.S., 1955, MmRAS, 67, 155

Hanner, M.S. 1988, NASA Conf. Pub. 3004, 22

Hambly N.C., Miller L., MacGillivray H.T., Herd J.T., Cormack, W.A., 1998, MNRAS 298, 897

Haro, G., 1953, ApJ, 117, 73

Haro, G., 1952, ApJ, 115, 572

Haro, G., Minkowski, R., 1960, AJ, 65, 490

Hartigan, P., Morse, J.A., Raymond, J.C. 1995, ApJ, 444, 943

Hartigan, P., Raymond, J., Meaburn, J., 1990, ApJ, 362, 624

Hartigan, P., Lada, C.J., 1985, ApJS, 59, 383

Hartley, M., Tritton, S.B., Manchester, R.N., Smith, R. M., Goss, W.M., 1986, A&AS, 63, 27

Hartmann, L., Kenyon, S.J., 1996, ARA&A, 34, 207

Hartmann, L., Raymond, J.C., 1984, ApJ, 276, 560

Heathcote, S., Morse, J.A., Hartigan, P., Reipurth, B., Schwartz, R.D., Bally, J., Stone, J.M., 1996, AJ, 112, 1141

Herbig, G.H., 1974, *Lick Observatory Bulletin No. 658.*

Herbig, G.H., 1968, ApJ, 152, 439

Herbig, G.H., 1951, ApJ, 113, 697

Herbig, G.H., 1950, ApJ, 111, 11

Herbig, G.H., Jones, B.F., 1983, AJ, 88, 1040

Herbig, G.H., Jones, B.F., 1981, AJ, 87, 1223

Herbst, W., Racine, E., Warner, J.W., 1978, ApJ, 223, 471

Herbst, W., 1975a, AJ, 80, 212

Herbst, W., 1975b, AJ, 80, 683

Hester, J.J., Stapelfeldt, K.R., Scowen, P.A., 1998, AJ, 116, 372

Hirth, G.A., Mundt, R., Solf, J., 1997, A&AS, 126, 437

Hildebrand, R.H., 1983, QJRAS, 24, 267

Hurt, R.L, Barsony, M., 1996, ApJ, 460, 45

Hodapp, K.-W, 1994, ApJS, 94, 615

Hodapp, K.-W., Deane, J., 1993, ApJS, 88, 119

Hunter, T.R., Churchwell, E., Watson, C., Cox, P., Benford, D.J., Roelfsema, P.R., AJ, 119, 2711

Jankovics, I., Appenzeller, I., Krautter, J., 1983, PASP, 95, 883

Johnstone, D., Bally, J., 1999, ApJ, 510, L49

Jones, B.F., Herbig, G.H., 1982, AJ, 87, 1223

Jones, B.F., Herbig, G.H., 1979, AJ, 84, 1872

Joy, A.H., 1942, PASP, 54, 15

Knee, L.B.G., Sandell, G., 2000, A&A, 361, 671

Königl, A., 1995, RMxAC, 1, 275

Koresko, C.D., Beckwith, S.V.W., Ghez, A.M., Matthews, K., Neugebauer, G., 1991, ApJ, 102, 2073

Kumar, M.S. Nanda, Anandarao, B.G., Davis, C.J., 1999, A&A, 344, L9

Kwan, J., Scoville, N., 1976, ApJ, 210, L39

Lada C.J., 1987, in *Star Forming Regions*, eds., Peimbert, M. & Jugaku, J., Reidel, p1

Lada, C.J., 1985, ARA&A, 23, 267

Lada, C.J., Wilking, B.A., 1984, ApJ, 287, 610

Lada, E.A., Evans, N.J., II, Depoy, D.L., Gatley, I., 1991, ApJ, 371, 171

Lada, E.A., Bally, J., Stark, A.A., 1991, ApJ, 368, L432

Langer, W.D., Wilson, R.W., Goldsmith, P.F., Beichman, C.A., 1989, ApJ, 337, 355

Lamzin, S.A., Teodorani, M., Errico, L., Vittone, A.A., Kolotilov, E.A., Miroshnichenko, A.S., Yudin, R.V., 1998, ARep, 42, 630

Launhardt, R., Mezger, P.G., Haslam, C.G.T., Kreysa, E., Lemke, R., Sievers, A., Zylka, R., 1996, A&A, 312, 569

Levine, D.M., Surace, J., 1993, in *IPAC User's Guide*, 5th ed., IPAC, 6-1

Levreault, R.M., 1988a, ApJS, 67, 283

Levreault, R.M., 1988b, ApJ, 300, 897

Leinert, C., Richichi, A., Hass, M., 1997, A&A, 318, L472

Liseau, R., Lorenzetti, D., Nisini, B., Spinoglio, L., Moneti, A., 1992, A&A, 265, 577

López, R., Rosado, M., Riera, A., Noriega-Crespo, A., Raga, A.C., Estalella, R., Anglada, G., Le Coarer, E., Langarica, R., Tinoco, S., Cantó, J., 1998, AJ, 116, 845

Maddalena, R. J., Moscowitz, J., Thaddeus, P., Morris, M., 1986 ApJ, 303, 375

Magazzu, A., Martin, E.L., 1994, A&A, 287, 571

Malin, D.F., Ogura, K., Walsh, J.R., 1987, MNRAS, 227, 361

Margulis, M., Lada, C.J., Young, E.T., 1989, ApJ, 345, 906

Martí, J., Rodríguez, L.F., Reipurth, B., 1998, ApJ, 502, 337

Martí, J., Rodríguez, L.F., Reipurth, B., 1993, ApJ, 416, 208

Massi, F., Lorenzetti, D., Vitali, F., 1997, in Poster Proc. IAU Symp. 182, Herbig-Haro Flows and the Birth of Low Mass Stars, eds. F. Malbet & A. Castets, Kluwer, p21

Masson, C., Chernin, L.M., 1993, ApJ, 414, 230

Machnik, D.E., Hettrick, M.C., Kutner, M.L., Dickman, R.L., Tucker, K.D., 1980, ApJ, 242, 121

Mattila, K., Liljeström, T., Toriseva, M., 1989, in ESO Workshop on *Low Mass Star Formation and Pre-Main-Sequence Objects*, ed. Bo Reipurth, p153

McCaughrean, M.J., 1997, in IAU Symp. 182, *Herbig-Haro Flows and the Birth of Low Mass Stars*, eds. B. Reipurth and C. Bertout, Kluwer, p597.

McCaughrean, M.J., Rayner, J.T., Zinnecker, H., 1994, ApJ, 436, L189

McKee, C.F., 1989, ApJ, 345, 782

Mill, J.D., O'Neil, R.R., Price, S., Romick, G.J., Uy, O.M., Gaposchkin, E.M., 1994, J. Spacecraft Rockets, 31, 900

Miller, L., Cormack, W., Paterson, M., Beard, S., Lawrence, L., 1992, in *Digitised Optical Sky Surveys*, MacGillivray, H.T. & Thomson, E.B., eds., Kluwer, p133

Moffat, A.F.J., Vogt, N., 1975, A&AS, 20, 125

Morgan, J.A., Schloerb, F.P., Snell, R.L., Bally, J., 1991, ApJ, 376, 618

Morgan, J.A., Bally, J., 1991, ApJ, 372, 505

Morse, J.A., Hartigan, P., Heathcote, S., Raymond, J.C., Cecil, G., 1994, APJ, 425, 738

Morse, J.A., Heathcote, S., Hartigan, P., Cecil, G., 1993, AJ, 106, 1139

Mundt, R., 1988, in *Formation and Evolution of Low Mass Stars*, A.K. Dupree, Lago, M.T.V.T., eds, Kluwer, p257

Mundt, R., Brugel, E.W., Bührke, T., 1987, ApJ, 319, 275

Mundt, R., Fried, J.W., 1983, ApJ, 274, L83

Mundt, R., Bastian, U., 1980, A&AS, 39, 245

Murphy, D.C., May, J., 1991, A&A, 247, 202

Noriega-Crespo, A., Garnavich, P.M., 1994, RMxAA, 28, 173

Ogura, K., 1995, ApJ, 450, 23

Ogura, K., 1993, MNRAS, 262, 735

Ogura, K., 1991, AJ, 101, 1803

Ogura, K., 1990, PASP, 102, 1366

Ogura, K., Nakano, M., Sugitani, K., Liljeström, T., 1998, A&A, 338, 576

Ogura, K., Sugitani, K., 1998, PASA, 15, 91

Ogura, K., Walsh, J.R., 1992, ApJ, 400, 248

Ogura, K., Walsh, J.R., 1991, AJ, 101, 185

O'Linger, J., Wolf-Chase, G., Barsony, M., Ward-Thompson, D., 1999, ApJ, 515, 696

Ossenkopf, V., Henning, Th., Mathis, J.S. 1992, A&A, 261, 567

Osterbrock, D.E., 1958, PASP, 70, 399

Parker, Q.A., Malin, D.F., Cannon, R.D., Phillipps, S., Russell, K.S., 2000, in preparation

Parker, Q.A., Phillipps, S., 1998a, PASA, 15, 28

Parker, Q.A., Phillipps, S., 1998b, A&G, 39, 10

Parker, Q.A., Bland-Hawthorn, J., 1998, PASA, 15, 33

Parker, Q.A., Phillipps, Morgan, D.H., 1995, in IAU Colloq. 148, ASP conf.ser. 84, eds. J. Chapman, R. Cannon, S. Harrison & B. Hidayat, p96

Phelps, R.L., Lada, E.A., 1997, ApJ, 477, 176

Pichè. F., Howard, E.M., Pipher, J.L., 1995, MNRAS, 275, 711

Poetzel, R., Mundt, R., Ray, T.P., 1992, A&A, 262, 229

Poetzel, R., Mundt, R., Ray, T.P., 1989, A&A, 224, 13

Pravdo, S.H., Rodríguez, L.F., Curiel, S, Cantó, J., Torrelles, J.M., Becker, R.H., Sellgren, K., 1985, ApJ, 293, L35

Prusti, T., Clark, F.O., Whittet, D.C.B., Laurijs, R.J., Zhang, C.Y., 1991, MNRAS, 251, 303

Pudritz, R.E., 1986, PASP, 98, 709

Raga, A.C., 1988, ApJ, 335, 820

Raga, A.C., Cabrit, S., 1993, A&A, 278, 267

Raga, A.C., Canto, J., Calvet, N., Rodríguez, L.F., Torrelles, J.M., 1993, A&A, 276, 539

Raga, A.C., Böhm, K.H., 1987, ApJ, 323, 193

Ray, T.P. 1987, A&A, 171, 145

Raymond, J.C., 1979, ApJS, 39, 1

Reike, G.H., Lebofsky, M.J., 1985, ApJ, 288, 618

Reipurth, B., Heathcote, S., Yu, K. C., Bally, J., Rodríguez, L.F., ApJ, 2000, 534, 317

Reipurth, B., 1999, *A General Catalogue of Herbig-Haro Objects*, 2. edition, http://casa.colorado.edu/hhcat

Reipurth, B., Bally, J., Fesen, R.A., Devine, D., 1998, Nature, 396, 343

Reipurth, B., Heathcote, S., Roth, M., Noriega-Crespo, A., Raga, A.C., 1993, ApJ, 408, L49

Reipurth, B., 1989a, RMxAA, 19, 38

Reipurth, B., 1989b, A&A, 220, 249

Reipurth, B., 1985, A&AS, 61, 319

Reipurth, B., 1981, A&AS, 44, 379

Reipurth, B., Yu, K.C., Rodríguez, L.F., Heathcote, S., Bally, J., 1999, A&A, 352, L83

Reipurth, B., Raga, A.C., 1999, in *The Origin of Stars and Planetary Sys-*

tems, C.J. Lada and N.D. Kylafis, eds., Kluwer, p267

Reipurth, B., Devine, D., Bally, J., 1998, AJ, 116, 1396 (RBD98)

Reipurth, B., Rodríguez, L.F., 1998, RMxAA, 34, 13

Reipurth, B., Bally, J., Devine, D., 1997, AJ, 114, 2708 (RBD97)

Reipurth, B., Aspin, C.A., 1997, AJ, 114, 2700

Reipurth, B., Nyman, L.-A., Chini, R., 1996, A&A, 314, 258

Reipurth, B., Raga, A.C., Heathcote, S., 1996, A&A, 311, 989

Reipurth, B., Zinnecker, H., 1993, A&A, 278, 81

Reipurth, B., Chini, R., Krugel, E., Kreysa, E., Sievers, A., 1993a, A&A, 273, 221

Reipurth, B., Heathcote, S., Roth, M., Noriega-Crespo, A., Raga, A.C., 1993b, ApJ, 408, L49

Reipurth, B., Raga, A.C., Heathcote, S., 1992, ApJ, 392, 145

Reipurth, B, Graham, J.A., 1988, A&A, 202, 219 (RG88)

Reipurth, B., Bally, J., Graham, J.A., Lane, A.P., Zealey, W.J., 1986, A&A, 164, 51

Rodgers, A.W., Campbell, C.T., Whiteoak, J.B., 1960, MNRAS, 121, 103

Rodríguez, L.F., Reipurth, B., 1994, A&A, 281, 882

Rodríguez, L.F., Ho, P.T.P., Torrelles, J.M., Curiel, S., Cantó, J., 1990, ApJ, 352, 645

Sandell, G., Avery, L.W., Baas, F., Coulson, I., Dent, W.R.F., Friberg, P., Gear, W.P.K., Greaves, J., Holland, W., Jenness, T., Jewell, P., Lightfoot, J., Matthews, H.E., Moriarty-Schieven, G., Prestage, R., Robson, E.I., Stevens, J., Tilanus, R.P.J., Watt, G.D., 1999, ApJ, 519, 236

Sandqvist, A., 1977, A&A, 57, 467

Sanduleak, N., 1971, PASP, 83, 95

Saraceno, P., André, P., Ceccarelli, C., Griffin, M., Molinari, S., 1996, A&A, 309, 827

Scarrott, S.M., 1988, MNRAS, 231, 1055

Schild, R., Weir, N., Mathieu, R.D., 1989, AJ, 97, 1110

Schmidt, G.D., Miller, J.S., 1979, ApJ, 234, L191

Schwartz, R.D., 1978, ApJ, 223, 884

Schwartz, R.D., 1977, ApJS, 35, 161

Schwartz, R.D., Dopita, M.A, 1980, ApJ, 236, 543

Sellgren, K., 1983, AJ, 88, 985

Sharpless, S., 1959, ApJS, 4, 257

Shepherd, D.S., Kurtz, S.E., 1999, ApJ, 523, 690

Shevchenko, V.S., Ezhkova, O.V., Ibrahimov, M.A., van den Ancker, M.E., Tjin A Djie, H.R.E., 1999, MNRAS, 310, 210

Shu, F.H., Adams, F.C., Lizano, S., 1987, ARA&A, 25, 23

Smith, M.D. 1993, ApJ, 406, 520

Smith, M.D. 1994, MNRAS, 266, 238

Snell, R.L., Schloerb, F.P., Heyer, M.H., 1989, ApJ, 337, 739

Snell, R.L., Loren, R.B., Plambeck, R.L., 1980, ApJ, 239, 17

Solf, J., Böhm, K.H., Raga, A., 1988, ApJ, 334, 229

Stanke, T., McCaughrean, M.J., Zinnecker, H., 2000, A&A, 355, 639

Stanke, T., McCaughrean, M.J., Zinnecker, H., 1999, A&A, 350, L43

Stanke, T., McCaughrean, M.J., Zinnecker, H., 1998, A&A, 332, 307 (SMZ98)

Stapelfeldt, K.R., Scoville, N.Z., Beichman, C.A., Hester, J.J., Gautier, T.N., III, 1991, ApJ, 371, 226

Steppe, H., 1977, A&AS, 27, 415

Strom, K.M., Strom, S.E., Merrill, K.M., 1993, ApJ, 412, 233

Strom, K.M., Strom, S.E., 1993, ApJ, 412, 63

Strom, K.M., Strom, S.E., Wilkin, F.P., Carrasco, L., Cruz-Gonzalez, I., Recillas, E., Serrano, A., Seaman, R.L., Stauffer, J.R., Dai, D., Sottile, J., 1990, ApJ, 362, 168

Strom, K.M., Margulis, M., Strom, S.E., 1989a, ApJ 346, L33

Strom, K.M., Margulis, M., Strom, S.E., 1989b, ApJ 345, L79

Strom, K.M., Strom, S.E., Wenz, M., Wolff, S.C., Morgan, J., 1986, ApJS, 62, 39

Strom, K.M., Strom, S.E., Vrba, F.J., 1976, AJ, 81, 320

Strom, S.E., Grasdalen, G.L., Strom, K.M., 1974, ApJ, 191, 111

Sugitani, K., Fukui, Y., Mizuni, A., Ohashi, N., 1989, ApJ, 342, L87

Tatematsu, K., Umemoto, T., Heyer, M.H., Hirano, N., Kameya, O., Jaffe, D.T., 1998, ApJS, 118, 517

Tatematsu, K. et al. 1993, ApJ, 404, 643

van den Bergh, S., 1966, AJ, 71, 990

van den Bergh, S., Herbst, E., 1975, AJ, 80, 208

von Hippel, T., Bell-Burnell, S.J., Williams, P.M., 1988, A&AS, 74, 431

Walsh, J.R., Ogura, K., Reipurth, B., 1992, MNRAS, 257, 10

Walter, F.M., 1987, PASP, 99, 31

Wilking, B.A., Blackwell, J.H., Mundy, L.G., 1990, AJ, 100, 758

Wilking, B.A., Lada, C.J., Young, E.T., 1989, ApJ, 340, 823

Wiramihardja, S.D., Kogure, T., Yoshida, S., Nagano, M., Ogura, K., Iwata, T., 1991, PASJ, 43, 27

Wiramihardja, S.D., Kogure, T., Nakano, M., Yoshida, S., 1986, PASJ, 38, 395

Woitas, J., Leinert, CH., 1998, A&A, 338, 122

Wolf-Chase, G.A., Barsony, M., O'Linger, J., AJ, 120, 1467

Wouterlout, J.G.A., Henkel, C., Walmsley, C.M., 1989, A&A, 215, 131

Wouterlout, J.G.A., Walmsley, C.M., 1986, A&A, 168, 237

Wu, Y., Huang, M., He, J., 1996, A&AS, 115, 283

Young, E.T., Lada, C.J., Wilking, B.A., 1986, ApJ, 304, 45

Yu, K.C., Billawala, Y., Bally, J., 1999, AJ, 118, 2940

Yu, K.C., Bally, J., Devine, D., 1997, ApJ, 485, L45

Zealey, W.J., Mader, S.L., Tabone, A.M.T., Randell, P.R., Walker, A.J., 2000, in preperation

Zealey, W.J., Mader, S.L., 1998, PASA, 15, 165

Zealey, W.J., Mader, S.L., 1997, PASA, 14, 200

Zealey, W.J., Moore, G.K.G., Ihnat, P., Suters, M.G., 1994, "Working group on Wide-field imaging", IAU Commission 9, Newsletter 6.

Zealey, W.J., Suters, M.G., Randall, P.R., 1993, PASA, 10, 203

Zealey, W.J., Williams, P.M., Taylor, K.N.R., Storey, J.W.V., Sandell, G., 1986, A&A, 158, L9

Zinnecker, H., Mundt, R., Geballe, T.R., Zealey, W.J., 1989, ApJ, 342, 337

Zuckerman, B., Kuiper, T.B.H., Rodriguez Kuiper, E.N., 1976, ApJ, 209, L137